Development of a Mechanism-Based Correlation Model to Predict the Effects of Freezing and Thawing on the Stability of Vesicular Dispersions

Sharanda Francis

Department of Chemistry

Imperial College London

A Thesis Submitted for the Degree of Doctor of Philosophy

October 2018

This thesis and the work within was written and carried out by Sharanda Francis

The copyright of this thesis rests with the author and is made available under a Creative Commons Attribution Non-Commercial No Derivatives licence. Researchers are free to copy, distribute or transmit the thesis on the condition that they attribute it, that they do not use it for commercial purposes and that they do not alter, transform or build upon it. For any reuse or redistribution, researchers must make clear to others the licence terms of this work.

Abstract

The phase behaviour of aqueous dioctadecyl dimethylammonium chloride (DODAC) solutions were studied to model the stability of liquid fabric enhancers, when exposed to the environmental stresses of cooler climate regions during transportation or storage. These effects were studied using; SAXS and WAXS, ^{1}H NMR, DOSY and polarised light microscopy, before and after freeze-thawing (FT) of the DODAC bilayers.

The effects upon FT resulted in a FT induced swelling, where the magnitude of this swelling decreased with the addition of $CaCl_2$ to the aqueous DODAC solution. Additionally, in the absence of $CaCl_2$, the cooling properties of the bilayers resulted in a temperature shift of the $L_\alpha \rightarrow L_{\beta'}$ transition from ~31 to ~35 ^{o}C after FT, instead of the two transitions given at ~31 and ~35 ^{o}C in the presence of $CaCl_2$ after FT. This suggests that $CaCl_2$ decreases the changes to the DODAC bilayers and properties, upon FT.

The DODAC aqueous solution is studied for the addition of glycerol and an ethoxylated alcohol surfactant. Glycerol caused swelling of the DODAC bilayers and the ethoxylated alcohol surfactant caused a lateral phase separation of a spherical→planar bilayers transition. These alterations to the DODAC bilayers, minimised the differences between the bilayers before and after FT. Also, it was shown that small unilamellar vesicles promoted the $L_\alpha \rightarrow L_{\beta'}$ transition temperature shift from ~31 to ~35 ^{o}C and a spherical→planar bilayers transition, after FT.

The freezing behaviour of the DODAC bilayers were observed as a cooling induced dehydration which took place after the $L_\alpha \rightarrow L_{\beta'}$ phase transition instead of ice formation

in the bulk water phase, at high pressure and low temperature. This resulted in a metastable freezing state with tilted bilayers, at ~ -2.0 ^{o}C which did not lead to a transition into the L_c phase until incubation at -18 ^{o}C. The effects upon thawing showed a lack of osmotic responsiveness between -5.0 and 15 ^{o}C, and an influx of water at 20 ^{o}C resulted in greater swelling of the DODAC bilayers than before FT.

Acknowledgments

Firstly, I would like to thank my family and friends for their support and for keeping me grounded whilst writing this thesis. I would also like to thank the Membrane Biophysics group for their support and help in my adjustment to the PhD life. Also, my supervisors; Oscar Ces, Rob Law, Nick Brooks, John Seddon and Joao Cabral, for their knowledge and guidance, and continued support. Especially, Oscar and Rob for the multiple updates and help throughout my research, and Nick for help with microscopy and x-ray scattering and all the high-pressure studies.

I would like to give a special thanks to the NMR technicians, especially Pete Haycock, for their endless patience from my multiple questions during the long DOSY experiments and developing my understanding in the technique. I would like to thank my supervisors at Procter and Gamble (P&G); Eric Robles, Pieter Saveyn and Marc Declercq, for my research and their support. Also, I would like to thank the i22 beamline mangers at Diamond Light Source.

I would like to thank my boyfriend for feeding me throughout this experience of writing my thesis.

Contents

1. Introduction 10
   1.1. Surfactants 10
   1.2. Surfactants in Aqueous Solution 11
   1.3. Surfactant Aggregates 13
      1.3.1. Curvature 15
   1.4. Phase 16
      1.4.1. Liquid Crystalline Phases 17
      1.4.2. Lamellar Phase 19
      1.4.3. Gel Phases 19
   1.5. Phase Changes (Fluid ↔ Gel ↔ Crystalline) 21
      1.5.1. Salt Concentration 22
      1.5.2. Surfactant Concentration 24
      1.5.3. Temperature Vs Pressure 24
      1.5.4. Thermal Fluctuations 25
   1.6. Effects of Preparation Techniques 26
   1.7. Research Overview 28
      1.7.1. Freezing Mechanism 28
      1.7.2. Dioctadecyl Dimethylammonium Chloride (DODAC) 30
      1.7.3. Thesis Outline 33
2. Materials and Methods 35
   2.1. Materials 35
      2.1.1. Preparation of Multilamellar Vesicles 35
   2.2. Nuclear Magnetic Resonance (NMR) 36
      2.2.1. Introduction 36
      2.2.2. Basis of NMR 36
      2.2.3. Relaxation Time Constants 37

2.2.4. Chemical Shifts 38
2.2.5. Spin Echo 39
2.2.6. Self-Diffusion 40
2.2.7. Diffusion Ordered Spectroscopy (DOSY) 41
2.2.8. Instrument 42
2.3. Polarised Light Microscopy 44
2.3.1. Introduction 44
2.3.2. Birefringence 44
2.3.3. Instrument 46
2.4. Differential Scanning Calorimetry (DSC) 46
2.4.1. Introduction 46
2.4.2. Measuring Heat Transfer 47
2.4.3. Instrument 48
2.5. X-Ray Scattering 48
2.5.1. Introduction 48
2.5.2. Braggs Peaks 49
2.5.3. Miller Indices 51
2.5.4. Identifying Lamellar Phases 52
2.5.5. Identifying Lamellar Gel Phases 53
2.5.6. Instrument 54
3. The Relationship between Temperature and Pressure for an aqueous DODAC Solution .. 56
3.1. Overview 56
3.2. Introduction 56
3.3. Results 58
3.3.1. Pressure Dependence 58

3.3.2. Pressure-Temperature Relationship 60
3.3.3. Pressure-Temperature Phase Behaviour 62
3.4. Conclusion 64
4. The Comparison between the Temperature and Pressure Controlled Systems 66
4.1. Overview 66
4.2. Introduction 66
4.3. Results 68
4.3.1. Temperature-Controlled Transitions 68
4.3.2. Pressure-Controlled Transitions 71
4.3.3. WAXS Comparisons 74
4.4. Conclusions 77
5. The Effects of $CaCl_2$ and Surfactant Levels on a DODAC System 79
5.1. Overview 79
5.2. Introduction 79
5.3. Results 81
5.3.1. The Effects of Surfactant Concentration 81
5.3.2. The Effects of Salt Concentration 83
5.3.3. Determining the Phase Behaviour using NMR 89
5.4. Conclusion 92
6. The Effects of Chemical Additives on the Behaviour Upon Freeze-Thawing 94
6.1. Overview 94
6.2. Introduction 95
6.3. Results 96
6.3.1. Characterising the DODAC Aqueous Solution 96
6.3.2. The Effects of Chemical Additives 101
6.3.3. The Effects of Glycerol on the Bilayers 104
6.3.4. The Effects of CAE10 on the Bilayers 106
6.4. Conclusion 110
7. Effects of Preparation Technique on the Phase behaviour of a DODAC Solution 112

7.1. Overview 112
7.2. Introduction 113
7.3. Results 114
7.3.1. Sonication Preparation 114
7.3.2. Effect of Sonication 115
7.3.3. Extrusion Preparation 119
7.3.4. Effects of Vesicle Size 119
7.4. Conclusion 123
8. Conclusion 125
8.1. The Effects of $CaCl_2$ on the FT Stability 125
8.1.1. The Effects of Repeat FT Cycles 127
8.2. The Effects of Chemical Additives on the DODAC Bilayers 129
8.2.1. The Effects of Glycerol Upon FT 130
8.2.2. The Effects of $C_{12\text{-}14}(EO)_{10}$ (CAE10) Upon FT 134
8.3. The Low Temperature Effects on a DODAC/$CaCl_2$ System 140
8.4. The Pressure-Temperature (P/T) Relationship 143
9. Appendix 150
10. References 179

1. Introduction

1.1. Surfactants

The word ‘surfactant’ means surface active agent. The definition comes from the ability of a surfactant to reduce the surface tension between two immiscible phases[1]. This is done by adsorption onto the interface between the two phases[2]. Surfactants are used widely in industry for a range of products[3,4], such as; lubrication oils, where surfactant additives increase the lubrication effectiveness of the oil by surfactant adsorption onto a frictional surface[5], food, where surfactants are used as emulsifiers[6], cleaning agents in the form of microemulsions of oil and water separated by surfactants and used to remove oil from cotton[7], drug carriers, where surfactants stabilise proteins that are loaded into lipid based drug-delivery systems[8], biotechnology for the use of surfactants as antimicrobials (microorganism killers) because of the ability of surfactants to dissolve into and alter a cell membrane[9], and microelectronics, where surfactants are used to optimise mixing between carbon nanotubes and a polymer matrix to increase the conductivity and stability of the nanocomposites[10].

Surfactants are molecules with both hydrophobic and hydrophilic parts, their molecular structure comprising a polar ‘head’ group and a hydrocarbon chain ‘tail’ group (figure 1.1). The polar ‘head’ group can be neutral, cationic or anionic. In the presence of a charged ‘head’ group, there will be a counterion present to balance the charge. A surfactant “head” group can also be zwitterionic which is when the single molecule contains both charges[11](figure 1.1c). The hydrophobic ‘tail’ can have various chain

lengths, and can be branched, saturated or unsaturated, where it can exhibit either ‘cis’ or ‘trans’ conformations (figure 1.1 a & b). The molecular structure of the surfactant has high importance because it controls how the surfactant behaves in solution. This chapter will discuss the behaviour of the surfactant molecules as monomer units in solution, for the various conformations of the monomers and the shape of their aggregates, based on the factors that govern the size and shape of the surfactant aggregates in solution including the importance of the surfactant type.

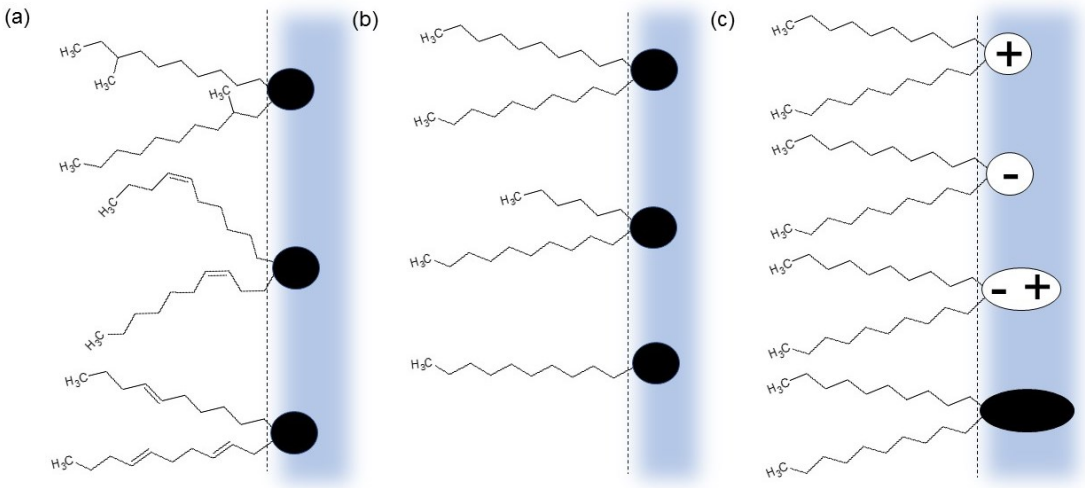


Figure 1.1. Shows a schematic of the different variations for a surfactant molecule, where (a) and (b) are the different types of surfactant “tail” groups which can also have variations in the chain length and (c) are the different types of “head” groups, where the black circles represent non-ionic “head” groups and the cations and anions will have a counterion present. The dashed line represents the air-water boundary, where the blue rectangle is the water phase.

1.2. Surfactants in Aqueous Solution

As mentioned, the surfactants spontaneously aggregate in solution to form various packing structures, where the structures are governed by various factors of the surfactant-solution mixtures, but before these factors can be explained first the process that drives the surfactant aggregation in solution is discussed. The aggregation of the

surfactants is predominantly driven by the 'hydrophobic effect' which is driven by entropy. The formation of aggregates increases disorder of both the water molecules in the aqueous phase and the hydrophobic "tails" in the oil phase. Also, the organised structure of the aggregates reduces the surface tension and promotes more thermodynamically stable interactions of Van der Waals' forces between the surfactant molecules[12]. This thermodynamic contribution leads to the most efficient packing for a single layer of atoms, ie close-packed hexagonal array, where the packing arrangement consist of an atom surrounded by six other atoms (figure 1.2). In this example, the atoms are surfactants.

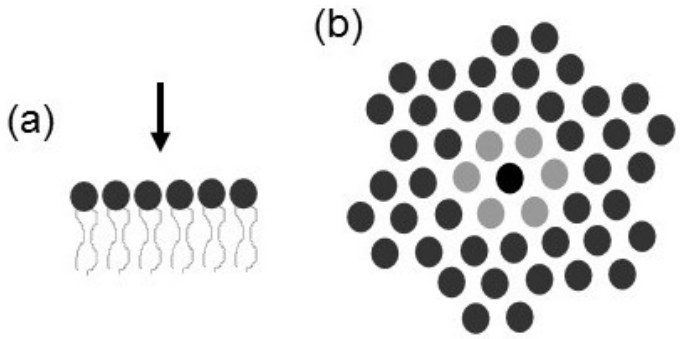


Figure 1.2. Represents the hexagonal packing for a surfactant layer (a), where (b) is the top view of the surfactant layer shown by the arrow in (a). The circles represent the surfactant "head" groups and the lines in (a) represent the hydrophobic "tails". The close-packed hexagonal array (b), is shown by a central black circle surrounded by six light grey circles.

Various factors can change the packing order of the surfactant monomers, such as; branching in the alkyl chains[13] or "cis" unsaturation[14] which increases disorder in surfactant packing, where these variations can change the shape of the surfactant monomer and can create positive or negative curvature in the resultant structure (see

section 1.3.1), ionic effects can impact the repulsive forces between surfactant monomers[15], which are effected by the type or size of the counterions (see section 1.7.2) or the salt concentration of the aqueous solution (see section 5.3.2). The packing order can also be controlled by external factors, such as temperature or pressure, or the preparation method of the surfactant solution[16], where the structure of the aggregate can vary by the degree of mixing[17]. This chapter will discuss these factors, in detail for the effects they have on the structure that surfactants adopt in solution.

1.3. Surfactant Aggregates

Surfactant solutions contain surfactant aggregates that adopt various structures driven by enthalpy. As surfactants are added to an air-water interface, the surfactant monomers will form a binary mixture of (1) surfactants dissolved into the aqueous phase as free amphiphiles and (2) surfactants layered at the boundary with their polar head groups interacting with the aqueous phase[18] (figure 1.3a). This follows a pre-micellar solution of grouped amphiphiles as the surfactant concentration increases[19]. The critical micellar concentration (CMC) is the surfactant concentration which micelles begin to form in the pre-micellar solution (figure 1.3 b). Therefore, micelles are formed at low surfactant levels.

Micellar formation can be measured by its dependency on temperature, where the minimum temperature that micelles are formed is known as the Kraft point[20]. So, a micellar solution exists above the CMC and Kraft point. These parameters measure the effectiveness of the surfactant molecules to form aggregates in solution, and is determined through changes in the solution properties, such as; a sudden decrease in the surface tension[21] or increase in electrical conductivity[22], of the solution.

Micelles are globular structures of surfactant monomers in solution, with the polar “head” groups on the outside surface and the hydrophobic “tail” groups within the globular structure (figure 1.3c). Micellar structures can also have the polar “head” groups within the globular structure and the non-polar “tails” on the outside surface which is driven by the addition of surfactants to a non-polar solvent, where the micelles are considered as inverted. The micellar structure can extend into elongated tubular structures with increasing surfactant chain length and aggregation number (figure 1.3d), where the globular micellar structure is no longer thermodynamically stable when the micelle radius is greater than the length of the surfactant “tail” group. These elongated tubular structures can then organise into various liquid crystalline structures[23,24].

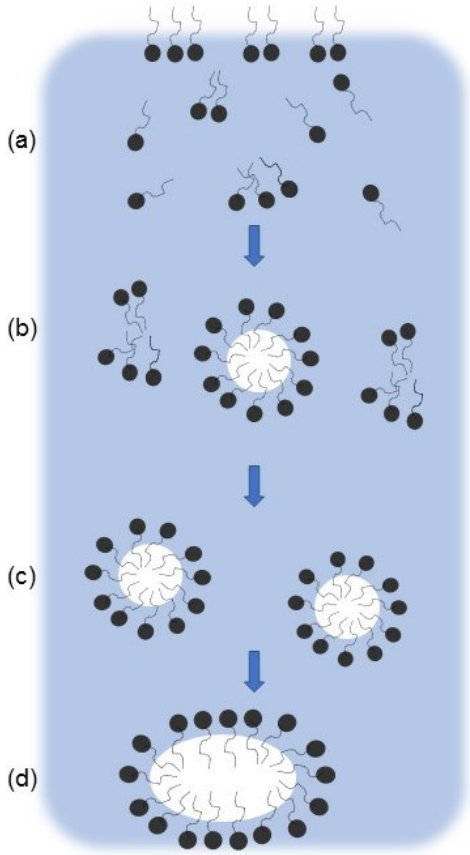


Figure 1.3. Shows a schematic of single tail surfactants in aqueous solution as a binary mixture of dissolved free amphiphiles and a monolayer of amphiphiles that interact at the air-water boundary (a). The dissolved surfactants start to group and form micelles (b). The micellar solution

(c) extends into tubular structures (d), where the micellar structures are represented as a cross-section of their globular structures.

1.3.1. Curvature

The shape of the surfactant structure can be used to determine the most thermodynamically stable curvature that the aggregates will adopt, based on the surfactant volume which is given by the volume of a cone.

$$v = \pi r^2 h/3 \quad [1.1]$$

Where the expression πr^2 is equal to the interfacial area of the surfactant "head" group, a, and h is equal to the length of the surfactant, l.

The surfactant volume is dominated by the hydrocarbon chain(s) volume, v_o, because v_o increases with increasing temperature for a constant hydrocarbon "tail" length, l_c, due to increasing alkyl chain disorder in the "tail" group(s)[25]. Therefore, v = v_o and the approximate length, l, is equal to l_c. So, we can rewrite equation 1.1, in terms of v_o, l_c and a.

$$v_o = a\, l_c/3 \quad [1.2]$$

The packing parameter, P, is defined by v_o, l_c and a, for a spherical aggregate as;

$$P = v_o/a\, l_c \quad [1.3]$$

Therefore, the combination of equations 1.2 and 1.3 gives P = 1/3 for a spherical aggregate with a single "tail" group (v_o is double the size for two "tail" groups, so P = 2/3)[23]. This packing parameter resembles a spherical aggregate with positive curvature (figure 1.4b), with a radius equal to l_c[26].

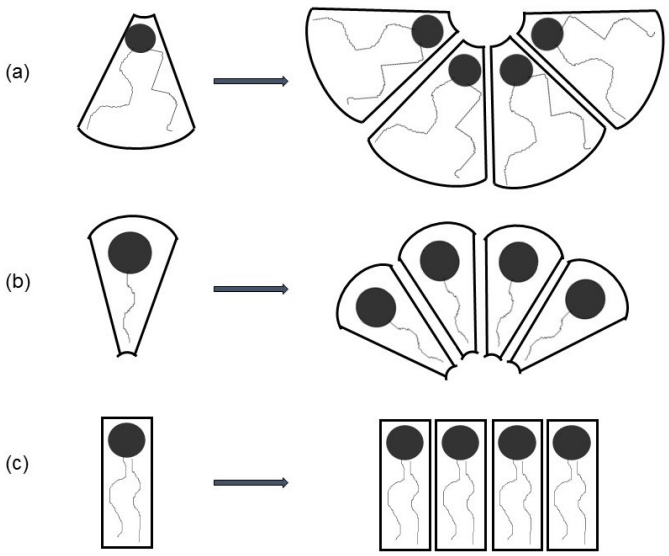


Figure 1.4. Shows the different types of surfactant geometry and the curvature they adopt, where (a) is negative curvature, (b) is positive curvature and (c) no curvature.

The packing parameter defines the shape of the aggregates from spherical to “rod-like” micelles as $1/3 < P \leq 1/2$ and “rod-like” micelles to planar bilayers as $1/2 \leq P \leq 1$, for single tail amphiphiles. Therefore, positive curvature exists when, $P < 1$ and no curvature exists when, $P = 1$ (figure 1.4c). Since positive curvature is given by $P < 1$, the inverse is true for negative curvature, ie $P > 1$[27] (figure 1.4a). Therefore, $P = 3$ (or 3/2 for double “tail” amphiphiles) for an inverse spherical aggregate. The geometry of a surfactant molecule a good approximation for predicting the shape of the surfactant aggregates, but the aggregation shape is predominantly driven by thermodynamics.

1.4. Phase

The phase of matter is governed by structure on an atomic or molecular scale and is uniform throughout that structure. Phase can be used to describe the physical state that can be viewed macroscopically or microscopically. Examples of macroscopic phase are

the three states in which matter exists; gas, liquid and solid. In this sense, phase is defined by the amount of space between particles within an atomic system.

For surfactants in solution the macroscopic phase exists in a fluid, gel or crystalline state[20]. These phases are defined by the mobility of the alkyl "tail" groups of the surfactant molecules within a microscopic phase. When the surfactant systems are crystalline, the movement of the alkyl chains is restricted, where the structure of the aggregates are rigid and frozen in a specific conformation. The gel phase has limited movement in the alkyl chains and can exist in multiple conformations, giving different gel phases. The types of gel phases will be discussed later in this chapter. Finally, the fluid phase which has the highest degree of freedom in the alkyl chains. These macroscopic phases are used to describe the state of a microscopic phase, where the structure which surfactants adopt in solution governs its microscopic phase which can be micellar (as described above) or liquid crystalline.

1.4.1. Liquid Crystalline Phases

In solution, surfactants arrange into various structures. As mentioned previously, these structures are formed by increased polar-polar interactions and the simplest structure is micellar which can grow into tubular structures with various arrangements and greater order. The structures with greater order are known as liquid crystalline states. Surfactant monomers can form multiple bilayer stacks in solution separating into polar and non-polar layers. This is known as a lamellar phase (figure 1.5a). These extended bilayers can join end-on-end to form spherical structures, known as vesicles (figure 1.5b), where the transition between these lamellar structures are common[28,29]. The spherical bilayer can be uni- or multi-lamellar which is to have a single or multiple bilayer(s), respectively, and their size (x) can be defined as giant ($x \geq 1$ μm), large ($1 > x \geq 0.1$ μm) or small ($x < 0.1$ μm)[30,31,32].

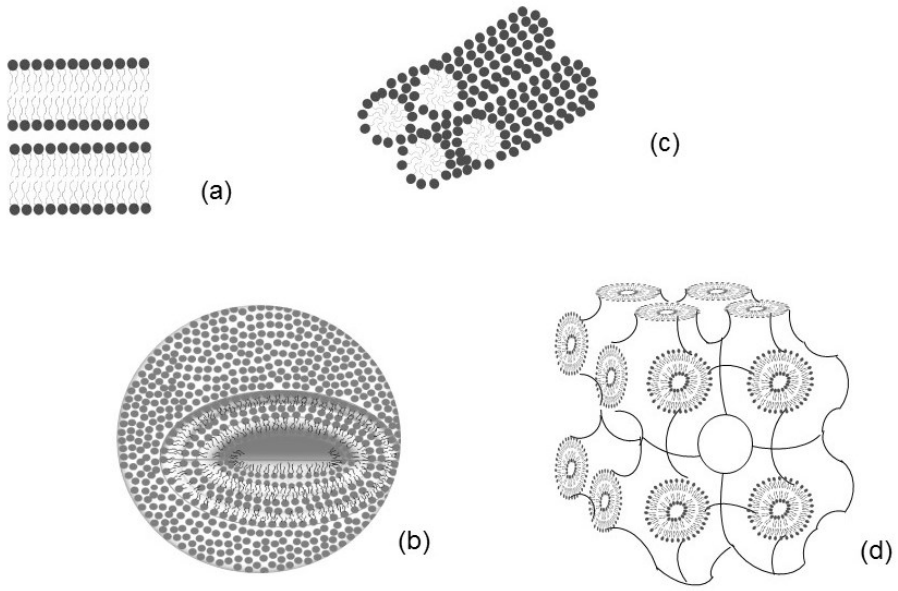


Figure 1.5. Shows an example of the different types of liquid crystalline phases, where (a) is lamellar bilayers, (b) is lamellar vesicles, (c) is hexagonal phase and (d) is an example of a primitive surface type cubic phase.

Liquid crystalline phases can increase in complexity to form hexagonal (figure 1.5c) and cubic (figure 1.5d) structures. Hexagonal phases are extended micellar structures of spherical rods arranged in a hexagonal array separated by a polar solvent or non-polar solvent for an inverted hexagonal phase[33,34,35]. Cubic phases are the most complex of the liquid crystalline phases, with long range order across three-dimensions forming nanochannels throughout the cubic structure, where the main types of cubic phase surfaces are; gyroid (Ia3d), diamond (Pn3m) and Primitive (Im3m) (figure 1.5d) [36,37,38,39]. However, these studies will focus on lamellar liquid crystalline phases of a vesicular nature and the types of gel phases in which they exist.

1.4.2. Lamellar Phase

The lamellar phase can exist in three different states which were explained above as macroscopic phases, where the lamellar phase can be fluid (L_α), gel (L_β) or crystalline (L_c). The microscopic structure of these phases where described as a continuous array of bilayers generally separated by a polar solvent (ie water), where the bilayer thickness is generally the length of two surfactant molecules which depends on the alkyl chain length of the "tail" group[40] and the degree of disorder in the alkyl chain, where the bilayer thickness of the $L_\alpha < L_\beta \leq L_c$[41]. However, this general trend can depend on the concentration of non-polar solvents or solutes, where some solutes can promote interdigitation in the gel phase making the bilayer thickness of the $L_\beta \leq L_\alpha$ [42].

The distance between the bilayers can vary with the interactions between polar "head" groups, and through the concentration of salt and polar solvents[43,44]. The effects of concentration on the bilayer thickness and the distances between them, is dominated by the amount of solvent between the bilayers and ionic interactions[45,46,47]. External factors, such as temperature and pressure can alter the concentration effects causing variations in the bilayer thickness and the distances between them[48,49,50]. These factors result in structural changes that causes phase transitions on a macroscopic scale (see section 1.5.3).

1.4.3. Gel Phases

As mentioned, the lamellar gel phase can exist in different conformations depending on the various factors, such as repulsive effects from solvents or solutes that govern the structure of the surfactant aggregates in solution. Thus, a lamellar gel phase can have multiple variations in the structure. Generally, a lamellar gel phase (L_β) (figure 1.6d), is a bilayer with limited movement between the surfactant molecules and its alkyl chains from increased Van der Waals' interactions between the alkyl chains compared to that of an

L_α phase. Though, there are other well-established gel phases known in literature, such as tilted ($L_{\beta'}$), rippled ($P_{\beta'}$) and interdigitation ($L_\beta I$) gel phases (figure 1.6). These gel phases are similar with small structural variations that causes transitions between the different gel conformations, thus the metastability of the "gel" phase.

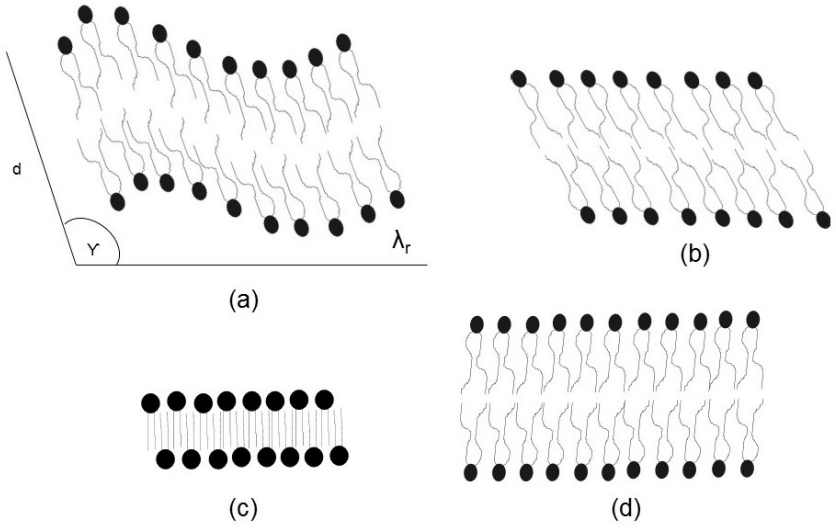


Figure 1.6. Shows a diagram representing the different types of gel phases; (a) ripple ($P_{\beta'}$), (b) tilted ($L_{\beta'}$), (c) interdigitated ($L_\beta I$) and (d) normal gel phase (L_β). The ripple wavelength (λ_r), tilt angle (Y) and bilayer thickness (d) is defined for the $P_{\beta'}$ phase.

The main characteristic of a $L_\beta I$ phase is the reduced bilayer thickness to an almost monolayer state (figure 1.6c). This effect causes increased interactions between the polar "head" groups and the terminal methyl groups on the hydrophobic "tail", with increasing interdigitation. The $L_\beta I$ phase has been reported extensively for lipids with large zwitterionic phosphatidylcholine (PC) head groups[51], where they can be stabilised by addition of alcohols to aqueous lipid mixtures[52,53] or fluorination of the hydrophobic tail group[54]. The alcohols stabilise the $L_\beta I$ phase by insertion into the bilayer to interact with both the polar and nonpolar groups to decrease polar-nonpolar interaction. Similarly, the increased polarity from fluorination balances the nonpolar-polar interactions. The $L_\beta I$

phase is reported by Furuike et. al. as an increase in repulsion between the PC groups, without the use of alcohols or fluorination of lipid "tail" groups[55].

The $L_{\beta'}$ and $P_{\beta'}$ phases both experience tilting of the amphiphiles and can be characterised by the degree of tilting from a point perpendicular to the bilayers plane. The repeat unit of the lamellar gel phases are defined by the repeat bilayer spacing (d) (see section 2.5.5), though the $P_{\beta'}$ repeat unit is also defined by its periodicity, ie the ripple wavelength (λ_r) and the ripple angle which equates to 90° minus the tilt angle (ϒ) (figure 1.6a) [56]. Due to the similarities in the $L_{\beta'}$ and $P_{\beta'}$ phases, transitions between $L_{\beta'}$ ↔ $P_{\beta'}$ phases are can take place and are observed as pre-transitional forms of one another through temperature cycles[57,58].

The general observations are $L_{\beta'}$ → $P_{\beta'}$ transitions upon heating and $P_{\beta'}$ → $L_{\beta'}$ transitions upon cooling within a "gel" state, where the transition from L_α → $P_{\beta'}$ phase was suggested by Heimburg et. al. to be a result of one-dimensional defects of a monolayer in the L_α phase when the bilayers change their thickness upon cooling which leads to localised bending forming the $P_{\beta'}$ phase[59]. Therefore, further cooling will result in a bilayer with a constant thickness and the $P_{\beta'}$ → $L_{\beta'}$ phase transition. This behaviour of the bilayers, to form $L_{\beta'}$ and $P_{\beta'}$ phases, are mostly reported for PC lipids[60]. The differences between $L_{\beta'}$ and $P_{\beta'}$ phases are discussed further in sections 2.5.5 and 4.3.1.

1.5. Phase Changes (Fluid ↔ Gel ↔ Crystalline)

The transitions between macroscopic phases are driven by certain factors, such as temperature, concentration and pressure, where these factors govern the phase behaviour of a surfactant in solution which defines the properties of the surfactant system. This section will discuss the various factors that govern the phase of a surfactant

solution and the impact those factors have on a lamellar phase. The phase behaviour of a surfactant solution is given by the most thermodynamically stable state of the surfactant aggregates at a given temperature, pressure or concentration. Though, there are specific points where more than one phase can exist, ie the phase boundary. The phase of a surfactant aggregate can depend on the thermodynamic pathway, ie the rate of change of the controlling factor, where the conformation of the surfactants can depend on the thermal treatment of the solution. This was shown by Seddon et. al. for the formation into two different crystalline gel phases of a phosphoethanolamine (PE) lipid phase upon storage of the L_α and L_β phases, where the resultant crystalline gel phases depended on the thermal treatments of the lipid solution[61]. Therefore, the conformation of the surfactant molecule can lead to a kinetically stable state of a metastable form which will reinvert into a thermodynamically stable state that has very slow kinetics.

1.5.1. Salt Concentration

The salt levels can influence the packing structure of the surfactant aggregates through osmotic or ionic effects. An example of the former would be an osmotic stress on a surfactant solution when salt is added to the bulk phase. In terms of vesicles, this results in movement of interlamellar and core water into the bulk phase. Consequently, the dehydrated bilayers lead to a decrease in the bilayer separation[62] and in some cases, reported to form defects in the bilayers[63,64].

The degree of shrinkage between the bilayers through dehydration depends on the electrostatic interactions between the polar “head” groups, where the interactions between amphiphiles is defined as the contribution of two factors; Van der Waals’ and electrostatic forces, by the Derjaguin-Landau-Verwey-Overbeek (DLVO) theory[65,66,67]. This theory states that the stability of interacting particles depends on their rate of coagulation, where the Van der Waals’ attraction is constant, and the rate is determined

by the electrostatic repulsion between the interacting particles. The DLVO theory approximates the behaviour of electrolytes in solution[68] on the interacting particles based on the Debye-Hückel theory (see below). Therefore, the DLVO theory predicts the interaction between two equal hard sphere particles (ie surfactant “head” groups) in aqueous solution of electrolytes, as a function of distance.

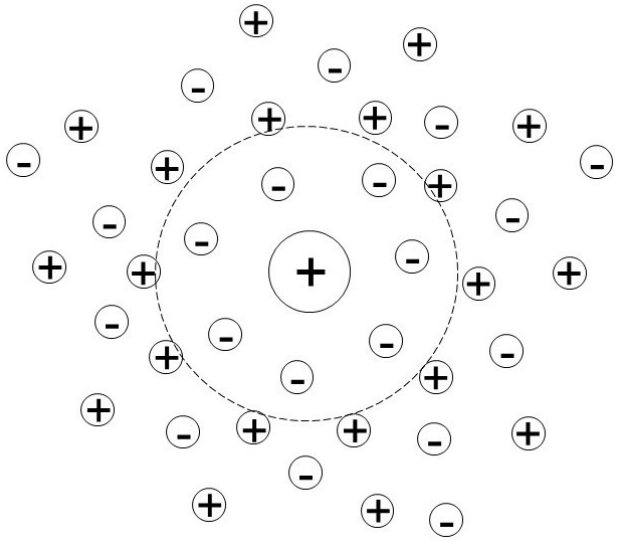


Figure 1.7. Shows a schematic that represents the Debye-Hückel theory, where a central positive charge is surrounded by negative ions decreasing the potential around that positive charge in a neutral system. The circle represents the decreasing potential area of the positive charge, where the radius of the circle is known as the Debye length.

The ionic contribution for increasing levels of salt can be explained by the Debye-Hückel theory for ionic solutions which states that a given ion will always be surrounded by a counter ion in a charged balanced solution[69,70]. Therefore, the average distribution of ions in solution will result in a spherical ionic atmosphere for a specific ion surrounded by its counterion. The radius of the ionic atmosphere is known as the Debye length (figure 1.7). This ionic atmosphere causes the columbic potential of the central ion to decrease much faster with distance due to the shielding effect of the ionic atmosphere. Thus, an

increase in salt levels can increase the Debye length and result in a net attraction from the Van der Waals' interaction which decreases the distance between the bilayers (see section 5.3.2). Also, this net attraction has been reported to decreases the distance between vesicles and increase vesicle size[71]. These osmotic and ionic effects describe salts that reside in the aqueous phase as opposed to salts that interact with the surfactant "head" groups, so behaviour of salts in amphiphilic solutions depend on the type of salt. These studies examine the behaviour of a single type of salt on the bilayers, where the salt resides in the aqueous phase (see section 1.7.2).

1.5.2. Surfactant Concentration

The surfactant levels can govern the structure of a surfactant aggregate, where the example was given for micellar growth of a surfactant molecule that promotes positive curvature ($P < 1$, see section 1.3.1) will transition from micelles → "rod-like" micelles phases[72,73] ($1/3 < P \leq 1/2$), with increasing levels of surfactant. Therefore, high levels of surfactant can result in an increase in the size of the aggregates, but vesicle growth is slightly different to the growth of micelles. As mentioned in section 1.3, micelles extend into tubular structures when the radius of the aggregate is greater than l_c because it reduces interactions between the alkyl chains which is thermodynamically unfavourable[23]. However, vesicles exist as bilayers, where the bilayer thickness is given by $2l_c$ and is constant (for non-interdigitated bilayers). So, an increase in aggregation number will increase the vesicle size. Furthermore, the increasing surfactant levels can increase the packing of amphiphiles and decrease the distance between the bilayers, where the larger vesicles will have greater lamellarity (see section 5.3.1).

1.5.3. Temperature Vs Pressure

The temperature and pressure effects the phase of a surfactant system through changes in the molecular kinetics of the surfactant molecule which is dominated by the alkyl "tail"

group movement. Increasing temperature causes an increase in alkyl chain disorder from an increase in thermal energy which, for a lamellar phase, promotes $L_c \rightarrow L_\beta \rightarrow L_\alpha$ transitions. Conversely, the increase in pressure increases the alkyl chain order through a decrease in volume which promotes $L_\alpha \rightarrow L_\beta \rightarrow L_c$ transitions. As mentioned (section 1.4.2), an increase in alkyl chain disorder results in a decrease in the bilayer thickness. Therefore, the general effects of temperature on the surfactant bilayer is, for increasing temperature, a decrease in bilayer thickness, where an increase in pressure will have the reverse effect of increasing bilayer thickness. Thus, the effects of temperature and pressure on a liquid-crystalline phase, is inversely related[74].

1.5.4. Thermal Fluctuations

The effects of temperature on the bilayers has been explained for the bilayers thickness as a function of the alky chain length (previous section). However, the temperature effects on the bilayers can also cause bilayer fluctuations. The structure of the vesicles and their bilayers are held by weak Van der Waals' forces, so movement can exist in the form of vibrations of amphiphiles in and out of the bilayer planes, ie fluctuations. The fluctuations of the bilayers depend on the shape of the amphiphiles and the interactions between them and the aqueous phase. These fluctuations can be described as an oscillatory function which can increase in amplitude. This increase in amplitude causes a decrease in the distance between fluctuating surfaces (adjacent bilayers or vesicles) and result in a repulsion between these surfaces which is entropically driven[75].

The fluctuation forces are steric repulsions between surfaces or molecules which compete with Van der Waals' interactions. The Van der Waals' interactions are theoretically more dominant than these repulsions[76]. Furthermore, the energy of this attractive interaction is proportional to $1/d^2$, so for a large bilayer separation the long-range repulsions dominate. However, the sort-range repulsions are dominant over much

shorter distances than the long-range repulsions due to steric hinderance between fluctuating amphiphiles. These fluctuations can depend on the property of the bilayers ie if they are in a fluid- or gel-like state. The latter experiences very little fluctuations due to an increase in Van der Waals interactions between the alkyl chains, so the repulsions associated with bilayer fluctuations only govern the bilayer separation of fluid-like bilayers[77].

Besides random fluctuations, there are two modes of fluctuation; protrusion and undulation. The former is the motion of individual amphiphiles bobbing in and out of the bilayers plane and the force associated to this movement (as a function of distance between two protruding molecules) is described as short-range protrusion forces. The motion of amphiphiles, in and out the bilayers plane, can result in a collective ripple-like motion across the bilayers and can be determined by the bilayers bending modulus. This mode of fluctuation is given by long-range undulation forces. Both modes of fluctuation can cause an overlap between the surfactant "head" groups of neighbouring bilayers and give rise to repulsion either between the protruding amphiphiles back into the bilayers plane or the neighbouring undulating bilayers. However, the overlap of surfactant "head" groups can take place in the absence of protrusion and undulation forces for large flexible surfactant "head" groups[78].

1.6. Effects of Preparation Techniques

The microstructure of a surfactant solution can be manipulated via the method of preparation. Certain techniques, such as sonication and extrusion, can drive the formation of specific microstructures. These preparation techniques govern the size and the polydispersity of the vesicle structure. This control on the vesicle structure can control the temperature of the phase boundaries for a surfactant-solution mixture because the temperature of the phase transitions can depend on the vesicle structure[79].

Extrusion is a technique that involves the process of driving a polydisperse vesicular solution through a membrane with a specific pore size, x (figure 1.8a), creating vesicles with a narrow size distribution centred around x, in diameter. This process is used to decrease polydispersity by the formation of unilamellar vesicles of a similar size[80,81].

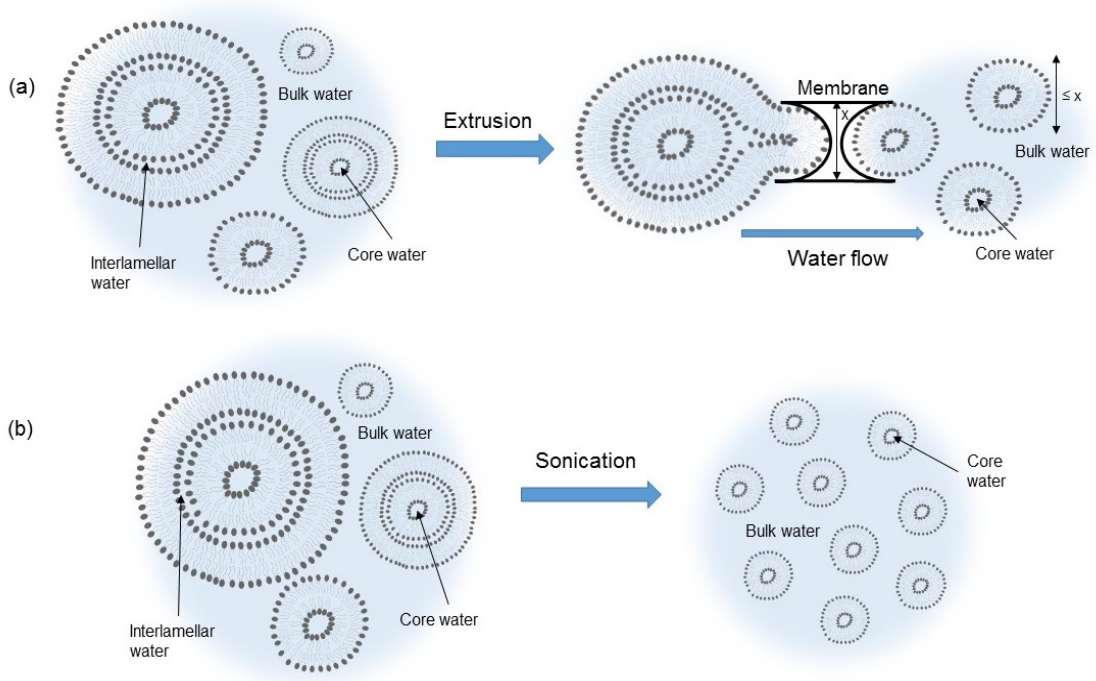


Figure 1.8. (a) Diagram for the extrusion mechanism, showing the polydisperse vesicular solution being forced though a membrane with a pore size of x. (b) Shows the aggregation via sonication of a polydisperse vesicular solution to monodisperse unilamellar vesicles.

Sonication is a technique that creates aggregation in a surfactant solution through high frequency ultrasonic waves (figure 1.8b). Thus, sonication is mixing on a molecular scale and generally form small unilamellar vesicles with increased sonication time[82,83,84]. Therefore, both techniques tend to result in the reduction of polydispersity and form

unilamellar vesicles. The effects of these techniques on the phase behaviour for a DODAC solution is reviewed further in Chapter 7.

1.7. Research Overview

The purpose of this research is to build a correlation-based mechanism for the effects upon freezing and thawing on a lamellar-vesicle structure. The effects upon freeze-thawing (FT) have been studied for lipid membranes and surfactant lamellar phases to understand the impact of environmental stresses on its structure for the purposes of transportation, storage and preparation. The effects upon freezing on lamellar phases are reported to impact the structure in various ways, ie increased encapsulation efficiency[85], change vesicle size (via fusion, fission or remixing)[86,87,88,89], change lamellarity[90] and promote vesicle → fragmented/extended bilayers transitions[91]. In most cases, these FT effects on the bilayers are a result of FT induced mixing. Therefore, the changes to a lamellar phase will vary depending on electrostatic interactions between the amphiphiles and the rate of cooling and heating.

1.7.1. Freezing Mechanism

The mechanism upon freezing for a lamellar phase is reported to be the result of osmotic stress caused by ice formation in the bulk phase[92]. This stress upon freezing takes place during heterogenous ice crystal formation around the solutes in the bulk aqueous phase, leaving regions of high salt concentration which increases the bulk solution potential[93]. Then follows the movement of interlamellar and core water into the bulk phase, leading to dehydration of the vesicle, where the dehydration causes a decrease in the bilayer spacing (figure 1.9). As the temperature decreases the diffusion rate of water decreases[94] and depending on the concentration of water, the frozen state of the vesicular system can lead to supercooled water encapsulated between the bilayers.

The effects upon FT, is reported by Gordon-Kamm et. al. as the result of dehydration instead of low temperature exposure. This was examined by a direct comparison between isolated protoplasts in hypertonic and isotonic solutions, at low temperature[95]. The low temperature exposure of dehydrated protoplasts is reported to cause a lateral phase separation in the bilayer, resulting in lamellar → hexagonal phase transitions[96,97,]. These reports suggest three types of freezing mechanisms that depend on the degree of dehydration, where; (1) is a dehydrated bilayer which is still intact, (2) is the lateral phase separation and (3) is defects/fractured planes in the bilayer, in order of increasing dehydration.

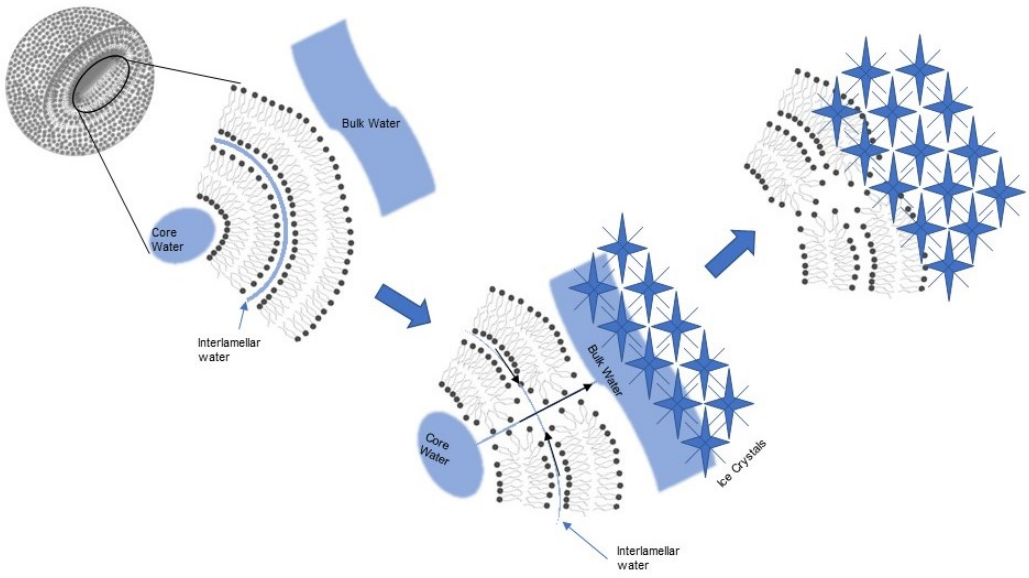


Figure 1.9. Shows a schematic for the general freezing mechanisms of a multilamellar vesicle in an isotonic solution, where dehydration of the bilayers is induced by ice formation in the bulk phase. The black arrows show the movement of interlamellar and core water into the bulk water, during heterogenous ice formation in the bulk water phase.

Upon thawing, the three different freezing mechanisms (see above) is reported by Steponkus et. al. to result in either lysis induced by swelling of the bilayers or the loss of osmotic responsiveness[98]. The latter is the result of freezing mechanisms (2) and (3) and the former is the result of freezing mechanism (1). These outcomes all result in disrupted bilayers which cause changes in the lamellar structure and the bilayers properties and was discussed as the reorganisation of the bilayers, ie FT induced mixing.

1.7.2. Dioctadecyl Dimethylammonium Chloride (DODAC)

The FT behaviour of a lamellar vesicle phase was studied for the aqueous solutions of polydisperse multilamellar dialkyl quaternary ammonium surfactant, DODAC (figure 1.10). The aqueous DODAC solutions were used to model that of liquid fabric enhancers (LFEs), where LFEs are made up of dialkyl ester ammonium surfactants mixtures and form multilamellar polydisperse vesicles in solution[99]. LFEs are extensively used as fabric softeners, where the fabric softener increases the softness and freshness of the treated fabrics, controls static electricity, and prevent wrinkling and abrasion of the fabric[100]. These LFEs may undergo freezing during transportation and storage in lower climate regions, where FT of the LFEs result in an increase in the solution viscosity. This increase in solution viscosity effects the function of the LFEs which relies on the even distribution onto the fabric surface.

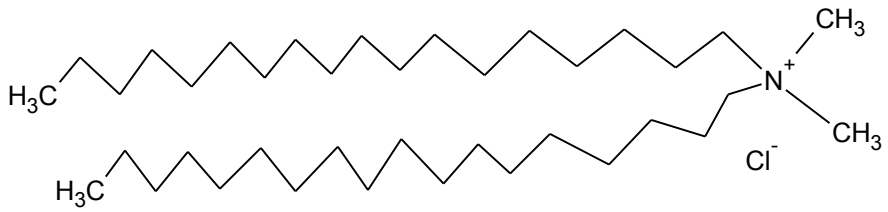


Figure 1.10. Shows the molecular structure of dioctadecyl dimethylammonium chloride. The structure consists of two C18 alkyl chains with an ammonium ion “head” group and a chloride counterion.

There is extensive research on aqueous DODAC solutions, where some of the earlier work reported by Kunieda et. al.[101] gives the phase behaviour of an aqueous DODAC solution with a chain melting transition temperature of 37 ^{o}C which is similar to the findings in these studies (~38 ^{o}C) and was found that hydrated DODAC solutions form lamellar phases for hydration levels as high as 96 wt%, where the highest hydration level used in these studies is 95 wt%. The phase behaviour of DODAC was also studied by Laughlin et. al.[102,103], where DODAC hydration was achieved through dry DODAC exposure in humid air (35-45 % humidity) which formed hydrated DODAC crystals and the hydration rate of the dry DODAC increased with temperature. Also, the reports show a decrease in the average particle size and lower viscosity of the DODAC solutions, through mechanical shearing by a piston mixing device and sonication, in comparison to DODAC solutions that were not mixed. This information describes the effective hydration of DODAC solutions and the phases that they form, where DODAC exclusively forms vesicles in solution.

The phase behaviour of the DODAC solutions result in kinetically stable lamellar phases which in time transitions into a coagel phase. The coagel phase is a hydrated crystalline gel phase which resembles the L_c phase but with a bilayer separation much greater than the L_c or L_β phases, so bilayers with frozen alkyl chains separated by aqueous layers[104,105]. The gel→coagel transition is an instability that takes place over a period of months or years as a slow nucleation of frozen alkyl chains in the gel phase, forming coagel domains for DODAC crystals with low solubility[106]. This instability of DODAC is similar to that mentioned earlier (see section 1.5) for PE lipid solutions which resulted from various thermal histories of the PE lipid solutions.

The coagel transition is reported by Shearman et. al.[107] for biodegradable dialkyl ester quaternary ammonium surfactants solutions, where the gel→coagel transition took place after hours instead of the months or years reported for DODAC. The gel→coagel transition is also reported by Cassin et. al. for aqueous monoglyceride solutions which resulted from the lack of thermal fluctuations (see section 1.5.4) in the gel phase[108]. Therefore, the gel→coagel transition rate is influenced by; the structure of the surfactant, the thermal history of the solution and the effective hydration. Also, the addition of salt to the DODAC solution is discussed (see section 5.3.1) to have an influence on the rate of the coagel instability.

There are reports from Tsuruta et. al.[109] on the DODAX counterion, where X is C or B for a Cl^- or Br^- ion, respectively. The report shows a preference of Cl^- ions to reside in the aqueous phase and Br^- ions bound to ammonium ion "head" group of the surfactant. This was determined by the reported interdigitation of DODAC bilayers which stabilised the vesicle growth of DODAC vesicles compared to DODAB vesicles which ruptured, where this behaviour was explained by an increased repulsion of the DODAB "head" groups from bound Br^- ions.

The counterion behaviour was also studied by Cuccovia et. al.[110], where the size of DODAX solutions were measured by dynamic light scattering to give a sonicated DODAC vesicle size smaller then that DODAB vesicles by 120 Å in diameter and the dissociation energy of the ions were measured by the effective surface potential of the bilayers giving a higher dissociation of Cl^- ions than Br^- ions. These results explain the effective binding of the Cl^- ions and how they influence the bilayers properties (discussed in section 1.5.1). The effects of salt and surfactant concentration on an aqueous DODAC solution is discussed (in chapter 5) where the increased levels of salt and surfactant

results in an increase in the aggregation size and a decrease in the bilayers separation, creating larger vesicles with greater lamellarity.

The bilayer thickness for a DODAC system has been reported for values between 40-50 Å. This is approximated through the relative interactions between two vesicles by Carmona-Ribeiro et. al., to be 50 Å at 25 ^{o}C[111] and determined through electron microscopy for DODAC levels of 0.6 wt% by Kano et. al. to be 50 Å (± 5 Å)[112]. The interdigitation of the DODAC bilayers are calculated in recent studies by Gonçalves et. al., for a 33 to 28 Å decrease in the bilayer thickness from 50 to 25 ^{o}C, respectively, which was given at 35 wt% DODAC[113]. The experimental value for a DODAC bilayer thickness of 40.249 Å is reported by Shearman et. al., through swelling of the DODAC (starting DODAC levels of 14.3 wt%) fluid lamellar bilayers[171]. In most cases the DODAC bilayers exist in the L_{β} phase except for the reports by Gonçalves et. al.[113] and Tsuruta et. al.[109], where they exist in the L_{β}I phase at high DODAC levels.

1.7.3. Thesis Outline

In Chapter 3, the temperature-pressure phase behaviour of a DODAC aqueous solution is determined with pressure cycles between 0.001-4 kbar under isothermic conditions at 65, 25, 10 and 5.0 ^{o}C. The relationship between temperature and pressure is compared directly between a temperature-controlled and a pressure-controlled DODAC system, in chapter 4, which showed differences in the temperature-pressure relationship between 65-25 ^{o}C and in the L_{β}-L_{c} transition for low-temperature and high-pressure, both systems showed a general swelling of the DODAC bilayers after FT.

In chapter 5, the effects upon FT were compared for varying levels of $CaCl_2$ (0-0.15 wt%) in the DODAC aqueous solution, where all solutions showed changes in the bilayer

properties after FT. The DODAC solution containing 0.085 wt% $CaCl_2$ is then evaluated (in chapter 6) for the effects of chemicals additives on the DODAC bilayers through the addition of an ethoxylated alcohol surfactant and glycerol. These additives resulted in structures that were more robust against the FT induced swelling but at high levels resulted in swelling of the bilayers from the addition of glycerol and a spherical→planar bilayer transition from the addition of the ethoxylated alcohol surfactant.

In chapter 7, the effects of preparation techniques on the FT behaviour of the DODAC solution is discussed which showed that the polydispersity of the DODAC solution slows down the proposed freezing mechanisms (figure 1.9). The effects upon FT on a DODAC aqueous solution is concluded in chapter 8 which discusses the optimal conditions for a vesicular structure that is robust against the FT induced swelling and outlines the freezing behaviour of this DODAC solution containing 0.085 wt% $CaCl_2$.

2. Materials and Methods

2.1. Materials

Dioctadecyl dimethylammonium chloride (DODAC) was purchased from Sigma-Aldrich with a purity ≥97%. The excess water was removed by dissolving DODAC in a mixture of chloroform/methanol (3:1 v/v) then drying over N_2 gas and lyophilised under vacuum for over 24hrs (method extracted from Shearman et. al.)[114]. The methanol was analytical grade with a purity ≥99.8 % and the chloroform was chemically pure with a purity of 99.0 %, both chemicals were purchased by VWR chemicals (VWR International). DODAC was hydrated in an aqueous solution of calcium chloride and HPLC grade water, both purchased by VWR International or deuterium oxide (for ^{1}H NMR samples) which was purchased from Sigma-Aldrich with a purity of 99.9 atom% D. The 12-14 carbon chain alcohol ethoxylate (CAE10) and glycerol (glycerol 4833) was gifted by Procter and Gamble (Brussels Innovation Centre) and used without further purification.

2.1.1. Preparation of Multilamellar Vesicles

DODAC levels between 5-14 wt% were hydrated in aqueous solution containing $CaCl_2$ (between 0-0.15 wt%) and stirred at 65 ^{o}C (well above the chain melting temperature of ~37 ^{o}C), for samples containing chemical additives, glycerol (0-7.5 wt%) or CAE10 (0-5 wt%) was added to the aqueous DODAC solution at 65 ^{o}C and stirred further for ~2mins, then samples were left to cool at room temperature (~20 ^{o}C). The surfactant and salt levels were chosen to model that of industrial multilamellar dispersions of liquid fabric enhancers, such as fabric softeners (see section 1.7.2). Some samples were then extruded and/or sonicated to increase the homogeneity of the solution, through methods described in chapter 7. Unless specified, the DODAC solution was of 8 wt% DODAC in an aqueous solution containing 0.085 wt% $CaCl_2$. The freeze-thawed DODAC solutions

were frozen in liquid nitrogen and heated above the chain melting transition (~37 °C), this process is repeated where specified, then left to cool at room temperature (~21 °C).

2.2. Nuclear Magnetic Resonance (NMR)

2.2.1. Introduction

NMR is a quantitative technique used to determine the orientation and the environment of an observed nuclei given by a peak intensity corresponding to the population of the observed nuclei with a chemical shift corresponding to the electronic environment of the nuclei. The term environment relates to the electronic current of the electrons surrounding the observed nuclei, caused by the applied magnetic field, which is perturbed by the different types of interactions in the molecular system. NMR can be used to determine the micro- and macroscopic phase of an amphiphile in solution[115,116,117]. The fundamental theory has been developed to provide more information about interactions and translational movement of components within a liquid crystalline structure[118].

2.2.2. Basis of NMR

Structural information is given by the small release of radiofrequency (rf) energy during relaxation of an excited spin state. The combination of charge and spin within nuclei causes a magnetic moment. When an external magnetic field is applied to that magnetic spin, the spin aligns itself in the direction of the external magnetic field. This describes the ground spin state of the nuclei and gives rise to other possible energetically defined spin states. The effect of the alignment results in a rotating and wobbling motion about that axis, denoted as a precession. The precession frequency known as the Larmor frequency (ν_L), is proportional to the strength of the external magnetic field (B_o).

$$v_L = \frac{\gamma B_o}{2\pi} \quad [2.1]$$

Where γ is the gyromagnetic ratio of the nuclei. The Larmor frequency defines the amount of energy needed to excite the spin to a higher spin state[119].

2.2.3. Relaxation Time Constants

The relaxation of excited spin states is defined as the loss or gain of its net magnetisation in an axial plane or direction. The spin states are excited through a short rf "90° burst" which changes the direction of the net magnetisation from the z-direction into the x,y plane. The net magnetisation resonates as a combination of spin states which is averaged throughout the system. That resonance decays over time due to variations in the interactions between the nuclei and its environment or due to lack of uniformity in the external magnetic field.

There are two types of relaxation; longitudinal (T_1) and transverse (T_2) relaxation. The latter is also known as the spin-spin relaxation. It is the loss of net magnetisation in the x, y plane after a "90° burst". The T_2 relaxation is dominated by variations in the precession frequencies of the nuclei due to differences in the nuclei environment. The longitudinal or the spin-lattice relaxation is the gain of net magnetisation in the z-direction. Thus, T_1 will always be ≥ T_2[120].

The length of the relaxation varies with the electromagnetic interactions between the observed nuclei and its surroundings. In a fluid or gaseous environment, the interactions between the nuclei and the surrounding particles are similar due to translational movement and molecular tumbling. The constant changes to the environment results in

a zero-average interaction between the nuclei and its environment, increasing the relaxation rate.

Conversely, a solid or “gel-like” environment will have more localised positions resulting in fewer to zero translational movement and molecular tumbling, and increased dipole-dipole interactions between the particles. Therefore, the different interactions between the nuclei and its environment will cause a decrease in the net magnetisation of the precession, ie a decreased relaxation rate. This behaviour is used to determine the macroscopic liquid crystalline phase and can be observed through the shape of ^{1}H NMR signal for the alkyl chains of the amphiphile which is given by the half-height width of the ^{1}H NMR signal. The half-height width is inversely proportional to the time constants[121].

2.2.4. Chemical Shifts

The chemical shift gives information on the electronic environment of the observed nuclei. Thus, the electron density surrounding the observed nuclei can influence B_o, changing the frequency of the nuclei resonance. The magnetic field creates an electric current within the electron cloud forming a small magnetic field that opposes B_o. This opposing electric current “shields” the nuclei from B_o. The degree of shielding depends on the distribution of electrons in the nuclei environment, and the lack of electrons defines nuclei that are “deshielded” from B_o.

The chemical shift can be predicted by the type of bonding the nuclei experiences. For example, the ^{1}H NMR of a bonding pair H-X (where H is hydrogen and X is a group with certain chemical properties) will give a chemical shift of H which will depend on X. If X was a group that pulls electron density away from H ie electron withdrawing, then H will be deshielded from B_o. In this case, examples of X will be RCO_2H (carboxylates), RHC=O

(aldehydes) or $RCO_2NH_2\underline{H}$ (amides). Similarly, a group with high electron density can decrease the shielding on $\underline{H}$, for X = I^-, Br^-, Cl^-, F^- (in order of increasing electron density). Though, the effects of electron density on the shielding of $\underline{H}$ is smaller than that of electron withdrawing groups. The most shielded $\underline{H}$ will be an example of X = $\underline{H}CH_2$ (methyl)[122]. Shielding and deshielding are basic terms used to describe the chemical shift patterns of molecular systems and these basic terms are enough to explain the ^1H NMR of aqueous DODAC solutions.

The chemical shift can depend on solvent interactions, such as hydrogen bonding in an aqueous phase. The presence of H-bonding can deshield the nuclei involved in the dipole-dipole interaction[123]. The extent of H-bonding depends on the temperature of the system and so in this example the chemical shift is dependent on temperature. The behaviour for increasing temperature for an aqueous solvent, is a decrease in H-bonding which will cause a decrease in the chemical shift.

2.2.5. Spin Echo

When a rf "burst" is applied to nuclei spin states which are parallel to B_o, all the spins states collectively precess at the same frequency resulting in a net magnetisation as the spins states tend to the x,y plane. The length of the rf "burst" is equal to the time it takes for the spin states to tend to the x,y plane. When the applied rf "burst" is removed, the net magnetisation decreases due to inhomogeneity of the magnetic field or differences in the individual spin state environments. The decay of the net magnetisation is known as the free inductive decay (FID).

After a time of τ, a second longer rf "burst" is applied to the spin states, rotating the spin states by 180^o in the x,y plane. Therefore, the dephasing spin states are now rephasing

causing the net magnetisation to increase. Once the spin states are completely phased, the spin echos and the net magnetisation decrease (figure 2.1).

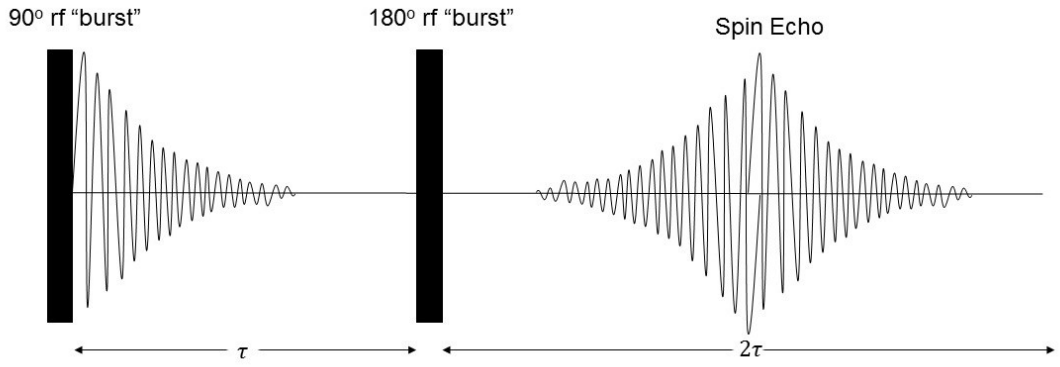


Figure 2.1. Shows the exponential FID of the net magnetisation after the 90° "burst", then the spin echo after the 180° "burst".

The echo decay and FID may differ in magnitude due to differences in the phase of the net magnetisation, where the differences are due to one of two reasons; the return of nuclei spins states to its ground state through the transfer of the magnetic energy to the molecule as kinetic energy (ie T_1 relaxation), or from translational movement of the nuclei where the rephrasing process is perturbed by changes in the nuclei environment[124].

2.2.6. Self-Diffusion

All molecules are said to abide by Brownian motion which states that a molecule suspended in fluid will have random motion due to continuous bombardment from atomic particles[125]. Therefore, if molecules can have random movements in various directions they can also have translational movement which describes the self-diffusion of a molecule. This behaviour was observed by Einstein for the diffusion of a "Stokes" particle

undergoing Brownian motion, where the Stokes-Einstein's relationship for the diffusion (D) of a spherical particle was derived.

$$D = \frac{kT}{6\pi\eta r_s} \qquad [2.2]$$

Where k is Boltzmann constant, T is the temperature, r_s is the hydrodynamic radius of the particle and η is the viscosity. The assumption of a spherical particle, when defining the self-diffusion of a molecule, is a limitation to this relationship[126]. However, this idea of random translational movement developed the theory in quantifying the self-diffusion of a molecule using NMR.

2.2.7. Diffusion Ordered Spectroscopy (DOSY)

As mentioned, the spin echo method can be used to determine the translational movement of the observed nuclei. Though, the measurement of the self-diffusion requires an applied magnetic field gradient (g) after the 90° and 180° "burst", where the length of the gradient is defined by δ. Thus, the spin echo method remains the same but instead of a gradual decrease in the net magnetisation, a gradient is applied in the x,y plane to redistribute the spins states in the direction of the field gradient.

Then a second gradient is applied shortly after the 180° "burst", where the diffusion is measured by change in position between the two gradient pulses and given by the time Δ (figure 2.2). This process is called the pulse program where the method stated is a simple representation of a DOSY experiment, where the parameters gradient length (δ) and diffusion time (Δ) are varied for different diffusing bodies. The diffusion is obtained from a linear expression, given by:

$$\ln(I/I_o) = -(\gamma g \delta)^2 D(\tfrac{\Delta-\delta}{3}) \qquad [2.3]$$

Where, I is the intensity at the spin echo and I_o is the initial intensity[127].

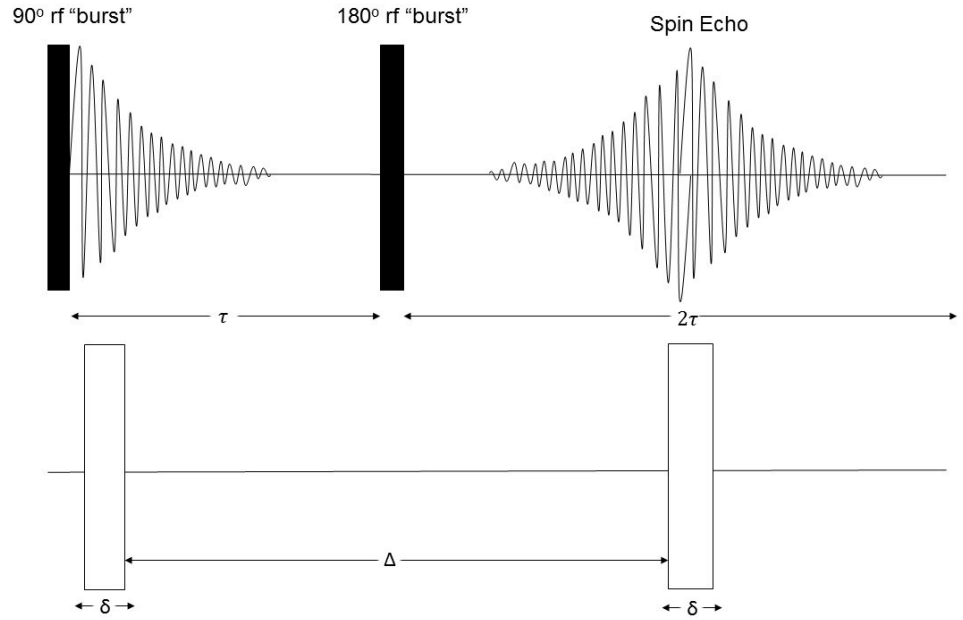


Figure 2.2. Shows a simple pulse program which is an extension of the spin echo method with the addition of two applied gradients, where the time between the two gradients (Δ) defines the given for diffusion.

2.2.8. Instrument

The ^{1}H NMR DOSY experiments were performed on a Bruker 500 MHz AVANCE III HD spectrometer running TopSpin 3.2, equipped with a z-gradient bbfo/5 mm tuneable SmartProbe and a GRASP II gradient spectroscopy accessory providing a maximum gradient output (100%) of 53.5 Gcm^{-1} (5.35$Gcm^{-1}A$). Measurements were obtained at 25 and 5.0 ^oC for aqueous DODAC solutions before and after FT, where the solutions were loaded into standard NMR tubes. The Bruker ledbpgp2s pulse program (figure 2.3) was used at a frequency of 500.13 MHz with a spectral width of 5000 Hz centred at the water signal (at ~4.7 ppm) and 32768 data points.

The gradient strength increased from 2 % to 95 % linearly, or exponentially for very slow and very fast diffusion pairs in the sample, with a recovery delay of 0.2 ms. The diffusion time (Δ) and the bipolar gradient pulses (δ/2) were varied due to large differences in the diffusion rate across samples, where Δ varied between 0.05-3 s and δ/2 between 1-5 ms. These parameters were varied because slow diffusing water required longer Δ and δ, these parameters were determined through a 1D DOSY.

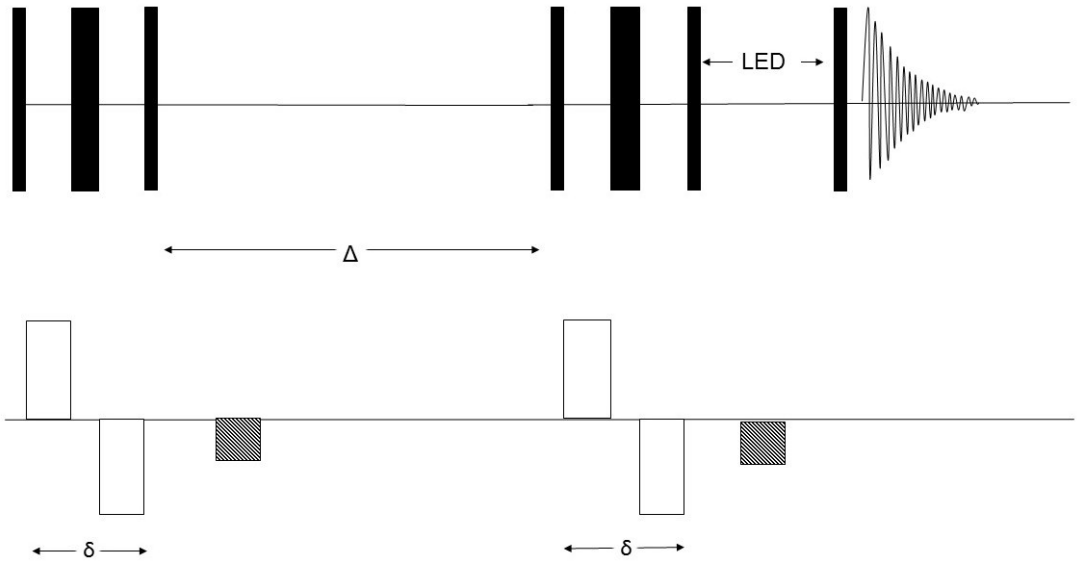


Figure 2.3. Shows a representation of the ledbpgp2s pulse program, where the black blocks represent the 90° "burst" and the wider blocks are the 180° "burst". The bipolar gradients are represented as white blocks with opposing signs. The blocks with black and white stripes are the homospoil gradient pulses.

All experiments had a longitudinal eddy current (mechanical artifact that generates electrical currents during pulse programs) delay (LED) of 5 ms and two homospoil gradient pulse of 0.6 ms with a gradient strength of 17.13 % and 13.17 %. The data was processed using the Bruker Dynamics Centre software (version 2. 1. 1) and the error was estimated by a Monte Carlo stimulation with a confidence level of 95 %.

The ^{1}H static solid-state NMR experiments were performed on a Bruker 600 MHz with a standard bore superconducting magnetic with a power of 14.1 T, running TopSpin 3.2. The solutions were contained in a 4 mm MAS rotor ZrO_2 BL4 (80 µl) with a Kel-F cap and mounted in a MAS double resonance probe for static measurements between 65 and 20 ^{o}C, where the temperature is controlled using an electric chiller unit.

2.3. Polarised Light Microscopy

2.3.1. Introduction

Polarised light microscopy is an imaging technique used to view optically anisotropic structures and can be used to distinguish between the different liquid crystalline states (see section 1.4.1). Liquid crystalline phases have long-range order and short-range disorder which is where the anisotropic nature comes from and results in optically visible liquid crystalline phases under crossed polarised light. Though, cubic phases have long- and short-range order, and are found to be isotropic in nature. The anisotropic phases can be identified by the specific patterns they form under crossed polarised light[128,129,130]. For a lamellar phase, a typical representation of the phase is the observation of “Maltese crosses” (see section 6.3.1).

2.3.2. Birefringence

Polarised light microscopy takes plane-polarised light and passes it through a polariser that is rotated by 90^{o} in the same plane, where the planes of the polariser are now crossed, where no light can pass through (figure 2.4a). However, if an anisotropic crystal was placed between these polarisers, the interaction between the crystal and the plane-polarised light will result in a partial polarisation of the incident light which is resolved through the second polariser (figure 2.4b). This behaviour between an anisotropic crystal

and the path of light is due to the crystals' birefringence, where the path of light through the sample is doubly refracted into two transverse waves.

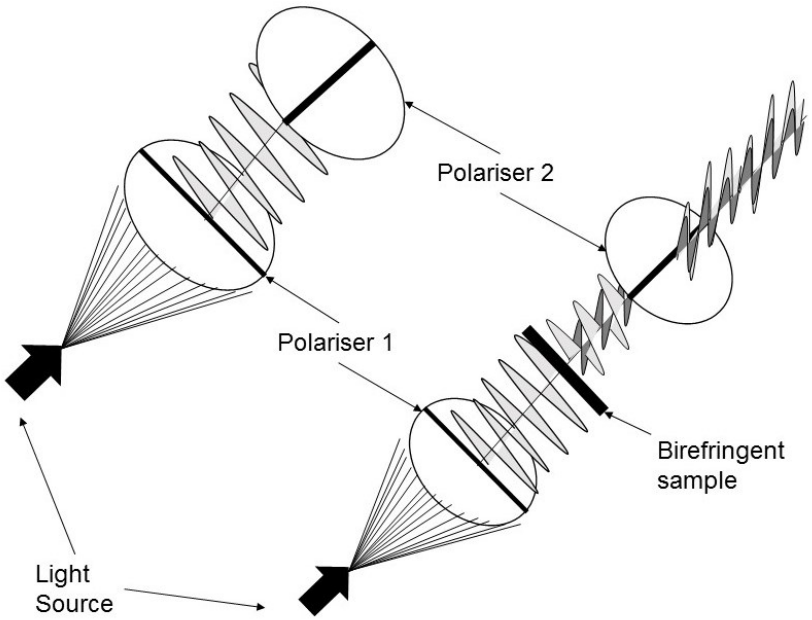


Figure 2.4. Shows the path of light through polariser 1 and 2, comparing the difference between the path of light through (a) no sample and (b) a birefringent sample. The lines from the arrow (source of light) represent a beam of light and the plane polarised light is represented as an oscillating wave in one plane, where the O ray is light-grey, and the E ray is dark-grey.

These waves are denoted as the ordinary (O) ray for light parallel to the incident beam and the extraordinary (E) ray for light perpendicular to the beam. The resolution of the O and E rays can be observed through the optic axis which is the point where the O and E rays are parallel. Thus, this optical property of the crystal varies with the orientation of the incident beam[131].

This technique is limited in resolution and can only view images on a micron scale which was ideal for the surfactant solutions prepared by hydration and mixing at 65 ^{o}C which

form a polydisperse vesicular solutions with vesicles sizes on the micron scale. Though, the phase behaviour for samples prepared by sonication and extrusion could not be verified (see chapter 7 for the differences in preparation technique).

2.3.3. Instrument

Polarised light images were obtained using a Nikon Eclipse E600 Pol polarising microscope fitting with a Qimaging Qicam 12-bit Fast 1394 camera at room temperature (~21 ^{o}C) and varied temperature (vt) between 25 and -18 ^{o}C at 5 or 10 ^{o}Cmin^{-1}, using a Linkam LTS 350 temperature stage connected to Linkam temperature control LNP 94/2 and TMS 94, with a liquid nitrogen line connected to a 2 L DF2 dewar. Samples were placed on a glass slide and covered with a glass slip. The microscope imagines were calibrated using a 1 mm graticule and all images were processed in ImageJ 1. 6. 0_24 (64-bit).

2.4. Differential Scanning Calorimetry (DSC)

2.4.1. Introduction

DSC is a type of thermal analysis, it measures the energy associated to a phase transition based on heat transfer between the environment and a sample as a function of temperature. DSC uses this heat exchange to measure the thermotropic behaviour of a sample, where the transfer of heat from the environment to the sample is given by an endotherm and the reverse process for an exotherm. The DSC traces are known as thermographs and are used to locate the positions of the phase transitions which can be identified for the microscopic structure through other techniques, such as NMR or x-ray scattering.

2.4.2. Measuring Heat Transfer

The heat transfer as a function of temperature is measured against a reference, where the temperature during a heating and cooling cycles, are kept constant between the sample and its reference. For a reference that does not behave thermotropically, an excess of heat energy is transferred to or from the reference during phase transitions to maintain the constant temperature between the sample and its reference. So, the heat transfer is a measure of the excess energy (q_{ex}) supplied to the system when the temperature of the sample varies from its reference. This excess energy is proportional to the heat capacity ($C_{p,ex}$) of the sample[132].

$$C_{p,ex} = \frac{q_{ex}}{\Delta T} \qquad [2.4]$$

The thermographs represent endo and exo isotherms as an influx (positive curve) or efflux (negative curve) of heat capacitance, respectively. These transitions are characterised by the temperature which the heat capacity is at a maximum which is denoted as the transition temperature, and the heat flow is equal to the enthalpy of the transition which is given by the area under the transition curve.

The heating and cooling thermograph for a DODAC aqueous solution can be viewed in figure 6.2, where the aqueous DODAC solution generally experiences large endotherms for ice melting and exotherms for ice forming. However, the main transitions in which liquid crystalline phases are characterised is between the gel and fluid phases ie chain transitions, where phase changes are observed between different gel states, ie microscopic changes can be viewed, and so the stability of the aggregates can be observed[133].

2.4.3. Instrument

Samples were measured using a Perkin-Elmer PYRIS Diamond DSC equipped with a Intracooler 2P cooling accessory and a N_2 gas flow of 2 bars. The aqueous DODAC solutions (weighing between 8-11 mg) were hermetically sealed in 20 µL aluminium pans and an empty pan was used as reference. The sample temperature was calibrated for a known mass of indium, with an expected melting point of 156.6 ^oC which was measured as 160.6 ^oC and ΔH = 27.78 J/g, where the expected value is 28.45 J/g. All samples were measured between 70 and -40 ^oC at 10 $^oCmin^{-1}$. The enthalpy was measured using PYRIS software by measuring the area under the transition curve within an upper and lower temperature limit. The enthalpy was given in joules and then divided by the number of moles of DODAC in the bulk DODAC solution the samples were collected from before being placed in the DSC pans, where the samples were collected at ~21 ^oC (collection from gel phase).

2.5. X-Ray Scattering

2.5.1. Introduction

X-ray scattering is a common technique used to identify a liquid crystalline phase, by the combination of small and wide-angle x-ray scattering (SAXS and WAXS). SAXS is used to determine the liquid crystalline phase and has a resolution of ~1-300 nm, where it distinguishes between microscopic phases through the sequence of the measured bilayer spacing. WAXS has a higher resolution of ~0.1-1 nm and is used to determine the orientation of the packing structure, where it can distinguish between macroscopic phases and the different conformations that exist in the “gel phase”.

2.5.2. Braggs Peaks

The long-range order in liquid crystal phases is due to repeat bilayers that have translational symmetry. The repeat bilayer distance can be determined through Bragg's law which defines stacks of 2D lattice planes separated by d and the points that make up these lattices, X and b (figure 2.5). Points X and b are defined as scattering bodies in which the incident x-rays are scattered off X and b, where the scattered x-rays can behaviour constructively or destructively. When waves interact destructively the sum of the intensity is zero, where the scattered beam is a sum of waves that behave constructively and so the waves are in phase.

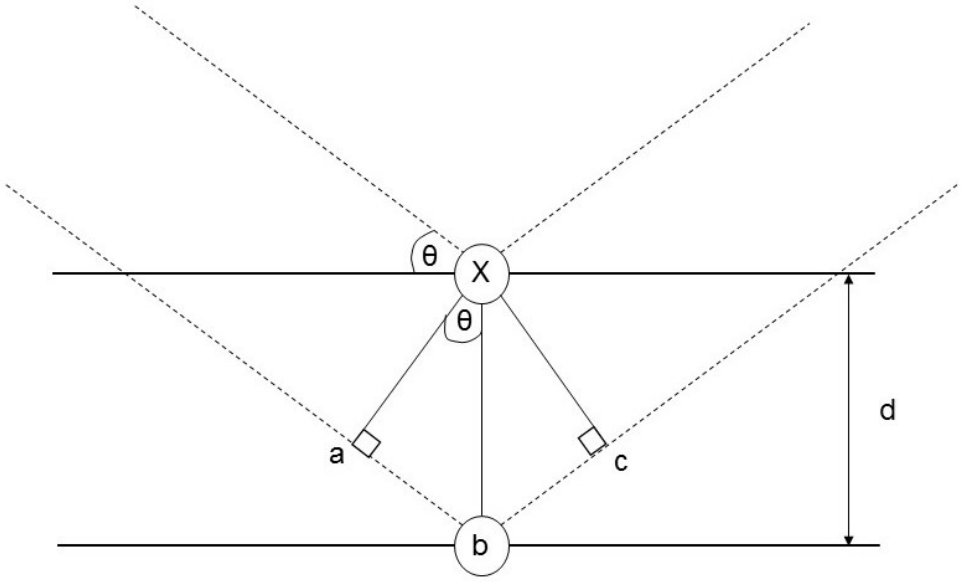


Figure 2.5. Shows a schematic representing Bragg's law, where to two 2D lattices are separated by d and the scattering angle is determined by the path difference of the incident and scattered rays of the scattering bodies X and b.

The x-ray path difference between X and b needs to be established so that the x-rays scattering off X and b can be in phase. The x-rays scattering off b travels an extra distance of ab and bc compared to that of scattering body, X, where the length of ab and

bc are both equal to $d \sin \theta$ and so the path difference is $2d \sin \theta$. Furthermore, the 2D scattering planes (n) must be an integer number of wavelengths apart for the x-rays to behave constructively and so Bragg's law is given by

$$n\lambda = 2d \sin \theta \qquad [2.5]$$

Where θ is the glancing angle which is equal to the scattered angle, and λ is the x-ray wavelength. Thus, the d-spacing can be determined from θ and λ[134].

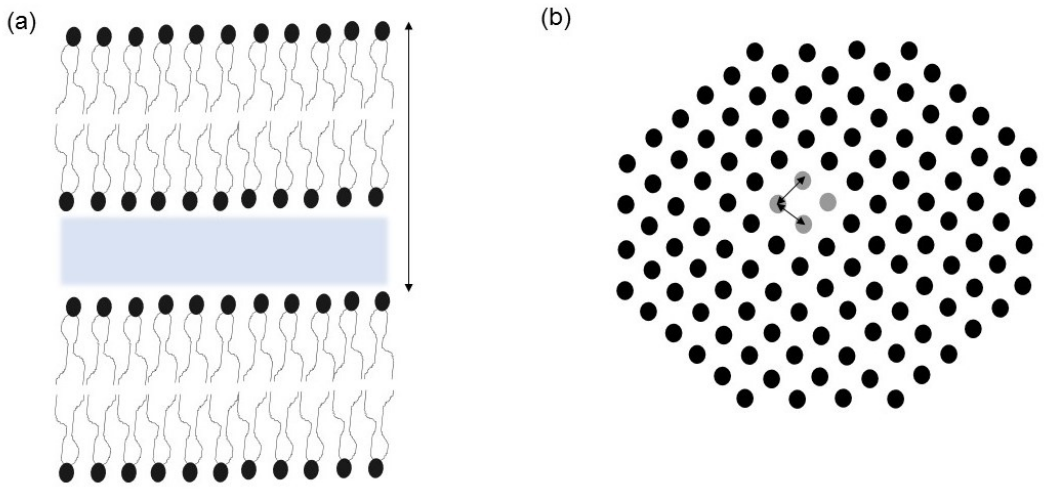


Figure 2.6(a). Shows the two bilayer stacks separated by water (blue rectangle) and (b) is the horizontal plane of the bilayer stacks shown in (a), where the black dots represent the surfactant "head" groups and the grey dots highlight the repeat unit. The double headed arrow represents the d-spacing given by Bragg's law, for (a) SAXS and (b) WAXS.

This Bragg's model is extended further through the idea of rotation planes to approximate from the different conformation of a crystalline structure. Therefore, the scattering angle is rotated around the incident beam with a rotating scattering angle of 2θ to form scattering rings in a reciprocal space of s or q (scattering vectors), where s = 2πq. Therefore, the scattered rings are circular n planes in reciprocal space s distance apart, where s = 1/d[135]. This pattern is then integrated as a plot of scattered intensity against s

or q which is the distance from the scattered centre. The d-spacing is defined differently for SAXS and WAXS. SAXS defines the d-spacing as the repeat bilayer and water distance (figure 2.6a) and WAXS defines the d-spacing as repeat packing unit of the packing structure based on a hexagonal packer order (figure 2.6b).

2.5.3. Miller Indices

The repeat crystal planes (n) are defined by their orientation in a 3D reciprocal space through Miller indices (hkl). In real space n is first defined by the orientation in 2D space by x and y as vectors a_x and a_y, where these vectors are defined by the distance where n intersects a_x and a_y. For example, if n intersects a_x and a_y at $a_x/2$ and $a_y/2$, respectively, then the position of the plane in 2D space is $\left(\frac{1}{2},\frac{1}{2}\right)$ (figure 2.7, for 2D space). In 3D space, this plane, n, is infinitely present in the z-direction which is given by the vector a_z (figure 2.7, for 3D space) and the orientation of n is given by $\left(\frac{1}{2},\frac{1}{2},\infty\right)$, where the Miller indices in reciprocal space is defined as (2 2 0)[136].

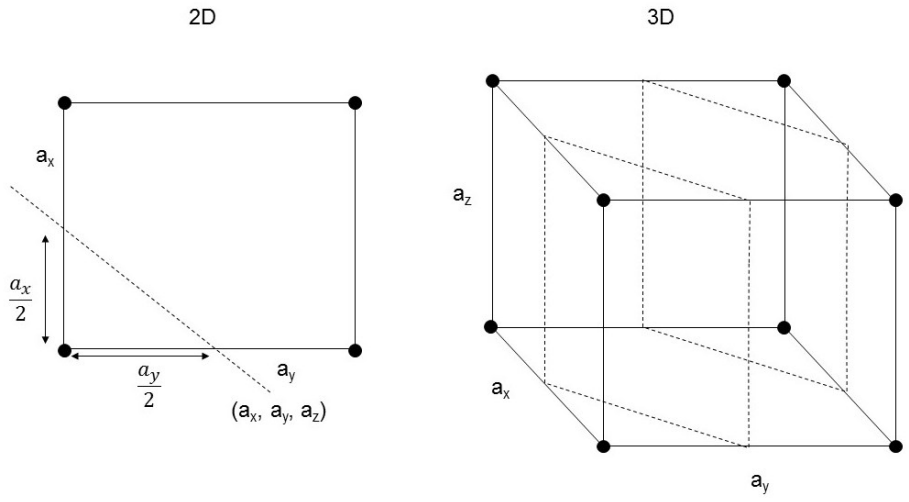


Figure 2.7. Shows the orientation of n (dotted line) in 2D and 3D space (solid lines), where the planes' real space positions are $\left(\frac{1}{2},\frac{1}{2},\infty\right)$ and the reciprocal space is defined by Miller indices as (2 2 0).

2.5.4. Identifying Lamellar Phases

The repeat planes in a lamellar phase will extend along the z-axis, as a 1D stack of planes which will define the miller indices as (0 0 l) where l = 1, 2, 3, 4… etc. Thus, these planes are separated by a ratio of 1:2:3:4… etc., from the scattering centre. The integrated WAXS pattern can determine the macroscopic phase, ie crystalline, gel, or fluid phase, where the fluid phase is presented as a board peak due to lateral disorder from the alkyl chains and is centred around ~5 Å, the gel peak is generally a single sharp peak at ~4 Å due to increased lateral order from the alkyl chains in the hexagonal packing and the crystalline phase will have multiple high intensity peaks due to the high positional order from a frozen structure.

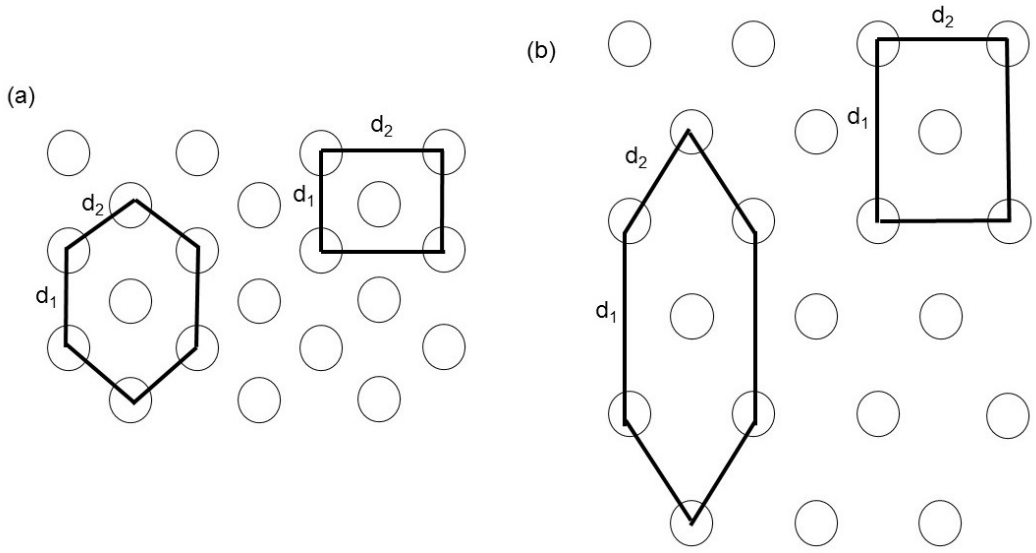


Figure 2.8. Shows a schematic of the (a) hexagonal packing and the (b) distorted hexagonal packing of the surfactant packing in a liquid crystalline phase.

2.5.5. Identifying Lamellar Gel Phases

The different types of gel phases were explained in section 1.4.3, where the different conformations of a gel phase are L_{β}, $L_{\beta'}$, $P_{\beta'}$, or $L_{\beta}I$. The $L_{\beta'}$ and $P_{\beta'}$ are tilted with respect to the L_{β} and $L_{\beta}I$ phases, where the L_{β} and $L_{\beta}I$ phases have a hexagonal packing with a separation of $d_1 = d_2$ (figure 2.8a). The tilted structures will cause a distortion of the hexagonal packing that will result in a lateral separation in the direction of tilt. Thus, elongating the repeat unit in one direction, where the distorted hexagonal pattern has a separation of $d_1 > d_2$ (figure 2.8b). The distorted hexagonal packing is observed in the WAXS as two separate d-spacings which is shown in the integrated scattering patterns as widening of the gel peak or the presence of two gel peaks[137].

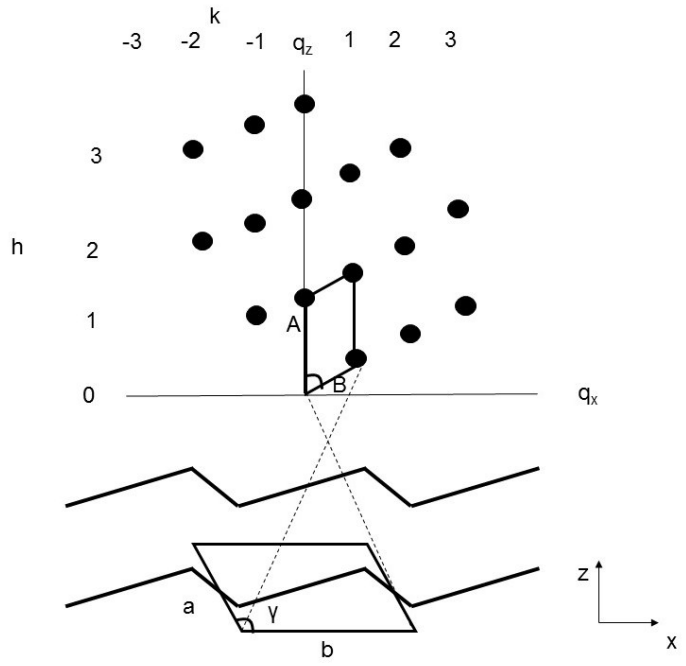


Figure 2.9. Shows a schematic adapted from Sun et. al.[138] (redrawn) of the $P_{\beta'}$ phase in real space (below the q_x line) and reciprocal space (above the q_x line), for the different lamellar reflections given in the $P_{\beta'}$ phase. The bold zig zag lines show the asymmetric ripple layers and the parallelogram is the repeat unit, where the vectors a and b are the d-spacings and ripple wavelength, respectively.

Further differentiation of these phases is given by the SAXS patterns, where the L_{β}l phase will have a drastic decrease in the bilayer distance compared to the L_{β} phase and the $L_{\beta'}$ phase will show a single lamellar reflection, for lamellar bilayers that are in equilibrium, compared to that of the $P_{\beta'}$ phase. As mentioned (see figure 1.6), the $P_{\beta'}$ phase repeat unit is characterised by the ripple wavelength (λ_r), the ripple tilt angle (ϒ) and the repeat bilayer unit (d, ie d-spacing), and so the repeat lamellar unit is 2D instead of the 1D stacks of normal lamellar bilayers, where the Miller indices in the $P_{\beta'}$ phase are defined as (h k 0). The asymmetric $P_{\beta'}$ phase is given by a series of lamellar reflections shown (figure 2.9) by their positions in reciprocal space, where the (0 1) peak of the first lamellar reflection is equal to the ripple wavelength.

2.5.6. Instrument

Synchrotron x-ray data was obtained at Diamond Light Source (Harwell Campus, Didcot) on the i22 beamline through simultaneous SAXS and WAXS recordings which were achieved through two detectors, Pilatus P3-2M (SAXS) and Pilatus P3-2M-L (WAXS), placed at different distances from the sample. The detectors were calibrated using silver behenate (AgBe), with a lattice spacing d_{001}= 58.38 Å, to define the centre of both SAXS and WAXS detectors.

The i22 beamline was equipped with a pressure cell that can generate hydrostatic pressure up to 5 kbar, where the sample is contained between two flat single crystal diamond windows in the x-ray path[139]. The aqueous DODAC solutions were cycled from atmospheric pressure to a maximum of 4 kbar in 0.2 kbar steps at constant temperature, where the temperature is specified for each experiment. The pressure samples were loaded in polycarbonate capillaries and sealed with a rubber stopper, cut from an O-ring, and epoxy resin glue.

The room temperature and temperature-controlled samples were loaded into either heat-sealed glass or parafilm sealed polycarbonate capillaries and mounted in a capillary rack, where the temperature, when not 25 ^{o}C, was cycled between 65 and 20 ^{o}C with 5.0 ^{o}C steps. The low temperature measurements, between 25 and -18 ^{o}C with 5.0 ^{o}C steps, were obtained with a DSC600 Linkam capillary stage that was mounted vertically in the x-ray path and connected to a CI94 Linkam temperature control unit and the samples were loaded in Quartz capillaries and sealed with parafilm.

The integrated scattering patterns were processed in Dawn version 2.3.1 (Diamond Light Source) and fitted in OriginPro (OriginLab Corp.) and the peaks were fitted using a gaussian peak function:

$$\mathrm{y} = y_o + mx + Ae^{-}\left(\frac{(x - x_c)^2}{w}\right) \qquad [2.6]$$

Where w is the width of the gaussian, A is the amplitude and x_c is the centre. A gradient (m) was introduced to correct for the sloping baseline.

3. The Relationship between Temperature and Pressure for an aqueous DODAC Solution

3.1. Overview

The WAXS reflections of the aqueous DODAC solutions are studied between pressures of 0.001-4.0 kbar with 0.2 kbar steps under isothermal conditions at 65, 25, 15 and 5.0 ^{o}C, to build a pressure/temperature (P/T) relationship for this DODAC system. The L_{α}, L_{β} and $L_{\beta'}$ phases are given by the WAXS d-spacings (see section 2.5.4) for each pressure cycle. The pressure cycles at 25, 15 and 5.0 ^{o}C, give a pressure for the $L_{\beta} \rightarrow L_{\beta'}$ phase transition of 1.4, 0.8 and 0.2 kbar, respectively, and the d-spacing trend with pressure at those temperatures followed a similar pattern with an offset of 0.6 kbar. Therefore, the P/T relationship was given as 0.06 kbar/^{o}C, where this relationship was used to build a theoretical pressure phase diagram between 0.001-7.6 kbar, for a constant temperature of 65 ^{o}C.

3.2. Introduction

As mentioned in chapter 1, the structure of a liquid crystalline states can depend on concentration, size and type of surfactant or the counterion, where; the concentration can increase the aggregation size, mixed surfactant systems with surfactants types that adopt different curvatures can promote curvature of the dominant (ie with highest concentration) surfactant[140,141], the thickness of the bilayers increases with alkyl chain length[48], and DODAX counterions of X = Br^- and Cl^- give a chain melting transition temperatures for DODAB < DODAC[142]. These variations in lamellar phases are highly dependent on temperature and pressure. For example, micellar solutions of dialkyl quaternary ammonium surfactants are formed from predominantly lamellar vesicle phases with increasing temperature, so temperature can lower the lamellar→micellar

transition boundary[143]. Also, pressure can shift the temperature phase boundary to predict for low temperature phase behaviour[144]. This effect of pressure on the temperature phase behaviour was discussed (section 1.5.3) as an inverse relationship between the temperature and pressure phase behaviour which was extensively reviewed by Winter et.al. for liquid crystalline phases showing the inverse behaviour of temperature and pressure and the general temperature/pressure (T/P) relationships of ~220 ^{o}C/GPa (~0.045 kbar/^{o}C) at the chain melting transition of phosphatidylserine (PS), PE and PC (mentioned in sections 1.4.3 & 1.5) lipids types[145,146,147]. Therefore, the behaviour of a liquid-crystalline phase with increasing pressure is the same as decreasing temperature[148], where an increase in alkyl chain order is dominated by high pressures and low temperatures[149].

The pressure study was completed for this aqueous DODAC system, to gain information on the mechanisms behind the change in the DODAC bilayers structure and properties after FT. The importance of this study stems from the physical changes of personal care products which effect the function of the products upon freezing, during transportation and storage (see section 1.7.2). The low temperature phase behaviour can be predicted from the P/T relationship of the DODAC systems, where the changes in pressure can observe greater changes to the bilayers through faster equilibration rates compared to that of temperature-controlled systems[150]. Therefore, pressure-controlled systems can provide a more detailed account for the changes to the DODAC bilayers upon FT. In these studies, the P/T behaviour is determined through various pressure cycles of 0.001-4.0 kbar under isothermal conditions for temperatures of 65, 25, 15 and 5.0 ^{o}C, where the information is used to build a phase diagram with respect to the WAXS d-spacings of the L_{α}, L_{β} and $L_{\beta'}$ phases.

3.3. Results

3.3.1. Pressure Dependence

The aqueous DODAC solutions were pressurised using hydrostatic pressure, through methods described in section 2.5.6. The pressure was cycled up and down between 0.001-4.0 kbar with 0.2 kbar steps, at 65, 25, 15 and 5.0 ^{o}C. The DODAC solution was replaced at each temperature before the pressure cycles, to eliminate error from possible changes to the DODAC bilayers properties or structure. This chapter only records the phase behaviour of the DODAC bilayers through WAXS patterns, where the corresponding SAXS measurements are poorly resolved below 25 ^{o}C, above 1.0 kbar and for the repeat experiment after FT (see appendix, figure A3.1-A3.6), so cannot to support any microscopic phase changes. However, the SAXS results verified the presence of a lamellar phase for all temperatures at atmospheric pressure (see section 2.5.4).

The integrated WAXS patterns are given at 25 ^{o}C (Figure 3.1), where the aqueous DODAC solution is in the L_{β} phase which is shown by the gel peak at 4.10 Å (1.53 Å^{-1}), for reasons described in section 2.5.2. The gel peak d-spacing decreases from 4.10-4.06 Å (average fitting error ± 1 x 10^{-3} Å) with increasing pressure between 0.001-1.2 kbar. This decrease in the WAXS d-spacing corresponds to the increase in alkyl chain order with increasing pressure. At 1.4 kbar the gel d-spacing starts to increase from 4.05-4.10 Å as the pressure increases to 2.0 kbar, where a second peak is introduced at 1.6 kbar with a d-spacing of 3.93 Å (1.40 Å^{-1}).

The second gel peak, introduced at 1.6 kbar, is due to distortion in the hexagonal packing structure of the surfactant molecules in the gel phase, where typical changes to the hexagonal packing structure was discussed (section 2.5.5) as a distortion of the repeat

unit giving lengths of $d_1 > d_2$ which, in this case, resulted in two gel peaks. This effect was given for the $L_{\beta'}$ and $P_{\beta'}$ phases in section 2.5.5, where the $P_{\beta'}$ phase is generally viewed as an intermediate phase between the L_α and $L_{\beta'}$ phases due to uneven bilayer thickness as discussed in section 1.4.2 and is said to be both "solid"-like and "fluid"-like[151].

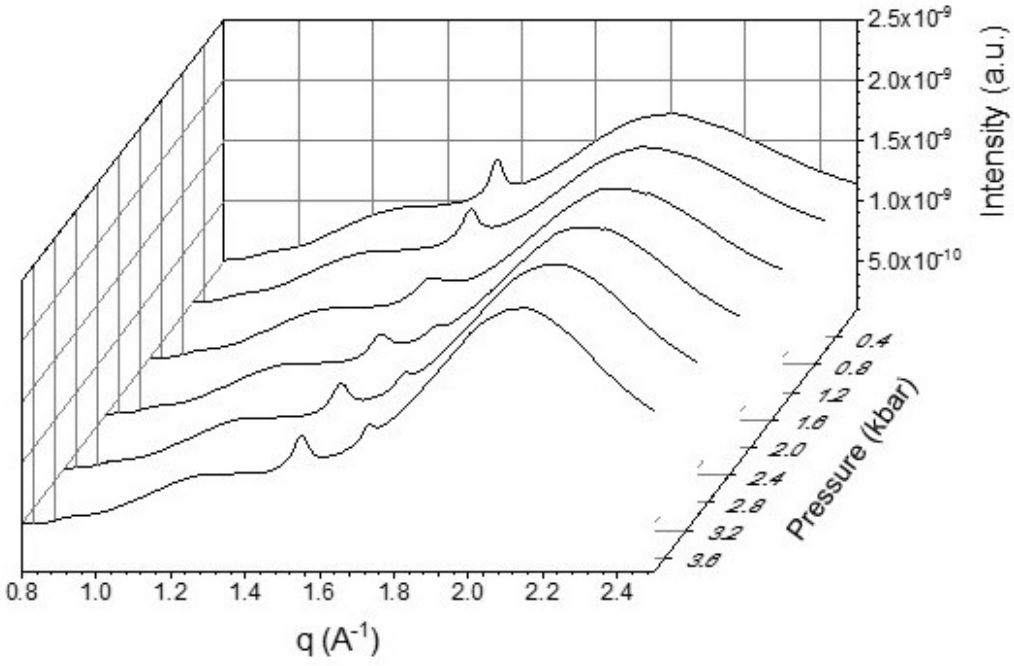


Figure 3.1. Shows the integrated WAXS patterns for a DODAC solution containing 0.085 wt% $CaCl_2$ at 25 °C, for pressures; 0.001, 0.6, 1.4, 2.2, 3.0 and 3.8 kbar. The gel peak is given at ~4.1 Å, where its d-spacing starts to increase with pressure until a second peak is introduced at 1.6 kbar with a d-spacing of ~3.7 Å, denoted as the $L_\beta \rightarrow L_{\beta'}$ transition. The average accuracy of the gaussian fitting for the WAXS gel peak is ± 1 x 10^{-3} Å.

At 25 °C (figure 3.1), the behaviour of the second gel peak d-spacing results in a decrease from 3.93 – 3.77 Å as the pressure increases from 1.6 to 2.0 kbar. Above 2.0 kbar, both gel peaks steadily decrease in d-spacing by 0.1 and 0.4 % every 0.2 kbar as the pressure increases to 4 kbar for the gel peak with the highest (~4.1 Å) and lowest (~

3.7 Å) d-spacing, respectively. This could be the result of the small gradual decrease in tilting of the bilayers in the $L_{\beta'}$ as the volume decreases.

3.3.2. Pressure-Temperature Relationship

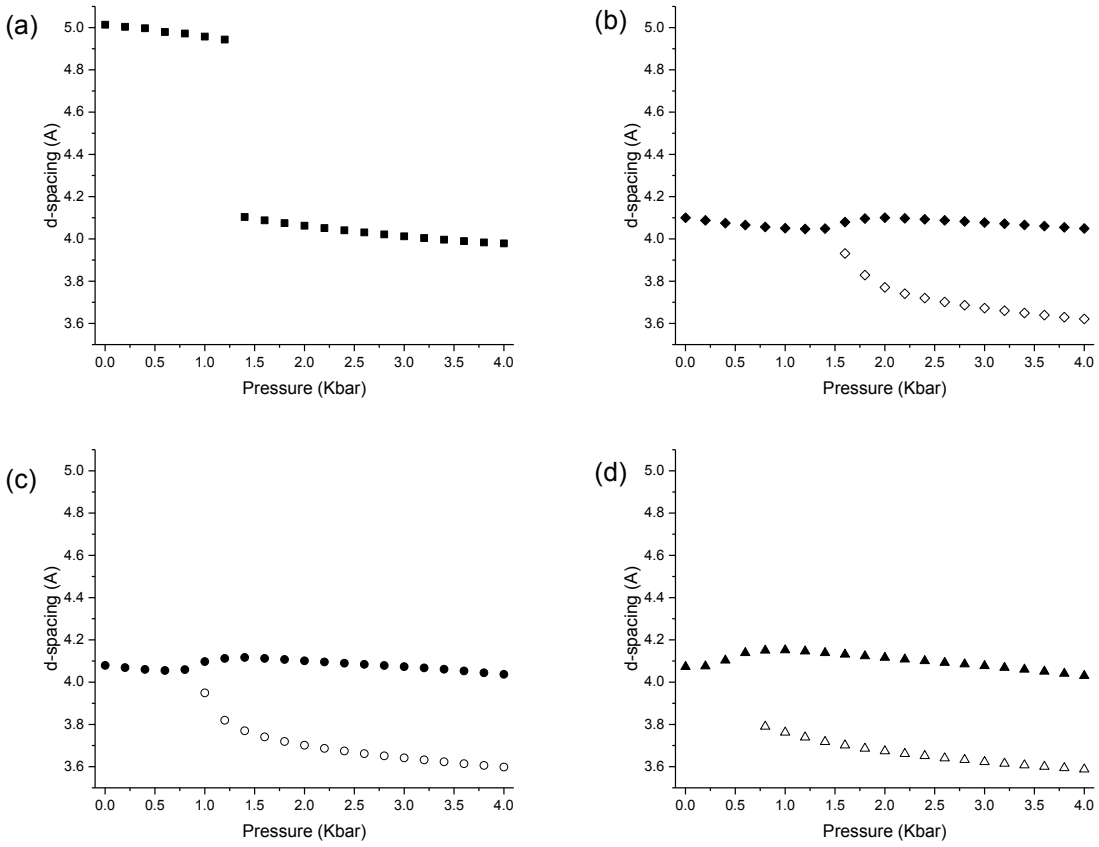


Figure 3.2. Shows the WAXS d-spacings of the L_α (~5.0 Å), L_β (~4.1 Å) and the $L_{\beta'}$ (from the distortion in the hexagonal packing given two gel peaks) phases, for increasing pressure between 0.001-4 kbar at temperatures; (a) 65, (b) 25, (c) 15 and (d) 5.0 ^oC. The second gel peak is given by; (b) ◊, (c) o and (d) Δ. The average accuracy of the gaussian fitting for the WAXS gel peak is ± 1 x 10^{-3} Å.

The WAXS d-spacings of the L_α (~5.0 Å), L_β (~4.1 Å) and $L_{\beta'}$ (~3.7 Å) phases are given for increasing pressure (0.001-4.0 kbar) at constant temperatures 65, 25, 15 and 5.0 ^oC (figure 3.2). The results at 65 ^oC (figure 3.2a) give the $L_\alpha \rightarrow L_\beta$ phase transition at 1.4 kbar,

so the L_α/L_β phase boundary lies between 1.2 and 1.4 kbar. For temperatures; 25, 15 and 5.0 ^oC (figures 3.2b, c & d), the introduction of the second gel peak which signifies the $L_\beta \rightarrow L_{\beta'}$ phase transition was given at 1.6, 1.0 and 0.8 kbar, respectively. The general behaviour of this transition, where the second gel phase peak appears, begins with an average 1 % increase of the first gel peak (at ~ 4.1 Å) d-spacing in the L_β phase. This increase takes place at 1.4, 0.8 and 0.2 kbar for temperatures 25, 15 and 5.0 ^oC, respectively. Although, the pressure phase behaviour of the aqueous DODAC solution at 5.0 ^oC (figure 3.2d), does not result in a second gel peak when the first gel peak (at ~4.1 Å) starts to increase, due to the freeze induced tilting of the L_β phase at 0.2 kbar. The differences in phase behaviour at 5.0 ^oC may be due to a low intensity gel peak (at ~3.7 Å) or convoluted gel peaks, which can be viewed as an increase in the gel peak (at ~ 4.1 Å) width.

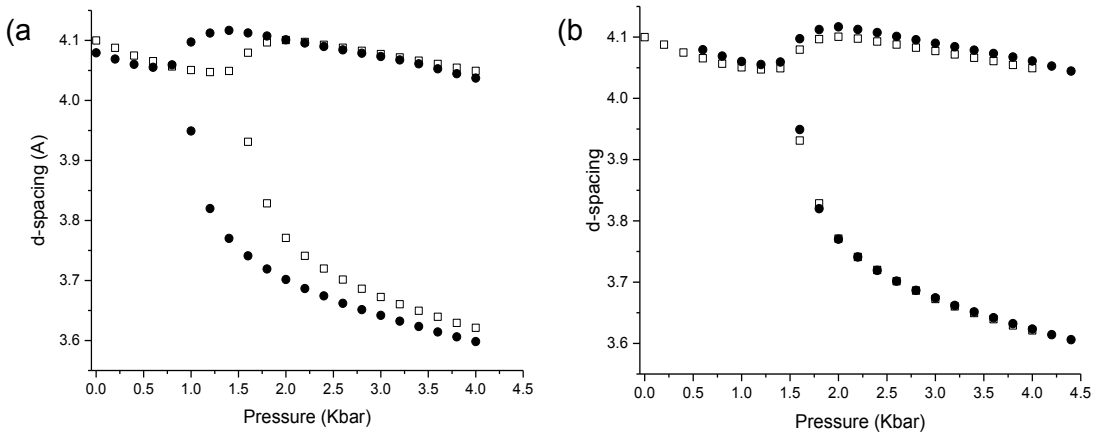


Figure 3.3. Shows the changes in the WAXS d-spacings for increasing pressure between 0.001-4.0 kbar, for temperatures; □ 25 and ●15 ^oC. (a) Shows original data (given in figure 3.2b & c), where the WAXS d-spacings follow a similar trend for increasing pressure and (b) shows the same results but with a positive 0.6 kbar shift in the pressure cycle given at 15 ^oC. The average accuracy of the gaussian fitting for the WAXS gel peak is ± 1 x 10^{-3} Å.

Following the differences in the $L_\beta \rightarrow L_{\beta'}$ phase transitions, where the transitions was suggested to take place when the L_β phase gel peak begins to increase, shows the pattern of a 0.6 kbar difference between the $L_\beta \rightarrow L_{\beta'}$ phase transition pressures at 25, 15 and 5.0 ^oC. This 0.6 kbar pattern was investigated through the comparison of the pressure cycles given at 25 and 15 ^oC (figure 3.3a), where the change in WAXS d-spacing with increasing pressure followed a similar trend between the 10 ^oC difference of 25 and 15 ^oC with an offset of 0.6 kbar. These patterns were combined by off-setting the pressure cycle completed at 15 ^oC by 0.6 kbar in the positive x-direction (figure 3.3b), giving a P/T relationship of 0.06 kbar/^oC for this aqueous DODAC system.

3.3.3. Pressure-Temperature Phase Behaviour

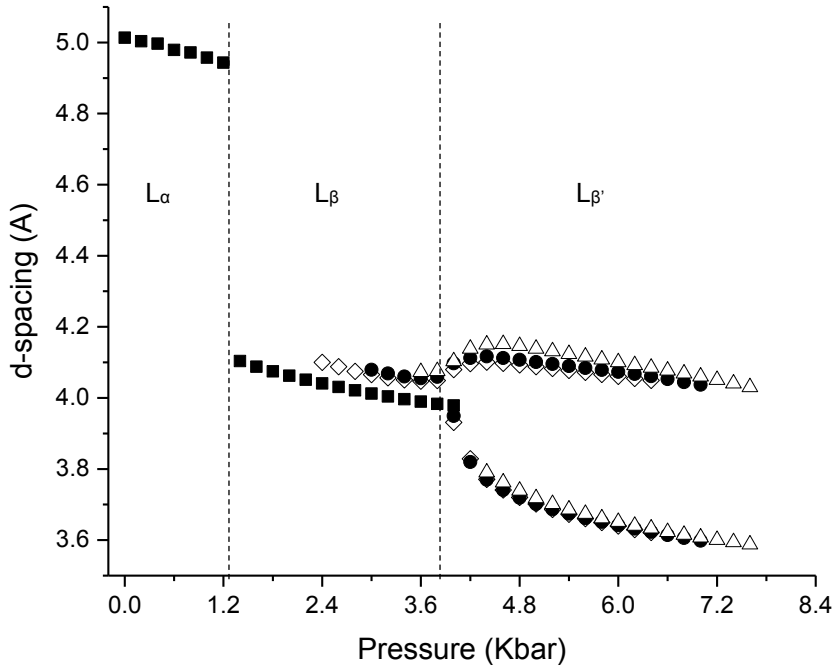


Figure 3.4. Shows the theoretical pressure plot for the WAXS d-spacings at temperatures; ■ 65, ◊ 25, ● 15 and Δ 5.0 ^oC. The plot shows the changing d-spacing for increasing pressure based on a temperature of 65 ^oC, where the results taken from figure 3.2 are offset by the P/T relationship of 0.06 kbar/^oC. The phase transitions of the $L_\alpha \rightarrow L_\beta$ and the $L_\beta \rightarrow L_{\beta'}$ phases take place

at 1.4 and 3.8 kbar, respectively. The average accuracy of the gaussian fitting for the WAXS gel peak is ± 1 x 10^{-3} Å.

The pressure cycles at 65, 25, 15 and 5.0 ^{o}C were combined to form a theoretical pressure phase diagram between 0.001-7.6 kbar for a constant temperature of 65 ^{o}C (Figure 3.4). The phase diagram shows the transitions of the $L_{\alpha} \rightarrow L_{\beta}$ and $L_{\beta} \rightarrow L_{\beta'}$ phases at 1.4 and 3.8 kbar, respectively. Based on the P/T relationship of 0.06 kbar/^{o}C and a starting temperature of 65 ^{o}C, the theoretical transition pressures of 1.4 and 3.8 kbar corresponds to calculated temperatures of 42 and 1.7 ^{o}C, respectively.

The maximum pressure of the new plot (figure 3.4) is 7.6 kbar, so the calculated minimum temperature of the plot in figure 3.4, based on the P/T relationship (0.06 kbar/^{o}C) is -62 ^{o}C. Therefore, the calculated temperature from the theoretical plot (figure 3.4) is low enough for a $L_{\beta'} \rightarrow L_{c}$ transition. However, there are no changes to the WAXS d-spacings indicating a crystalline phase above a theoretical pressure of 4.4 kbar (-8. 3 ^{o}C), instead both gel peaks have a steady decrease with increasing pressure.

The theoretical plot for the pressure down cycle (Figure 3.5), shows $L_{\beta'} \rightarrow L_{\beta}$ and $L_{\beta} \rightarrow L_{\alpha}$ transitions at 3.8 and 1.2 kbar, respectively, where the pressure cycle at 65 ^{o}C show a hysteresis of 0.2 kbar between the up and down pressure transitions. The transition from $L_{\beta'} \rightarrow L_{\beta}$ phase takes place at the same theoretical pressure (3.8 kbar), for both up and down pressure cycles. Also, the second gel peak (~3.7 Å) is present for all temperatures in figure 3.5 at 4.0 kbar.

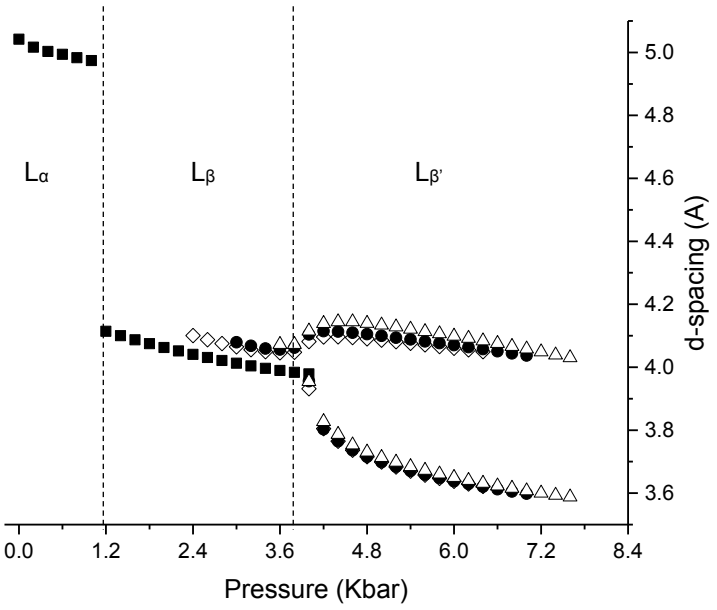


Figure 3.5. Shows the theoretical plot of the sample in figure 3.4 for the changes in WAXS d-spacing with decreasing pressure at 65 ^{o}C, where the pressure down cycles at temperatures; ■ 65, ◊ 25, ● 15 and Δ 5.0 ^{o}C, was offset using the P/T relationship of 0.06 kbar/^{o}C. The deceasing pressure transitions of the $L_{\beta'} \rightarrow L_{\beta}$ phase takes place at 3.8 kbar, and of the $L_{\beta} \rightarrow L_{\alpha}$ phase takes place at 1.2 kbar, where there is a hysteresis between the up and down pressure cycles at the $L_{\beta} \rightarrow L_{\alpha}$ phase transition.

3.4. Conclusion

The P/T relationship for this aqueous DODAC system was determined to be 0.06 kbar/^{o}C, where this P/T relationship is similar to the general P/T relationship for lipid systems of ~0.045 kbar/^{o}C, as mentioned earlier. This P/T relationship was consistent for the repeat experiment (see appendix, figure A3.7 & A3.8) with the same conditions for the aqueous DODAC solutions before and after FT (see appendix, figure A3.9 & A3.10). The P/T relationship matches perfectly between the pressure cycles at 25, 15 and 5.0 ^{o}C which show a strong correlation between the WAXS d-spacings at a given pressure, where this correlation can be used to predict the low temperature behaviour for this aqueous DODAC solution. Although, the model is not perfect, because the pressure cycle given at 65 ^{o}C show no indication of the $L_{\beta} \rightarrow L_{\beta'}$ phase transition.

At 3.8 kbar, the L_β phase gel peak d-spacings starts to increase, before the $L_\beta \rightarrow L_{\beta'}$ transition, where the pressure cycle at 65 ^oC does not share this same behaviour and there is no introduction of a second gel peak at ~3.7 kbar for both the up and down pressure cycles. There is also a kinetic lag between the up and down pressure cycles for the L_α and L_β phase boundary, where there is no hysteresis between the up and down pressure cycles at the L_β and $L_{\beta'}$ phase boundary. These differences between the phase boundaries and the lack of $L_\beta/L_{\beta'}$ phase boundary for pressure cycles given at 65 ^oC, may be due to a different P/T relationship between 65-25 ^oC or different phase behaviour between temperature and pressure, between 65-25 ^oC. Therefore, these studies have a 40 ^oC gap in the P/T phase model. So, a direct comparison between; the pressure-controlled system at 65 ^oC and a temperature-controlled system at atmospheric pressure or pressure cycles given at constant temperatures between 65-25 ^oC, is needed to give a more accurate P/T relationship for this aqueous DODAC system.

4. The Comparison between the Temperature and Pressure Controlled Systems

4.1. Overview

The P/T relationship of 0.06 kbar/^{o}C, was previously (section 3.3.3) derived for the DODAC aqueous solution, but the pressure phase behaviour did not match between constant temperatures of 65 and 25 ^{o}C. In this chapter, the P/T relationship is studied between 65-25 ^{o}C by the direct comparison between thermotropic isobaric (temperature driven) and barotropic isothermal (pressure driven) systems. The temperature driven system was cooled from 65 to 20 ^{o}C at atmospheric pressure and SAXS/WAXS results were given in 5.0 ^{o}C steps. The pressure driven system was pressurised from 0.001 to 4.0 kbar in 0.2 kbar steps for a constant temperature of 62.6 ^{o}C, but the results displayed are shown for a maximum pressure of 2.6 kbar. This pressure range (0.001-2.6 kbar) give calculated temperatures of 63-19 ^{o}C using the P/T relationship. These systems resulted in different gel conformations, where the temperature driven system transitioned from the $L_{\alpha} \rightarrow L_{\beta}$ phase and the pressure driven system transitioned from $L_{\alpha} \rightarrow L_{\beta'}$ (or $P_{\beta'}$) phase. The effects upon FT was studied for both the temperature and pressure driven systems, which resulted in a general FT induced swelling of the bilayers with little changes to the hexagonal packing structure given by the WAXS d-spacings (see section 2.5.4).

4.2. Introduction

In chapter 3, the behaviour upon freezing was characterised at high pressures for this aqueous DODAC system (8 wt% DODAC in a 0.085 wt% $CaCl_2$ solution) through the changes in the WAXS d-spacings of the L_{α}, L_{β} and $L_{\beta'}$ phases, during pressure cycles between 0.001-4.0 kbar at constant temperatures of 65, 25, 15 and 5.0 ^{o}C. The results

gave a P/T relationship of 0.06 kbar/^{o}C, but the P/T relationship at 65 and 25 ^{o}C behaved differently, where no $L_{\beta} \rightarrow L_{\beta'}$ transition was given at 3.8 kbar for the pressure cycle at 65 ^{o}C. This suggests a difference in the thermotropic and barotropic behaviour between 65 and 25 ^{o}C, where the P/T relationship at the L_{α} and L_{β} phase boundary is different to the one at the L_{β} and $L_{\beta'}$ boundary and/or more phases exist in the phase behaviour of this aqueous DODAC solution. Thus, the importance of the direct comparison between the pressure- and temperature-controlled systems.

The extensive research on DODAC aqueous solutions (see section 1.7.2) have little records of the DODAC bilayers existing in a gel phase other than the L_{β} phase (when not in the coagel phase, described in section 1.7.2). However, the existence of an L_{β}I phase was discussed (see section 1.7.2) with reports by Gonçalves et. al.[113], for a 35 wt% DODAC (DODAC levels in this chapter are of 8 wt%) solution and by Tsuruta et. al.[109], from DODAC adhesion onto polystyrene microspheres at high DODAC concentrations. Additionally, the properties of the DODAC bilayers were reported by Kodama et. al, through DSC studies, as a constant phase behaviour for DODAC bilayers between 15 and 80 wt% DODAC[152]. So, studies suggest an L_{β}I phase between 15-80 wt% DODAC and an L_{β} phase below 15 wt% DODAC, for the DODAC bilayers.

There is also a lack of research on the freezing behaviour of DODAC and none on the property and structural changes to the bilayers before and after FT. There is extensive research on the chain melting $L_{\beta} \rightarrow L_{\alpha}$ phase transitions of DODAC aqueous solutions, where the cooling transitions are mentioned but in relation to the position of the chain melting transition and there are no indications of freezing in the reports[153,154]. However, there are reports by Liu et. al.[155], where the comparison was made for the L_{α}/L_{β} transition boundary between sonicated DODAC samples before and after freezing. This report mentioned an increase in the local viscosity of the DODAC bilayers after freezing,

compared to the local viscosity before freezing. Therefore, the results given in this chapter are covering an area in the DODAC phase behaviour that has been neglected.

4.3. Results

4.3.1. Temperature-Controlled Transitions

The L_α and L_β phase boundary was assessed between 65-20 ^oC at atmospheric pressure before and after FT to determine the effects of freezing on the DODAC bilayers. The temperature was equilibrated at each temperature step, with an initial temperature of 65 ^oC and a decrease of 5.0 ^oC intervals.

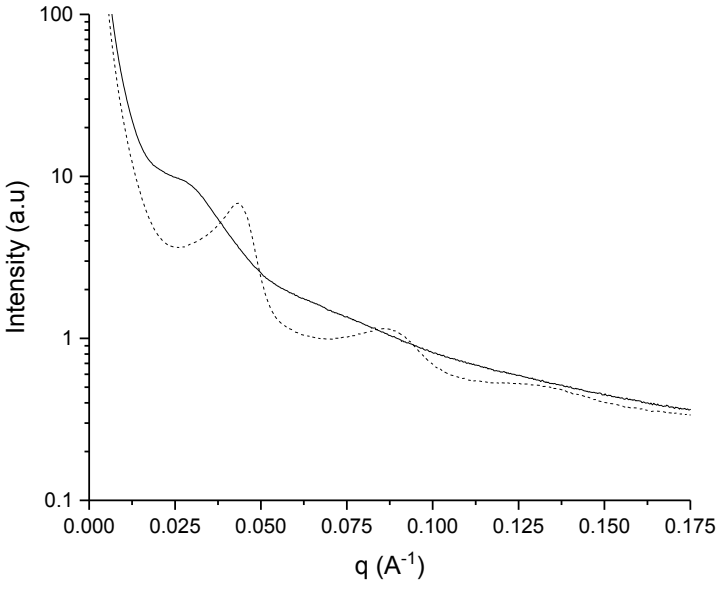


Figure 4.1: Shows the integrated SAXS patterns for a temperature driven system at 35 ^oC, for before (dashed line) and after freeze-thawing (solid line), where the lamellar phase resides in a gel phase at 35 ^oC. The results shown are for an 8 wt% DODAC solution containing in 0.085 wt% $CaCl_2$.

Figure 4.1 shows a typical lamellar SAXS pattern with a 1: 2: 3… peak position ratio (see section 2.5.2), where a maximum of three peaks could be indexed (dashed line) and only one after FT (solid line). The SAXS peaks are diffused with low resolution which decreases after FT and with decreasing temperature. This low SAXS resolution could be due to the high levels of water in the system, low lamellarity and the increased water levels between the bilayers after FT.

The integrated SAXS patterns are shown at 35 ^{o}C (figure 4.1), where the $L_{\alpha} \rightarrow L_{\beta}$ phase transition takes place. This is given by a WAXS gel peak at ~4.1 Å (figure 4.5). The d-spacings of this system was determined using a gaussian curve function for the peak fitting (see section 2.5.6). For each indexed peak of the SAXS reflections, the best fit to the gaussian function was for a two-component gaussian which suggests that there is more than one lamellar reflection for this system. This is likely, based on the lack of symmetry either side of the peak maximum. Thus, the d-spacings for two lamellar repeat units was plotted with decreasing temperature (figure 4.2), where the lamellar reflections show a general increase in the d-spacings of the bilayers after FT.

Before FT, the two lamellar reflections are ~27 Å in difference (figure 4.2a) and both increase in d-spacings between 65-35 ^{o}C with decreasing temperature by 0.4 and 1.0 % every 5.0 ^{o}C for the (■) and the (x) lamellar reflections, respectively. So, the variations in the d-spacings with decreasing temperature are very small in the L_{α} phase. However, this variation is much smaller for the (■) lamellar reflection which could be due to suppressed temperature effects from inner vesicle layers of a lamellar structure with uneven bilayer thickness or water thickness. This suggests a lack of uniformity in the system and across the bilayer planes. When transitioning from $L_{\alpha} \rightarrow L_{\beta}$, the lack of uniformity can result in localised tilting within the bilayers (see sections 1.4.3 & 2.5.5) which is characteristic for $L_{\alpha} \rightarrow P_{\beta'} \rightarrow L_{\beta'}$ phase transitions. Though, the lamellar reflections

are unresolved and a $P_{\beta'}$ phase cannot be certain, based on the reported lamellar reflections for $P_{\beta'}$ phases given by PC lipids[156,157].

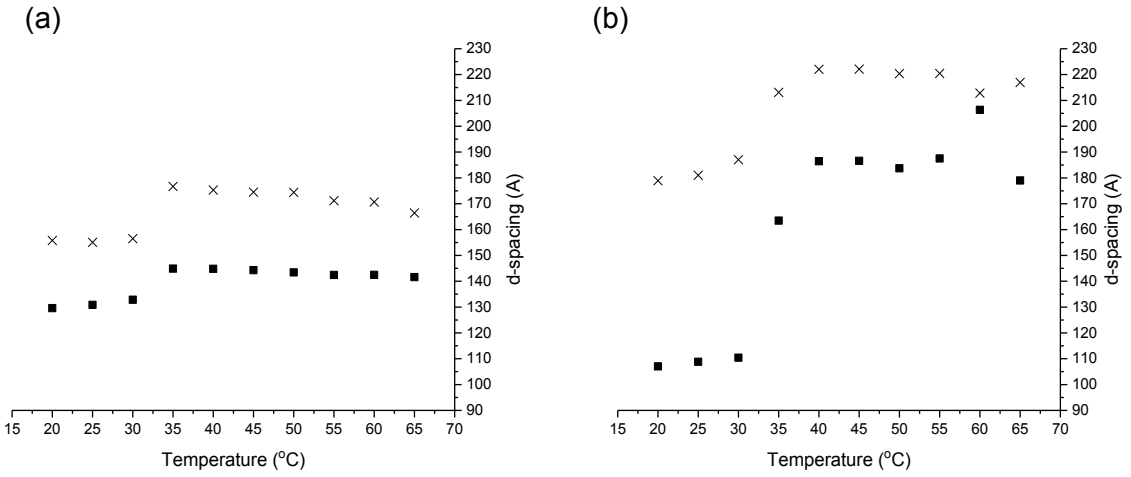


Figure 4.2: Shows the d-spacing changing with temperature for (a) before and (b) after freeze-thawing. The SAXS peaks fit to a two component gaussian function giving two lamellar packing units labelled x and ■. The indexed lamellar peak fitting is accurate to ± 1 Å.

As mentioned, the aqueous DODAC solution at 35 °C is in a gel state (see figure 4.5) and the P/T relationship gave a $L_\alpha \rightarrow L_\beta$ phase transition temperature of 42 °C (section 3.3.3). This transition temperature given by the P/T relationship lies within the 5.0 °C temperature step of the acquired result for the temperature-controlled system. Therefore, the P/T relationship provides a good approximation for the L_α and L_β phase boundary. After this transition to the L_β phase (the gel phase is referred as the L_β phase until it is fully defined), between 35 and 30 °C, there is an 11 (for x) and 8.0 (for ■) % decrease in d-spacing for the two lamellar reflections (in figure 4.2a). This change in the bilayers spacing after the $L_\alpha \rightarrow L_\beta$ phase transition, proves that the gel transition is slow and could result in the pre-transitional $P_{\beta'}$ phase at 35 °C then a $L_{\beta'}$ phase at 30 °C which is a common behaviour of the $P_{\beta'}$ phase (see section 1.4.3).

After FT (figure 4.2b), the $L_\alpha \rightarrow L_\beta$ phase transition gives a 12 (for x) and 4.0 (for ■) % drop in the d-spacings between 40-35 ^oC, for the larger and smaller lamellar reflections, respectively. This is followed by a second drop in the lamellar d-spacings of 32 % for the larger lamellar reflection and 12 % for the smaller lamellar reflection, from 35 to 30 ^oC. There are more changes in the d-spacings after FT which is shown by the structural differences in the DODAC bilayers at 35 and 30 ^oC, where at 35 ^oC before FT the structure of the bilayers is similar to that of the L_α phase and after FT the structure is similar to that of the L_β phase. The DSC thermographs show a similar behaviour of the DODAC bilayers at the L_α/L_β phase boundary, where a double transition is given after FT (see figures 5.4, 6.3 & 7.4).

There is an overall decrease in the d-spacings from the $L_\alpha \rightarrow L_\beta$ phases. The behaviour of the bilayers upon cooling generally (except for transitions to the $L_\beta I$ phase) result in a bilayer thickness for the $L_\alpha < L_\beta$ phase (see section 1.5.3), so the decrease in bilayers distance from the $L_\alpha \rightarrow L_\beta$ phase is either from a decrease in aqueous solution between the bilayers or due to a $L_\alpha \rightarrow L_\beta I$ phase transition. If the former is true, this decrease in the d-spacing between the fluid and gel states, is due to a decrease in the undulating pressure (see section 1.5.4) between the bilayers from the increase in the chain packing density and bilayers rigidity in the gel phase[158,159].

4.3.2. Pressure-Controlled Transitions

The pressure-controlled system was cycled between 0.001-4.0 kbar with 0.2 kbar steps at a constant temperature of 63 ^oC. For comparison with the temperature-controlled system, only the pressure range of 0.001-2.6 kbar is shown in these studies which is equivalent to a temperature range of 63-19 ^oC (based on the P/T relationship for this system). Like the temperature-controlled system, the integrated SAXS patterns are diffused and decrease in resolution after FT (figure 4.3). Though, the second lamellar

reflection is more obvious in the pressure-controlled system after FT showing a peak at 0.0324 $Å^{-1}$ (194 Å) and 0.0464 $Å^{-1}$ (135 Å) which do not match as a single lamellar (indicated by the black arrows in figure 4.3).

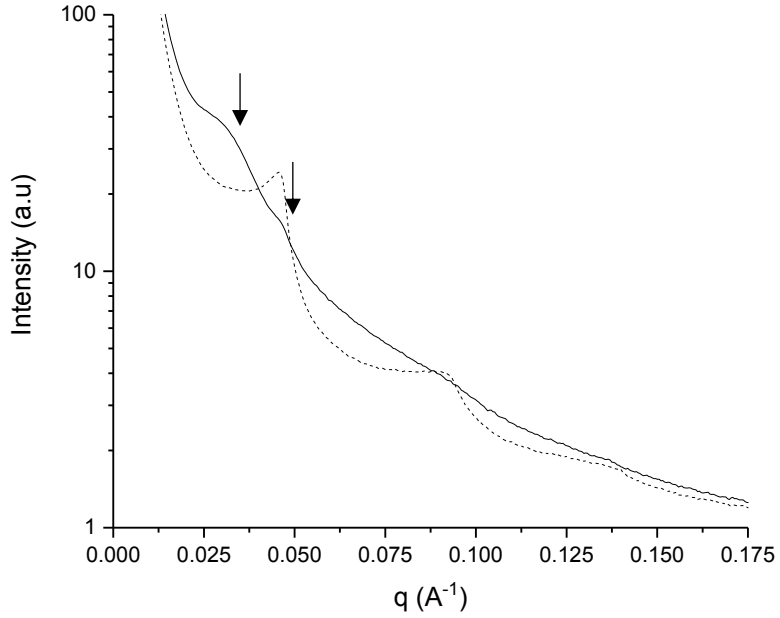


Figure 4.3: Shows the SAXS comparison for pressure induced transitions at 1.2 kbar and a constant temperature of 63 ^{o}C, before (dashed lines) and after freeze-thawing (solid lines). The $L_{\alpha} \rightarrow L_{\beta}$ phase transition is complete at 1.2 kbar (given by the presence of the gel peak in figure 4.5b) which is equivalent to a calculated temperature of 43 ^{o}C, using the P/T relationship for this system. The black arrows indicate the first indexed peak for the two different lamellar reflections in the integrated SAXS patterns after FT (solid lines).

The change in d-spacings for the two lamellar reflections with increasing pressure was plotted for before and after FT (figure 4.4). Also, the plot includes the temperature equivalent for each pressure which was calculated by the P/T relationship of 0.06 kbar/^{o}C (see figure 3.4). Although the P/T relationship was shown in chapter 3 to be incorrect for

the L_α/L_β phase boundary, the relationship can still be a good approximation to compare both the temperature- and pressure-controlled systems.

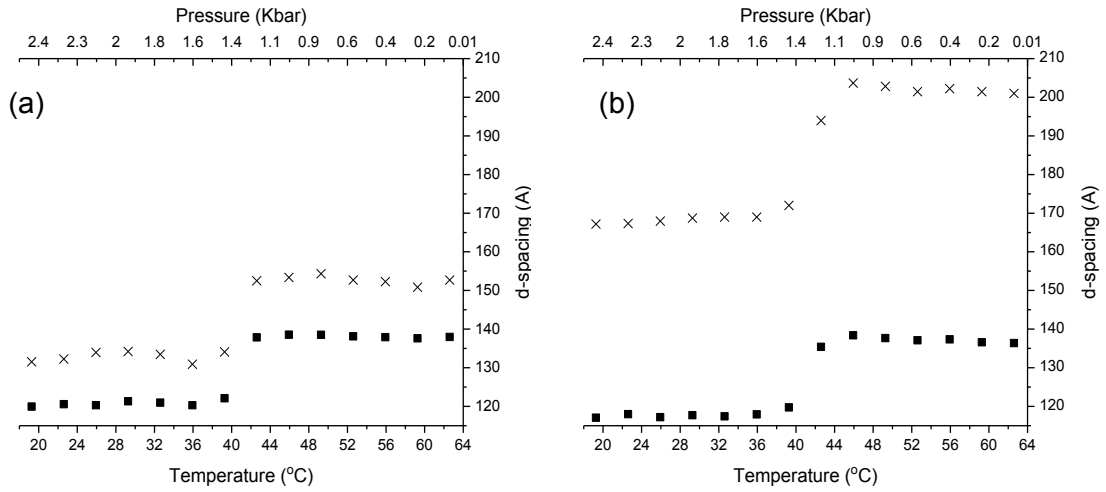


Figure 4.4: Shows the SAXS d-spacings with decreasing temperature/increasing pressure for (a) before and (b) after freeze-thawing. The two lamellar reflections are labelled as (x) for the larger d-spacings and (■) for the smaller d-spacings. The temperature was calculated using the P/T relationship (0.06 kbar/°C) for 8 wt% DODAC in an aqueous solution containing 0.085 wt% $CaCl_2$ (see figure 3.4). The $L_\alpha \rightarrow L_\beta$ phase transition is complete at 1.2 kbar which is equivalent to 43 °C as seen by the presence of the gel peak in figure 4.5b. The indexed lamellar peak fitting is accurate to ± 1 Å.

The pressure-controlled system is in the L_β phase at 1.2 kbar with a calculated (using P/T relationship, section 3.3.3) temperature of 43 °C (± 1 °C based on previous results) which was compared to the temperature-controlled system (L_β phase transition takes place between 40-35 °C) in the previous section. In comparison to the 5.0 °C steps of the temperature-controlled system, the pressure-controlled system has equivalent calculated temperature steps of 3.3 °C and as mentioned in section 3.2, pressure propagates through a system faster than temperature. So, the transition temperature given by the pressure-controlled system is more precise, for an accurate P/T relationship.

The change in d-spacings with increasing pressure follows a similar trend to that of decreasing temperature. The effect of increasing pressure is almost constant before and after FT between 0.001-1.2 kbar (calculated to 63-43 ^{o}C) and between 1.6-2.6 kbar (calculated to 36-19 ^{o}C). This lack of variation in the d-spacings with increasing pressure is probably due to the greater data points acquired from the equivalent 3.3 ^{o}C steps, compared to that of the temperature-controlled system where the variations in the d-spacings are already quite small for 5 ^{o}C steps (figure 4.2).

Before FT (figure 4.4a), between 1.2-1.4 kbar (calculated temperatures of 43-39 ^{o}C) the d-spacings has a 12 % drop for (x) and an 11 % drop for (■). Also, similar to the behaviour of the temperature-controlled system, there are two transitions after FT (figure 4.4b). This is represented as a decrease in the (x) d-spacings of 5 and 11 % between 1.0-1.2 kbar (calculated temperatures; 46-43 ^{o}C) and 1.2-1.4 kbar (calculated temperatures; 43-39 ^{o}C), respectively. The same behaviour was shown for the smaller d-spacings (■), given by the second lamellar reflection (figure 4.4b), as a decrease in the d-spacings of 2 and 12 % between pressures 1.0-1.2 kbar (calculated to 46-43 ^{o}C) and 1.2-1.4 (43-39 ^{o}C), respectively. The FT induced swelling of the bilayers shown by the increase in d-spacings between the d-spacings before (figure 4.4a) and after FT (figure 4.4b), shows no changes for the smaller d-spacings (■) besides the second transition given after FT between 1.0-1.2 kbar. This is the result of a suppressed lamellar phase that is unaffected by the FT induced swelling.

4.3.3. WAXS Comparisons

The temperature- and pressure-controlled systems follow similar tends in the SAXS d-spacings for decreasing temperature and increasing pressure, respectively, though the effects upon FT for the smaller lamellar reflection are different and this could be a relation

to the type of phase each system resides. The WAXS gel peaks are given for both temperature- and pressure-controlled systems (figure 4.5) to identify the type of gel phase. The temperature-controlled system gives (figure 4.5a(i)) a double gel peak with d-spacings of ~4.2 and ~4.1 Å at 35 ^{o}C, where this double gel peak is given after FT (see appendix, figure A4.1) and the WAXS d-spacings given before and after FT remains constant by three significant figures. This distortion in the gel peak is the result of tilting in the bilayers with respect to normal bilayers (see section 2.5.4).

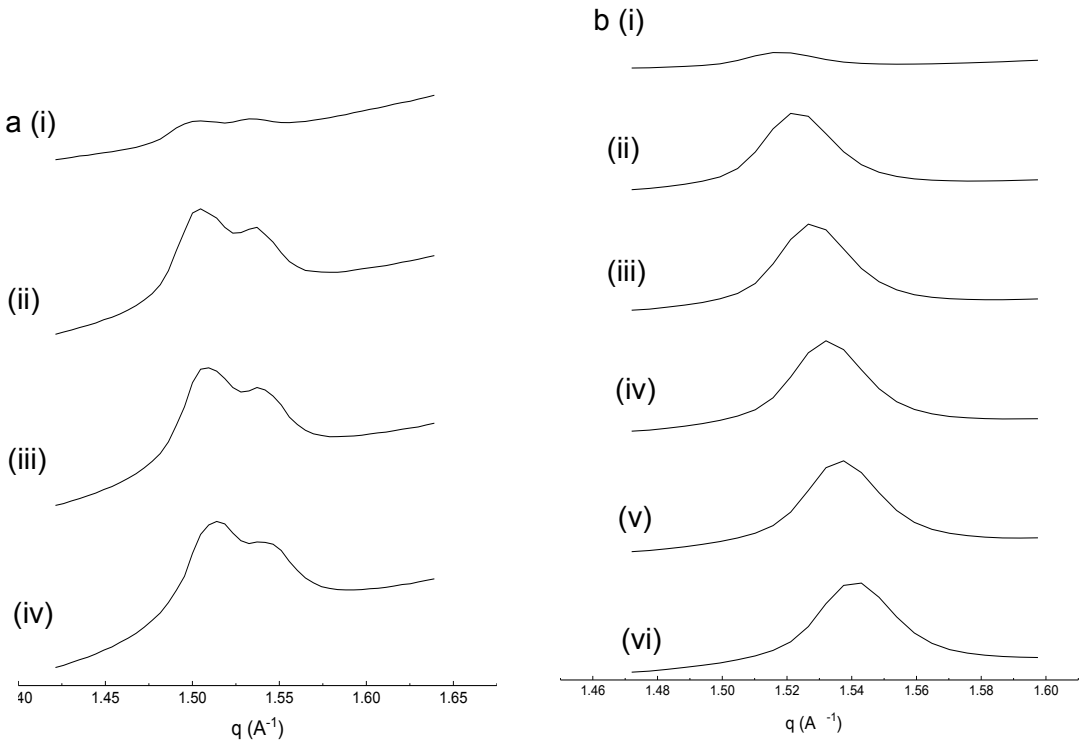


Figure 4.5: Shows the WAXS gel peaks for (a) temperature- and (b) pressure-controlled systems. For the temperature-controlled system the $L_{\beta'}$ phase exists at; (i) 35, (ii) 30, (iii) 25 and (iv) 20 ^{o}C. For pressure-controlled system at 63 ^{o}C, the $L_{\beta'}$ phase exist peak exists at; (i) 1.2, (ii) 1.4, (iii) 1.6, (iv) 1.8, (v) 2.0 and (vi) 2.2 kbar.

The pressure-controlled system has a WAXS gel peak at 1.2 kbar (calculated to 43 ^{o}C), which exists as a single peak at ~4.1 Å. The WAXS results are consistent between the

WAXS peaks given before and after FT (see appendix, figure A4.2). The differences in the gel peaks between the temperature- and pressure-controlled systems were assessed further by the comparison of the calculated gel peak width (figure 4.6), where the distortion in the hexagonal packing structure can be observed by widening of the WAXS gel peak (see section 2.5.4). For this comparison, the pressure was converted into temperature using the P/T relationship (0.06 kbar/^{o}C, see figure 3.4) and the comparison also includes the gel peak widths for after FT.

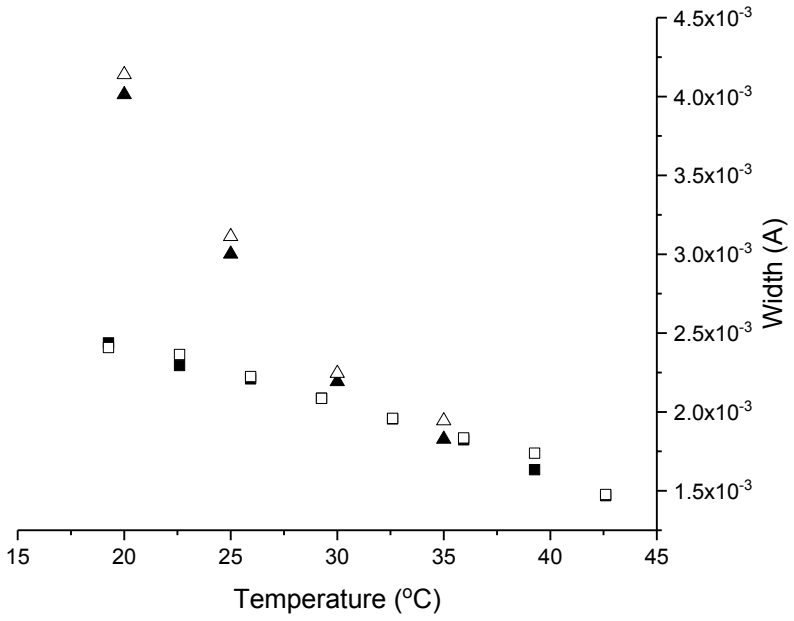


Figure 4.6: Shows the increasing WAXS gel peak width with decreasing temperature for; (▲) temperature-controlled transitions before freeze-thawing and (Δ) after, and the (■) pressure-controlled transitions before and (□) after freeze-thawing. The pressure was converted to temperature using the P/T relationship for this DODAC system (see figure 3.4), giving a calculated temperature. The accuracy of the WAXS width gaussian fitting is ± 2 x 10^{-4} Å.

There is a general increase with the gel peak width with decreasing temperature. After 35 ^{o}C, the temperature-controlled system (Δ) continues to increase in gel peak width as the pressure-controlled system (□) starts to plateau. For both systems the trend before

and after FT remain the same. This supports that there are no changes to the local packing structure of the surfactant aggregates which is given by the almost constant gel peak d-spacings before and after FT (see appendix, figures A4.1 & A4.2).

The differences in the WAXS gel peak widths and the differences between the shape of the WAXS gel peaks proves that the pressure-controlled system at 65 ^{o}C takes a different transition path to the temperature-controlled system, where the WAXS gel peaks for the temperature-controlled system is similar to that of the $L_{\beta'}$ or $P_{\beta'}$ phase and the pressure-controlled system resides in the L_{β} or $L_{\beta}I$ phase. The $L_{\beta}I$ phase was discussed earlier as a possible reason for the decrease in SAXS d-spacing during the fluid to gel phase transition but due to how the DODAC bilayers are susceptible to change upon FT, it is unlikely that there is interdigitation of these bilayers because they would be more robust to the changes upon FT. These results were repeated for both systems giving similar results in the gel peak widths (see appendix, figures A4.3 & A4.4).

4.4. Conclusions

Based on the P/T relationship (0.06 kbar/^{o}C, see figure 3.4) for this aqueous DODAC system, the differences in the phase behaviour takes place above 25 ^{o}C, as shown here by the different phases given for the temperature- and pressure-controlled systems. This was assumed (in section 3.4) from the perfect match of the phase behaviour at 25, 15 and 5.0 ^{o}C and the not so perfect match at the L_{α} and L_{β} phase boundary between the pressure-controlled system at 25 and 65 ^{o}C. Therefore, the P/T relationship is not 0.06 kbar/^{o}C at the L_{α} and L_{β} phase boundary and other phases exist in the aqueous DODAC system.

The phase assignments were made for the pressure- and temperature-controlled systems, where the temperature-controlled system was suggested to be in a $L_{\beta'}$ or $P_{\beta'}$

phase. However, the resolution of the integrated SAXS patterns are too low to distinguish between the $L_{\beta'}$ and $P_{\beta'}$ phases, where the SAXS patterns are given by broad lamellar reflections, and so the phase of the temperature-controlled system cannot confirm a $P_{\beta'}$ phase, but it also cannot be ruled out. Generally, the $P_{\beta'}$ phase would give multiple lamellar reflections (as seen in figure 2.9) in the SAXS integrated patterns, due to the different planes in the ripple phase. The number of lamellar reflections would depend on the periodicity of the rippled repeat unit, where a longer rippled wavelength (λ_r) would give a smaller B valve (see section 2.5.5) and the lamellar reflections will be closer together resulting in boarder SAXS patterns than a shorter λ_r[160].

The effects after FT on this system has shown a general increase in the SAXS d-spacing and no change to the local structure of the surfactant aggregates, given by the constant WAXS peak positions before and after FT. This suggest that if there is a disruption in the vesicle structure upon freezing, after thawing the surfactants reorganise into the same localised packing structure. Thus, the change in microstructure after FT is due to increased levels of aqueous solution between the bilayers.

5. The Effects of $CaCl_2$ and Surfactant Levels on a DODAC System

5.1. Overview

This chapter shows the effects of varying levels of $CaCl_2$ on the DODAC bilayers distance which proves a decrease in d-spacing with increasing $CaCl_2$ levels. This behaviour is suggested to be due to ionic effects through the reduced ionic potential in the Debye length (section 1.5.1) which cause a shielding effect between the positively charged ammonium "head groups" of the DODAC bilayers. The increase in the Debye length suppresses the effects of increasing DODAC levels from 5-14 wt%, on the aqueous-surfactant mixture, where the general behaviour of the bilayers d-spacing without $CaCl_2$ is a decrease from 210 to 142 Å (± 5 Å) for a 9 wt% increase of DODAC levels. Upon the introduction of 0.15 wt% (0.024 mol%) $CaCl_2$, the bilayer spacing remains constant for increasing surfactant levels.

The phase behaviour for 8 wt% DODAC was assessed further between 65-25 ºC (5.0 ºC steps) for varying levels of $CaCl_2$; 0, 0.085 (0.014) and 0.15 (0.024) wt% (mol%). In the absence of $CaCl_2$, the properties of the DODAC bilayers changes after FT which cause a shift in the $L_\alpha \rightarrow L_{\beta'}$ (or $P_{\beta'}$) transition temperature from ~31 to ~34 ºC. For all levels of $CaCl_2$, before FT, the $L_\alpha \rightarrow L_{\beta'}$ (or $P_{\beta'}$) transition is accompanied by an average 10 % decrease of the SAXS d-spacing and an average decrease of 67 % in the relative peak height through the static solid state ^1H NMR alkyl peak height.

5.2. Introduction

The behaviour of salt on DODAC systems have been reported by Carmona-Ribeiro et. al., as a relative increase in fluctuation of DODAC bilayers (see section 1.5.4) with the

addition of $CaCl_2$ (0.3-1 mol%) for sonicated DODAC vesicles, where the rate of fluctuation is inversely proportional to the vesicle stability, ie coagulation rate[161]. This decrease in stability is reported by Hoffmann et. al., as a linear decrease in the storage modulus after the addition of excess salt[162]. A recent report by Saveyn et.al, shows an increase in $CaCl_2$ levels (from 0.04-0.1 wt%) results in a ~40 % decrease in DODAC bilayer d-spacing[163]. These reports show that small variations in the $CaCl_2$ levels can influence the thermal fluctuations of the bilayers and bilayer spacings of a lamellar structure. The results shown in this chapter have a high sensitivity of the bilayer spacings to the addition of $CaCl_2$ (0-0.15 wt%) which result in a stabilisation of the lamellar structure from the effects on increasing DODAC levels.

The stability of the vesicular microstructure was assessed further for the effects upon freeze-thawing (FT). The mechanism upon freezing was discussed in the section 1.7.1, where the resultant frozen structure and the effects upon thawing differed by the concentration of water and ionic interactions between the amphiphiles. Most reports on FT are on lipid vesicles which presents fusion or disruption of vesicles to increase the homogeneity[164,165,166], and the increase in solubility of hydrophobic solutes in an aqueous solution[167]. Though, there are reports by Na Du et. al. on the formation of single tailed surfactant vesicles using a rough glass surface which presented to be stable against FT after the template was removed[168,169]. The stability of the single tailed surfactants was due to partial interdigitation of the surfactants which increased the robustness of the vesicles against FT.

The FT effects result in the disruption and/or reorganisation of the lipid structure to a more thermodynamically stable organisation of amphiphiles in solution. In this study, the effects upon FT for a DODAC aqueous solution was shown through changes in the DSC cooling thermographs during temperature cycles between 70 and -40 ^{o}C. These changes

are shown as a shift in the $L_\alpha \rightarrow L_\beta$ transition temperature from ~31 to ~34 ^oC after FT which remains constant for up to 2 FT cycles and after storage over 2 days (see appendix, figure A5.1). The changes in the cooling thermographs were compared for different $CaCl_2$ levels (0, 0.085 and 0.15 wt%), where the introduction of $CaCl_2$ resulted in a second transition that took place ~2.0 ^oC after the $L_\alpha \rightarrow L_\beta$ transition and denoted as a transition between two unidentified "gel" phases, gel and gel'.

5.3. Results

5.3.1. The Effects of Surfactant Concentration

The microstructure for the vesicular solution was assessed for increasing levels of DODAC and $CaCl_2$ levels. The mixtures contained surfactant levels between 5-14 wt% in an aqueous solution containing 0, 0.015, 0.085 and 0.15 wt% of $CaCl_2$ (figure 5.1). The variations to the vesicle microstructure were compared by the lamellar repeat d-spacing at 25 ^oC, in figure 5.1. All samples are in a lamellar phase which was determined through the peak ratio of the integrated SAXS patterns at 25 ^oC (see section 2.5.2).

Figure 5.1 shows a general decrease in the lamellar d-spacing with increasing DODAC levels. The d-spacing decreases almost linearly from 220-140 Å with increasing DODAC levels. The increase in DODAC levels will increase the vesicle size and lead to an attraction of amphiphiles for constant ionic effects which may increase the lamellarity. The relationship between the increasing DODAC levels and decreasing bilayer thickness is reported by Tsuruta et. al. for DODAC bilayers deposited on polystyrene microspheres, where the increase in attraction between amphiphile lead to the interdigitation of bilayers[170].

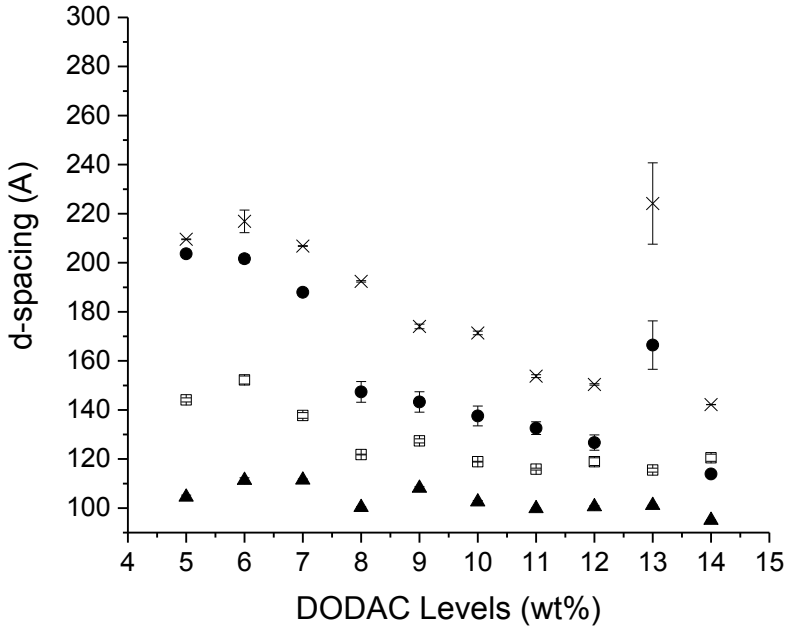


Figure 5.1: Shows the change in the SAXS d-spacing with increasing DODAC levels for $CaCl_2$ levels of; (▲) 0.15, (□) 0.085, (●) 0.015 and (x) 0 wt%. Results obtained at room temperature and pressure in a lamellar gel phase. The error bars are the standard deviation from the fitting of the indexed lamellar peak ratio.

This trend of decreasing d-spacing with increasing DODAC levels does not stand for 13 wt% DODAC in an aqueous solution containing 0 and 0.015 wt% $CaCl_2$ which is shown by the bilayers spacing of 224 and 166 Å, respectively. This deviation from the trend could be related to a phase transition, where an increase in d-spacing is reported by Shearman et. al. as a lamellar gel→coagel phase transition for DODAC bilayers[171]. As mentioned (section 1.7.2), the coagel is a crystalline gel phase which can form at 25 ºC over prolonged time periods.

The gel to coagel phase transition has been reported for DODAC as a nucleation of sub gel regions forming (over months or years) a two-phase system of gel and coagel states[172]. Therefore, it is likely that the d-spacing in figure 5.1 for 13 wt% DODAC is due to the presence of coagel domains, where short-range attraction (for increasing levels of

surfactant) dominates in the absence of long-range repulsion (thermal fluctuations discussed in sections 1.5.4 & 1.7.2). However, that would also be true for 14 wt% DODAC, so this behaviour may due to variations in the thermal history (see section 1.5).

In figure 5.1, the effects on increasing DODAC levels on the lamellar d-spacing is the same for increasing $CaCl_2$ levels in the aqueous solution. These effects of $CaCl_2$ (0.15 wt%) are greater for lower levels of DODAC, showing a 50 % decrease of the d-spacing at 5 wt% DODAC compared to the 33 % decrease at 14 wt% DODAC. This is due to both variables ($CaCl_2$ and DODAC levels) tending to the same structure of large multilamellar vesicles and the rate of change to the vesicle structure decreases as the vesicles approach its structural limit. Thus, showing (figure 5.1) an almost constant d-spacing with increasing surfactant levels at 0.15 wt% $CaCl_2$.

The solution of 13 wt% DODAC containing 0.15 wt% $CaCl_2$ results in a 55 % decrease in d-spacing in comparison to a solution containing no $CaCl_2$ (figure 5.1). If in fact, as discussed earlier, the high d-spacing of 224 Å at 13 wt% DODAC (no $CaCl_2$) was due to increasing coagel domains, then the long-range attraction between the bilayers from the zeroing potential between them decreases the rate of the gel→coagel transition.

5.3.2. The Effects of Salt Concentration

The increasing levels of $CaCl_2$ in aqueous solution was assessed for a DODAC level of 8 wt% between temperatures 70 and -40 ^oC at 10 $^oCmin^{-1}$ across three heating/cooling cycles, through DSC. The heating thermographs remained the same across all cycles and $CaCl_2$ levels (see figures A5.3 & A5.5 in appendix, and figure 6.3). However, the cooling thermographs between 40-25 ^oC shows a shift in the L_α→gel transition temperature from ~31 to 35 ^oC after FT (figure 5.2). This shift in the L_α→gel transition

temperature was accompanied by a second cooling transition in the gel phase denoted as a gel→gel' transition at ~31 °C, for $CaCl_2$ levels of 0.085 and 0.15 wt% (figure 5.2).

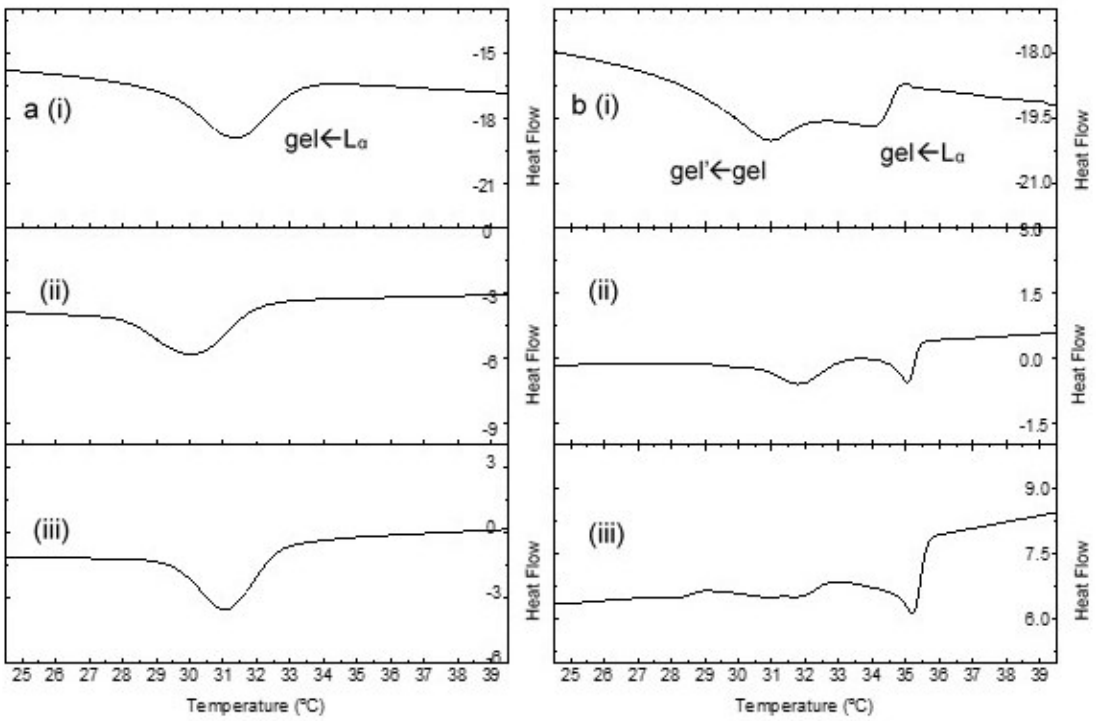


Figure 5.2. Shows the (a) first and (b) second cooling cycle between 39-25 °C for 8 wt% DOODAC in an aqueous solution of; (i) 0.15, (ii) 0.085 and (iii) 0 wt% $CaCl_2$. The DODAC solution was cycled between 70 and -40 °C at 10 °Cmin^{-1} and showed a double transition after FT, denoted as L_α→gel at ~35 °C and gel→gel' at ~31 °C.

The enthalpy of the gel→gel' transition increases from -10 to -35 $Jmol^{-1}$ (± 1 $Jmol^{-1}$) with increasing $CaCl_2$ levels (table 5.1), where the enthalpy of the transition is directly related to the magnitude of the transition (see section 2.4.2). Furthermore, table 5.1 shows a decrease from -34 to -6.0 $Jmol^{-1}$ of the L_α→gel transition enthalpy with increasing $CaCl_2$ levels. Therefore, the introduction of $CaCl_2$ suppresses the changes upon FT by decreasing the enthalpy of the gel state given at ~35 °C and promoting the gel→gel' transition at 31 °C which is assumed to be the same transition given as the L_α→gel

transition before FT. The changes to transition temperature were assessed further between 70-20 °C with 5.0 °C steps using SAXS/WAXS analysis.

$CaCl_2$ Levels / wt%	**$\Delta H_{l\rightarrow g}$ / Jmol^{-1}**	**$T_{l\rightarrow g}$ / °C**	**$\Delta H_{g\rightarrow g'}$ / Jmol^{-1}**	**$T_{g\rightarrow g'}$ / °C**
0	-34	35	-10	32
0.085	-17	34	-34	30
0.15	-6.0	34	-35	31

Table 5.1. Shows a list of the enthalpy changes, ΔH (accuracy of ± 1 Jmol^{-1}), for the $L_\alpha \rightarrow$gel (l→g) and the gel→gel' (g→g') transition and the temperature, T (accuracy of ± 5.0 °C) of the transitions, for a DODAC solution of 8 wt% DODAC and varying levels of $CaCl_2$ (0, 0.085, 0.15 wt%). The enthalpies are shown for the second cooling DSC thermographs of the DODAC solution. The enthalpy changes of the transitions were obtained from the DSC thermographs (see section 2.4.2).

The integrated SAXS (figure 5.3(i)) and WAXS (figure 5.3(ii)) patterns are shown for the $L_\alpha \rightarrow$gel transition temperature at 35 (figure 5.3a) and 30 °C (figure 5.3b), for 0, 0.085 and 0.15 wt% $CaCl_2$. The integrated WAXS patterns in figure 5.3(ii), are centred around the gel peak at ~4 Å which is generally given by a sharp peak due to an increase in lateral order in a gel phase. Figure 5.3(ii) shows a double WAXS gel peak (as seen in figure 4.5a) which is a distorted gel peak caused by lateral tilting from a normal bilayer structure which is characteristic of a $L_{\beta'}$ or $P_{\beta'}$ phase (see section 2.5.5). In chapter 4, the differences between the $L_{\beta'}$ and $P_{\beta'}$ phases were discussed and concluded that the resolution of the integrated SAXS patterns are too low to distinguish between the two phases for these DODAC systems.

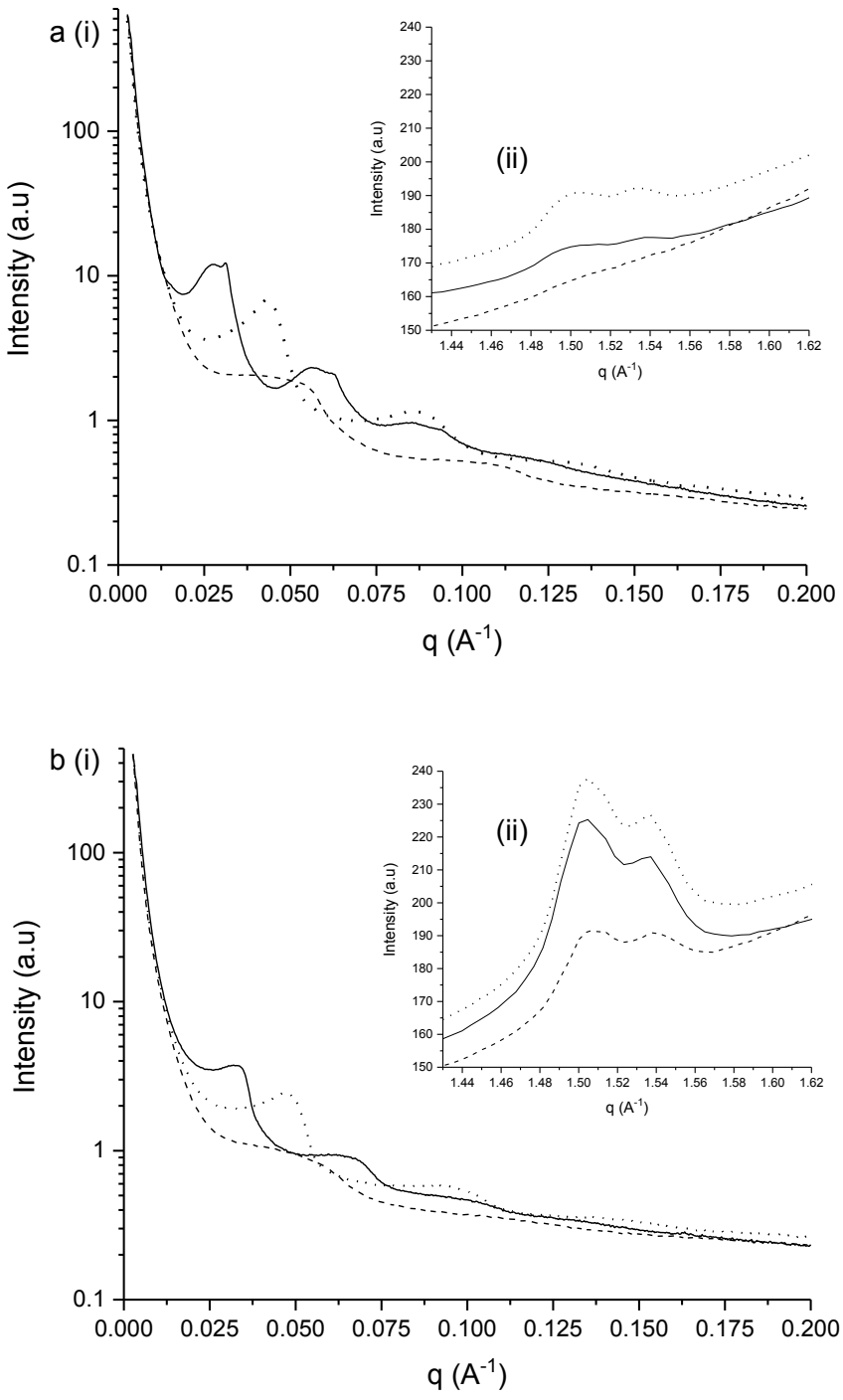


Figure 5.3. Shows the integrated SAXS/WAXS patterns for 8 wt% DODAC in an aqueous solution containing; 0.15 (dashed line), 0.085 (dotted line) and 0 (solid line) wt%. The integrated patterns are shown for (i) SAXS and (ii) WAXS at (a) 35 and (b) 30 ^{o}C. The L_{α}→gel transition takes place for 0.085 and 0 wt% $CaCl_2$ at 35 ^{o}C and for 0.15 wt% $CaCl_2$ at 30 ^{o}C. The WAXS patterns are centred around the gel peaks at ~4 Å, where the gel peak is distorted by tilting of the bilayers (see section 2.5.5). Thus, the lamellar gel phase is given as a $L_{\beta'}$ or $P_{\beta'}$ gel phase.

In figure 5.3a(ii), the WAXS gel peak is not present at 35 °C for a $CaCl_2$ level of 0.15 wt%. The temperature which the WAXS gel peak is present is recorded as the $L_\alpha \rightarrow L_{\beta'}$ (or $P_{\beta'}$) transition temperature, where this transition takes place at 35 °C for $CaCl_2$ levels of 0 and 0.085 wt%. Though, in the case of a DODAC aqueous solution containing 0.15 wt% $CaCl_2$, the transition temperature is decreased to 30 °C. Thus, the long-range attraction from increasing levels of $CaCl_2$ causes a decrease in the $L_\alpha \rightarrow L_{\beta'}$ (or $P_{\beta'}$) transition temperature upon cooling, before FT. After FT, for the DODAC aqueous solution containing 0.15 wt% $CaCl_2$, the $L_\alpha \rightarrow L_{\beta'}$ (or $P_{\beta'}$) transition temperature increases to 35 °C which is shown through the WAXS gel peak (see appendix, figures A5.8 & A5.9). This suggests that the changes upon FT causes an increase in repulsion that dominates over the long-range attraction from the zeroing potential between the bilayers.

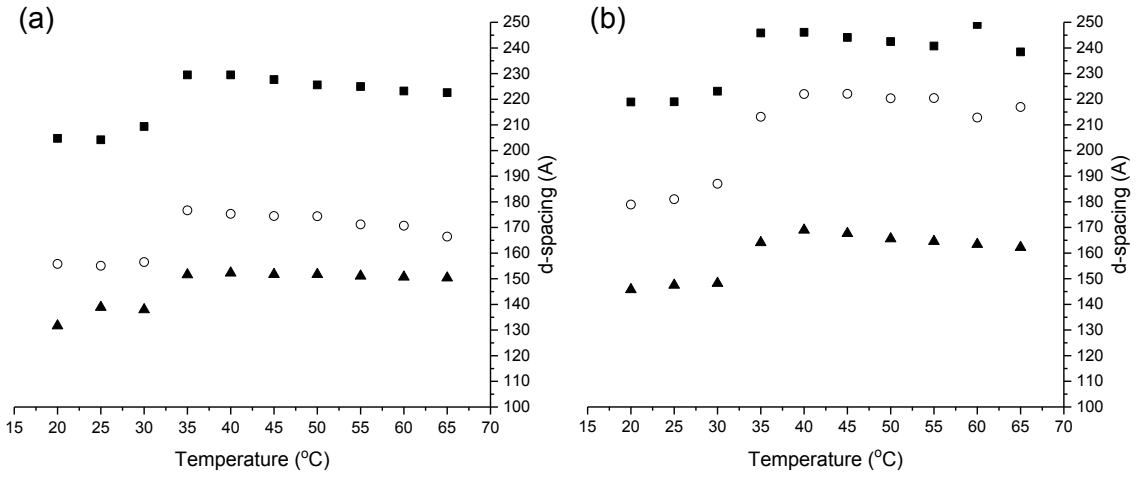


Figure 5.4. Shows the SAXS d-spacing for decreasing temperature (a) before and (b) after FT. The results were taken between 65-20 °C with -5.0 °C steps, for 8 wt% DODAC in an aqueous solution containing; ■ 0, ○ 0.085 and ▲ 0.15 wt% $CaCl_2$. As seen in figure 4.3, the SAXS patterns have a second lamellar phase shown by low resolved peaks or distorted peaks which best fit to a two-component gaussian giving two lamellar d-spacing with an indexed lamellar peak fitting accurate to ± 1 Å. The results are shown in this figure as the comparison between the highest indexed lamellar phase for the different $CaCl_2$ levels (see section 2.5.4, for identifying lamellar phases).

The WAXS gel peak intensity increases from 35 to 30 ^{o}C (figure 5.3(ii)), due to increasing lateral order through the transition from a disordered fluid phase to a more ordered gel phase. This reiterates the assumption that the structure at 35 ^{o}C is a pre-transitional (ie $P_{\beta'}$ phase) structure to that at 30 ^{o}C which is why the d-spacing in figure 5.4 decreases further after the $L_{\alpha} \rightarrow L_{\beta'}$ (or $P_{\beta'}$) transition temperature. The SAXS d-spacing is also compared for decreasing temperature between 70-20 ^{o}C, before and after FT (figure 5.4).

Before FT (figure 5.4a), there is an 11 % max. drop in the lamellar d-spacing for all $CaCl_2$ levels from 35 to 30 ^{o}C, where the $L_{\alpha} \rightarrow L_{\beta'}$ (or $P_{\beta'}$) phase transition takes place, which was discussed at the end of section 4.3.1. After FT (figure 5.4b), there's a 10, 12 and 9 % decrease in d-spacing from 35 to 30 ^{o}C, for a DODAC aqueous solution containing 0.15, 0.085 and 0 wt% $CaCl_2$, respectively. This decrease in d-spacing is greater for $CaCl_2$ levels of 0.085 wt% where the effects upon FT (increased bilayers separation) is dominant over the ionic effects (decreased bilayer separation). However, the increased ionic effects on the DODAC bilayers cause by $CaCl_2$ addition is dominant over the FT effects for a $CaCl_2$ level of 0.15 wt%. This results in a decrease in the d-spacing difference between 35 and 30 ^{o}C after FT (figure 5.4b) and a smaller difference in the d-spacing before and after FT.

Between temperatures 40 and 35 ^{o}C (figure 5.4b), there is a 4 % max decrease in d-spacing for $CaCl_2$ levels of 0.085 and 0.15 wt% which may correspond to the gel phase present after FT at ~34 ^{o}C in the DSC results (as seen in figures 4.2 & 4.4). This decrease in the lamellar d-spacing from 40 to 35 ^{o}C is not shown for a system with 0 wt% $CaCl_2$.

5.3.3. Determining the Phase Behaviour using NMR

In the ^{1}H NMR, the alkyl chain peak height can give information on the mobility of the alkyl chains in the vesicle structure, as mentioned in section 2.2.3. The half-height width can provide information on the phase through its inverse relationship with the T_2 relaxation which deceases with greater dipole-dipole interactions, due to closer ^{1}H-^{1}H distances[173]. However, the broad hidden signal given by the alkyl peak, labelled -$C_{18}\underline{H}_{37}$ at 1.17 ppm (figure 5.5), makes it difficult to deconvolute the alkyl peak from the methyl "head" groups, labelled –N($C\underline{H}_3$)$_2$ at 3.31 ppm and the water peak at 4.75 ppm (at 25 ^{o}C). Thus, the alkyl peak height is measured instead of the half-height width which are inversly related.

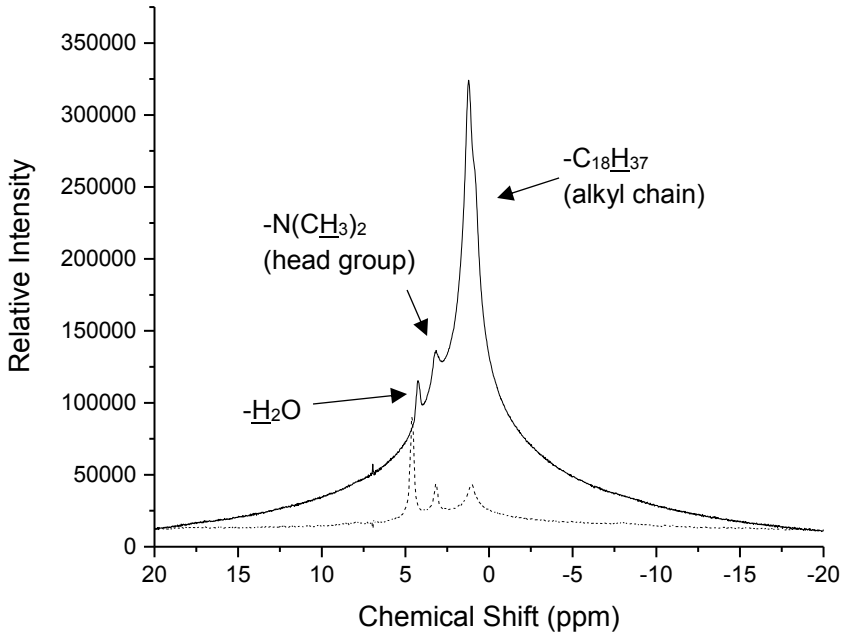


Figure 5.5. ^{1}H NMR of a DODAC/$CaCl_2$ aqueous solution before FT. Solid line plot was taken at 65 ^{o}C and dashed line plot at 25 ^{o}C. The chemical shift of 4.75 ppm at 25 ^{o}C is due to H_2O which shifts to 4.40 ppm at 65 ^{o}C. This upfield shift of the water peak with increasing temperature is a known phenomenon (see section 2.2.4). The methyl groups on the polar head group labelled [N-($C\underline{H}_3$)$_2$] has a chemical shift of 3.31 ppm and the carbon-18 alkyl chains has a chemical shift of 1.17 ppm.

The ^{1}H NMR spectra of a DODAC aqueous solution containing 0.085 wt% $CaCl_2$ was compared at 65 and 25 ^oC (figure 5.5), showing diference in the relative intensity of the alkyl peak height for the L_α and $L_{\beta'}$ (or $P_{\beta'}$) phases, respectively. This change in the alkyl peak height is given by the decrease in molecular motion (lateral and rotational diffusion) and an increase in the dipole-dipole interactions in the gel phase, compared to that of the L_α phase, which broadens the alkyl chain signal and results in a hidden signal that lies beneath the noise, causing a decrease in the alkyl peak height (refer to section 2.2.3).

The static SSNMR results are shown (figure 5.6) for the changes in the alkyl chain peak height with $CaCl_2$ levels of 0.15, 0.085 and 0 wt% between 65-25 ^oC with -5.0 ^oC steps, before (figure 5.6a) and after (figure 5.6b) FT. Before FT (figure 5.6a), there is a 70, 72 and 80 % decrease in the relative intensity of the alkyl peak height which corresponds to the $L_\alpha \rightarrow L_{\beta'}(P_{\beta'})$ phase transition from 35 to 30 ^oC, for a DODAC aqueous solution containing 0.15, 0.085 and 0 wt% $CaCl_2$, respectively. This difference in the alkyl peak height between the L_α and $L_{\beta'}$ (or $P_{\beta'}$) phases is 10 % greater for a DODAC aqueous solution containing 0 wt% $CaCl_2$ which is due to the alkyl chains mobility in the L_α phase. The fluctuating pressure (see section 1.5.4) in the L_α phase is greater with $CaCl_2$ based on reports by Carmona-Ribeiro et. al.[161], which restricts the movements of amphiphiles in confined space, within the bilayers. So, the solution containing no $CaCl_2$ will have more alkyl chain mobility in the L_α phase.

After FT (figure 5.6b), there is a general decrease in the alkyl peak height suggesting that the effects upon FT causes an increase in the dipole-dipole interactions for a more “gel-like” environment. The effects upon FT for a DODAC system containing 0.085 and 0.15 wt% $CaCl_2$, given by a second gel phase transition in the cooling DSC thermograph at ~34 ^oC (figure 5.2b) and a decrease in the SAXS lamellar d-spacing when cooling

between 40-35 °C (figure 5.4b), is shown through a decrease in the alkyl peak intensity from 40 to 35 °C which is greater than the average 2 % decrease every -5.0 °C between 65-40 °C (figure 5.6b).

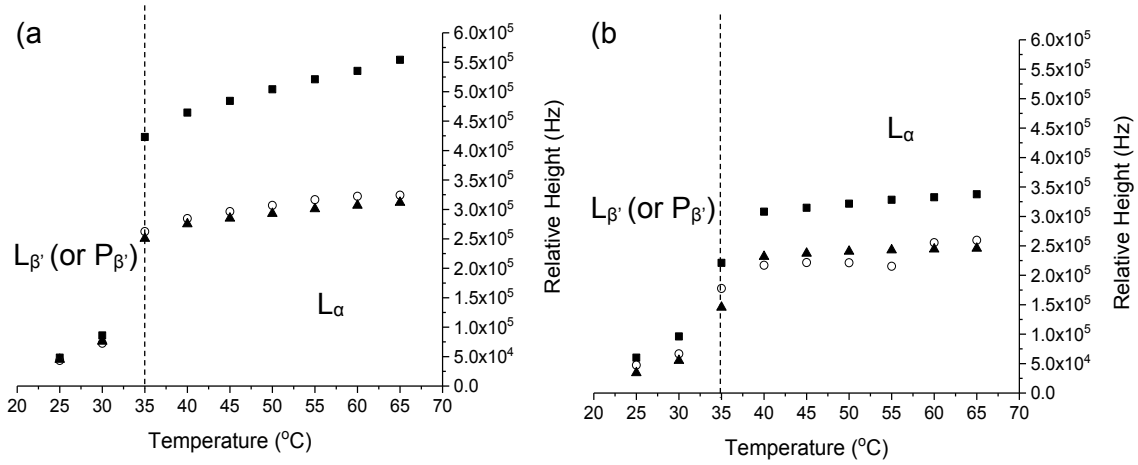


Figure 5.6. Shows the change in the relative alkyl peak intensity at 1.17 ppm (shown in figure 5.5) with decreasing temperature of the ^{1}H NMR results (a) before and (b) after freeze-thawing. Each plot compares results for $CaCl_2$ levels of; ■ 0, ○ 0.085 and ▲ 0.15 wt%. The phase assignments are based on the results given in chapter 4.

Between 40-35 °C (in figure 5.6b) there is a 37, 18 and 28 % decrease when cooling for a DODAC solution containing 0.15, 0.085 and 0 wt% $CaCl_2$, respectively. However, the second gel state (shown in figures 5.2b and 5.4b) never existed upon cooling from 40 to 35 °C for a DODAC solution containing 0 wt% $CaCl_2$. Therefore, this decrease in the relative intensity of the alkyl peak is due to slow $L_\alpha \rightarrow L_{\beta'}$ (or $P_{\beta'}$) phase transition. So, the information given by the ^{1}H NMR of the alkyl peak height is limited by transitions between microscopic phases.

In the $L_{\beta'}$ (or $P_{\beta'}$) phase at 25 °C (figure 5.7), for $CaCl_2$ levels of 0.085 and 0 wt%, the alkyl peak height increases after FT by 9 and 25 %, respectively, where the behaviour of

the DODAC system containing 0.15 wt% $CaCl_2$ results in a 24 % decrease in alkyl peak height after FT. This behaviour at 0.15 wt% $CaCl_2$ could be a result of the decrease in the $L_\alpha \rightarrow L_{\beta'}$ (or $P_{\beta'}$) transition temperature (see figure 5.3(ii)) which will result in a 5.0 ^oC shift of the thermotropic behaviour relative to the DODAC solutions containing 0.085 and 0 wt% $CaCl_2$. This theory is supported by the linear trend of decreasing alkyl chain height with increasing $CaCl_2$ levels, which mirrors the general trend seen in this chapter between the alkyl chain mobility and $CaCl_2$ levels, after FT where the $L_\alpha \rightarrow L_{\beta'}$ (or $P_{\beta'}$) transition temperature is the same for all $CaCl_2$ levels (see appendix, figure A5.8).

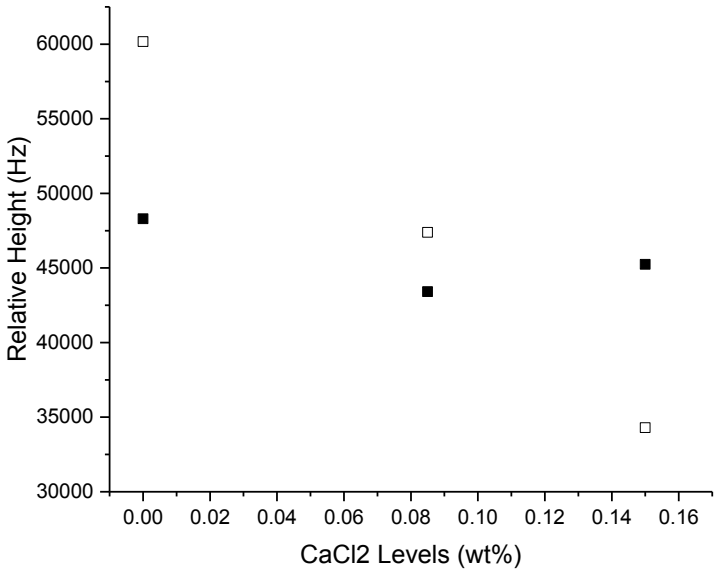


Figure 5.7. Shows the static ^1H SSNMR for the relative alkyl peak height at 1.17 ppm (shown in figure 5.5), (■) before and (□) after FT at 25 ^oC.

5.4. Conclusion

The increase in DODAC and $CaCl_2$ levels result in an increase in the lamellar bilayer packing which reduces the bilayer thickness and/or the amount of interlamellar water. For a system containing no $CaCl_2$ at 13 wt% DODAC, the lamellar d-spacing was higher than expected when compared to the trend for increasing levels of DODAC where the trend followed for a d-spacing of ~145 Å instead of the 224 Å shown for 13 wt% DODAC

(see figure 5.1). This behaviour was suggested to be a result of increasing coagel domains in the lamellar gel phase which is given by a second lamellar phase with a larger d-spacing in the integrated SAXS patterns that generally decreases with increasing salt levels (see appendix, figures A5.10-A5.13). The behaviour of the bilayers from the addition of salt causes an increase in fluctuation pressure in the fluid phase (see section 1.5.4) which can prevent any alkyl chain interactions to form crystalline bilayers and a zeroing potential (see section 1.5.1) between the cationic surfactant "head" groups in the gel phase (less fluctuations in and across the bilayers) which will dehydrate the bilayers. Therefore, based on the fact the a coagel is a hydrated crystalline gel phase, both behaviours of salt on the bilayers will cause the rate of the gel→coagel phase transition to decrease.

Before FT, the increased levels of $CaCl_2$ (0.15 wt%) resulted in a decrease in the $L_\alpha \rightarrow L_{\beta'}$ (or $P_{\beta'}$) transition temperature which suggest an increase in structural disorder. This was explained for the static ^1H SSNMR for the alkyl chain peak intensity which showed a decrease in alkyl chain mobility for increasing levels of $CaCl_2$, as an increase in fluctuating pressure restricting the alky chains interaction. Therefore, the fluctuations are across the bilayers from the unison of individual amphiphiles fluctuating together instead of against each other which increases in amplitude with increasing $CaCl_2$ levels.

The results given by static ^1H SSNMR showed that the effects upon FT result in a more "gel-like" environment and by comparing these results with that of the SAXS shows, the structure given after FT is that of a fully hydrated gel. So, the effects upon FT may also increase the rate of the gel→coagel transition, based on the resultant structure of the bilayers after FT.

6. The Effects of Chemical Additives on the Behaviour Upon Freeze-Thawing

6.1. Overview

The phase behaviour of DODAC aqueous solutions were assessed at room temperature with varying levels of glycerol or a non-ionic alcohol ethoxylate surfactant of $C_{12\text{-}14}(EO)_{10}$ (CAE10), added to the system. In the previous chapter, the effects upon FT resulted in the temperature shift of the $L_\alpha \rightarrow L_{\beta'}$ (or $P_{\beta'}$) phase transition by ~4.0 ^oC, which was met with a second gel transition at ~31 ^oC for an aqueous DODAC solution containing 0.085 wt% $CaCl_2$, where the presence of $CaCl_2$ seem to limit the changes upon FT. This behaviour of the DSC thermographs for 8 wt% DODAC in an aqueous solution containing 0.085 wt% $CaCl_2$ was compared for increasing levels of the chemical additives which were expressed as decreasing hydration levels, for comparison. As the hydration levels decrease, the enthalpy of the gel→gel' transitions at ~31 ^oC increases from 27 to 136 $Jmol^{-1}$ as the enthalpy of L_α→gel transitions at ~35 ^oC trends to zero giving a single gel transition at ~31 ^oC.

The self-diffusion of water was measured through methods described in section 2.2.8, for increasing levels of glycerol (0-7.5 wt%) and CAE10 (0-5.0 wt%) added to the DODAC solution. The self-diffusion of water was measured for bulk, interlamellar a core water in the multilamellar system, where the diffusion rate of bulk water decreased by 51 and 56 % upon the addition of 1.25 wt% glycerol and 0.6 wt% CAE10, respectively, then remained constant with increasing levels of both chemical additives. The effects of FT resulted in a general decrease in the self-diffusion of bulk water, where the differences in the self-diffusion before and after FT, decreased with increasing levels of both chemical additives.

The SAXS patterns of the DODAC solution shows structural differences in the lamellar phase at 25 ^{o}C for increasing levels of glycerol and CAE10, where the bilayers separation increases by 11 % for a 0-7.5 wt% increase in glycerol and a lateral phase separation causing a 71 % increase in the bilayer separation for 1.4 wt% CAE10, then a vesicle to fragmented vesicle/extended bilayer transition for a DODAC solution containing 5 wt% CAE10.

6.2. Introduction

The effects upon FT on amphiphiles in solution has a high importance for the behaviour of lipid membranes and surfactant solutions upon environmental stresses during transportation and storage. The mechanism for freezing a cell membrane has been extensively reviewed by Steponkus et. al.[174,175], outlining the changes to the bilayers upon freezing which was illustrated in figure 1.9, showing the freezing impact on a multilamellar vesicle due to a build-up of osmotic stress from ice formation in the bulk water phase[176]. This osmotic stress can cause dehydration of vesicles, where the degree of dehydration depends on the levels of hydration before freezing, and a disruption of the bilayers from an influx of water or lack of osmotic responsiveness, upon thawing (see section 1.7.1). These effects upon FT depends on the rate of freezing and thawing, which can lead to disruption of a lamellar phase and mixing of monomer units or fusion/fission of vesicles[177,178].

In this chapter, the effects upon glycerol and CAE10 addition to the DODAC solution is discussed for the changes to the DODAC vesicle structure, before and after FT and to determine the role of glycerol and CAE10 in protection against the structural changes of the DODAC solution upon FT. Glycerol was investigated in this study for its cryoprotectant behaviour on lipid bilayers, where it's known to protect against osmotic

stress induced changes to the lipid structure by decreasing the chemical potential of water through preferential binding with the lipid bilayer or acting as a water replacement between the bilayers[179,180,181].

The behaviour of CAE10 on the DODAC solution was investigated for its ability to increase the "wettability" of the DODAC solution, which is a property that depends on the time dependent surface and interfacial tensions of the DODAC solution, where an increase in "wettability" is given by surfactant solutions with small surface tensions[182,183]. This property of increased "wettability" is generally given by low surfactant concentrations above the critical micellar concentration (CMC)[184]. The importance in "wettability" lies in the function of liquid fabric enhancers which this DODAC system models (see section 1.7.2). Derivatives of ethoxylated alcohols such as lipids substituted with polyethylene glycol (PEG), where the PEG group is covalently bonded to the lipid "head" group increasing its surface area, are used in lipid mixtures to increase interaction between the polymer group and the vesicle surface which dehydrates the vesicle surface and decreases the permeability of the bilayer[185,186,187], which could protect the vesicles against dehydration effects upon freezing.

6.3. Results

6.3.1. Characterising the DODAC Aqueous Solution

The phase was assessed at room temperature (~20 ^{o}C), under crossed polarised light (figure 6.1(ii)), showing the presence of "Maltese crosses" which is characteristic of the anisotropic liquid crystalline lamellar phase (see section 2.3.2) and for all DODAC mixtures in this study (see appendix, figures A6.1-A6.9). This discrete shape shown (figure 6.1b), is typical of a vesicle structure under crossed polarised light, where the node of these discrete shapes represents the isotropic aqueous core[188]. The

polydispersity of the DODAC solution is expressed in figure 6.1a(i), showing larger vesicles (≥ 50 μm) and vesicles a fraction of the that size (≤ 5 μm), visible in the image.

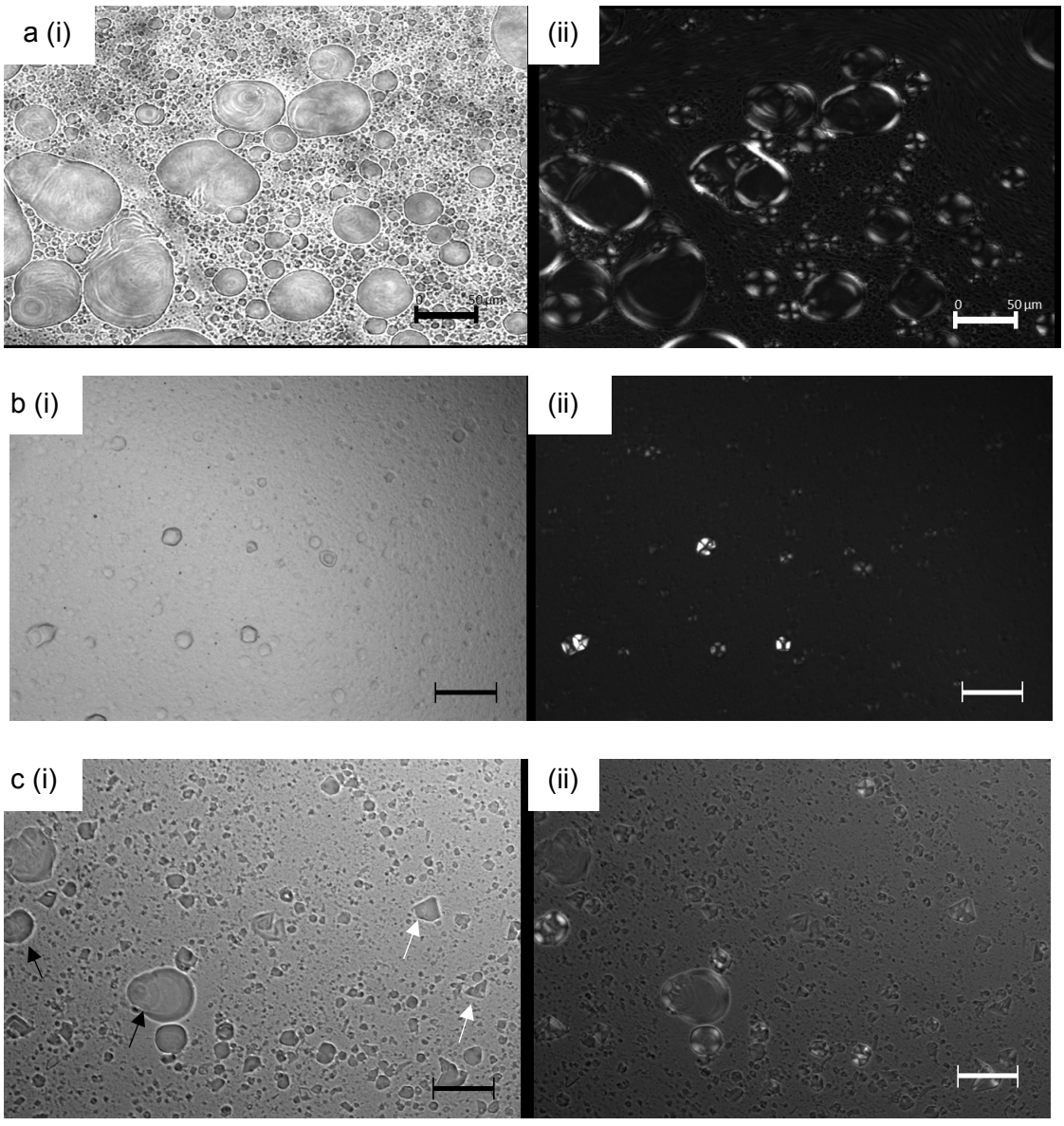


Figure 6.1. Polarised light microscopy images for DODAC aqueous solution containing (a) no glycerol or CAE10, (b) 1.4 wt% CAE10 and (c) 7.5 wt% glycerol, at ~20 ^{o}C. For (i) bright-field and (ii) crossed polarised light images. The bars represent a scale of 50 μm and in c(i) the white arrows indicate some changes to the vesicle shape and the back arrow indicate vesicle budding. Crossed polarised image pictures “Maltese crosses” which represents a lamellar phase.

There are small changes to the morphology of the vesicles (indicated by the white and the black arrows in figure 6.1c(i)) for a DODAC sample containing glycerol (7.5 wt%) which could indicate increased flexibility in the vesicle structure or a non-equilibrium solution. The latter may be true based on the vesicle budding (shown by black arrows in figure 6.1c(i)) which may be the result of vesicle fusion or fission. The sample texture for a DODAC solution containing CAE10 (1.4 wt%) (figure 6.1b) compared to the DODAC solution with no CAE10 (figure 6.1a) are different, where figure 6.1b appears to be more vesicle dense than figure 6.1a and 6.1c, but the differences in the sample texture could be due to the fraction of sample collected for imaging.

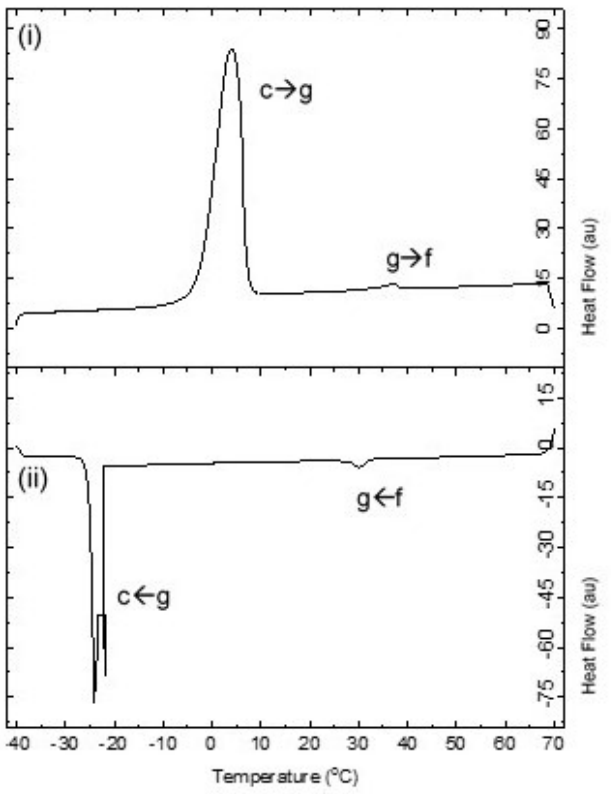


Figure 6.2. Shows DSC scans for (i) heating and (ii) cooling between temperatures 70 and -40 °C at a rate of 10 °C/min. This is a typical result for various DODAC levels in aqueous solution (see appendix, figures A6.10-A6.12), where the gel to fluid (g→f) and fluid to gel (g←f) transition are the chain transitions of DODAC and the water exo- and endo- isotherms for the gel to crystal transition (c←g) and crystal to gel transition (c→g), respectively.

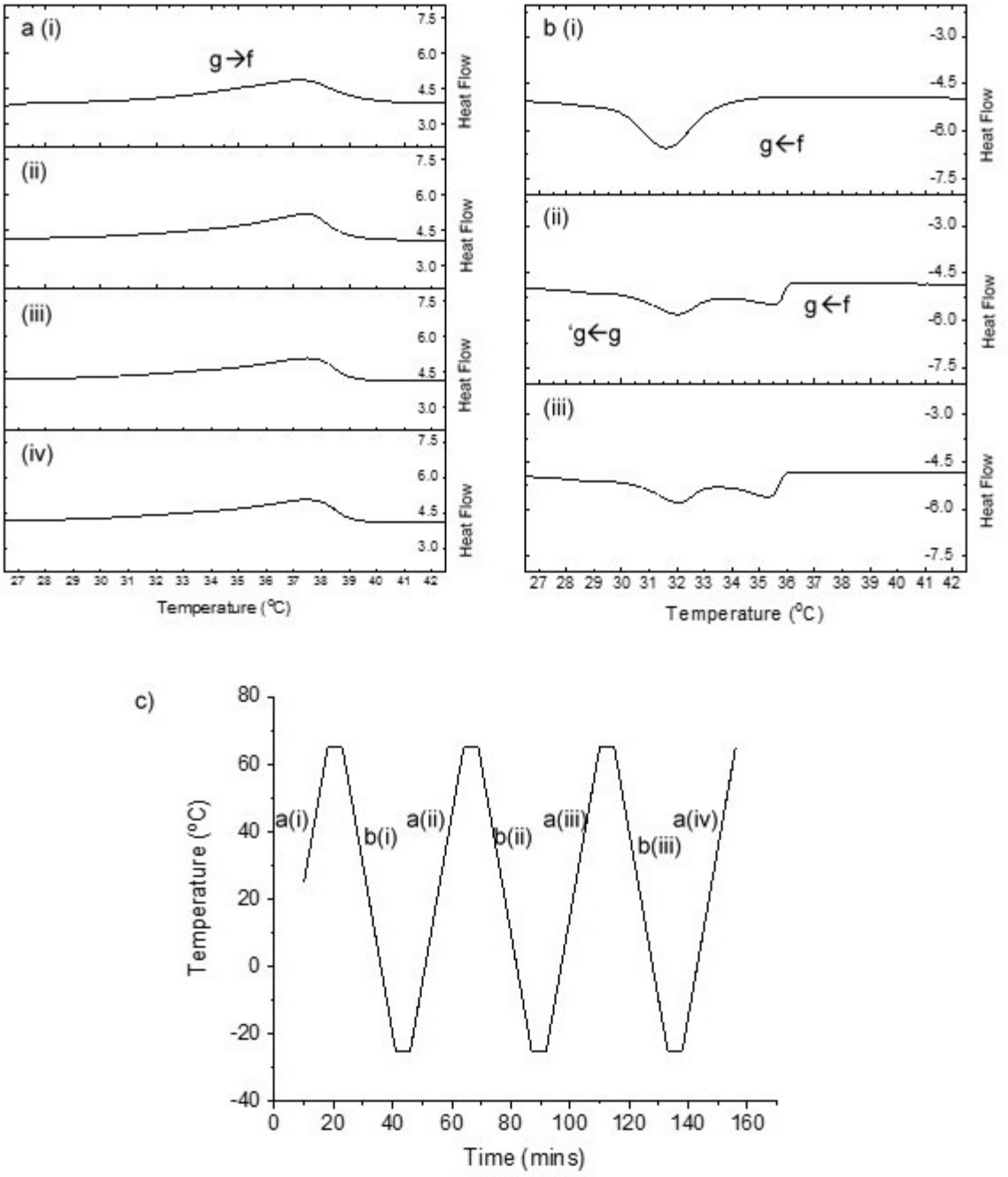


Figure 6.3. Shows thermographs centred at the (a) gel→fluid (g→f) and (b) fluid→gel (g←f) transitions for heating and cooling cycles, respectively, of the DODAC (8 wt %) aqueous solution shown in figure 6.2, but with a shorter temperature range of 65 to -25 °C, results are the same for both experiments. The thermal cycle is shown (c) which started at 25 °C and the sample was heated to 65 °C, where the first heating transition a(i) took place and the temperature was cycled from 65 to -25 °C at 10 °Cmin^{-1}, where the transitions shown in (a) and (b) are indicated in (c).

The thermographs in figure 6.2, show large endo (c→g) and exo (c←g) isotherms of the aqueous phase for ice melting and forming, respectively, and smaller endo (g→f) and exo (g←f) isotherms are for DODAC chain melting and forming, respectively. The temperatures of chain transitions for DODAC takes place at ~38 °C upon heating and ~31 °C upon cooling, where there is a 7.0 °C hysteresis between the heating and cooling transitions which is consistent for other DODAC aqueous solutions[189,152]. As mentioned in section 2.4.2, the chain transitions are significant to the properties of the DODAC bilayers because it's a direct measurement of the thermotropic behaviour of DODAC since the chain transitions are the energy changes between the different conformations within the gel phase.

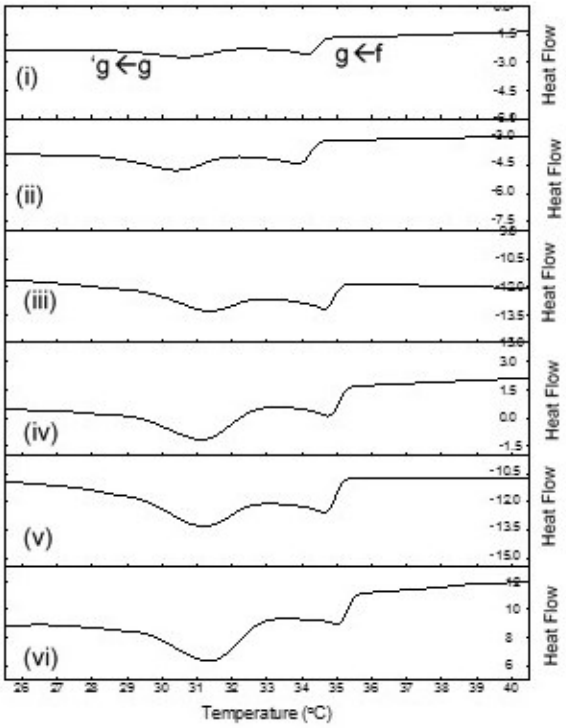


Figure 6.4. Shows the second cooling cycle, after FT for DODAC levels of; (i) 5, (ii) 8, (iii) 10, (iv) 11, (v) 12 and (vi) 14 wt%, showing the f→g and g→g' transitions. All samples were hydrated in an aqueous solution of 0.085 wt% $CaCl_2$.

The heating and cooling thermographs are shown (figure 6.3a and b) for the DODAC chain transitions of gel→fluid (g→f) and fluid→gel (g←f), respectively. As seen in figure 6.3a, the heating cycles are consistent across the three cycles, showing no changes to the number of transitions and little changes to the transition temperature with variations smaller than the accuracy of the results (± 5.0 ^{o}C). So, the g→f transitions of 8 wt% DODAC in an aqueous solution of 0.085 wt% $CaCl_2$ remain constant at ~37 ^{o}C across the three heating cycles.

6.3.2. The Effects of Chemical Additives

The significance of a second cooling cycle for the DODAC aqueous solutions, where a second transition of a g→g' at ~31 ^{o}C was introduced (see figures 5.2 & 6.3b), is consistent for varying DODAC levels of 5, 8, 10, 11, 12 and 14 wt% (see figure 6.4). This behaviour is also consistent for DODAC solutions containing glycerol and CAE10 (see appendix, figure A6.13), but at glycerol levels of 7.5 wt% and CAE10 levels of 5 wt% only one transition exists after FT, at ~31 ^{o}C (figure A6.13).

For increasing levels of DODAC, there is a visible increase in the amplitude of the g→g' transition peak (figure 6.4), where the area under the transition peak is equal to the energy of the transition (see section 2.4.2). Thus, the enthalpies of the f→g and g→g' transitions were plotted for DODAC solutions with DODAC levels between 5-14 wt% (figure 6.5a), and a solution of 8 wt% DODAC containing glycerol levels between 0-7.5 wt% and CAE10 levels between 0-5 wt% (figure 6.5b), where the DODAC level is kept constant at 8 wt% and the levels of chemical additives replaced the levels of aqueous solution. Therefore, the f→g and g→g' transition enthalpies were compared for varying levels of hydration which was between 95-84.5 wt% aqueous solution (figure 6.5).

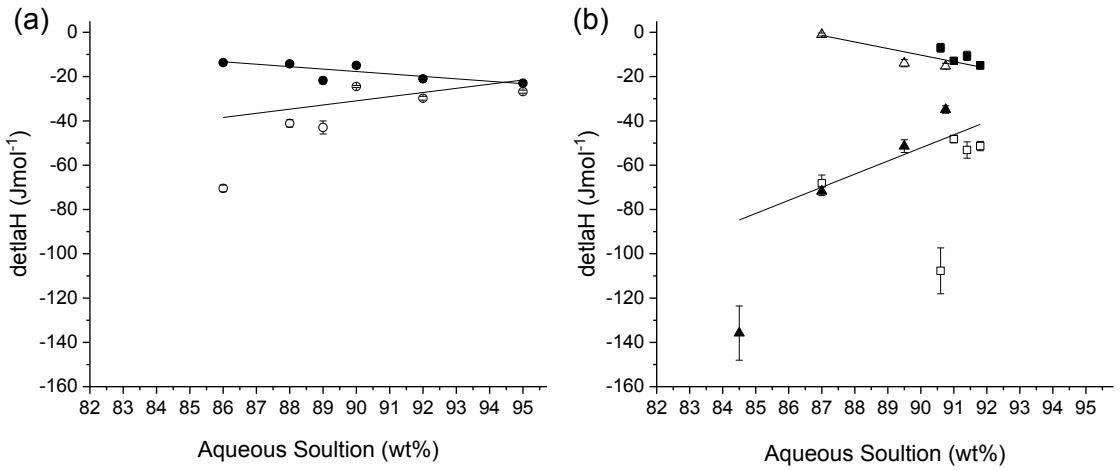


Figure 6.5. Shows the average enthalpy of the second cooling transitions (f→g and g→g') taken by the area under the transition peak at ~31 and ~35 °C for decreasing levels of aqueous solution, based on (a) increasing DODAC levels (figure 6.4), and (b) increasing levels of CAE10 and glycerol (see appendix, figures A6.13). (a) shows (●) f→g and (○) g→g' transition for varying DODAC levels between 5-14 wt% expressed as aqueous solution levels between 95-86 wt%. (b) shows 8 wt% DODAC with the addition of; non-ionic surfactant (■) f→g and (□) g→g', and glycerol (Δ) f→g and (▲) g→g'. The error bars were determined by the standard deviation of the calculated peak height and a linear line was fitted to group all f→g and g→g' phase transitions.

There is a general increase in the g→g' transition enthalpy for decreasing levels of aqueous solution, as the f→g transition enthalpy trends to zero (figure 6.5). This behaviour of the DODAC cooling transition has not been reported, where most reports of aqueous DODAC thermographs are of the narrow temperature range for the chain melting transition (g→f)[190] or for heating thermographs only [191] or have not undergone freezing cycles[192,193]. Though, Liu et. al.[155] reported an increase in the sonicated DODAC vesicles viscosity (as mentioned in section 4.2) after freezing for samples containing no $CaCl_2$, where the g→f transition remains the same before and after freezing and there is a hysteresis between the heating and cooling transitions for after freezing and not before[194]. This reported behaviour was explained for the similarities between the heating transitions before and after freezing and not for the differences upon cooling, where the

similarities in the heating transition was suggested to be due to a decrease in the local concentration of the viscous sample upon heating.

The f→g and g→g' enthalpy trends are fitted to a linear line (figure 6.5), where the f→g transition enthalpy follows a linear trend of -1.10 (± 0.33) and -2.97 (± 0.50) for the change in enthalpy per wt% of aqueous solution of a DODAC solution containing no chemical additives (figure 6.5a) and one containing chemical additives (figure 6.5b), respectively. For a DODAC solution containing no chemical additives (figure 6.5a), the rate which the f→g transition trends to 0 is slower by more than half of that for a DODAC solution containing chemical additives. This behaviour is the reason why a sample containing no chemical additives continue to have two "gel" transitions after FT at an aqueous solution level of 86 wt%, where a sample containing no chemical additives show one "gel" transition at an aqueous solution level of 87 wt% and below.

For a DODAC aqueous system containing chemical additives (figure 6.5b), the enthalpy of the f→g transition at ~35 ^{o}C is zero giving only the g→g' which is now the f→g transition at ~31 ^{o}C, when the aqueous solution level is 87.0 wt% and 84.5 wt% for a system containing CAE10 and glycerol, respectively. Thus, the interactions between the DODAC bilayers and CAE10 has a more stabilising effect on the changes to the DODAC bilayers after FT, compared to the behaviour of glycerol on the DODAC bilayers. So, CAE10 may have a greater ability to decrease the permeability of the bilayers and increase the interactions between amphiphiles within the bilayers.

The behaviour of CAE10 derivatives were reported by Feitosa et. al., for the addition of $C_{12}(EO)_n$ (n = 5, 7, & 8) to a DODAC aqueous solution showing an increase in bilayer solubility for decreasing n, where the addition of $C_{12}(EO)_n$ causes swelling of the DODAC bilayers which then result in disruption of the bilayers to form mixed micelles, as the

$C_{12}(EO)_n$/DODAC ratio increases from 0-5.1 (for n = 8)[195]. Therefore, CAE10 which has n = 10, will cause an increase in the bilayer separation as it solubilises into the bilayer, but may not result in a vesicle→micelle transition because the CAE10/DODAC ratio is kept below 1 and the bilayer swelling is due to steric repulsion (see section 1.5.4) of the large ethoxylated alcohol "head" group.

Conversely, based on previous reports that were mentioned earlier (section 6.2), glycerol will either dissolve into the aqueous phase and act as a water replacement or have preferential binding to the DODAC bilayers which will both result in swelling of the DODAC bilayers (see table 6.1). However, the interaction of CAE10 with the DODAC bilayer has a greater influence on the bilayer stability upon freezing which is the reason why the f→g transition enthalpy trends to zero fasters for CAE10 compared to glycerol (figure 6.5b).

6.3.3. The Effects of Glycerol on the Bilayers

The diffusion coefficient of water in the DODAC aqueous solutions were measured through methods described in section 2.2.8, using diffusion ordered spectroscopy at 25 ^oC. The measurements gave three separate diffusion coefficients corresponding to three different water environments; bulk, core and interlamellar water[196]. The diffusion coefficients were plotted for increasing levels of glycerol from 0-7.5 wt% (figure 6.6).

For an aqueous DODAC solution containing 1.25 wt% glycerol, the rate of diffusion for bulk water deceases by 51 % from a DODAC system containing no glycerol (bulk diffusion rate of 13.9 x 10^{-10} m^2s^{-1}) and the bulk diffusion rate remains constant at ~7 x 10^{-10} m^2s^{-1} for systems containing higher levels glycerol (figure 6.6a). After FT (figure 6.6b), there is a general decrease in rate of diffusion, shown by a decrease in the bulk water diffusion from 13.9 to 5.56 x 10^{-10} m^2s^{-1} at 0 wt% glycerol between figures 6.6 (a)

and (b), respectively. The differences between the diffusion coefficient before and after FT, decreases by 59, 65, 47 and 38 % with increasing glycerol levels of 1.25, 2.5, 5 and 7.5 wt%, respectively. So, generally there are smaller differences between the DODAC system before and after FT with increasing glycerol levels.

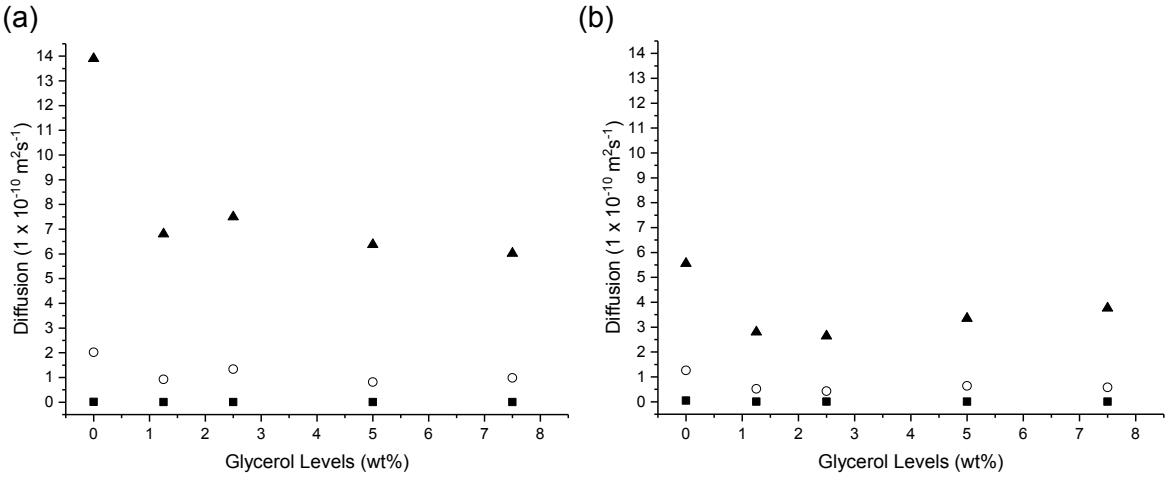


Figure 6.6. Shows the change in the diffusion rate for DODAC solutions containing increasing levels of glycerol, (a) before and (b) after FT. The diffusion rate is shown at 25 ^{o}C for; ▲ bulk, ○ core and ■ interlamellar water.

The SAXS and WAXS d-spacings are given (table 6.1) for increasing levels of glycerol at 25 ^{o}C and shows an 11 % increase in the SAXS d-spacing with the addition of 2.5 wt% glycerol. This swelling in the lamellar bilayer has been reported to be the cause of decreasing attractive Van der Waals' forces between the bilayers from an increase in repulsion as the glycerol concentration in the aqueous phase increases[197,198]. Therefore, the decrease in the bulk water diffusion coefficient between a DODAC solution containing 0 to one containing 1.25 wt% glycerol (figure 6.6a), is the result of increasing repulsion between the DODAC bilayers forming swollen bilayers of a hydrated lamellar gel phase as well as the replacement of bulk water with glycerol. Furthermore, the constant WAXS gel d-spacings (table 6.1), show that there are no changes to the gel phase arrangement

from the addition of glycerol. This suggests that glycerol does not interact with the DODAC bilayers.

Glycerol Levels/ wt%	Lamellar repeat unit/ Å	d-spacing/ Å	Width/ 1 x 10^{-3} Å
0	144	4.10	3.5
2.5	160	4.10	3.7
5.0	164	4.10	3.2
7.5	164	4.10	3.4

Table 6.1. Shows the lamellar repeat unit given by the SAXS d-spacing (accuracy of SAXS lamellar fit, ± 5 Å) and the WAXS gel peak width and d-spacing at 25 ^{o}C, where the WAXS d-spacing remains constant to 3 significant figures (accuracy of WAXS gaussian fit, ± 1 x 10^{-3} Å). The "normal" width for an L_{β} phase of this DODAC system at 25 ^{o}C is ~2.2 x 10^{-3} Å (see figure 4.6). The width matches that of a $L_{\beta'}$ phase (accuracy of the WAXS width gaussian fitting is ± 2 x 10^{-4} Å).

6.3.4. The Effects of CAE10 on the Bilayers

The diffusion rate of water was measured for the aqueous DODAC (8 wt%) solutions containing increasing CAE10 levels of 0-5 wt%, at 25 ^{o}C (figure 6.7). For a DODAC solution containing 0.60 wt% CAE10, the bulk water diffusion rate decreases to 6.17 x 10^{-10} m^2s^{-1} from a DODAC solution containing no CAE10, 13.9 x 10^{-10} m^2s^{-1} (figure 6.7a). The behaviour of the bulk water diffusion rate before and after FT follows a similar trend to that of a DODAC solution containing glycerol (see figure 6.6), where there is a general decrease in the bulk water diffusion rate between figures 6.7(a) and (b). This behaviour is shown through a decrease in the bulk water diffusion of 60, 44 and 54 % for increasing CAE10 levels of 0, 0.6 and 1.4 wt%, respectively.

However, for DODAC solutions containing CAE10 levels of 1.0 and 5.0 wt% there is an 78 and 28 % increase in the bulk water diffusion rate, respectively, between figures 6.7(a) and (b). The difference between the FT behaviour of DODAC solutions containing 0.6 and 1.0 wt% CAE10 suggests that the stability of the DODAC bilayers are different between the two CAE10 levels and that the structure of the bilayers may also be different. Therefore, the difference between the FT behaviour of DODAC solutions containing 1.4 and 5 wt% CAE10 may be due to a new trend for a different bilayers arrangement, but there are no data points between the two systems to verify this hypothesis.

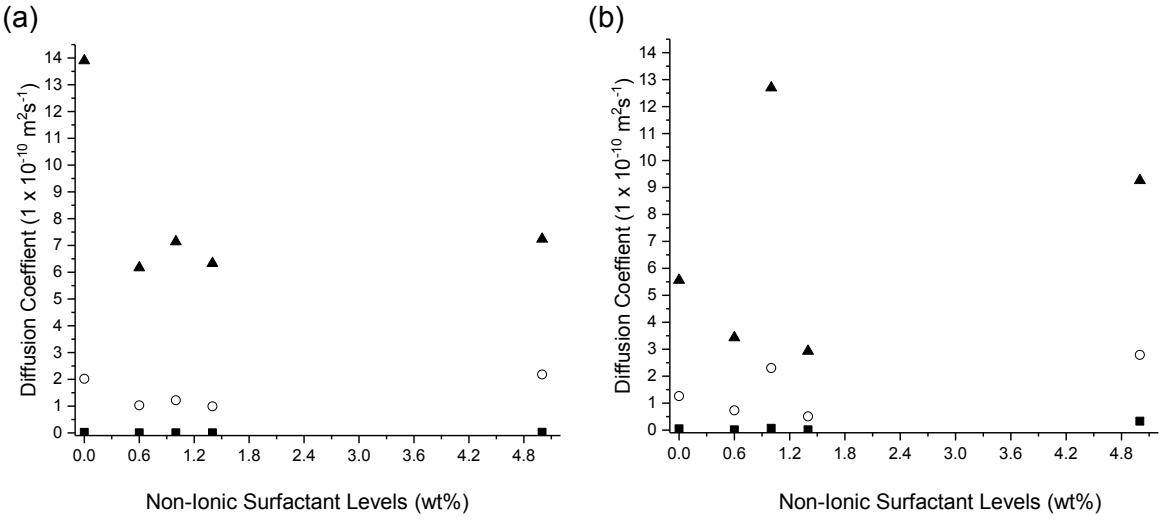


Figure 6.7. Shows the diffusion rate at 25 ºC for; ▲ bulk, ○ core and ■ interlamellar water. For DODAC solutions containing increasing levels of CAE10 (a) before and (b) after FT.

The integrated SAXS patterns were compared for aqueous DODAC solution containing increasing CAE10 levels of 0-5 wt% (figure 6.8), which shows a phase transition from a lamellar vesicle to extended lamellar bilayers. This transition is given by the transformation of the integrated SAXS patterns from board to sharp peaks which is due to increasing in lateral order from the transition between spherical to planar bilayers (see section 2.5).

The spherical→planar bilayer transition takes place for an aqueous DODAC (8 wt%) solution containing 1.4 wt% CAE10. As mentioned earlier (section 6.2), the addition of CAE10 could result in a vesicle→micelle transition for a CAE10/DODAC ratio > 5.1, where the vesicle→micelle transition is reported by López et. al.[199] and Silvander et. al.[200] to be the result of increasing micellar domains which causes holes in the vesicle structure forming bilayer fragments, following the transition of vesicles→bilayer-fragments→micelles.

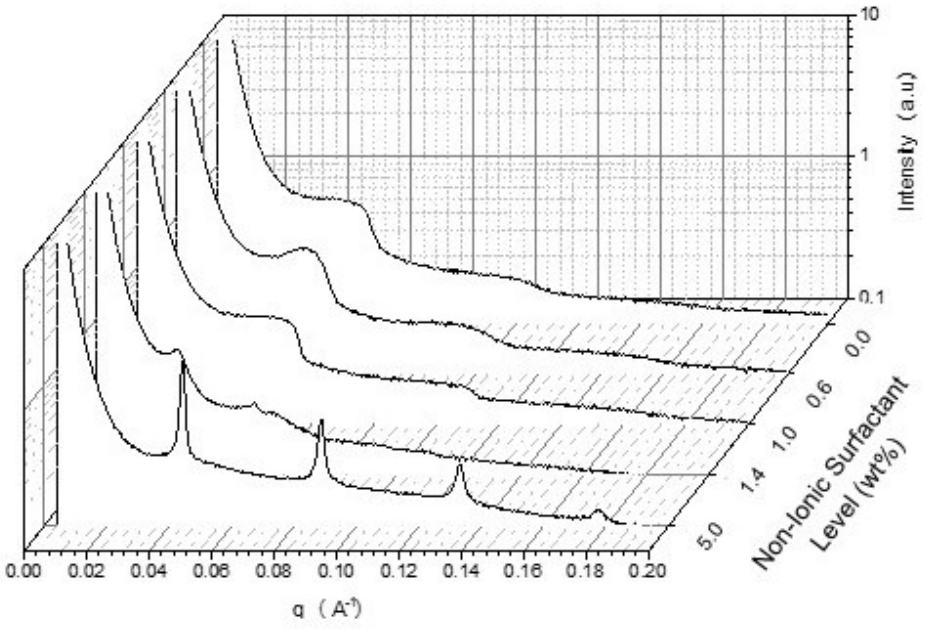


Figure 6.8. Shows the integrated SAXS patterns of an aqueous DODAC solution containing CAE10 levels of 0, 0.6, 1.0, 1.4 and 5.0 wt%, where the board peaks at 0, 0.6 and 1.0 wt% CAE10 are due to a lamellar vesicle phase and at 1.4 wt% CAE10, a vesicle to fragmented vesicle transition takes place then at 5 wt% CAE10, lamellar bilayers or bilayer fragments are formed. The sharp peaks are given by the increase in lateral order from spherical to planar bilayers transition.

For an aqueous DODAC solution containing CAE10, the SAXS d-spacing increases from 123 to 233 Å between CAE10 levels 1.0 and 1.4 wt%, respectively (table 6.2). This swelling of the bilayers was mentioned earlier as the incorporation of CAE10 to the DODAC bilayers causing a steric repulsion (see section 1.5.4) between the large ethoxylated alcohol "head" groups and reported by Barreleiro et. al. to also be the result of $C_{12}E_8$ incorporation into the DODAC bilayers[201]. The vesicle→fragmented-bilayers transition is driven by the large ethoxylated alcohol "head" group of CAE10 which promotes positive curvature in the DODAC system[202], where a vesicle structure contains both negative and positive curvature, so increasing levels of CAE10 will decrease the degree of negative curvature creating holes in the bilayers[203].

CAE10 Levels/ wt%	Lamellar repeat unit/ Å	Gel peak d-spacing/ Å	Width/ 1 x 10^{-3} Å
0	136	4.10	3.6
0.6	134	4.15	2.7
1.0	123	4.15	2.7
1.4	233	4.16	2.4
5.0	142	4.17	2.0

Table 6.2. Shows the lamellar repeat unit given by the SAXS d-spacings (in figure 6.8) and the WAXS gel peak width (accuracy of the WAXS width gaussian fitting is ± 2 x 10^{-4} Å) and d-spacing (accuracy of the WAXS gaussian fit, ± 1 x 10^{-3} Å). Showing the spherical→planar bilayers transition by the increase in the SAXS d-spacing (accuracy of SAXS lamellar fit, ± 5 Å) at 1.4 wt% of CAE10.

As mentioned, for a DODAC solution containing 1.0 wt% of CAE10, the bulk water diffusion rate increases by 78 % after FT (figure 6.7). This behaviour was suggested to be due to differences in the DODAC bilayer stability between DODAC systems containing 0.6 and 1.0 wt% CAE10. In comparison to table 6.2, the d-spacing between

CAE10 levels of 1.0 and 1.4 wt% shows a 90 % increase due to incorporation of CAE10 into the DODAC bilayers. Therefore, the difference in the FT behaviour of DODAC systems containing 0.6 and 1.0 wt% CAE10 is due to FT mixing of the CAE10 and DODAC surfactants which promotes the CAE10 incorporation into the DODAC bilayers and forms holes in the bilayers. So, the FT mixing of a DODAC mixture containing 1.4 wt% may result in planar bilayers or a mixed micellar solution giving a new trend for the bulk diffusion rate after FT (figure 6.7b). Also, no bilayer fragments are formed before FT because the difference in bulk diffusion rate (see figure 6.7) between the binary spherical/planar bilayer solution (at 1.4 wt% CAE10, before FT) is 100 % lower than the fragmented bilayers solution (at 1.0 wt% CAE10, after FT).

6.4. Conclusion

Increasing levels of glycerol or CAE10 has similar effects on the bulk water diffusion rate in the DODAC aqueous solution, before and after FT (figure 6.6 and 6.7) due to the replacement of aqueous solution and the similar behaviour of increasing DODAC bilayer separation for increasing levels of glycerol and CAE10. However, the latter is given by different mechanisms for the addition of glycerol and CAE10 to the DODAC vesicles. The addition of CAE10 causes a lateral separation of the DODAC bilayers from increasing micellar domains upon CAE10 which causes the DODAC bilayers to transition from spherical to planar bilayers or a mixed micellar solution, where the outcome can be determined from SAXS results after FT.

However, swelling of the DODAC lamellar phase due to addition of glycerol is the result of glycerol dissolving into the aqueous phase and acting as a water replacement which increases solvent repulsion between the bilayers. The addition of CAE10 has a greater influence on the DODAC bilayers stability which was shown by the enthalpy of the f→g transition (figure 6.5b) trending to zero faster than a DODAC solution containing glycerol.

The behaviour upon FT was shown in figure 6.6 (for glycerol) and 6.7 (for CAE10) to have smaller differences in the bulk water diffusion rate between the DODAC system before and after FT. This difference in the bulk water diffusion rate, when small, is suggested to have less structural changes upon FT, where after FT there is an increase in the bilayer separation (see figures 4.2, 4.4 and 5.4). Although there are less changes after FT, the DODAC bilayers had to undergo certain structural changes before FT to withstand the effects upon FT, where the DODAC solutions containing 5 wt% CAE10 caused a lateral phase transition and 7.5 wt% glycerol resulted in dehydrated bilayers from glycerol replacement which increased the bilayers separation. Also, both chemical additives resulted in a decreased bulk water diffusion rate which is not ideal for LFE's (see section 1.7.2).

7. Effects of Preparation Technique on the Phase behaviour of a DODAC Solution

7.1. Overview

Experimental preparation techniques, such as extrusion and sonication, were compared for the effects upon FT on the aqueous DODAC solutions through the changes to the bilayer properties, given by the second cooling thermographs (see figures 5.2 & 6.3), and by the diffusion rate of water in the aqueous DODAC solutions. The comparison was made for the differences between probe vs bath sonication, and for various extrusion membrane pore sizes of 1, 0.8, 0.4, 0.2 and 0.05 μm. The bulk water diffusion rate increases from 7.33 to 16.6 x 10^{-10} m^2s^{-1} with a decrease in membrane pore size from 1 to 0.05 μm, respectively, for DODAC solutions that were extruded. Also, the bulk water diffusion rate for a membrane pore size of 0.05 μm (16.6 x 10^{-10} m^2s^{-1}), closely matched that of a DODAC solution that was bath sonicated (14.1 x 10^{-10} m^2s^{-1}).

The DODAC solutions prepared by bath and probe sonication yielded small unilamellar vesicles and gave the same shift from ~31 to 35 ^oC, of the L_α→gel transition temperature as a DODAC solution containing no $CaCl_2$ (see figure 5.2b(iii)) during the second cooling cycle in the DSC thermographs. However, the DODAC solution prepared by probe sonication resulted in a two-phase system of an aqueous DODAC solution and dehydrated DODAC crystals. The temperature shift of the L_α→gel transition given by the second cooling thermographs favoured small unilamellar vesicles, where the changes to the bilayers properties were accelerated by small unilamellar vesicles prepared by sonication and extrusion. This behaviour is also shown through the ^1H NMR alkyl peak height, where the differences in the relative alkyl peak height between before and after

FT is greater for a membrane pore size of 0.05 μm compared to 0.8 μm which is given by a decrease of 42 and 6 %, respectively.

7.2. Introduction

As mentioned in section 1.6, both sonication and extrusion can be used to increase the monodispersity and unilamellarity of a polydisperse vesicular solutions. Extrusion is used to control the size of the vesicles and create unilamellar vesicles by passing a vesicular solution through the porous membrane multiple times. This process is mostly preformed above the chain melting transition temperature to decrease the local viscosity of the bilayers. Some studies on extrusion show that the minimum extrusion pressure through a specific membrane pore size increases with the viscosity of the solution and the minimum pressure, where extrusion is achieved, depends on the lysis tension of the bilayers and not the bending modulus. Also, the size of the vesicles depends on the extrusion pressure[204,205]. Therefore, the size of the vesicles is not completely dependent on the membrane pore size, where the vesicles can sometimes be slightly larger as well as smaller than the membrane pores[206]. So, extrusion through a specific membrane pore size can yield vesicles with diameters similar to the membrane pore size.

Sonication causes aggregation through ultrasonic sound waves. These sound waves can be exposed to a polydisperse vesicular solution through the sample container in a water bath or by direct contact between a probe and the surfactant solution. Direct exposure from probe sonication can cause an increase in thermal energy of the vesicular solution and has been reported to result in structural defects of the vesicular system or metal deposits from the probe into the sample. These defects can be reduced by prolonged cooling of the solution or a cool water bath during sonication[207,208,209]. Thus, only short intervals of ultrasonic waves are exposed over a short period. Comparatively, bath sonication is completed over longer time periods and there is greater control on the

temperature of the vesicular solution due to indirect exposure of the sound waves and a temperature-controlled water bath[210].

The similarities between sonication and extrusion were reported by Lapinski et. al. to be directly comparable despite the differences in the average size and size distribution, the arrangement of the bilayers did not depend on how they were formed but on the interactions between the constituents that form the bilayers[211]. The properties of the monodisperse unilamellar DODAC and DODAB vesicles were reported by Feitosa et. al. to have a decrease in the chain melting transition temperatures with decreasing vesicles sizes which were achieved by sonication or extrusion, suggesting that the chain melting transition depends on curvature, where the effects of both preparation techniques on the bilayers are the same[212]. Therefore, DODAC solutions that are sonicated or extruded will give the same properties for the DODAC bilayers.

7.3. Results

7.3.1. Sonication Preparation

The aqueous DODAC solution was prepared by the addition of an aqueous $CaCl_2$ (0.085 wt%) solution to solid DODAC and sonicated until the DODAC dissolved and the solution was clear. The bath sonicated samples were sonicated in an Elmasonic P 30 H (Elma Schmidbauer GmbH) at a power of 80 kHz, in a hot water bath of 60 ^{o}C for 1.0-2.5 hrs. Conversely, the probe sonicated sample was sonicated in a Sonics vibra cell VCX500 (Sonics & Materials) at a power of 20 kHz (± 50 Hz) for 10-15 mins on a pulse program of 1s exposure with 1 s wait intervals. The probe sonicated sample was equipped with a temperature probe which showed a 10 ^{o}C increase in temperature after 5 mins and during the sonication period the temperature of the sample reached 76 ^{o}C.

Sample	Diffusion at 25 °C (x 10 $^{-10}$ m^2/s)			Diffusion at 5.0 °C (x 10 $^{-10}$ m^2/s)		
	Bulk	**Core**	**Interlamellar**	**Bulk**	**Core**	**Interlamellar**
DODAC solution	13.9	2.02	0.02	8.41	1.00	-------
FT	5.56	1.26	0.05	4.47	0.93	-------

Table 7.1. Shows the diffusion rate of water for the aqueous DODAC solution prepared by DODAC hydration at 65 °C (as described in section 2.1.1). The table shows the diffusion rate (methods described in section 2.2.8) for bulk, interlamellar and core water at 25 and 5.0 °C, for before and after FT. The diffusion rate of interlamellar water at 5.0 °C was too slow to record.

7.3.2. Effect of Sonication

Bath and probe sonication were compared with a non-sonicated sample prepared by DODAC hydration at 65 °C (as described in section 2.1.1) which was stirred until the DODAC dissolved to form a white opaque solution. The self-diffusion of the different water environments in the aqueous DODAC solution was measured for the different preparation techniques (table 7.2). For non-sonicated samples, there were three different diffusion rates for the three different water environments; bulk, interlamellar and core water (table 7.1). Comparatively, the unilamellar vesicles formed from sonication had only two water environments, denoted as bulk and core water in table 7.2.

The diffusion rate of bulk water is faster for a sonicated sample compared to that of a non-sonicated sample (comparison between tables 7.1 & 7.2) by 1 and 17 % for bath and probe sonicated solutions, respectively. This increase in the bulk water diffusion rate is due to the small unilamellar vesicles which result in a decrease in viscosity of the

vesicular solution[213] and is also shown by the bulk water diffusion rates of a DODAC solutions extruded through a membrane pore size of 0.05 μm (16.6 x 10^{-10} m^2s^{-1}, figure 7.4) which closely matches that of the $CaCl_2$ aqueous solution (19.1 x 10^{-10} m^2s^{-1}, table 7.3). After FT, the number of water environments decreases for a solution that has been bath sonicated and probe sonicated then extruded. This suggests that sonication leads to spherical→planar bilayers phase transition upon FT. Thus, non-sonicated samples are more robust to the effects upon FT.

Preparation Techniques	**Diffusion (x 10^{-10} m^2/s)**		**Diffusion after FT (x 10^{-10} m^2/s)**	
Water Environment	**Bulk**	**Core**	**Bulk**	**Core**
Bath Sonication	14.1	2.23	5.34	n/a
Probe Sonication	16.2	2.16	10.5	1.16
Probe Sonication/Extrusion	18.0	5.41	7.38	n/a

Table 7.2. Lists the diffusion rates for the different types of preparation. Both bath and probe sonication result in the formation of unilamellar vesicles, having only bulk and core water environments. Samples that were bath sonicated, and probe sonicated followed by extrusion through a 1 μm membrane, were reduced to a single water environment after FT.

Probe sonication lead to the same number of water environments for before and after FT, but after extrusion through a 1 μm porous membrane the number of water environments reduced to one after FT (table 7.2). The general vesicle size for probe-sonicated DODAC solutions were reported to have a maximum size of 80 nm[214,215,216], so presumably the size distribution of the probe-sonicated sample was not affected by extrusion through a 1 μm pore size. Furthermore, the polarised light images indicated some isotropic fragments on the micron scale, which was suggested to be dehydrated

DODAC crystals (see appendix, figure A7.1). Therefore, the extrusion removed the dehydrated DODAC crystals formed from probe sonication[217].

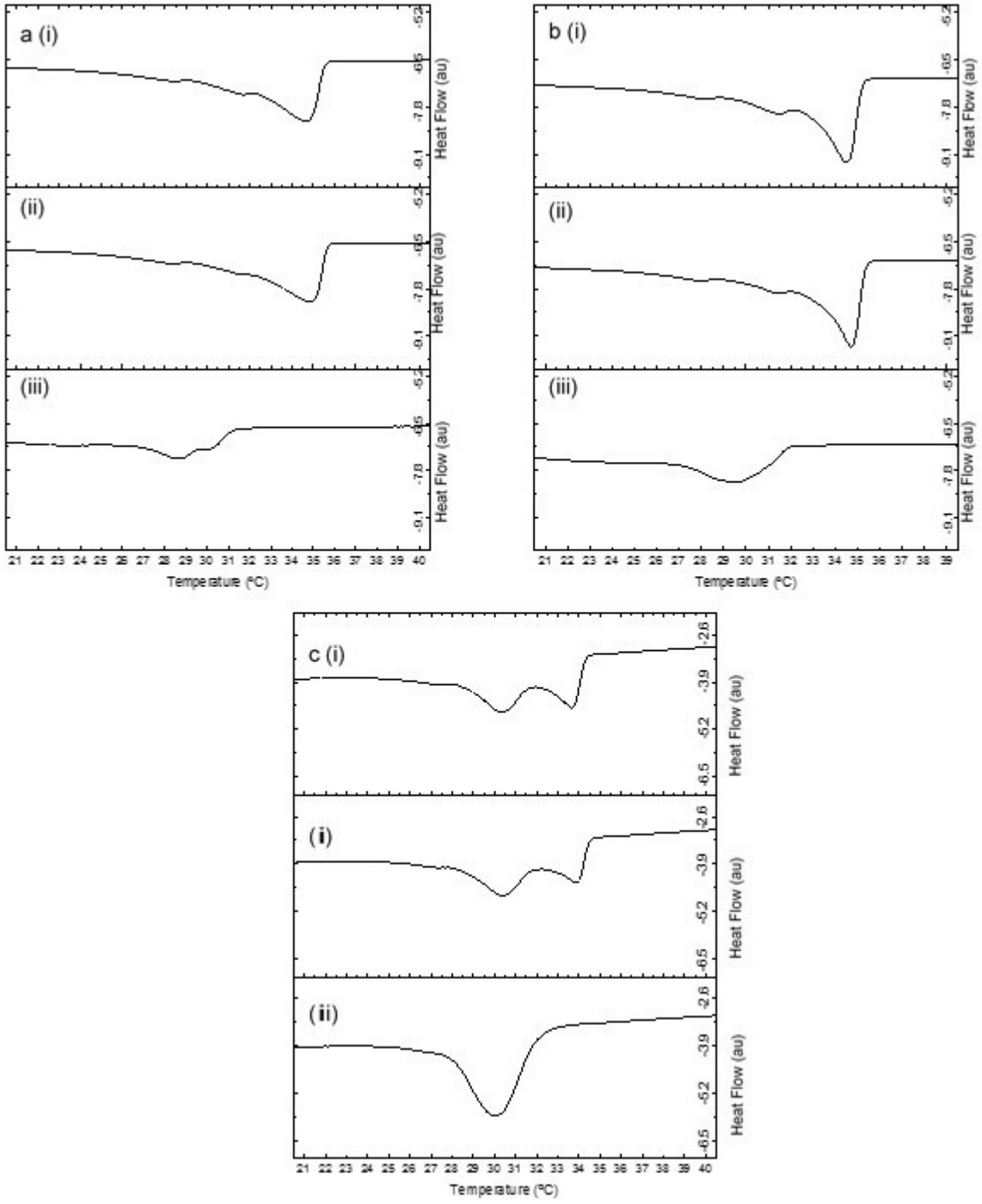


Figure 7.2. Shows thermographs for the (i) third, (ii) second and (iii) first cooling cycles. (a) is the result for a sample that has been sonicated in a water bath at 60 °C for 2.5 hrs, (b) is the result for a sample that was probe sonication with intervals of 1 s sonication and 1 s wait for 10-15 mins

and (c) is the result for a DODAC sample that was hydrated with a $CaCl_2$ aqueous solution at 65 ^oC (normal vesicle preparation, see section 2.1.1).

The differences between the number of water environments before and after FT for a DODAC solution that was probe sonication and probe sonication with extrusion, supports the presence of bilayer fragments or dehydrated DODAC crystals. Since the number of water environments after FT decreases when the probe sonicated sample is extruded (table 7.2). Also, for a probe sonicated sample, the presence of two water environments with a decreased diffusion rates by 35 and 46 % after FT, for bulk and core water, respectively, could be the result of larger unilamellar vesicles formed by mixing of the bilayer fragments/dehydrated crystals in the aqueous vesicular solution upon FT.

Sample	**Diffusion at 25 ^oC (x 10^{-10} m^2/s)**	**Diffusion at 5.0 ^oC (x 10^{-10} m^2/s)**
H_2O[i]	23.0	13.1
$D_2O/CaCl_2$[ii]	19.1	10.8

Table 7.3. Shows the diffusion rates for free water compared the that of a $CaCl_2$ solution in D_2O for temperatures at 25 and 5.0 ^oC. (i) values taken from M. Holz et. al.[218] and (ii) values measured in these studies for $CaCl_2$ levels the same as the DODAC aqueous solution, 0.085 wt% $CaCl_2$. The lower diffusion rate of $D_2O/CaCl_2$ compared to H_2O is expected due to reports by McCall et. al.[219] which shows that $CaCl_2$ lowers water activity.

The cooling thermographs were compared between 36-26 ^oC for sonicated samples and non-sonicated samples (figure 7.2). The fluid→gel cooling transition is broader for sonicated samples compared to the non-sonicated sample, where the broader transition could be due to the bilayer fragments/dehydrated DODAC crystals form during sonication

or two populations of vesicles sizes which was suggested earlier that the chain transition can depend on the size of the vesicles[220]. The latter is probably the reason for the results given by the bath sonicated sample before FT (figure 7.2a(iii)).

After FT (ie second cooling cycle (i)), for a non-sonicated sample (figure 7.2c), there is a second metastable gel phase upon cooling and the fluid→gel transition temperature increases from 30 to 34 °C (general behaviour seen in figures 5.2b & 6.3b). However, the thermographs of the sonicated samples after FT (figure 7.2a & b (i)) behaves similar to a non-sonicated sample extruded through a 50 nm pore (figure 7.4(i)), where the fluid→gel transition temperature shifts to ~34 °C and gives only one gel transition.

7.3.3. Extrusion Preparation

The DODAC aqueous solution was extruded through a polycarbonate membrane with pore sizes; 1, 0.8, 0.4, 0.2 and 0.05 μm. The extrusion was done manually with a 1000 μl syringe Avanti mini-extruder equipped with an Avanti heating block holder. A bulk surfactant solution was prepared by surfactant hydration at 65 °C (as described in section 2.1.1) which was then extruded by passing the solution through the polycarbonate membrane 15 times at 65 °C. The white opaque aqueous DODAC solution increased in clarity when extruding with decreasing membrane pore size, where the solution was completely clear for pore sizes 0.2 and 0.05 μm.

7.3.4. Effects of Vesicle Size

The diffusion rate of water in the aqueous DODAC solution was measured for increasing membrane pore sizes (figure 7.3). As mentioned, extrusion generally results in the formation of unilamellar vesicles, though the output of the DOSY experiment best fitted to a three-component curve (through methods described in section 2.2.7) for all pore

sizes, except for membrane pore sizes; 0.2 and 0.05 μm. The bulk water diffusion increases with decreasing membrane pore size which is predicted from the decreased viscosity of the aqueous DODAC solution due to the increase in the population of smaller unilamellar vesicles[213].

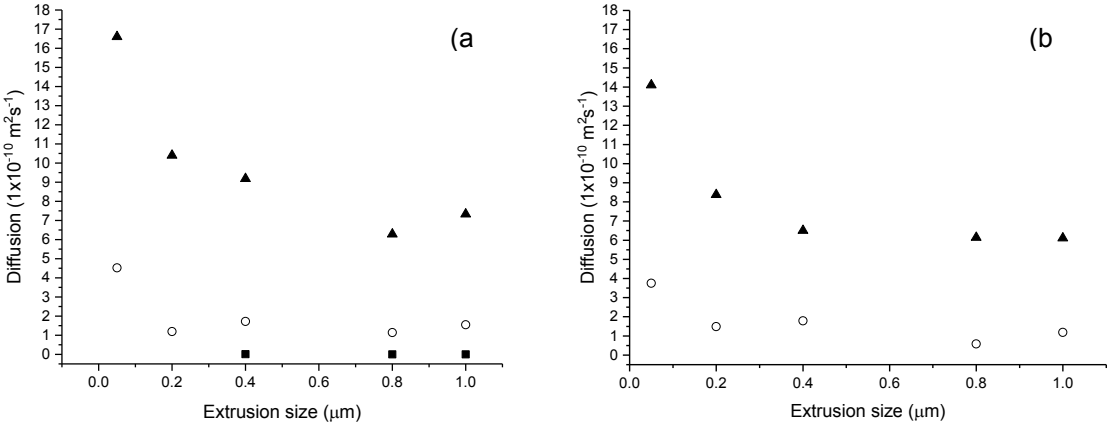


Figure 7.3. Shows the diffusion rates for extruded samples through different membrane pore sizes at 65 ^{o}C, (a) before and (b) after FT. The plot compares the extruded membrane pore size with the diffusion rate for (▲) bulk, (○) core and (■) interlamellar water. At 0.2 and 0.05 μm, the DOSY results showed a two-coefficient curve which suggest a vesicle population of only unilamellar vesicles. The bulk water diffusion rate for a polydisperse sample is 13.9 x 10^{-10} and 5.56 x 10^{-10} m^2s^{-1} (see table 7.1), for before and after FT, respectively.

After FT (figure 7.3b), unilamellar vesicles are formed, which is not the case for the non-extruded and non-sonicated sample (table 7.2). This suggest that as well as an increase in larger vesicles there is also an increase in the formation of unilamellar vesicles from the FT induced mixing. For a sample that was extruded through a 0.2 and 0.05 μm membrane pore the number of water environments remain the same for before and after FT (figure 7.3). Suggesting that these samples may still have some polydispersity and that the decrease in water environments upon FT is dependent on the vesicle size. Thus, the decrease in water environments for sonicated samples after FT is due to the

formation of smaller and/or greater monodisperse vesicles compared to vesicles formed via extrusion.

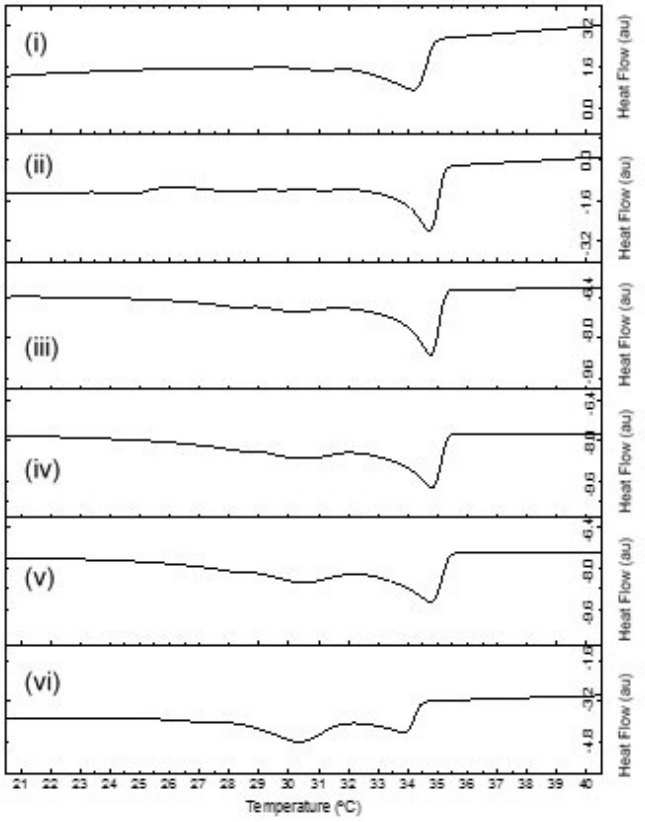


Figure 7.4. Shows the chain transitions for the second cooling cycles of aqueous DODAC solutions that were extruded through a membrane with a pore size; (i) 50 nm, (ii) 0.2 μm, (iii) 0.4 μm, (iv) 0.8 μm, (v) 1 μm, and (vi) the polydisperse aqueous DODAC solution (prepared by methods in section 2.1.1).

The thermographs for the second cooling transitions were compared decreasing vesicle size (figure 7.4). The results show a decrease in the g→g' transition magnitude with decreasing vesicle size, until only one gel transition existed for a sample that was extruded through a membrane pore size of 0.2 μm. Thus, for smaller size distributions of vesicles formed by extrusion, and more monodispersity in sonication vesicles (figure 7.2a &b), there is a shift in the chain transition temperature from ~31 to ~35 °C, after FT.

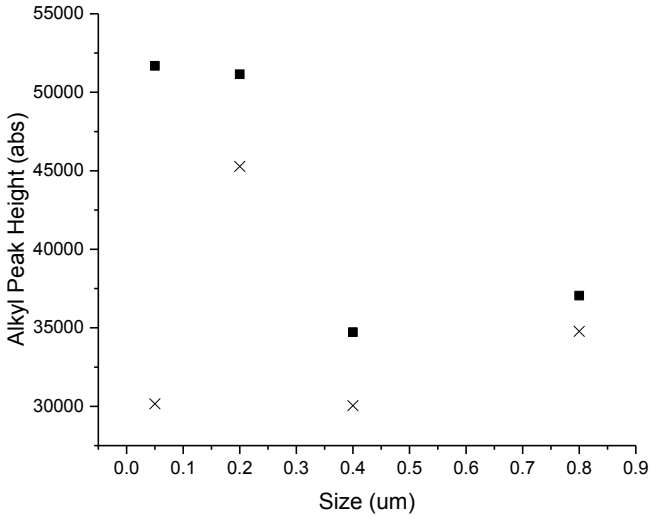


Figure 7.5. Displays the relative alkyl peak height taken from static solid state ^{1}H NMR of the alkyl peak height at 1.17 ppm (see figure 5.5) for the samples extruded through different membrane pore sizes. Results are shown at 25 ^{o}C for (■) before and (x) after FT. For the polydisperse DODAC solution (prepared via methods described in section 2.1.1), the alkyl peak height is 43000 and 47000 abs, before and after FT respectively.

The various extrusion membrane pore sizes of DODAC solutions that were extruded, was compared at 25 ^{o}C (figure 7.5) using static solid state ^{1}H NMR (through methods described in section 2.2.8) for the relative intensity of alkyl peak height of the DODAC molecules in the aggregates given at 1.17 ppm. The alkyl peak height was used in section 5.3.3, to measure the mobility of the alkyl chains which provided a good approximation for the macroscopic phase of the vesicular solutions.

Before FT (figure 7.5 (■)), there is a 47 % increase in the alkyl peak height for DODAC solutions that was extruded through decreasing membrane pore sizes from 0.4 to 0.2 μm. This increase may be related to the increase in unilamellarity shown (figure 7.3a) by the decrease in the number of water environments between the solutions prepared

through membrane pore sizes of 0.4 and 0.2 μm. Therefore, this is the point which the vesicles go from multilamellar to unilamellar and ~0.4 μm is the limiting vesicle size that can withstand a multilamellar structure, where there is an increased curvature close to the vesicle core as the vesicle sizes decrease. The differences in the alkyl peak height before and after FT of 6, 13, 11 and 42 %, has a general increase for DODAC solutions prepared with decreasing membrane pore sizes of 0.8, 0.4, 0.2 and 0.05 μm, respectively. So, the increased curvature from smaller vesicles result in larger changes to the alkyl chain mobility upon FT.

7.4. Conclusion

There were slight differences in the properties of the vesicular solution based on the type of preparation, where DODAC solutions that were sonication tend to form more monodisperse unilamellar vesicles than extruded DODAC solutions which even when unilamellarity was achieved there were still some polydispersity in the vesicle sizes. However, the similarities in the resultant structures caused the same changes upon FT, where the chain transition temperature increases from ~31 to ~35 ^{o}C and only one gel transition exits at the chain transition boundary. Thus, the effects upon FT for extruded and sonicated samples can be directly comparable, as suggested earlier. Though, this is only true for probe sonicated samples that are followed by extrusion to remove bilayer fragments/dehydrated DODAC crystals or metal residues and for extruded samples that are extruded through membrane pore sizes small enough to result in a clear DODAC solution.

These studies also support the effects upon freezing which results in a FT induced mixing (as mentioned in sections 1.7.1 & 6.2), through the decrease in the number of water environments for monodisperse and unilamellar vesicles and the lack of change for

polydisperse multilamellar vesicles. Therefore, the changes upon FT are accelerated by increasing monodispersity and unilamellarity.

8. Conclusion

8.1. The Effects of $CaCl_2$ on the FT Stability

The DSC thermographs for a DODAC aqueous solution was used to assess the changes upon FT, through the increase in the fluid→gel transition temperature. These changes varied with the introduction of $CaCl_2$ into the aqueous phase of a DODAC aqueous solution. The changes resulted in two "gel" phase transitions, where the temperature of the gel→gel' transition was the same as the fluid→gel transition temperature before FT, and the fluid→gel transition temperature increased by ~4.0 ^{o}C after FT. This suggests that the difference between thermographs before and after the addition of $CaCl_2$, results in a vesicle structure more robust to the effects upon FT.

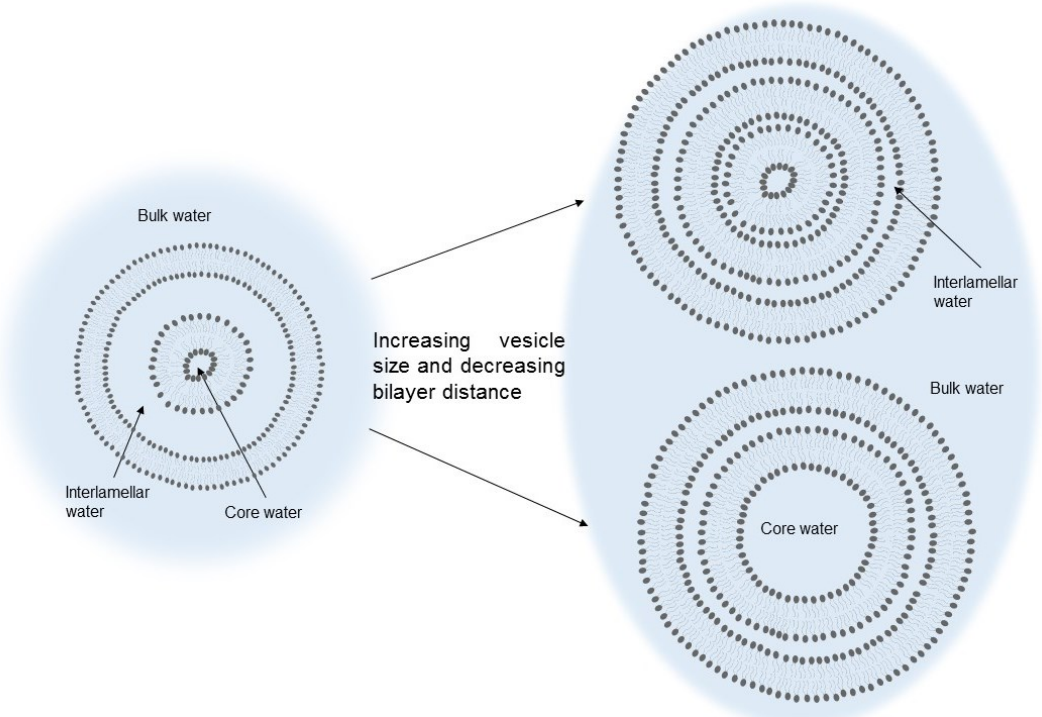


Figure 8.1. Shows a cross-section of a vesicle structure for the effects of increasing DODAC and $CaCl_2$ levels which result in an increase in vesicle size and a decrease in bilayer separation.

In chapter 5, the increasing amount of $CaCl_2$ in the aqueous solution showed less changes to the d-spacing trend with decreasing temperature upon FT (figure 5.4). This was shown through the difference between the d-spacing in the L_α and gel phases before and after FT for $CaCl_2$ levels of 0.15 wt%, where the ionic effects dominate over the effects upon FT which prevents an FT induced swelling. However, the ionic effects of the aqueous solution that caused a zeroing potential between the positive DODAC "head" groups, were less effective after FT at 0.085 wt% $CaCl_2$ which resulted in an increase in the bilayers separation. This suggests that the effects upon FT is due to solvent repulsion between the bilayers and is minimised for dehydrated bilayers because Van der Waal's attraction dominates in the absence of repulsion (from ionic shielding) which makes the bilayers more robust.

The increasing effects of salt and surfactant on the DODAC system both result in a decrease in the bilayer distance (figure 5.1). Furthermore, the increase in salt and surfactant levels was mentioned in section 1.5.1 with reports to have increased the size of the vesicle due to vesicle fusion or the increase in aggregation number, respectively. Therefore, the behaviour for increasing salt levels may lead to a large vesicle with multiple bilayers or a large vesicle with 1 or 2 bilayers and a large aqueous core (figure 8.1). The latter will cause an increase in the amount of encapsulated water and the former will form a dehydrated vesicle structure, where both purposed structures will decrease the effects upon freezing. So, low levels of $CaCl_2$ (i.e 0.15 wt%) will allow the vesicle to retain some of its internal structure upon FT.

Upon thawing, there is a large influx of water into the bilayers causing an increase in the bilayers separation, shown in figures 4.2, 4.4 & 5.4 as a general increase in the SAXS d-spacing. This effect was mentioned in section 1.7.1 which resulted in lysis of the bilayers before the bilayers reach their original hydration levels. Though, the hydration

of the bilayers increases to a d-spacing greater than the d-spacing before FT and there are no changes to the packing structure of the amphiphiles which could suggest that there is no swelling induced lysis upon thawing. Therefore, the freezing injuries may be a result of lateral phase separation or defects/holes within the bilayers.

8.1.1. The Effects of Repeat FT Cycles

The effects upon FT were evaluated for the repeat FT cycles of a DODAC solution containing 8 wt% DODAC in an aqueous solution of 0.085 wt% $CaCl_2$, showing the stability of the bilayers separation across 11 FT cycles (table 8.1) and the stability of the f→g and g→g' transition after FT for 4 FT cycles (table 8.2). The bilayers separation increases from 130 to 183 Å after FT, where this FT induced swelling is the typical behaviour of the DODAC bilayers. After the FT induced swelling, the separation of the bilayers is almost constant (decreases from 183 to 190 Å) after a further 10 FT cycles. Also, there are little changes to the WAXS d-spacing between 1-5 FT cycles. Therefore, besides the bilayers separation, the FT effects across the 11 FT cycles show little changes to the vesicle structure.

Number of FT Cycles	SAXS d-spacing (Å)	WAXS d-spacing (Å)	Gel Peak Width (1×10^{-3} Å)
0	130	4.17	2.5
1	183	4.17	2.5
5	189	4.16	2.7
11	190	4.16	2.7

Table 8.1. Shows the SAXS (accuracy of the SAXS lamellar fitting is ± 2 Å) and WAXS (accuracy of WAXS gaussian fit, ± 1×10^{-3} Å) d-spacing including the WAXS gel peak width (accuracy of the WAXS width gaussian fitting is ± 2×10^{-4} Å) of a DODAC solution containing 8 wt% DODAC in an aqueous solution of 0.085 wt% $CaCl_2$, for the differences in the bilayer parameters after 11

FT cycles, where the FT cycles were done prior to the experiment by freezing in liquid nitrogen and heated above the chain melting temperature (~37 ^{o}C).

The cooling transition temperatures for f→g and g→g' after FT (table 8.2), remain constant across the 4 FT cycles and the variation in the g→g' transition enthalpies show no correlation suggesting that it the variation is due to error in the enthalpy calculations (standard deviation for calculated enthalpies ± 3 Jmol^{-1}). Though, the l→g transition enthalpies increases from -14 to -23 Jmol^{-1} after 3 FT cycles, suggesting that the increase in l→g transition enthalpy may result in a decrease in g→g' transition enthalpy giving a similar behaviour to that of a sample containing no $CaCl_2$, where there is one transition of f→g at ~34 ^{o}C. This behaviour of the bilayers properties may be the result of swelling of the bilayers. Therefore, based on the SAXS and WAXS data (table 8.1), the suggested decrease in the g→g' transition enthalpy will be very slow because the d-spacing is constant between 1-5 FT cycles (table 8.1).

Number of FT Cycles	**$\Delta H_{l\rightarrow g}$ / Jmol^{-1}**	**$T_{l\rightarrow g}$ / ^{o}C**	**$\Delta H_{g\rightarrow g'}$ / Jmol^{-1}**	**$T_{g\rightarrow g'}$ / ^{o}C**
1	-14	34	-29	31
2	-18	34	-24	31
3	-23	34	-26	31
4	-23	34	-30	31

Table 8.2. Shows the enthalpy changes (accuracy of ± 1 Jmol^{-1}) and the temperature (accuracy of ± 5.0 ^{o}C) of the fluid→gel (f→g) and ge→gel' (g→g') transitions for 4 FT cycles, where the FT cycles were done through the DSC temperature cycles between 70 and -40 ^{o}C.

8.2. The Effects of Chemical Additives on the DODAC Bilayers

In chapter 6, the effects upon addition of CAE10 and glycerol to a DODAC solution containing 8 wt% DODAC in an aqueous solution of 0.085 wt% $CaCl_2$ was discussed for the changes to the DODAC bilayer stability before and after FT and the behaviour of the structure of the bilayers upon CAE10 and glycerol addition before FT at 25 ^{o}C. The stability of the bilayers was shown (figure 6.5b) by the rate which the enthalpy of the f→g transition trends to zero, after FT. This rate is shown (figure 8.2) as a gradient of -5.74 and -3.83 for the enthalpy change per wt% of aqueous solution for a DODAC solution containing CAE10 or glycerol, respectively. Therefore, the replacement of aqueous solution causes the new f→g transition enthalpy to decrease and so lowers the effects of FT on the DODAC bilayers. Also, CAE10 is more effective than glycerol at preserving the f→g transition temperature after FT.

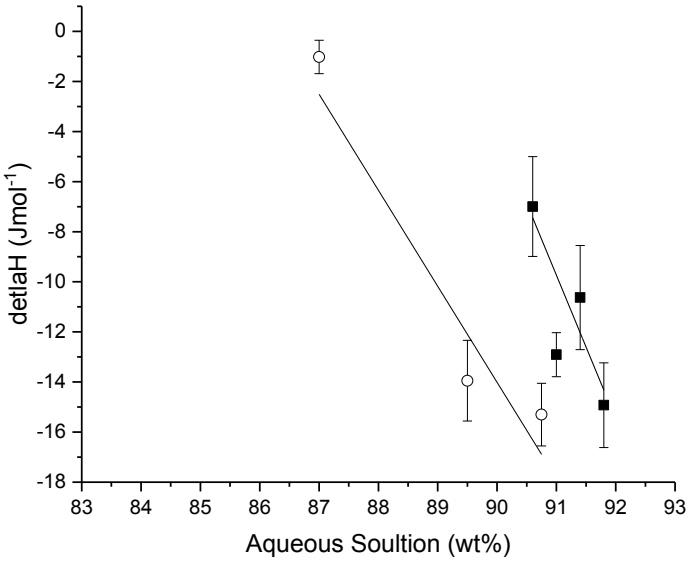


Figure 8.2. Shows the mean transition enthalpies for the second f→g cooling transition at ~35 ^{o}C from results shown in figure 6.5b. Transition enthalpies are shown for DODAC solutions containing (o) glycerol or (■) CAE10, where both are fitted to a linear line with a gradient of -5.74 and -3.83 for the enthalpy per wt% of aqueous solution for a DODAC solution containing CAE10 or glycerol, respectively. The errors bars represent the standard deviation from the mean calculated enthalpies.

8.2.1. The Effects of Glycerol Upon FT

The effects of glycerol on the DODAC bilayers are shown in figure 8.3 as an increase in the bilayer separation, where it was concluded in section 6.4 that the local structure of the bilayers remain the same and the increase in the bilayer separation is due to the addition of glycerol into the aqueous phase which increases the solvent repulsion between the DODAC bilayers.

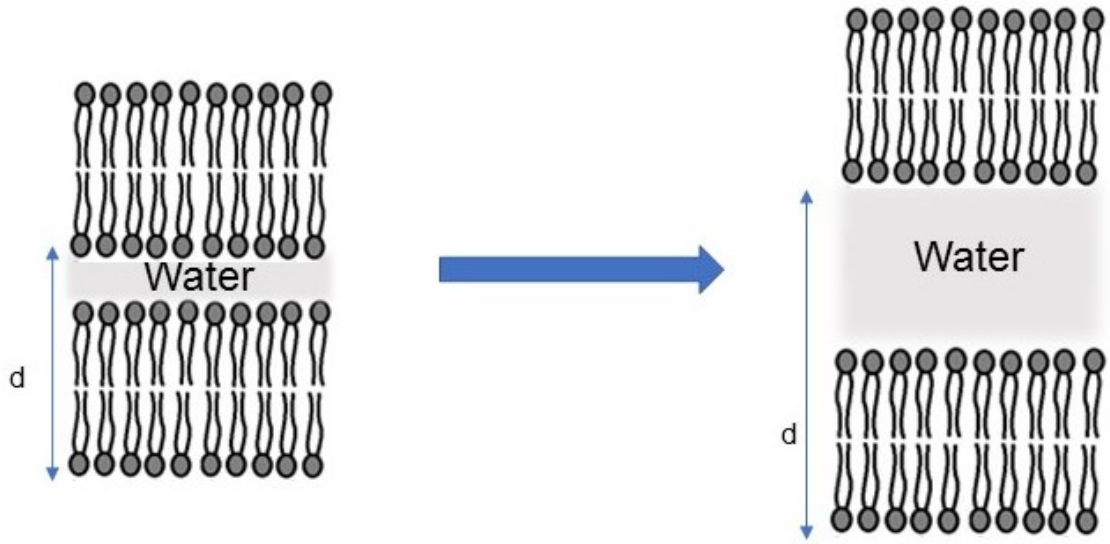


Figure 8.3. Shows a schematic for the increase in d-spacing from the addition of glycerol to the aqueous DODAC solution.

The changes to the DODAC bilayers (figure 8.3) upon addition of glycerol before FT and the behaviour of the bulk water diffusion rate after FT, where the bulk water diffusion rate decreased in comparison between a DODAC solution before and after FT (figure 6.6), suggested that the dehydration effects upon FT was reduced as the glycerol/H_2O ratio increased resulting in smaller changes to the bilayer separation before and after FT. This behaviour was established by a repeat in the SAXS and WAXS measurements of the

results presented in table 6.1 at 25 ^{o}C before FT and the inclusion of the measurements of the same sample that was treated with one FT cycle (figure 8.4).

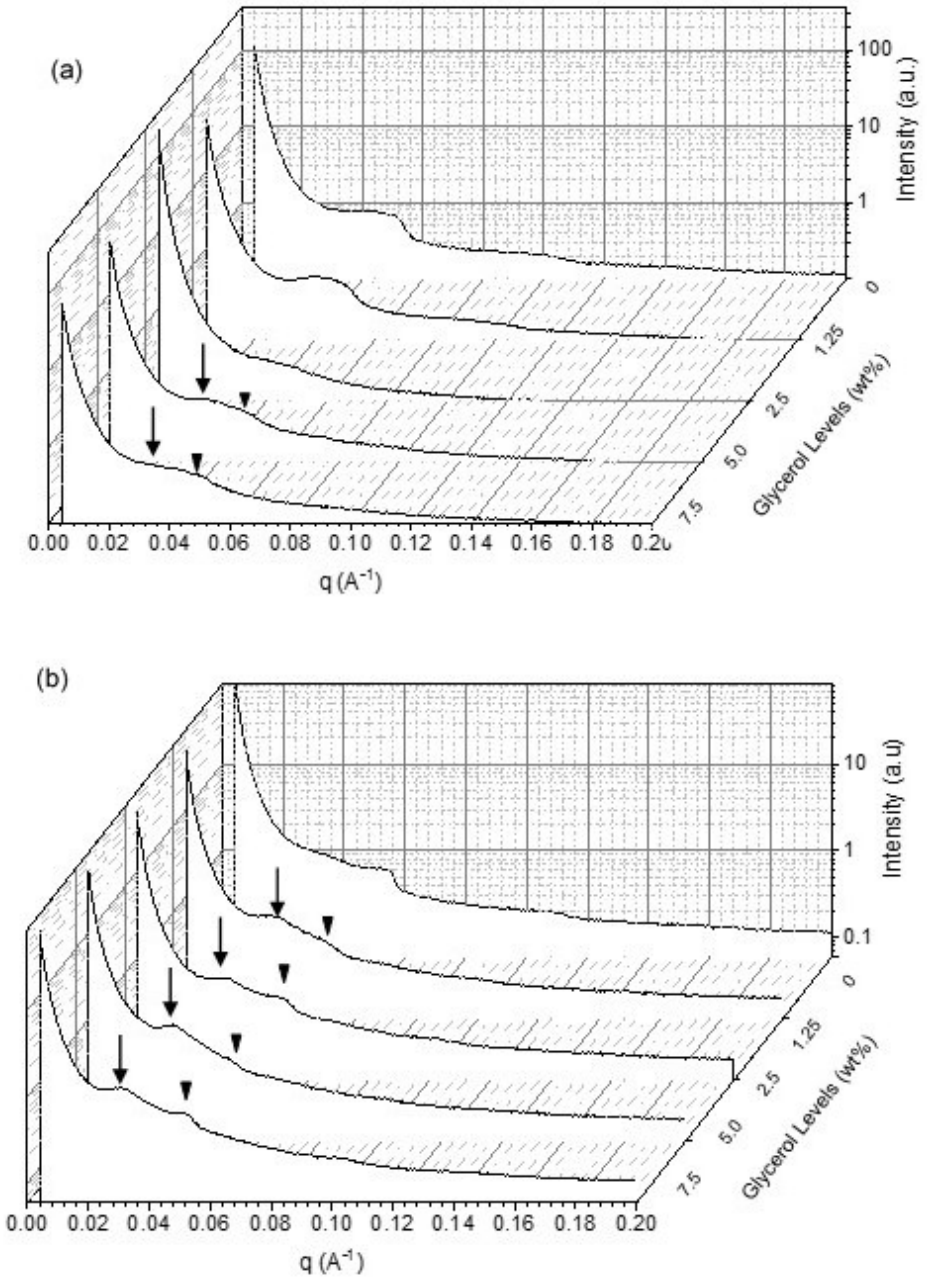


Figure 8.4. Shows the integrated SAXS patterns for the DODAC solutions containing 0, 1.25, 2.5, 5.0 and 7.5 wt% glycerol at 25 ^{o}C for (a) before and (b) after FT. The addition of glycerol to a DODAC solution resulted in uneven swelling giving two different lamellar d-spacing; one larger d-spacing (arrow) and a smaller d-spacing (arrow head).

The integrated SAXS patterns of the repeat experiment, shows an uneven swelling of the bilayers for a DODAC solution containing 5.0 and 7.5 wt% glycerol before FT (figure 8.4a), which resulted in two different bilayer separations of 167 (arrow) and 132 (arrow head) Å for 5.0 wt% glycerol, and 151 (arrow) and 128 (arrow head) Å for 7.5 wt% glycerol (variation in results ± 9 Å). After FT (figure 8.4b), the uneven bilayer swelling is shown for DODAC solutions containing 2.5, 5.0 and 7.5 wt% glycerol as; 188 (arrow) and 124 (arrow head), 192 (arrow) and 125 (arrow head), and 198 (arrow) and 123 (arrow head) Å, respectively (accuracy to lamellar fit ± 6 Å).

This uneven swelling (seen in figure 8.4) is not shown for the results given in table 6.1 (shown as one set of d-spacing) because the integrated SAXS patterns were poorly resolved (see appendix, figure A8.1) which could be due to how the results were obtained, where the first set of results were carried out in the pressure cell and the repeat results were carried out in the capillary holder. The pressure cell was explained (see section 2.5.6) as a chamber that generates hydrostatic pressure, so the water density is varied during the pressure cycles which can vary the background scattering. Also, defects in the diamond window can vary the background. Furthermore, no background subtraction was done for the analysis of the pressure cell samples because the low resolution (given by scattering of the water in the pressure cell chamber[221]) and varied background created more errors in the gaussian fit for the peak positions.

The SAXS d-spacing of the results shown in table 6.1 and the repeat in figure 8.4, for the larger d-spacing (indicated by arrows in figure 8.4), were compared (figure 8.5) for the reproducibility of the results and for the effects on the bilayer separation after FT for increasing levels of glycerol (0-7.5 wt%). In terms of reproducibility, aside from the

different sample environments, where the original results were in the pressure cell and the repeat were in the capillary holder, the d-spacing follows a similar trend.

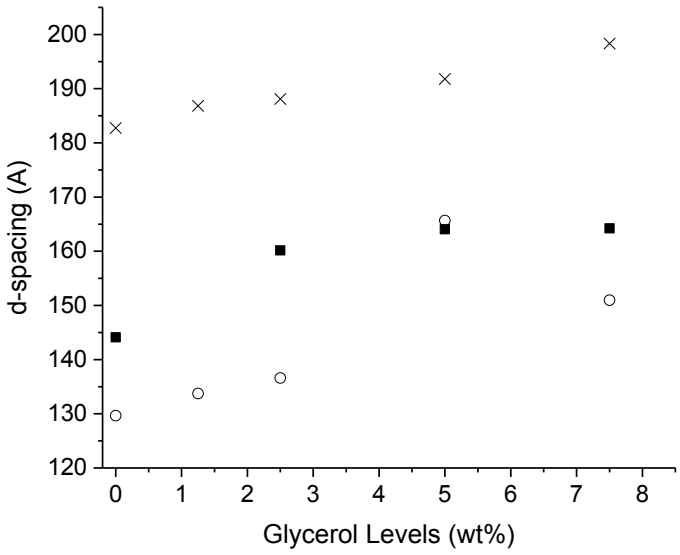


Figure 8.5. Shows the change in the SAXS d-spacing with increasing levels of glycerol at 25 °C; (■) before FT and the repeat for (o) before FT and (x) after FT. For the repeat experiment, the plot is of the larger d-spacing from the uneven swelling shown in figure 8.4. The accuracy of the SAXS lamellar fitting is ± 6 Å.

The behaviour of the DODAC bilayers upon FT, was previously assumed to have a decrease in the difference between the bilayers separation before and after FT. This is proven (see figure 8.5) by the percentage increase in the d-spacings from before to after FT which reduces from a 40 % (at 1.25 wt% glycerol) to a 16 % (at 5 wt% glycerol) increase. The swelling of the bilayers due to glycerol addition show no changes to the hexagonal packing (table 8.3), where the WAXS d-spacing of the gel peak at 25 °C decreases by only 0.01 Å from 0 to 1.25 wt% glycerol. However, after FT, there is a slightly greater decrease of ~0.03 Å between before and after FT for a DODAC solution containing glycerol, where small variations in the WAXS d-spacings are due to changes in the short-range interactions between the amphiphiles. So, there is a possible increase

in attraction between the DODAC monomers after FT which may be an increase in packing from vesicle fusion and/or lower curvature (ie larger vesicles).

Glycerol Levels (wt%)	WAXS Gel Peak (Å)	WAXS Gel Peak FT (Å)	Gel Peak Width (1×10^{-3} Å)	Gel Peak Width FT (1×10^{-3} Å)
0	4.17	4.17	2.5	2.5
1.25	4.16	4.13	2.6	3.1
2.50	4.16	4.13	2.7	3.2
5.00	4.16	4.13	2.9	3.1
7.50	4.16	4.14	2.8	3.1

Table 8.3. Shows the WAXS d-spacing (accuracy of WAXS gaussian fit, ± 1 x 10^{-3} Å) and gel peak width (accuracy of the WAXS width gaussian fitting is ± 2 x 10^{-4} Å) associated with the SAXS d-spacing shown in figure 8.4 of the results given by (o) before FT and (x) after FT for increasing levels of glycerol at 25 ^{o}C.

8.2.2. The Effects of $C_{12\text{-}14}(EO)_{10}$ (CAE10) Upon FT

The effects of CAE10 on the DODAC bilayers was shown (table 6.2) to cause swelling of the bilayers as CAE10 is incorporated into the bilayers, then a lateral phase separation from an increase in micellar domains with increasing CAE10 levels (figure 8.6). The interaction between CAE10 and the DODAC bilayers has been shown (figure 6.7) as a 28 % increase in the bulk water diffusion rate after FT, for a DODAC solution containing 5 wt% CAE10. However, this favourable increase in bulk water diffusion rate (after FT) is due to reconstruction of the lamellar phase (before FT) into a different lamellar structure which is more robust against the FT induced swelling.

The integrated SAXS patterns for a DODAC solution containing CAE10 is shown for before FT in figure 8.7a (as seen in figure 6.8) and after FT in figure 8.7b, which shows the increasing lateral order in the lamellar phase through the change in the Braggs peaks

(see section 2.5.2) from diffused to sharp peaks. In chapter 6, the spherical→planar bilayers transition was shown to take place (before FT) for a DODAC solution containing 1.4 wt% CAE10 (see figure 8.7a). This was indicated by a 90 % increase in the SAXS d-spacings, for increasing CAE10 levels of 1.0 to 1.4 wt% (table 6.2). Also, by the two lamellar reflexions present in the integrated SAXS patterns for a DODAC solution containing 1.4 wt% CAE10 (see figures 8.7a).

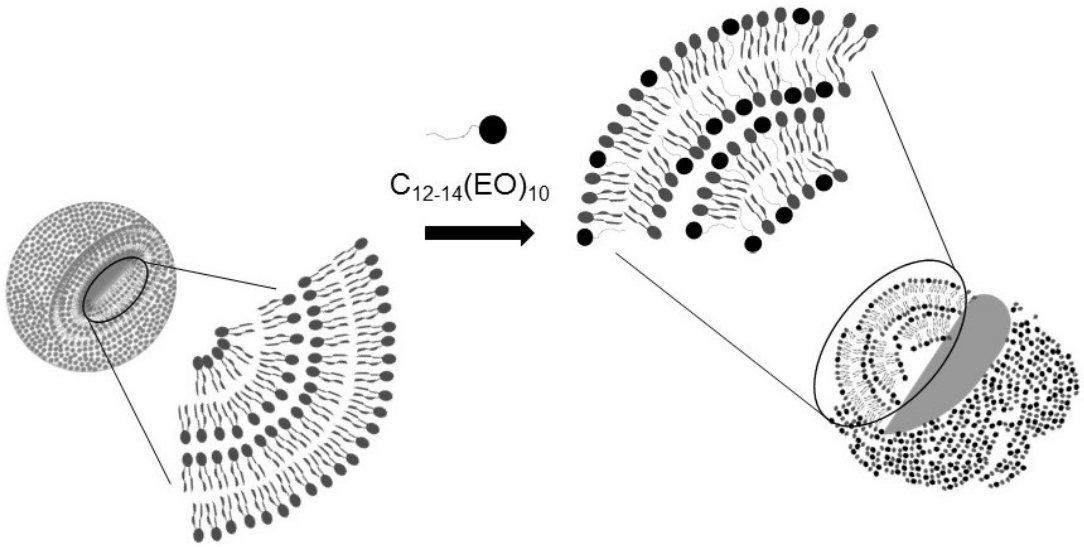


Figure 8.6. Shows a schematic for the changes to the DODAC bilayer from the addition of the CAE10. The single "tail" surfactant increases positive curvature and disrupts the negative curvature of the DODAC bilayers.

After FT, the assumption for a FT induced mixing of CAE10 and DODAC surfactants was made based on the behaviour of the bulk water diffusion of a DODAC solution containing 1.0 wt% CAE10 (figure 6.7) which increased by 78 % after FT. This resulted in a bulk water diffusion rate that is almost twice as fast as the bulk water diffusion rate for the planar bilayers solution at 5.0 wt% CAE10, after FT. So, it was purposed that FT induced mixing of a DODAC solution containing 1.0 wt% CAE10 formed a less uniform solution of fragmented bilayers as opposed to a uniform solution of planar bilayers (for 5.0 wt% CAE10). Furthermore, as expected, the different mechanisms of mixing, ie FT induced

mixing and mixing above the chain melting transition temperature (initial preparation), result in different structures for the DODAC/CAE10 bilayers from early CAE10 incorporation or different conformations of the large CAE10 surfactant “head” group.

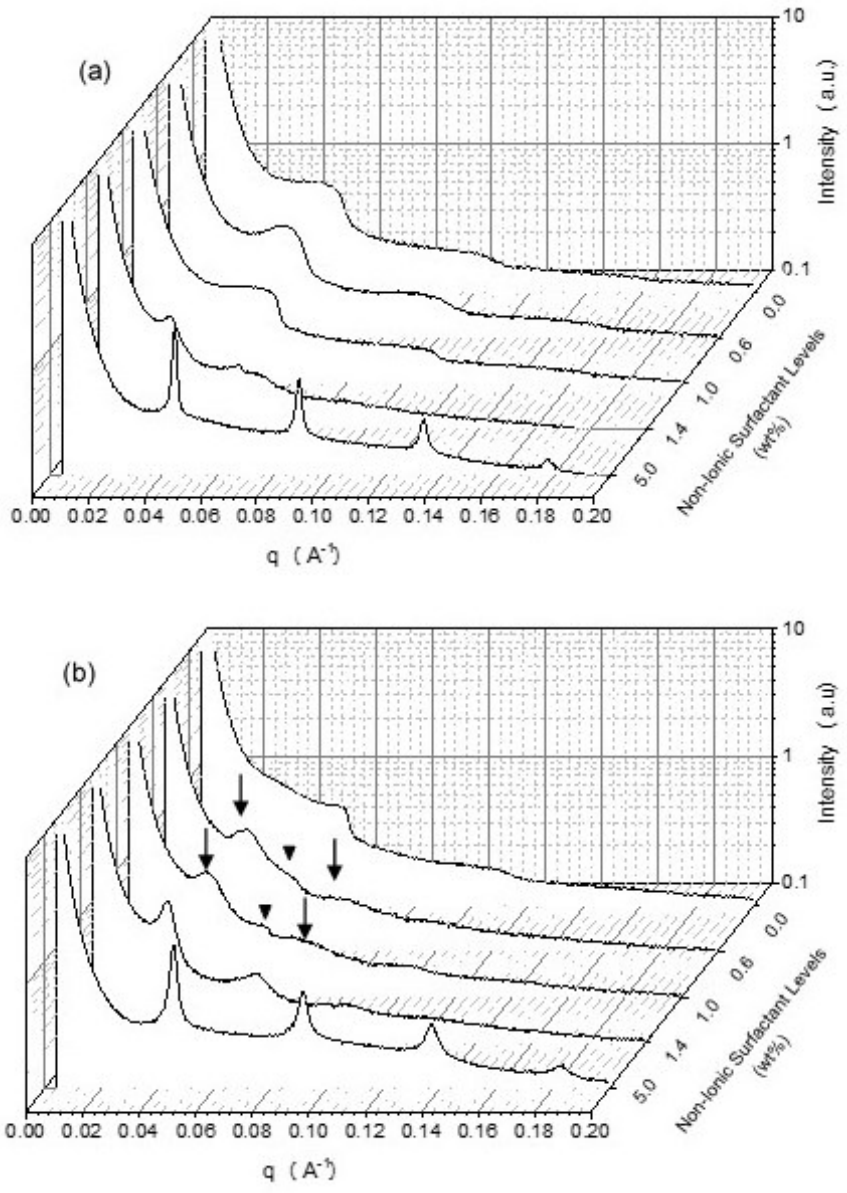


Figure 8.7. Shows the integrated SAXS patterns for the DODAC solutions containing 0, 0.6, 1.0, 1.4 and 5.0 wt% CAE10 at 25 ^{o}C for (a) before (taken from figure 6.8) and (b) after FT. There is an increase in structural order after FT and for increasing levels of non-ionic surfactant. The uneven swelling is shown for a DODAC solution containing 0.6 and 1.0 wt% CAE10, where the larger bilayers separation is shown by the arrows and the smaller bilayers separation is shown by the arrow heads.

The FT induced mixing is shown by the uneven swelling of the bilayers indicated (arrows in figure 8.7b) by the larger lamellar d-spacings which is due to CAE10 incorporation into the DODAC bilayers after FT, for a DODAC solution containing 0.6 and 1.0 wt% CAE10. In comparison to before FT, where there is no uneven swelling (figure 8.7a). Also, after FT, there is a linear increase of 25 Å per wt% in the SAXS d-spacings between DODAC solutions containing 0.6-1.4 wt% CAE10. This linear increase in the SAXS d-spacings is due to increasing levels of incorporated CAE10 into the DODAC bilayers which supports an FT induced mixing.

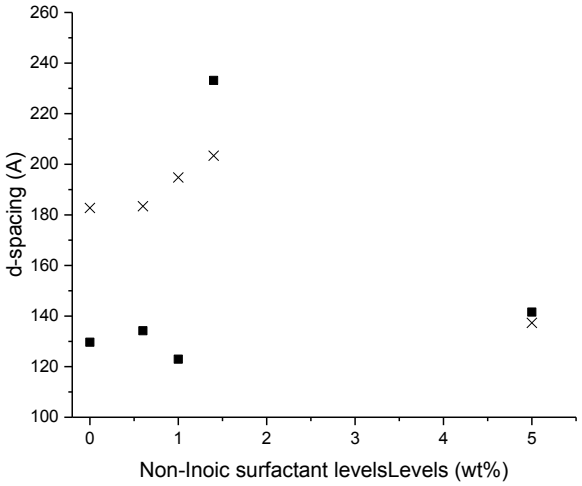


Figure 8.8. Shows the changes to the SAXS d-spacing (accuracy of the SAXS lamellar fit, ± 5 Å), based on the integrated SAXS patterns in figure 8.7 at 25 ^{o}C, with increasing levels of non-ionic surfactant for (■) before and (x) after FT for the larger d-spacings shown in figure 8.7 indicated by the arrows.

As mentioned, the assumption of structures for the DODAC solutions with CAE10 levels less than 1.4 wt% was that they form fragmented bilayers after FT. However, the uneven swelling of the bilayers for a DODAC solution containing 1.0 and 0.6 wt% CAE10 (figure

8.7b), suggest a solution of DODAC vesicles with an uneven distribution of CAE10 surfactants between the bilayers and vesicles. So, the FT induced mixing of CAE10 and DODAC surfactants do not induce the spherical→planar bilayers transition if the CAE10/DODAC ratio is too low and the increase in bulk water diffusion rate after FT for a DODAC solution containing 1.0 wt% CAE10 (figure 6.7b) could be due to the conformation for the ethoxylated "head" group of the CAE10 surfactant.

The behaviour of CAE10 within the bilayers is governed by the conformation of the large ethoxylated "head" group which can either tether to the surface of the DODAC bilayers or extend into the aqueous phase (mentioned in section 6.2). The former will decrease the permeability of the bilayers and decrease the interactions between the bilayers and water phase and the latter will increase steric repulsion between bilayers and vesicles. These will both result in a solution that behaves more "fluid like", so between tethering and extension of the ethoxylated "head" group there will be a varying effect on the bulk water diffusion rate which will have a general increase in the diffusion rate.

CAE10 Levels (wt%)	**WAXS Gel Peak (Å)**	**WAXS Gel Peak FT (Å)**	**Gel Peak Width (1 x 10-3 Å)**	**Gel Peak Width FT (1 x 10^{-3} Å)**
0	4.17	4.17	2.5	2.5
0.6	4.15	4.13	2.7	3.0
1.0	4.16	4.13	2.7	2.9
1.4	4.17	4.14	2.4	2.6
5.0	4.15	4.13	2.0	2.4

Table 8.4. Lists the WAXS gel peak width (accuracy of the WAXS width gaussian fitting is ± 2 x 10^{-4} Å) and d-spacing (accuracy of WAXS gaussian fit, ± 1 x 10^{-3} Å) for increasing levels of non-ionic surfactant for before and after FT.

The formation of planar bilayers results in a decrease in the bilayer separation after FT instead of the general behaviour of increasing bilayers separation (figure 8.8). This is shown by a 13 and 3 % decrease between the SAXS d-spacing before and after FT for a DODAC solution containing 1.4 and 5.0 wt% CAE10, respectively, showing no changes to the DODAC solution containing 5.0 wt% CAE10. These bilayers give three different water environments after FT (see figure 6.7b), suggesting that the holes formed from CAE10 incorporation causes vesicles to fuse together into a single giant multilamellar vesicle which retains the bulk, interlamellar and core water environments. Conversely, the three water environments could be due to bilayer stacks with closed ends and instead of a single bulk water environment, there are bound water environments (water interacting with surfactant head groups) and water between the closely stacked bilayers as well as a bulk water phase.

The robustness of the planar bilayers (upon FT) is because of decreased permeability from the CAE10 incorporation which is due to tethering of the ethoxylated “head” group as opposed to extension of the “head” group. This is suggested by a 39 % decrease in the SAXS d-spacing between the DODAC solutions containing 1.4 and 5.0 wt% CAE10 before FT. Therefore, tethering of the ethoxylate group could act as a support for the DODAC bilayers after the initial dehydration during the $L_{\alpha} \rightarrow L_{\beta'}$ transition and throughout the FT process. So, the incorporation of CAE10 into the DODAC bilayers can protect against the suggested freezing injury (that leads to lateral phase separation or defects/holes within the bilayers), by increasing bilayer interaction and decreasing migration of water between the different water environments. Also, more importantly (in terms of LFE’s function), a bulk water diffusion rate is either constant or faster after FT for the DODAC/CAE10 bilayers.

8.3. The Low Temperature Effects on a DODAC/$CaCl_2$ System

The behaviour of an aqueous DODAC solution was studied for the effects upon FT, where the results showed; a decrease in the bulk water self-diffusion rate (figures 6.6 & 6.7), a temperature shift from ~31 to 35 ^oC of the f→g transition upon cooling without the presence of $CaCl_2$ in the DODAC aqueous solution (figure 5.2), the stability of the g→g' transition across multiple FT cycles for a DODAC solution containing $CaCl_2$ (table 8.2), a decrease in polydispersity and lamellae (table 7.2) and an increase in the bilayer separation with no changed to the hexagonal packing (figure 4.6) which is stable over multiple FT cycles for a DODAC solution containing 0.085 wt% $CaCl_2$ (table 8.1). These outcomes are based on the FT behaviour of the DODAC solutions which was predicted by the general behaviour of the bilayers upon freezing and the effects upon thawing in the lamellar phase (see section 1.7.1).

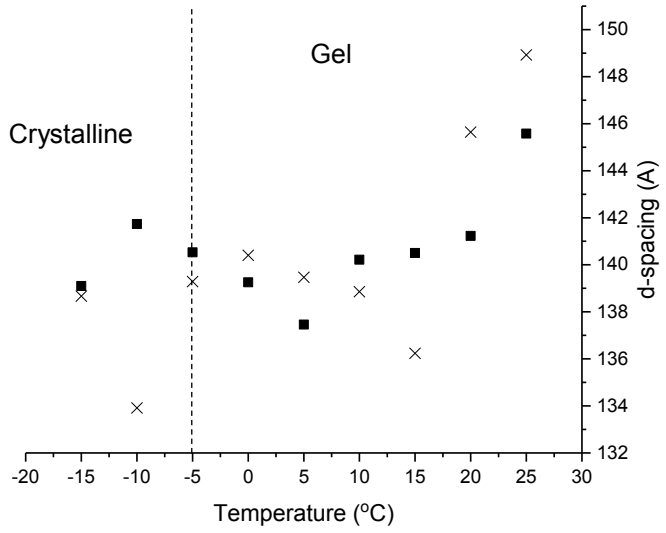


Figure 8.9. Shows the change in d-spacing with temperature of a DODAC solution containing 0.085 wt% $CaCl_2$, during (■) cooling and (x) heating. The temperature was varied between 25 and -18 ^oC at a rate of 5.0 $^oCmin^{-1}$. The mixture begins to form ice crystals at -5.0 ^oC (as shown in figure 8.10a). The accuracy of the SAXS lamellar fit is ± 5 Å.

The freezing mechanism was mentioned (section 1.7.1) to result in a decrease in the bilayers separation due to ice formation in the bulk water phase upon freezing (figure 1.9). Also, it was proposed (end of section 4.3.1) that the initial dehydration takes place during the $L_{\alpha} \rightarrow L_{\beta'}$ transition as the fluctuations of the bilayers reduce. In figure 8.10, nucleation of the crystalline phase begins at -5.0 ^{o}C for a DODAC solution containing 0.085 wt% $CaCl_2$ and continues freezing at -15 ^{o}C based on the intensity of the crystalline scattered rings (see appendix, figures A8.6-A8.10). Also, based on the behaviour of light microscopy under crossed polarised light (figure 8.11), complete crystallisation takes place after incubation at -18 ^{o}C. So, dehydration due to ice formation in the bulk phase would result in a decrease in the d-spacing between 0 and -18 ^{o}C upon cooling. However, the SAXS d-spacing remain constant when cooling from 15 to -18 ^{o}C (figure 8.9). Therefore, the dehydration of the DODAC bilayers takes place during the $L_{\alpha} \rightarrow L_{\beta'}$ phase transition (see figures 4.2, 4.4 & 5.4) and the d-spacing is almost constant with further cooling in the $L_{\beta'}$ phase, showing only an average 1% decrease in the d-spacing (figure 8.9) every -5 ^{o}C when cooling from 25-15 ^{o}C.

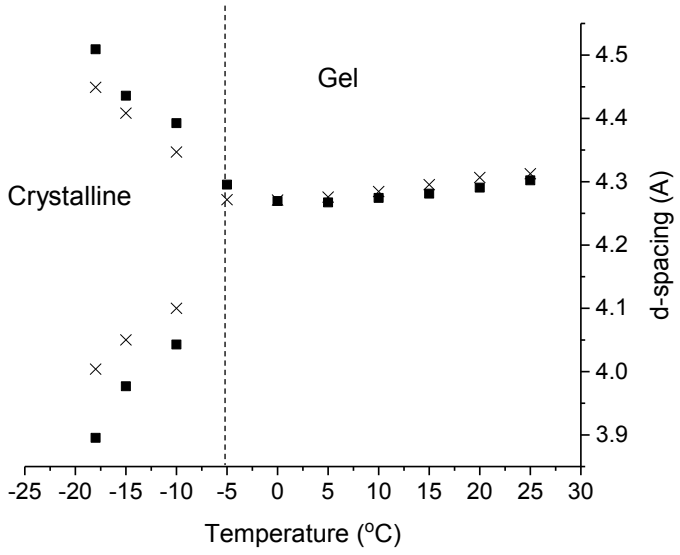


Figure 8.10. Shows the WAXS gel and crystalline peak d-spacing with varied temperature, for (■) cooling and (x) heating. The gel→crystalline transition takes place at -5.0 ^{o}C, show by the introduction of another peak at ~4 Å. The accuracy of the WAXS gaussian fit is ± 1 x 10^{-3} Å.

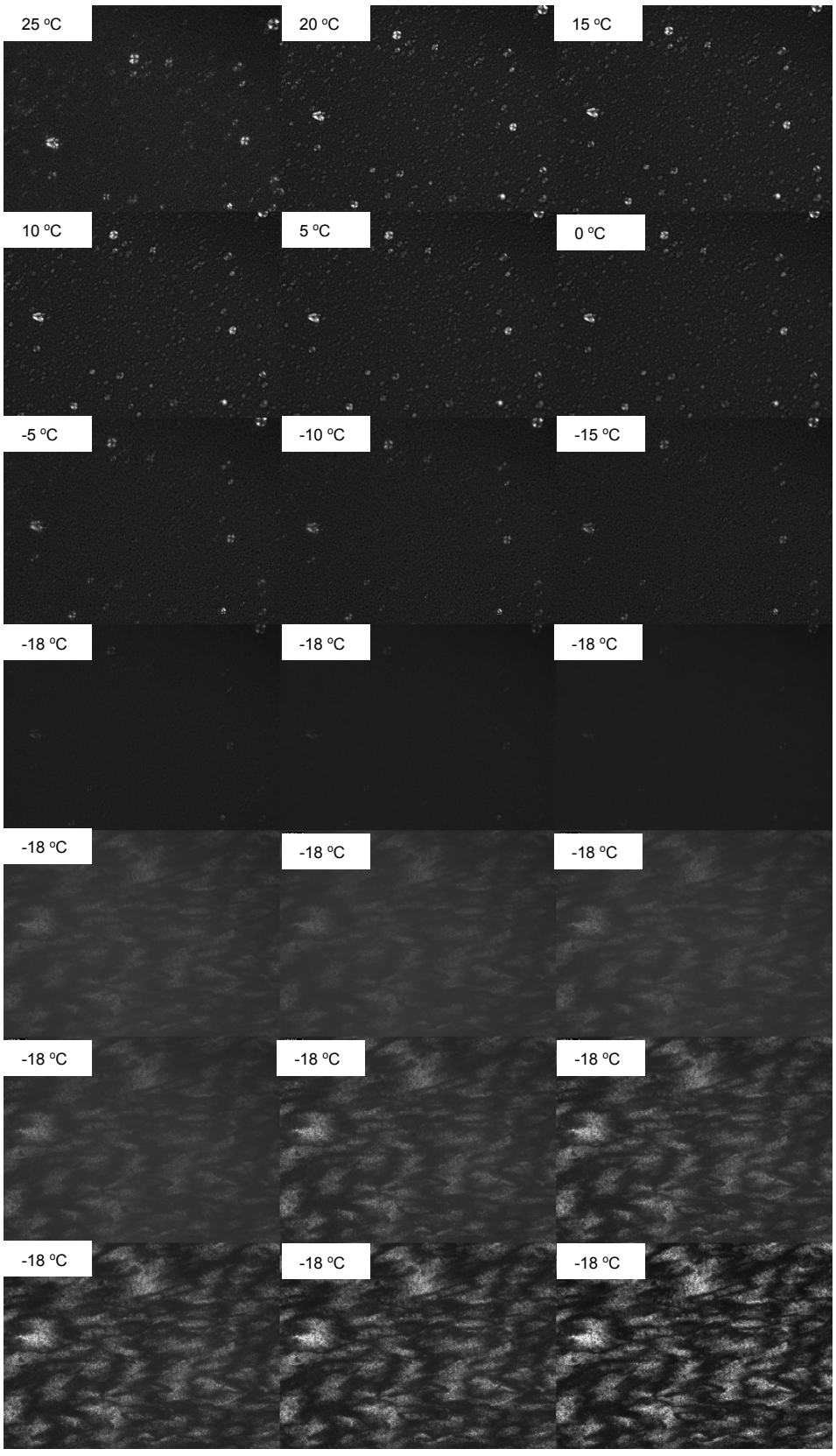


Figure 8.11. Shows the crossed polarised light images of a DODAC solution containing 0.085 wt% $CaCl_2$ for cooling from 25 to -18 °C at 5.0 °Cmin^{-1}, where images were taken every -1.0 °C (see appendix, figure A8.11), shown here for every -5.0 °C and held at -18 °C for 5mins, where the solution crystallises after 1 min.

Upon thawing, the assumed behaviour of a lamellar phase was a swelling induced lysis or a lack of osmotic responsiveness (section 1.7.1), where the swelling was apparent in the DODAC aqueous solutions (figures 4.2, 4.4 & 5.4) but the swelling was not assumed to be due to lysis and there was no evidence to the lysis of DODAC vesicles. The behaviour upon thawing is shown in figure 8.9, as an almost constant d-spacing with an average 1 % decrease every 5 ^{o}C, from 0 to 15 ^{o}C. Then a 7 % increase in the d-spacing from 15 to 20 ^{o}C. This increase in d-spacings is the start of the swelling behaviour giving a d-spacing at 25 ^{o}C that is 2 % greater than the bilayers separation before FT. So, the behaviour upon thawing is likely an increase in the bilayers attraction due to a decrease in the "hydration forces" from the lack of osmotic responsiveness after complete dehydration of the bilayers which causes the repulsion between the bilayers and allows aqueous solution into the bilayers[222,223].

There is a 5 % increase in the gel peak d-spacings (figure 8.10) between -5 and -18 ^{o}C, due to lateral separation in the gel phase. This could be the lysis event of the DODAC vesicle or tilting in the bilayers upon freezing. Upon thawing, the bilayers reorganised in a similar (but reverse) fashion as upon freezing, where the d-spacing follows the same 1 % difference in d-spacings every 5 ^{o}C between -5 and -18 ^{o}C, except with a decreasing d-spacing. This behaviour is more likely to be from tilting of the bilayers and so the transition indicated (figure 8.10) may not be due to nucleation of a crystalline phase which took place instantly (figure 8.11) at -18 ^{o}C after incubation.

8.4. The Pressure-Temperature (P/T) Relationship

The temperature and pressure relationship for a DODAC solution of 8 wt% DODAC in an aqueous solution of 0.085 wt% $CaCl_2$, was compared through a series of pressure cycles at 65, 25, 15 and 5.0 ^{o}C (chapter 3), where the relationship between temperature and pressure was determined to be 0.6 kbar for every -10 ^{o}C, but this relationship did

not match between the pressure cycles at 65 and 25 °C. Thus, the direct comparison was made between thermotropic/isobaric and barotropic/isothermal systems for the DODAC solution between 65 and 25 °C at atmospheric pressure and between 0.001-4 kbar at 65 °C, respectively (chapter 4).

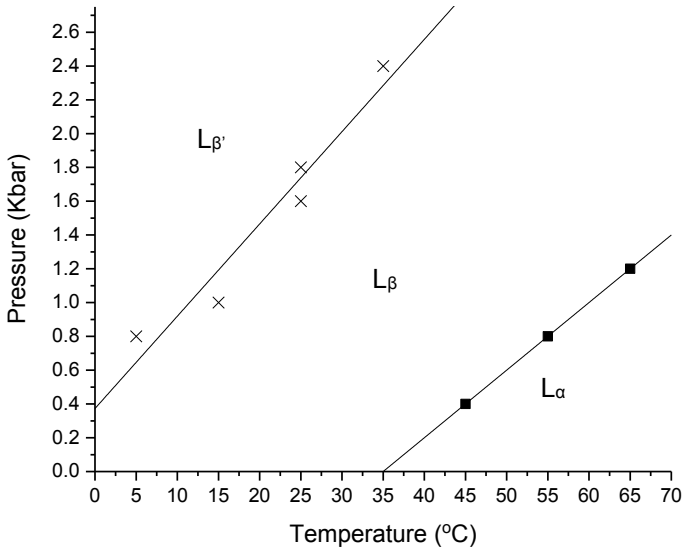


Figure 8.12. Shows the transition pressure at various temperatures for the main transitions of $L_\alpha \rightarrow L_\beta$ and $L_\beta \rightarrow L_{\beta'}$, where the transitions were determined (figure 3.4), for pressure cycles at 65, 55, 45, 35, 25, 15 and 5.0 °C. The transition gradient is different for the $L_{\beta'}$ and L_β transition boundary (0.06 kbar/°C) and the L_β and L_α transition boundary (0.04 kbar/°C).

The direct comparison between the transitions induced by pressure and induced by temperature gave different gel phases, shown by the width of the gel peak (figure 4.6), of L_β and $L_{\beta'}$ (or $P_{\beta'}$) phases, respectively. So, the series of pressure cycles were repeated, but between 0.001-3 kbar for temperatures 65, 55, 45, 35 and 25 °C. This is compared to the P/T relationship in figure 3.4 for the pressure which the main transitions took place, showing the phase boundaries (figure 8.12) L_α /L_β, and L_β/$L_{\beta'}$ for increasing pressure (phase assignments made in sections 3.3.1 and 3.3.2). The updated P/T relationship shown (figure 8.12), gives a P/T relationship of 0.04 kbar/°C at the L_α/L_β phase boundary, where the relationship remains constant for pressure cycles between

65 and 35 °C, and a relationship of 0.06 kbar/°C at the $L_{\beta}/L_{\beta'}$ phase boundary, where the relationship is constant between 35 and 5.0 °C. This phase behaviour at the L_{α}/L_{β} boundary agrees with Goto et. al., which uses high-pressure light transmittance and DSC to determine the main transitions of an aqueous DODAC solution, where the relationship is given as 0.23 K/MPa (~0.04 kbar/°C)[224].

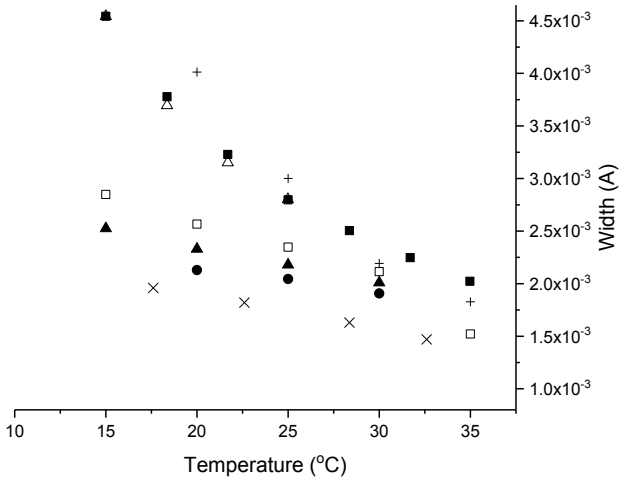


Figure 8.13. Show the WAXS gel peak width for pressure cycles at; (●) 65, (▲) 55, (□) 45, (■) 35 and (Δ) 25 °C compared to the gel peak widths for the pressure cycle at 65 °C (x) and temperature cycle at atmospheric pressure (+) shown in figure 4.6. The results for each pressure cycle were converted to temperature based on the new P/T relationship in figure 8.12. The accuracy of the gaussian fitting for the gel peak width is ± 2 x 10^{-4} Å.

The P/T behaviour was used to compare the width of the WAXS gel peak for the pressure cycles between 0.001-3 kbar at 65, 55, 45, 35 and 25 °C. This comparison includes the results given in figure 4.6, for the gel peak width of the pressure cycle between 0.001-4 kbar at 65 °C and the temperature cycle between 65-20 °C at atmospheric pressure (figure 8.12). These results gave the same $L_{\beta'}$ (or $P_{\beta'}$) gel phase for the temperature cycle at atmospheric pressure and the pressure cycles at 25 and 35 °C. Also, the same L_{β} gel

phase was given for the pressure cycles at 45, 55, 65 and 65 (repeat) ^{o}C. Therefore, the new P/T relationship is correct between 65 and 25 ^{o}C.

The temperature and the pressure induced transitions were assumed to behave differently at the L_{β}/L_{c} boundary, but it was shown in figure 8.10 that both mechanisms result in tilting of the bilayers instead of a L_{c} phase. This behaviour is compared directly (figure 8.14) by the low temperature WAXS results (shown in figure 8.10) and the high pressure WAXS results (shown in figure 3.4) using the P/T relationship (given in figure 8.12), where the trend of the gel peak d-spacing remains the same between the two mechanisms from 25 to 0 ^{o}C. The L_{β}/L_{c} phase boundary lies at ~ -2.0 ^{o}C for a pressure induced transition and between 0 and -5.0 ^{o}C for a temperature induced transition, suggesting that the L_{β}/L_{c} phase boundary is in fact ~ -2.0 ^{o}C.

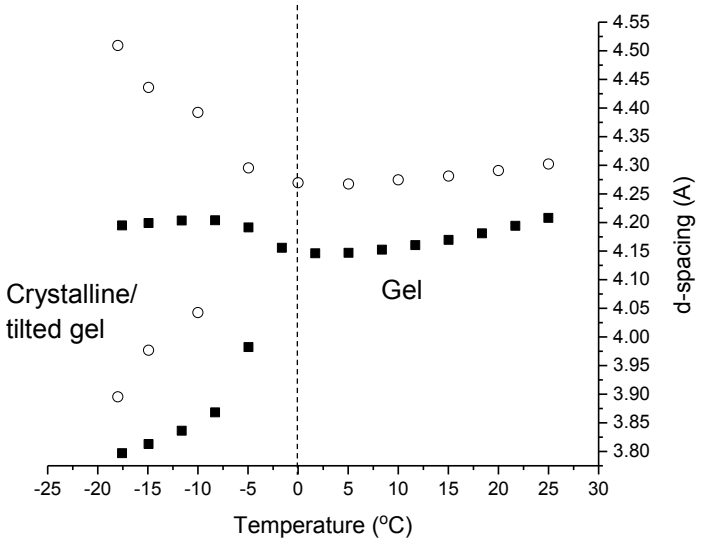


Figure 8.14. Shows the WAXS gel peak d-spacing for the temperature induced freezing (o), as shown in figure 8.10, and the high-pressure phase behaviour (■) of a DODAC solution containing 0.085 wt% $CaCl_2$, where the pressure results were converted using the P/T relationship at 25 ^{o}C of 0.04 kbar/^{o}C shown in figure 8.12. The accuracy of the WAXS gaussian fit is ± 1 x 10^{-3} Å.

Below the phase boundary (< -2.0 °C), the gel peak d-spacing (figure 8.14) for a pressure-controlled system (■) increases by 1 % between -2.0 and -8.0 °C, then reduces by 0.2 % from -8.0 to -18 °C, where the reduction in d-spacing is parallel to the reduction of the second d-spacing that appears below -2.0 °C. Conversely, the temperature-controlled system (o, figure 8.14) increases by 5 % from -5 to -18 °C, as the second d-spacing (introduced at -10 °C) decreases by 4 % for an 8 °C decrease. This behaviour of the WAXS d-spacing is shown as Y-transitions by Tenchov et. al.[225] for the freezing sub-phases SGII and L_{R1}, where the former is bilayers tilted with respect to normal bilayers and the latter is normal bilayers. For the L_{R1} phase, the distortion in the WAXS gel peak is due to a orthorhombic packing (as opposed to the distorted hexagonal packing of tilted bilayers, see figure 2.8) and depends on the interaction/packing of the alkyl chains[137].

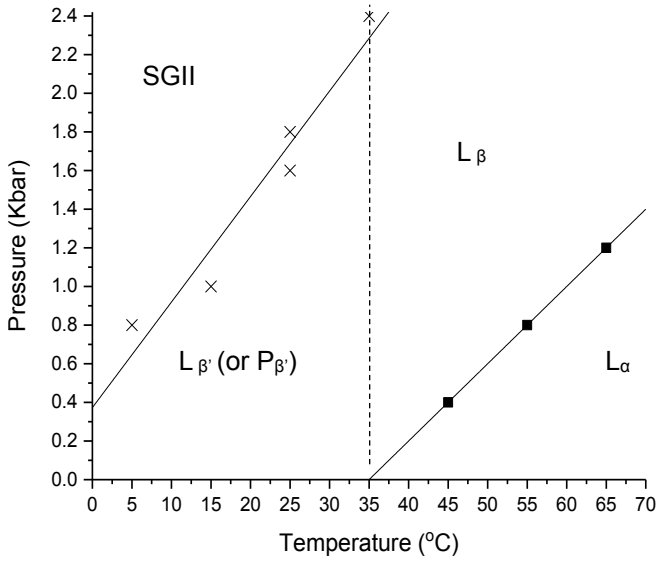


Figure 8.15. Shows the updated phase diagram of a DODAC solution containing 8wt% DODAC in an aqueous solution of 0.085 wt% $CaCl_2$, based on the results given in figures 8.12, 8.13 and 8.14, and the conclusions made in section 4.4.

The L_{R1} and SGII phases are formed upon freezing from the L_{β} or $L_{\beta'}$ phases, respectively, and are metastable in the sense that further cooling results in the L_c transition but upon heating (from the L_c phase), the SGII and L_{R1} phases do not form. The initial conclusion for the pressure-controlled system was for a $L_{\beta} \rightarrow L_{\beta'}$ transition with increasing pressure, but the distortion in the WAXS gel peak can be due to an arrangement of the alkyl chains that is not tilting with respect to the normal bilayers upon freezing. However, the new results given in figure 8.13, shows that the pressure-controlled system resides in the $L_{\beta'}$ phase under isothermal conditions at 35 and 25 ^{o}C. So, based on the maximum pressure used in this study and the isothermal temperature that resulted in a frozen sub-phase, the high-pressure phase behaviour (at a calculated temperature of -2 ^{o}C) is related to a $L_{\beta'} \rightarrow$SGII phase transition.

The temperature-controlled system was discussed (end of section 8.3) from the results given in figure 8.10, to also result in a freeze induced tilting. Therefore, both the pressure- and temperature-controlled systems result in a freeze induced tilting of the DODAC bilayers. Though, the degree of tilting is greater for a temperature-controlled system and the rate of tilting is faster for a pressure-controlled system (see figure 8.14). This difference in the freeze induced tilting mechanisms (see figure 8.14) for a pressure- and temperature-controlled systems, may be due to the faster equilibration rates of a pressure-controlled DODAC system.

These studies modelled the low temperature behaviour of DODAC in an aqueous solution using high pressure (figure 8.15). However, the uneven swelling in the lamellar phase for a thermotropic/isobaric system that was concluded as a possible $P_{\beta'}$ phase (section 4.3.1), suggests that more information can be gained from additional experiments with an isobaric pressure greater than 1 bar. This will provide more

information on the P/T relationship in the horizontal direction of the graph given in figure 8.15.

9. Appendix

Images for Chapter 3

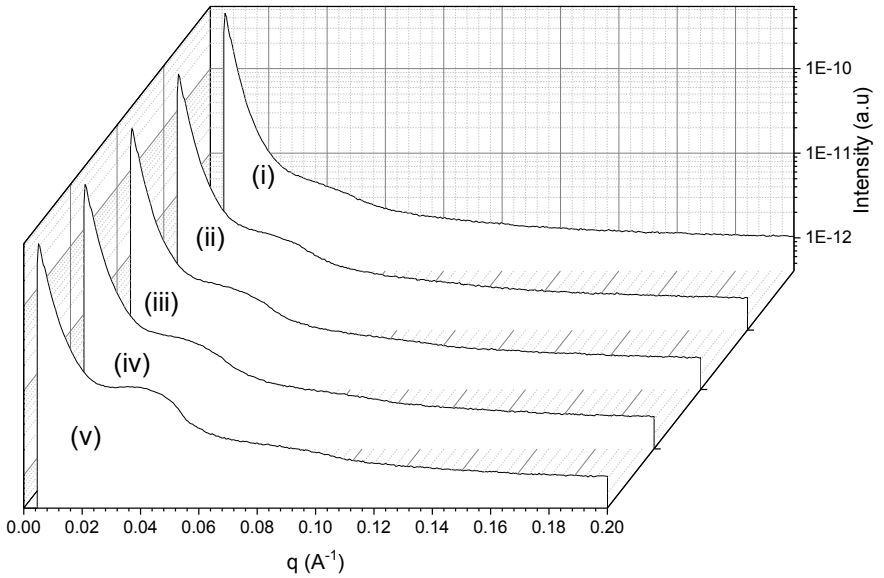


Figure A3.1. Integrated SAXS patterns (obtained July 2017) for a constant temperature of 15 ºC at pressures; (i) 0.001, (ii) 1.0, (iii) 2.0, (iv) 3.0 and (v) 4.0 kbar. The resolution of the SAXS reflections decrease with increasing pressure.

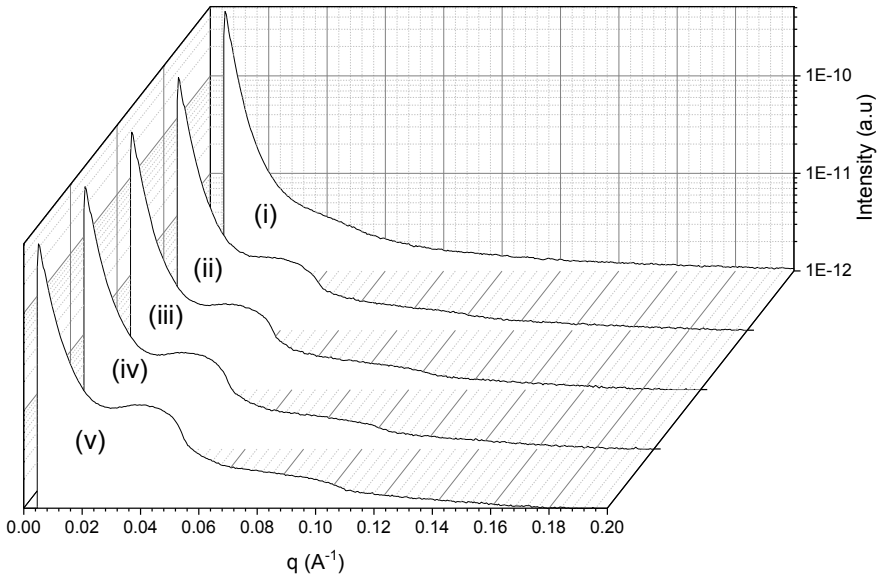


Figure A3.2. Integrated SAXS patterns (obtained July 2017) for a constant temperature of 15 ºC at pressures; (i) 0.001, (ii) 1.0, (iii) 2.0, (iv) 3.0 and (v) 4.0 kbar. The resolution of the SAXS reflections decrease with increasing pressure.

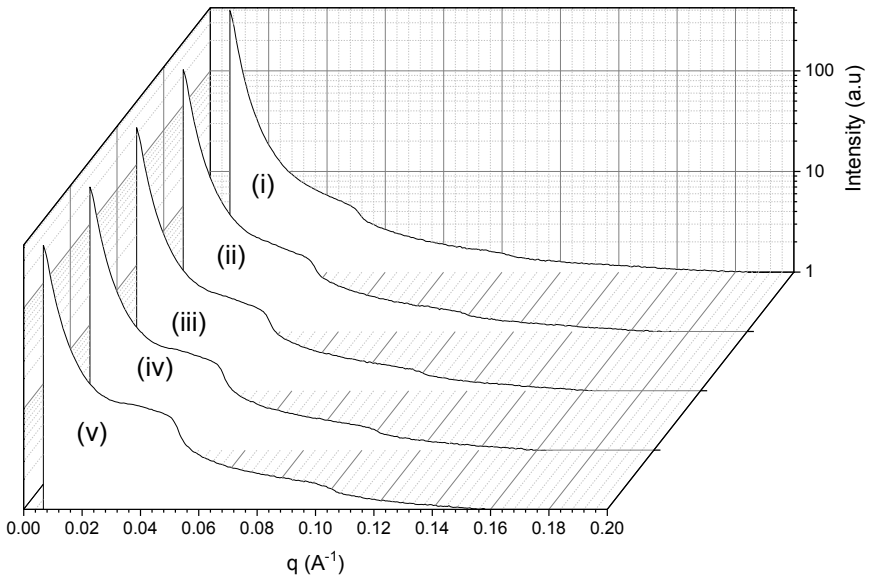


Figure A3.3. Repeat results obtained on November 2017. Integrated SAXS patterns for a constant temperature of 15 ^{o}C at pressures; (i) 0.001, (ii) 1.0, (iii) 2.0, (iv) 3.0 and (v) 4.0 kbar. The resolution of the SAXS reflections decrease with increasing pressure.

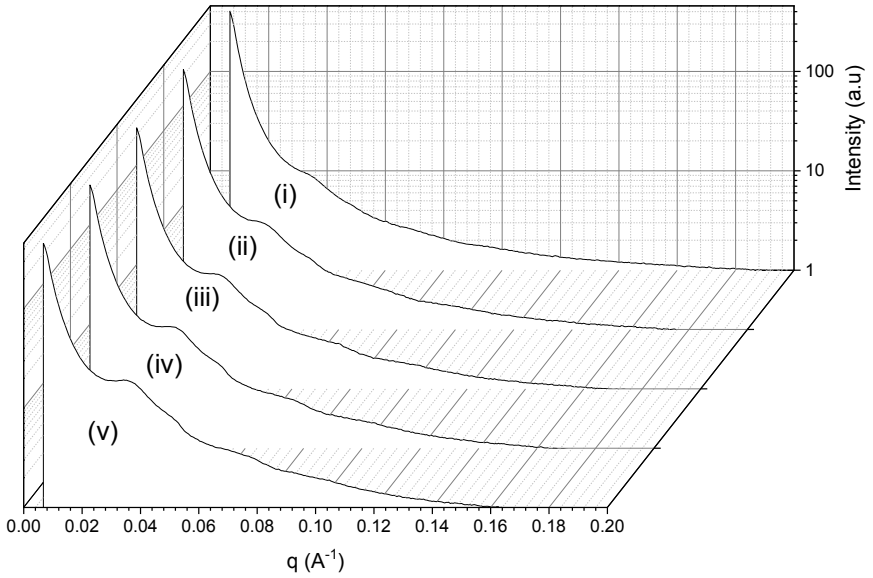


Figure A3.4. Repeat results obtained on November 2017. Integrated SAXS patterns for a constant temperature of 15 ^{o}C after FT at pressures; (i) 0.001, (ii) 1.0, (iii) 2.0, (iv) 3.0 and (v) 4.0 kbar. The resolution of the SAXS reflections decrease with increasing pressure and in comparison, to figure A3.3 before FT.

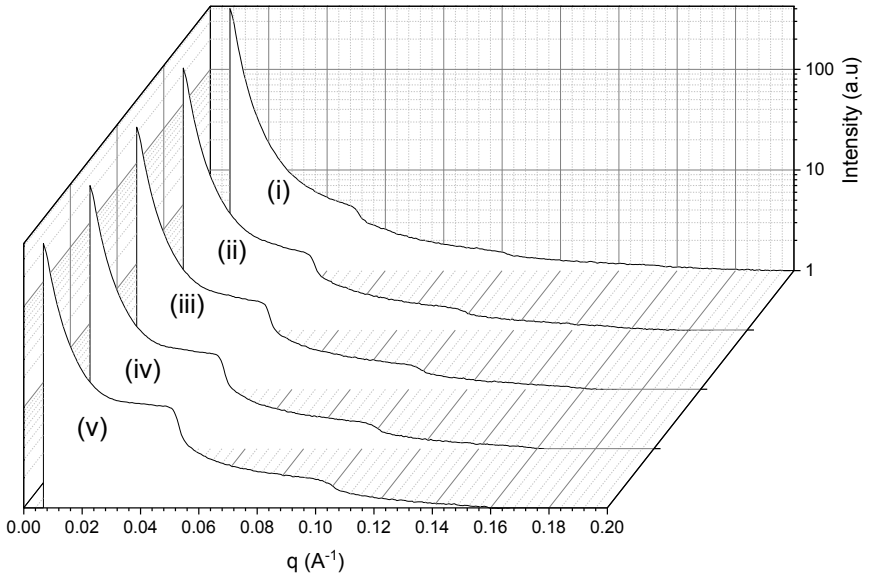


Figure A3.5. Repeat results obtained on November 2017. Integrated SAXS patterns for a constant temperature of 6.3 ºC at pressures; (i) 0.001, (ii) 1.0, (iii) 2.0, (iv) 3.0 and (v) 4.0 kbar. The resolution of the SAXS reflections decrease with increasing pressure.

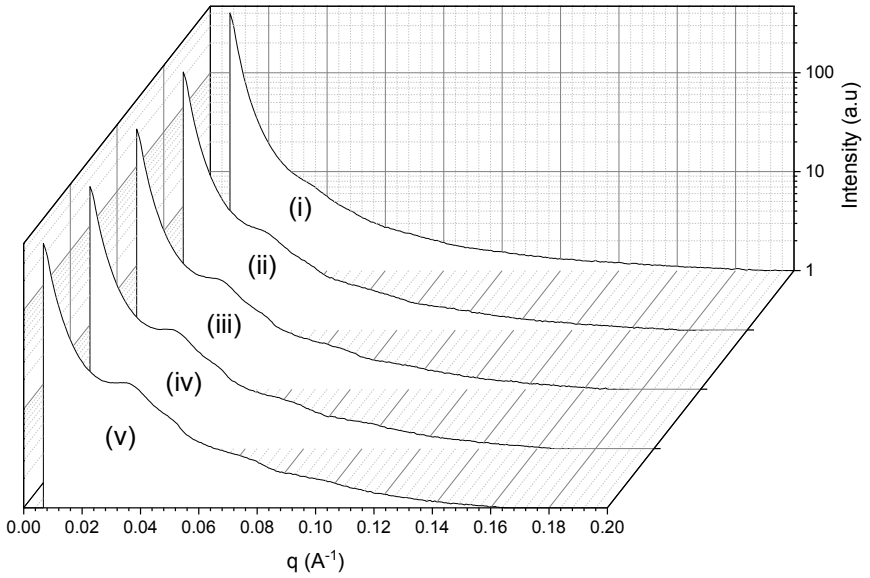


Figure A3.6. Repeat results obtained on November 2017. Integrated SAXS patterns for a constant temperature of 6.3 ºC after FT at pressures; (i) 0.001, (ii) 1.0, (iii) 2.0, (iv) 3.0 and (v) 4.0 kbar. The resolution of the SAXS reflections decrease with increasing pressure and in comparison, to figure A3.3 before FT.

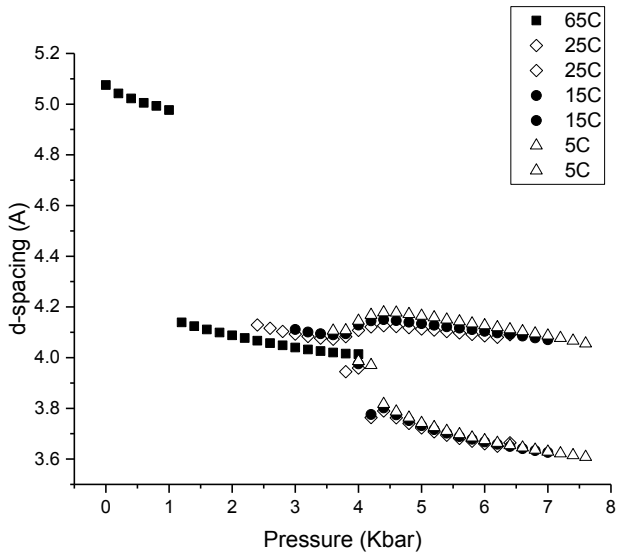


Figure A3.7. Theoretical pressure up cycle repeat (completed Nov 2017) for figure 3.4 (completed in July 2017), of various isothermic barotropic conditions. The L_α/L_β boundary lies between 1.0 – 1.2 kbar and the $L_\beta/L_{\beta'}$ boundary lies between 3.8 – 4.0 kbar.

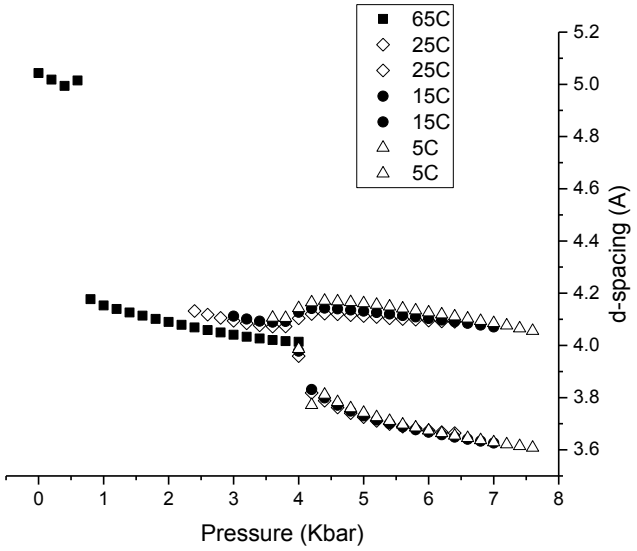


Figure A3.8. Theoretical pressure down cycle repeat (completed Nov 2017) for figure 3.5 (completed in July 2017), of various isothermic barotropic conditions. The L_α/L_β boundary lies between 0.6 – 0.8 kbar and the $L_\beta/L_{\beta'}$ boundary lies between 3.8 – 4.0 kbar.

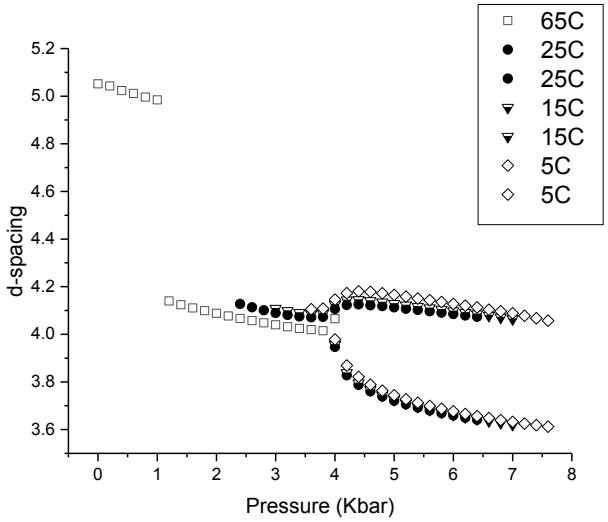


Figure A3.9. Theoretical pressure up cycle comparison at various temperatures of aqueous DODAC solution that was freeze thawed. The L_α and L_β between 1.0-1.2 kbar; the L_β and $L_{\beta'}$ boundary between 3.8-4.0 kbar

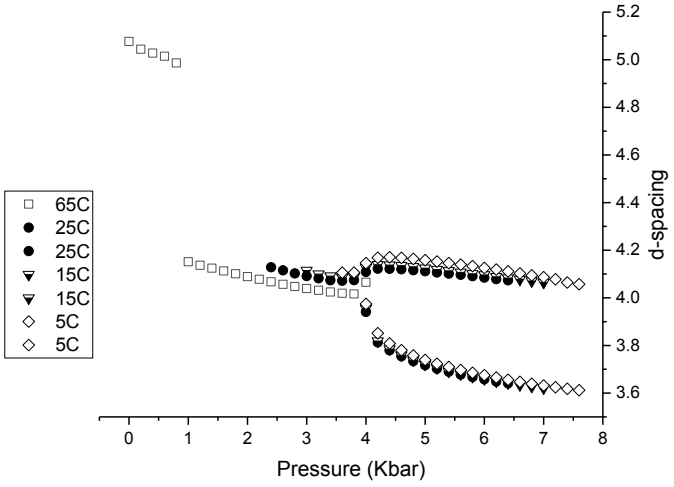


Figure A3.10. Theoretical pressure down cycle comparison at various temperatures of aqueous DODAC solution that was freeze thawed. The L_α and L_β between 1.0-0.8 kbar; the L_β and $L_{\beta'}$ boundary L_β between 3.8-4.0 kbar

Images for Chapter 4

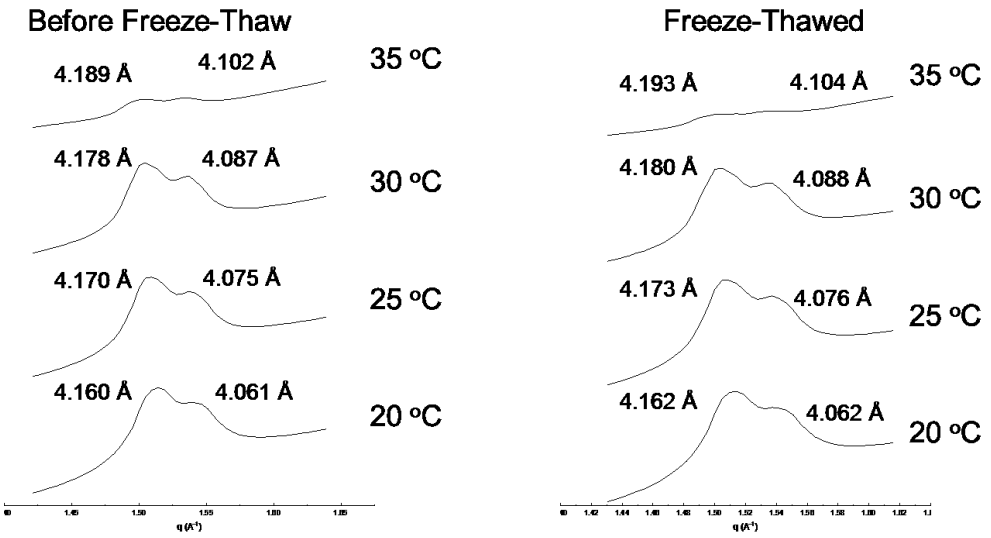


Figure A4.1. WAXS gel peaks for temperature-controlled system

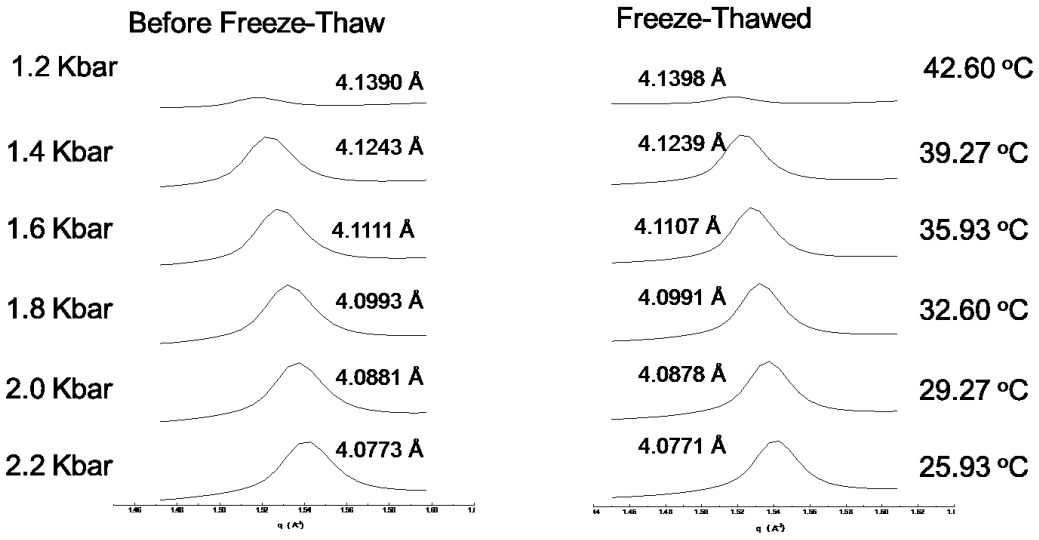


Figure A4.2. WAXS gel peaks for pressure-controlled system

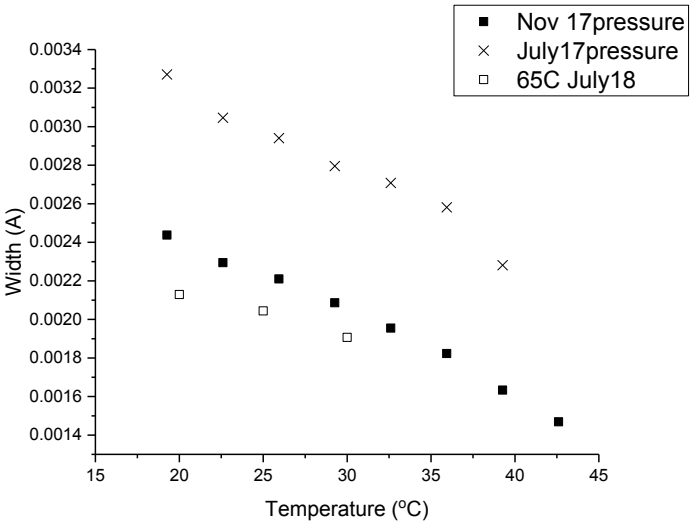


Figure A4.3. Comparison of the gel peak widths for the repeats pressure-controlled systems at 65 °C

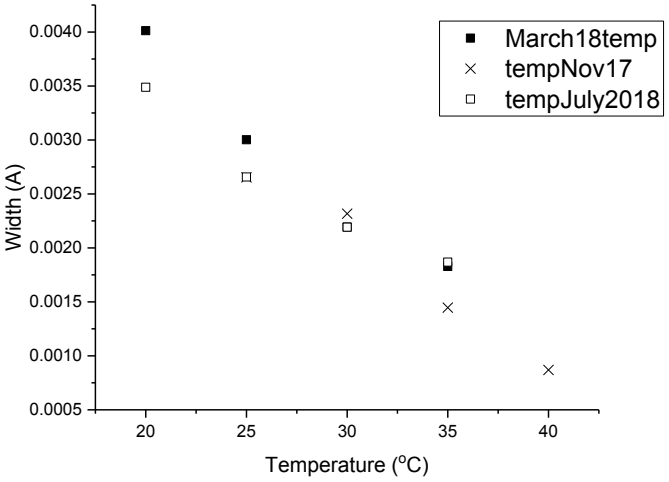


Figure A4.4. Comparison of the gel peak widths for the repeats temperature-controlled systems at atmospheric pressure

Images for Chapter 5

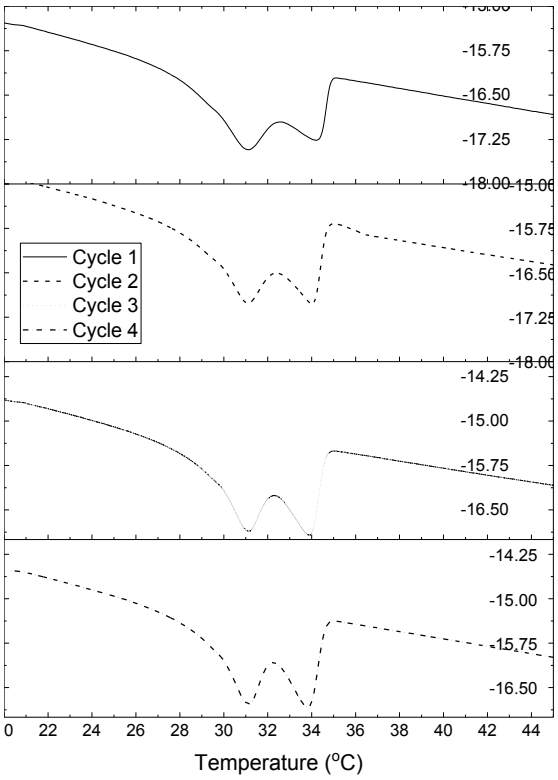


Figure A5.1. Repeat cooling cycles after FT for aqueous DODAC solution centred at chain transition

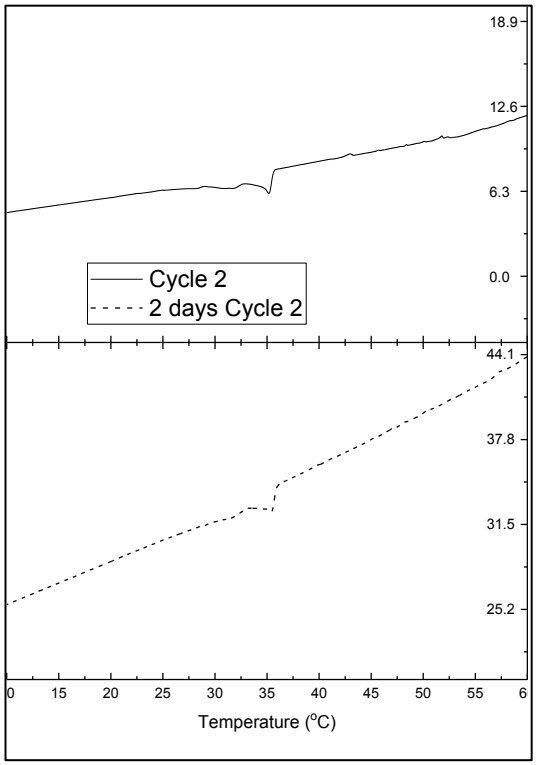


Figure A5.2. Shows stability of the shift in chain melting transition for a DODAC solution containing no $CaCl_2$ after two days of storage

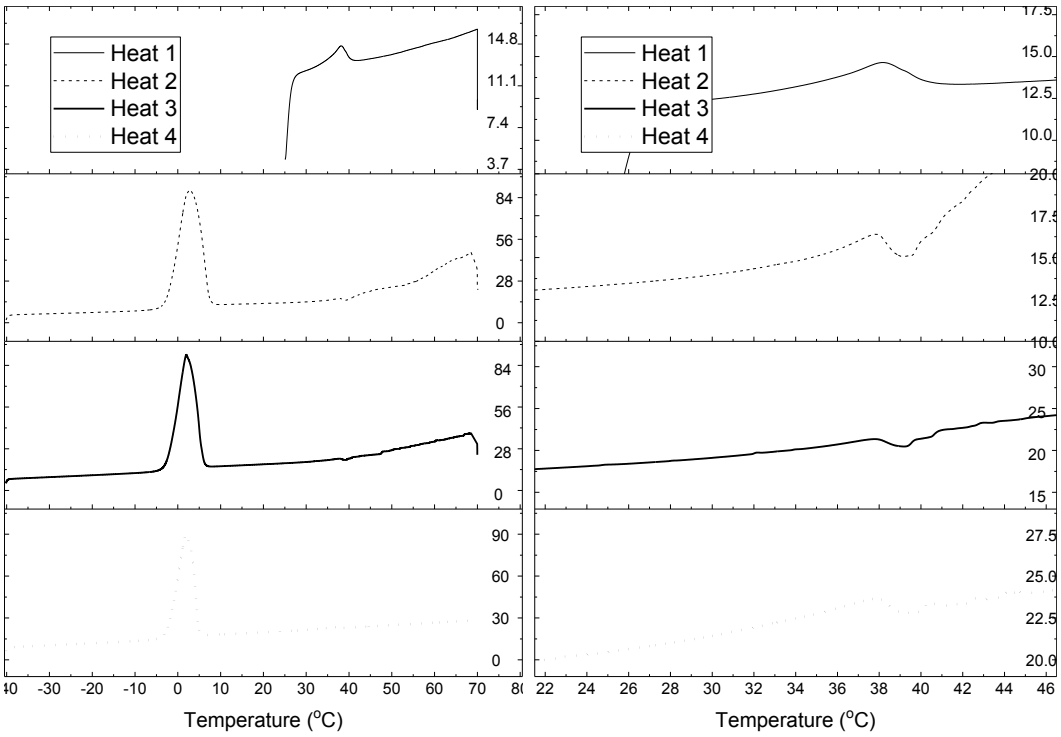


Figure A5.3. Heating thermographs for DODAC solutions containing no $CaCl_2$

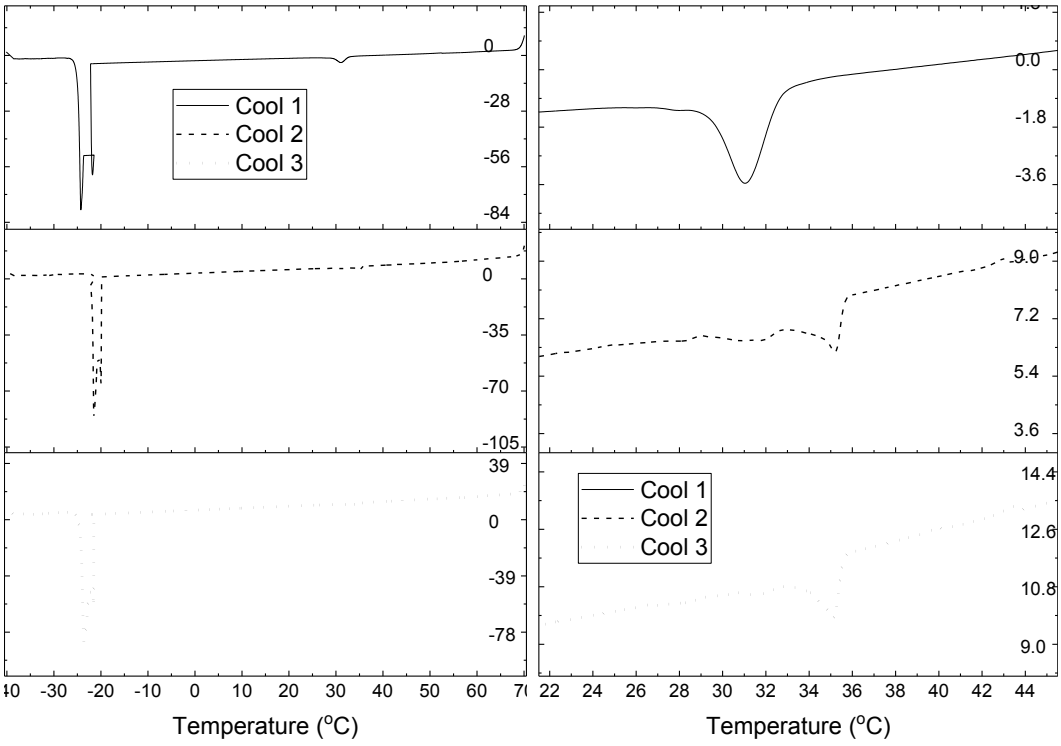


Figure A5.4. Cooling thermographs for DODAC solutions containing no $CaCl_2$

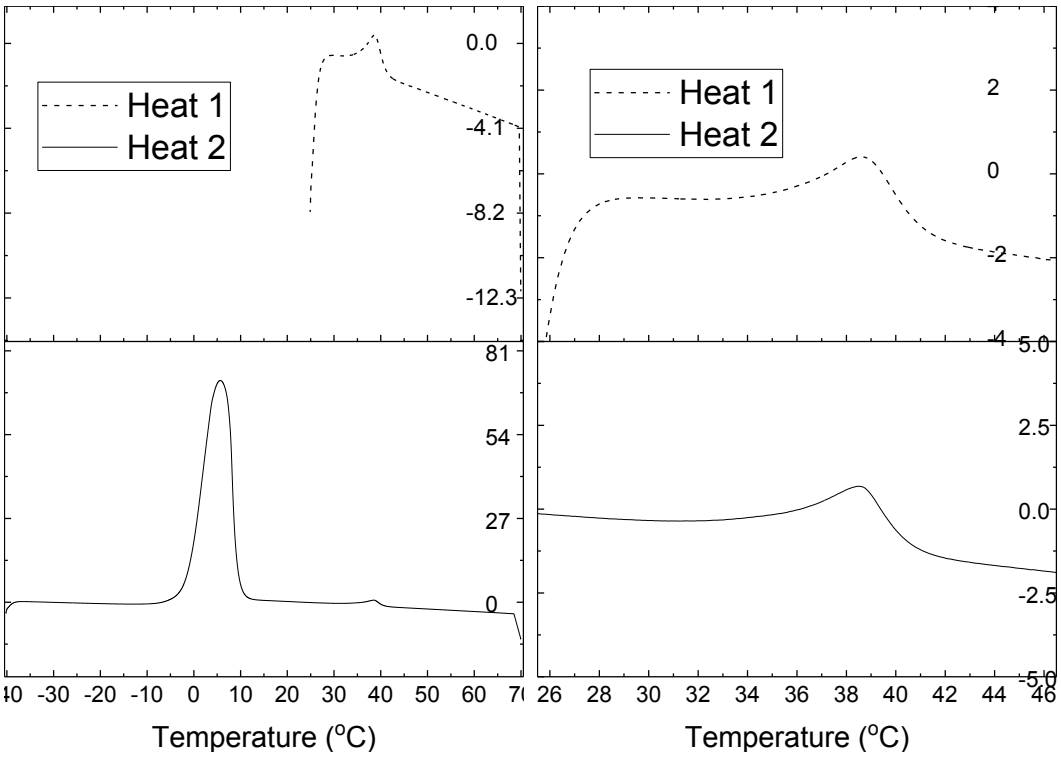


Figure A5.5. Heating thermographs for DODAC solutions containing 0.15 wt% $CaCl_2$

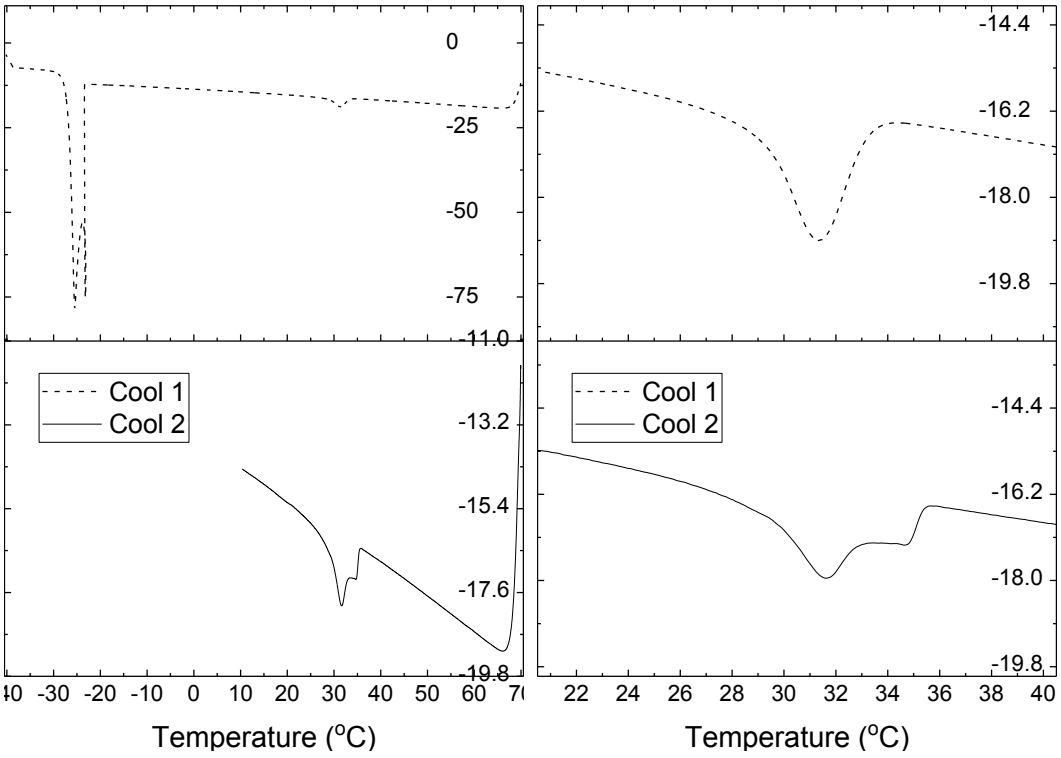


Figure A5.6. Cooling thermographs for DODAC solutions containing 0.15 wt% $CaCl_2$

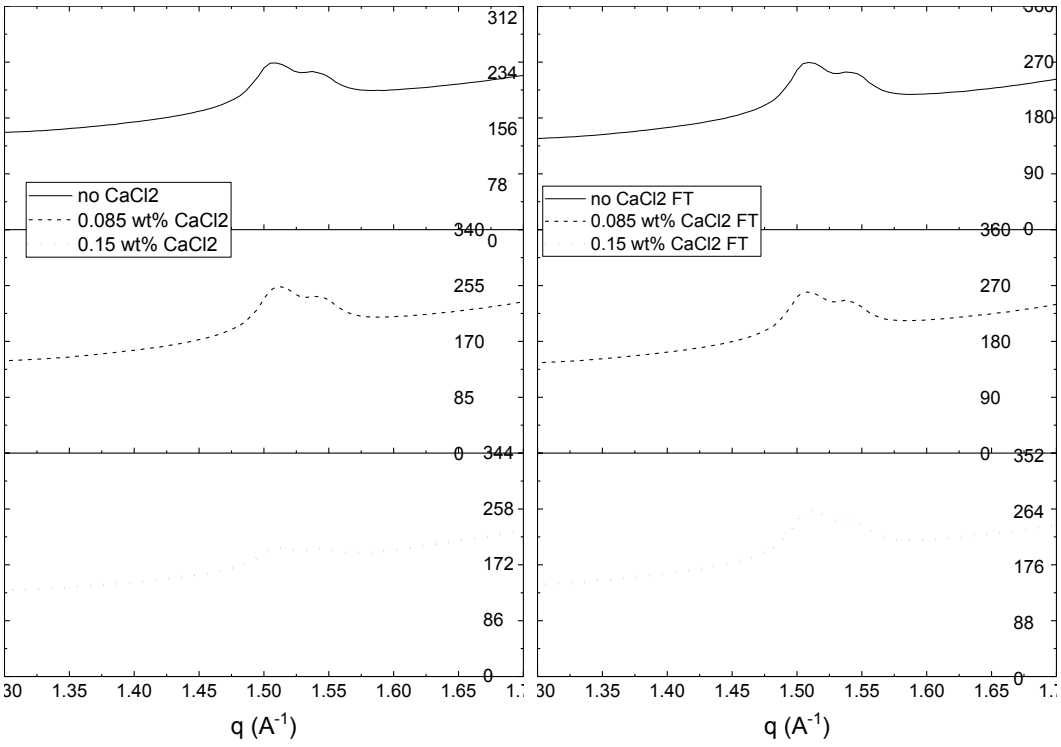


Figure A5.7. WAXS gel peaks as a function CaCl2 levels before and after FT at 25 ºC

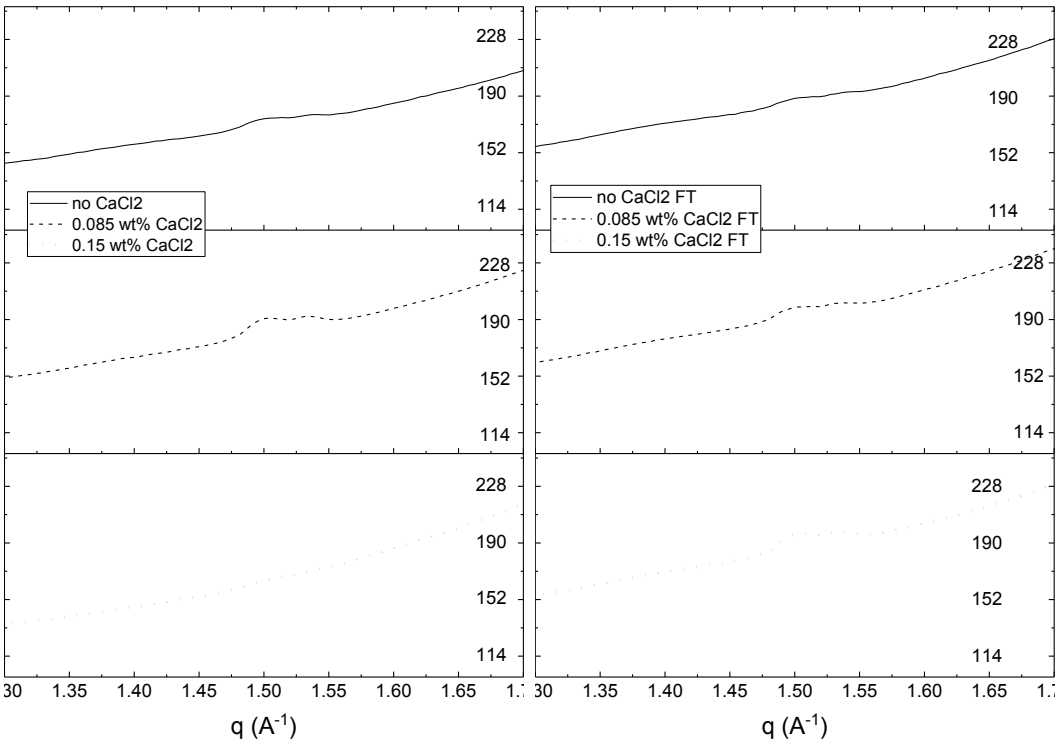


Figure A5.8. WAXS gel peaks as a function CaCl2 levels before and after FT at 35 ºC

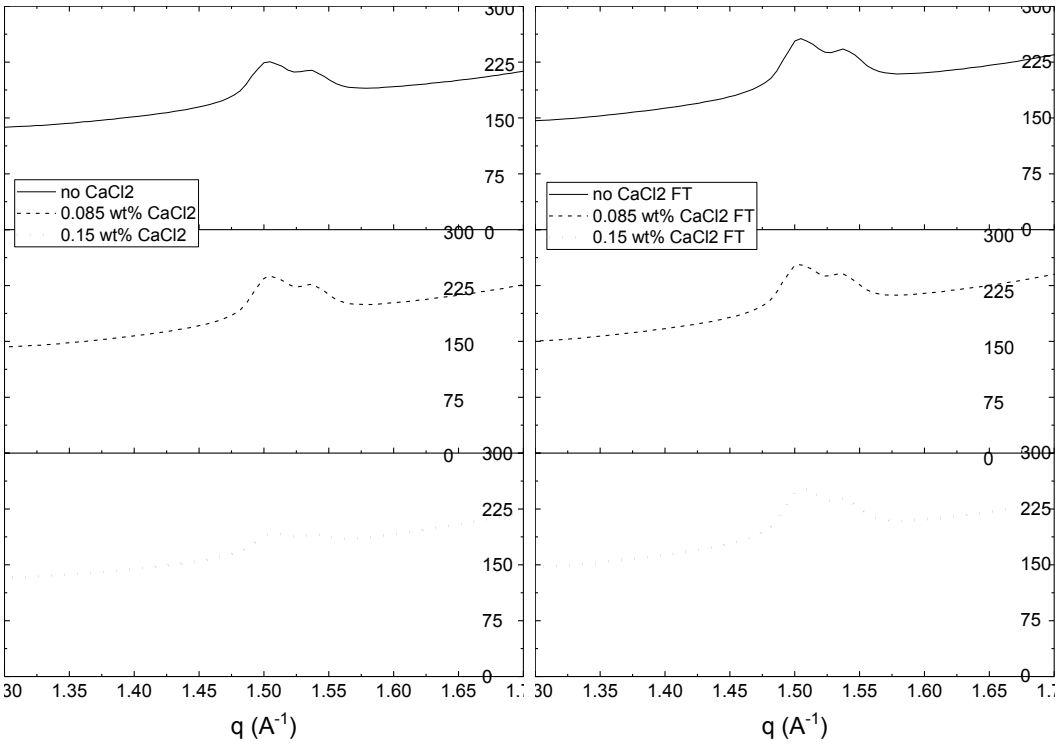


Figure A5. 9. WAXS gel peaks as a function CaCl2 levels before and after FT at 30 ^{o}C

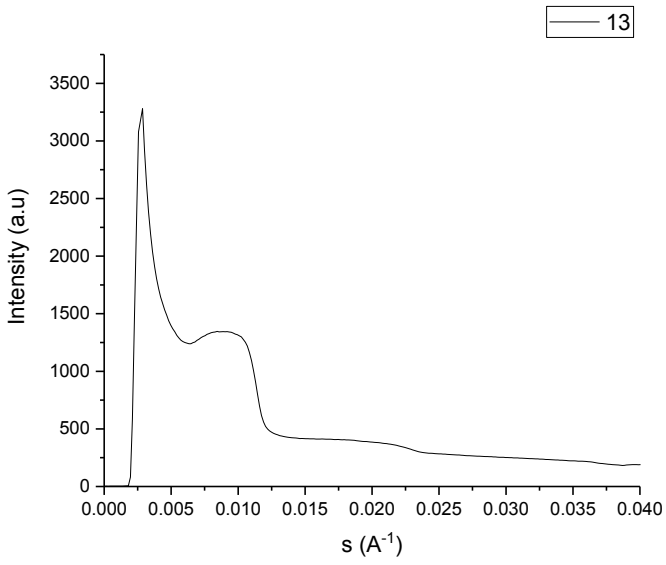


Figure A5.10. Integrated SAXS for 13 wt% DODAC in 0.15 wt% $CaCl_2$ at 25 ^{o}C

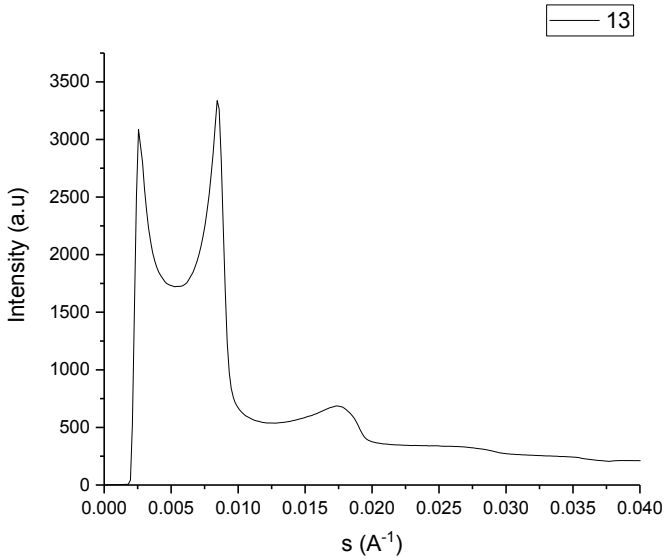


Figure A5.11. Integrated SAXS for 13 wt% DODAC in 0.085 wt% $CaCl_2$ at 25 ^oC

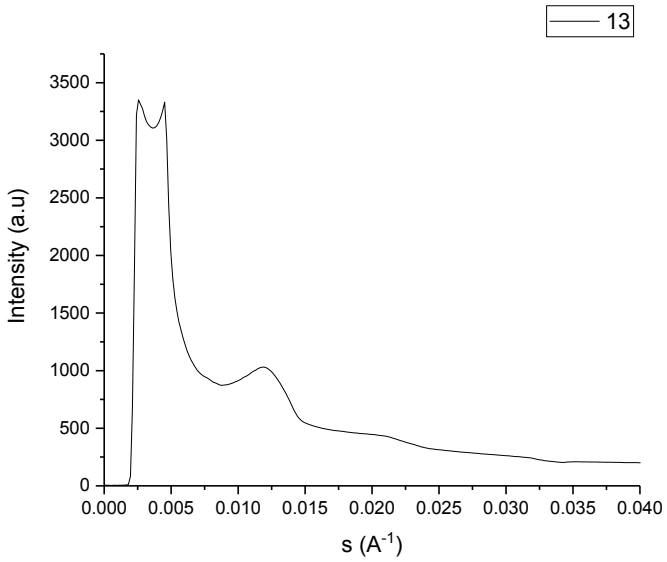


Figure A5.12. Integrated SAXS for 13 wt% DODAC in 0.015 wt% $CaCl_2$ at 25 ^oC

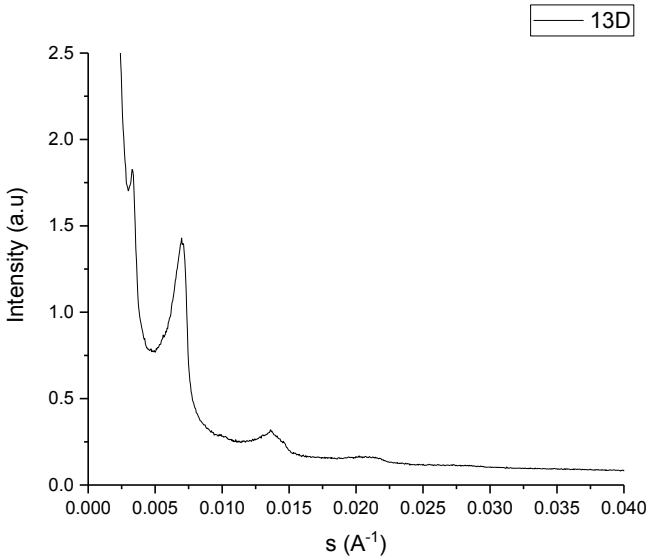


Figure A5.13. Integrated SAXS for 13 wt% DODAC in 0 wt% $CaCl_2$ at 25 ^oC

Images for Chapter 6

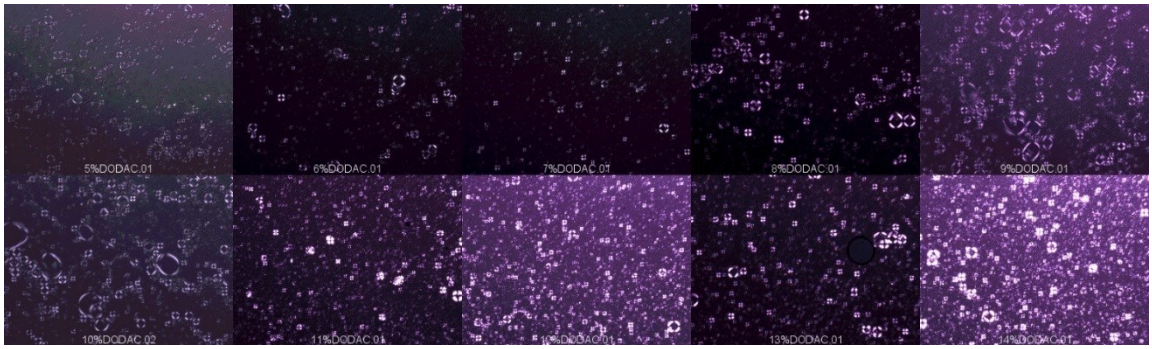


Figure A6.1. All samples containing 0.15 wt% CaCl2 under crossed polarised light at room temperature. Images taken with monochromatic camera and colour filter.

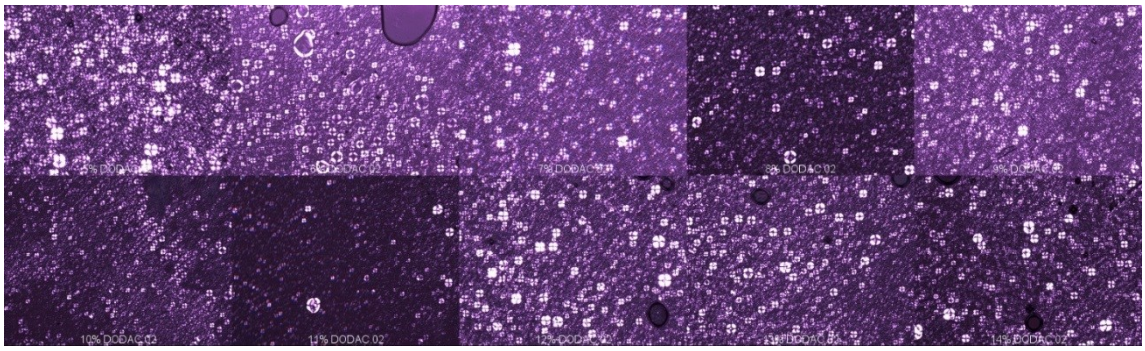


Figure A6.2. All samples containing 0.085 wt% CaCl2 under crossed polarised light at room temperature. Images taken with monochromatic camera and colour filter.

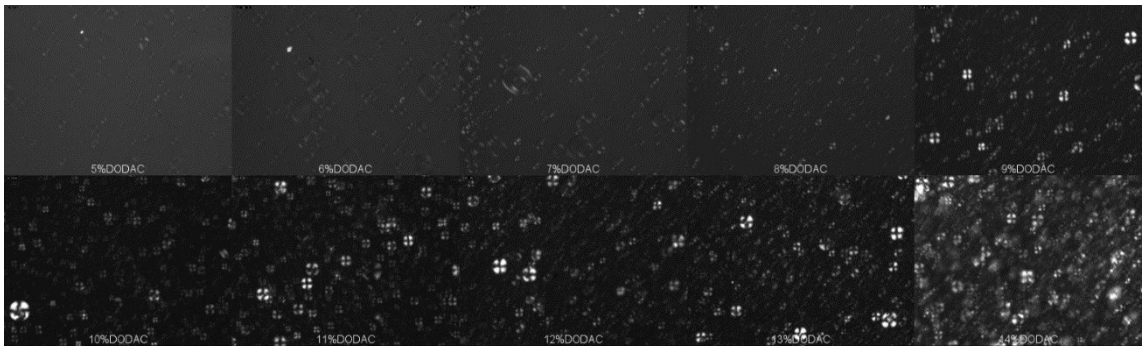


Figure A6.3. All samples containing 0.015 wt% CaCl2 under crossed polarised light at room temperature. Images taken with monochromatic camera.

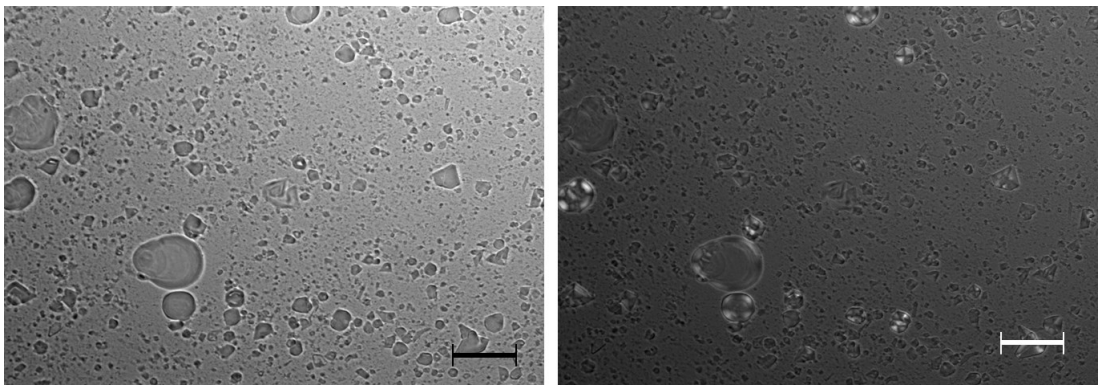


Figure A6.4. Shows 7.5 wt% Glycerol + 8 wt% DODAC in 0.085 wt% CaCl2 aqueous solution 50 um scale

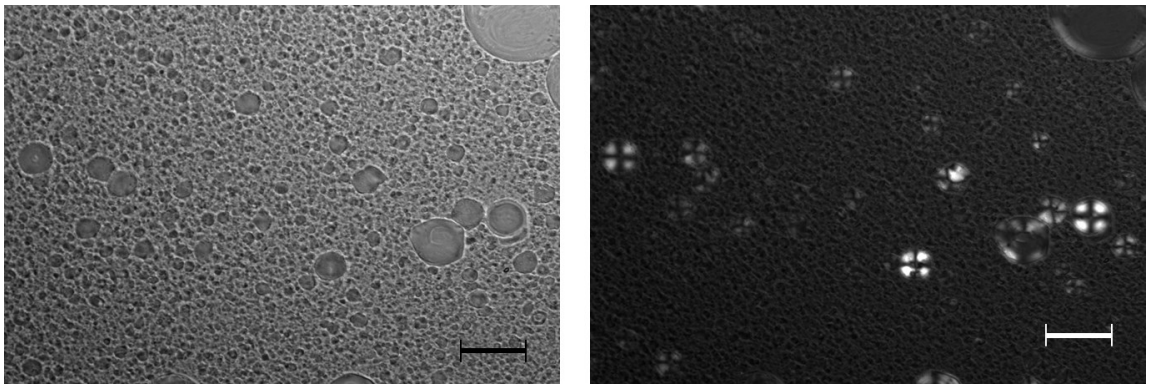


Figure A6.5. Shows 5 wt% Glycerol + 8 wt% DODAC in 0.085 wt% CaCl2 aqueous solution 50 um scale

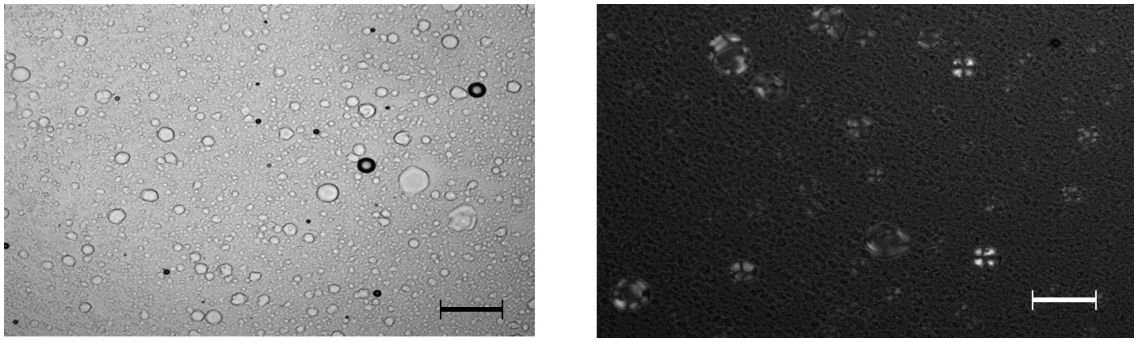


Figure A6.6. Shows 2.5 wt% Glycerol + 8 wt% DODAC in 0.085 wt% CaCl2 aqueous solution 50 um scale

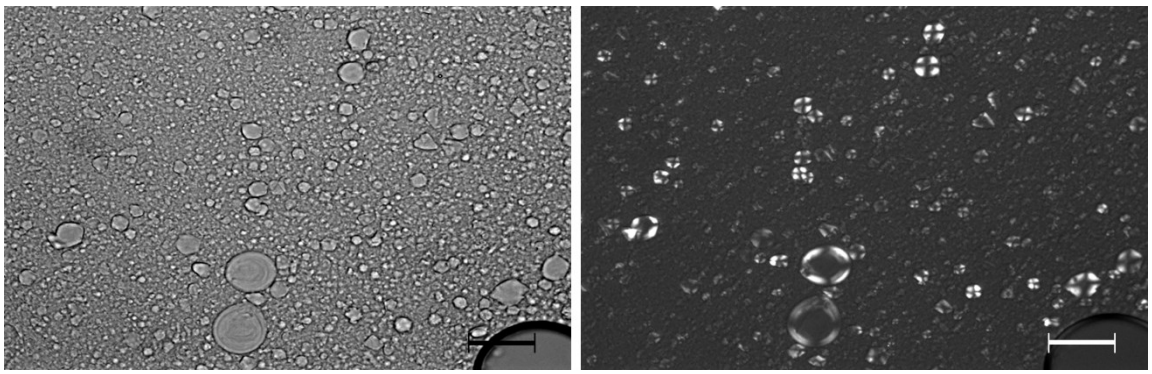


Figure A6.7. Shows 0.2 wt% CAE10 + 8 wt% DODAC in 0.085 wt% CaCl2 aqueous solution 50um scale

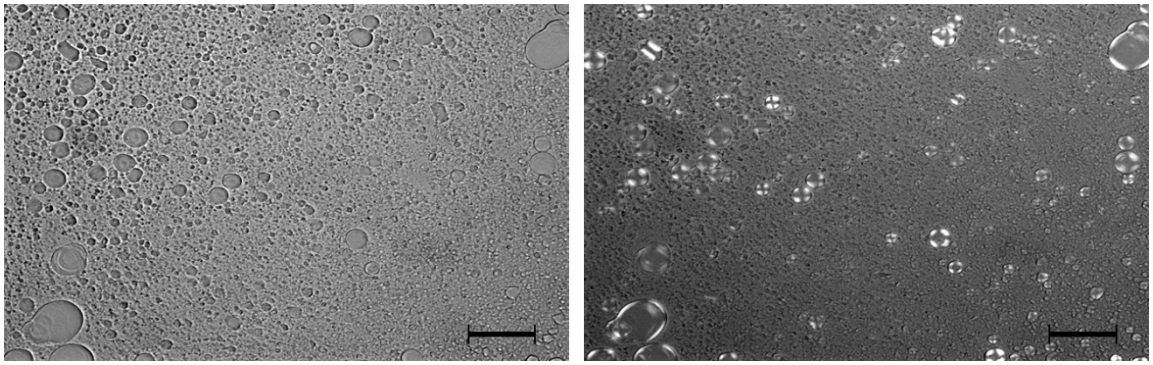


Figure A6.8. Shows 0.6 wt% CAE10 + 8 wt% DODAC in 0.085 wt% CaCl2 aqueous solution 50 µm scale

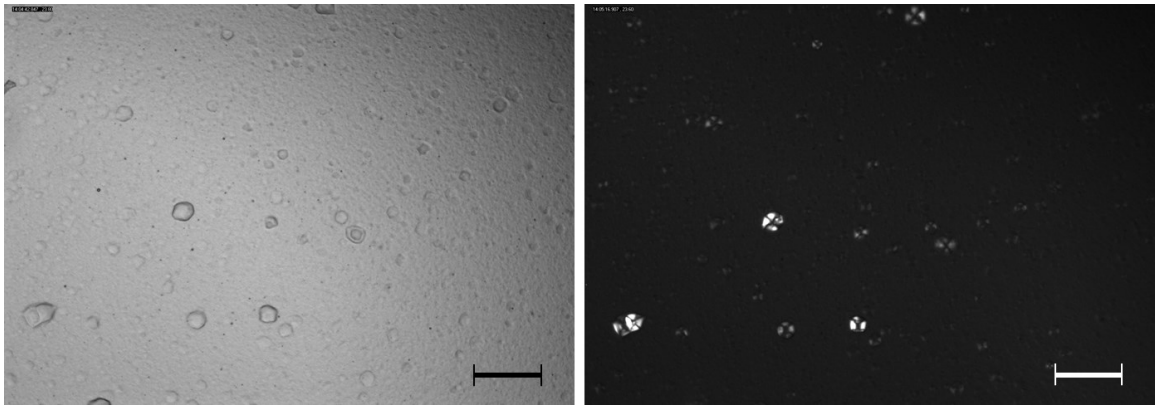


Figure A6.9. Shows 1.4 wt% CAE10 + 8 wt% DODAC in 0.085 wt% CaCl2 aqueous solution 50um scale

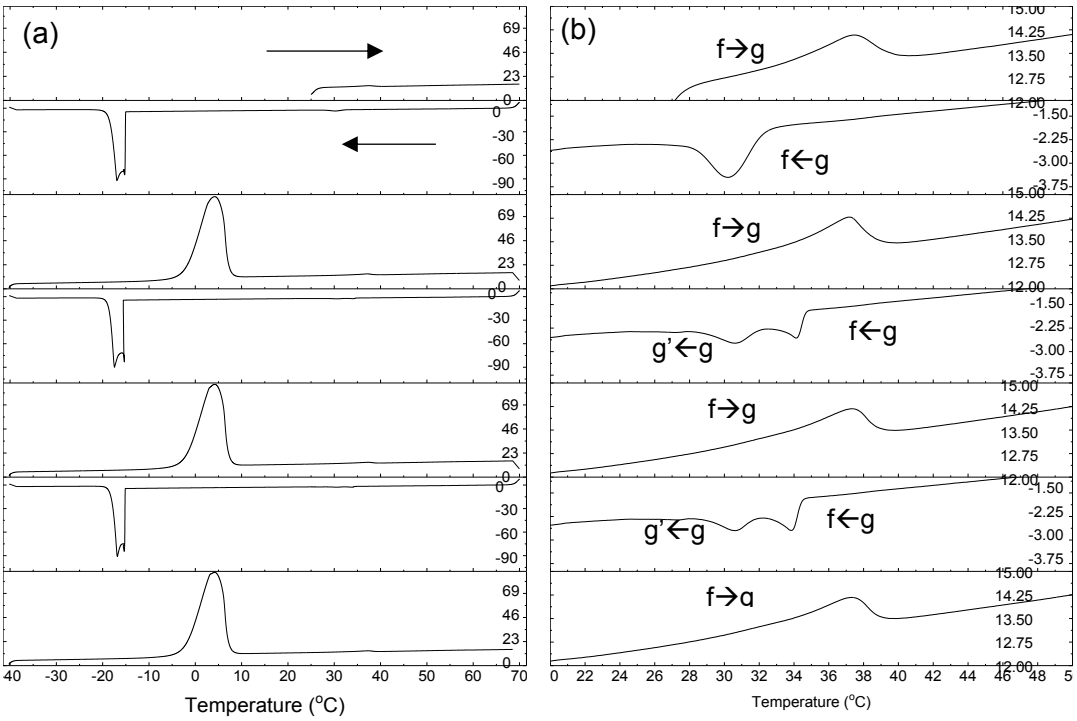


Figure A6.10. Shows the DSC thermographs for 5 wt% DODAC in an aqueous solution containing 0.085 wt% $CaCl_2$. The arrows represent the direction of the temperature, either heating or cooling and (b) is a zoomed in version of (a), showing the chain transitions. These are the same heating/cooling cycles as explained in figure 6.3, starting from the top and ending at the bottom.

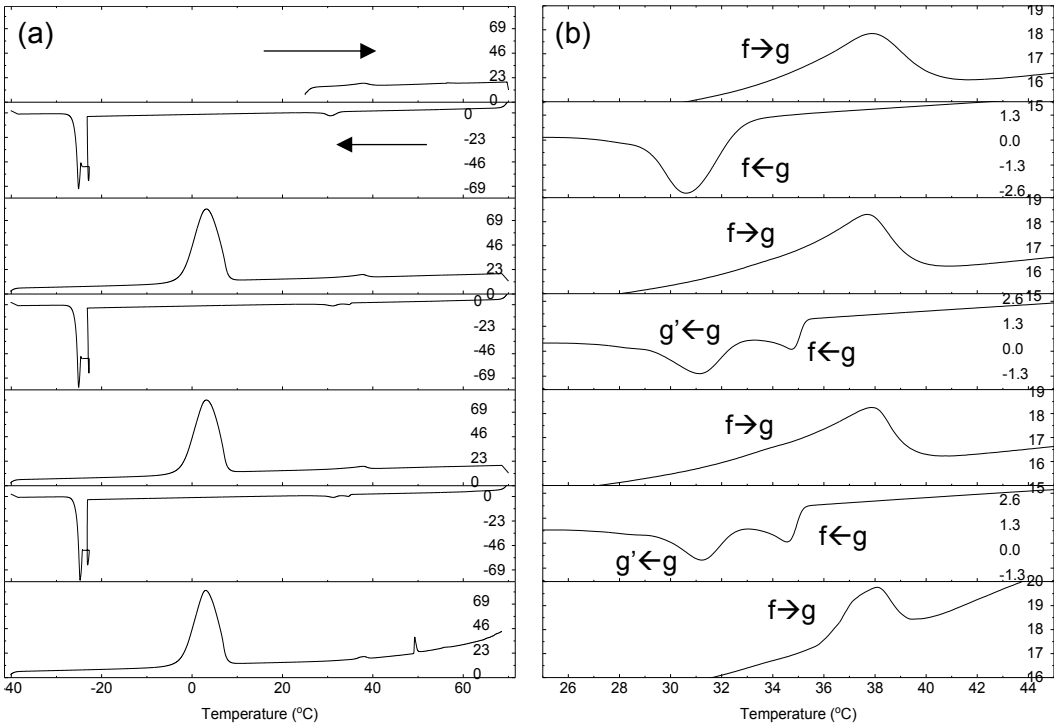


Figure A6.11. Shows the DSC thermographs for 11 wt% DODAC in an aqueous solution containing 0.085 wt% $CaCl_2$. The arrows represent the direction of the temperature, either heating or cooling and (b) is a zoomed in version of (a), showing the chain

transitions. These are the same heating/cooling cycles as explained in figure 6.3, starting from the top and ending at the bottom.

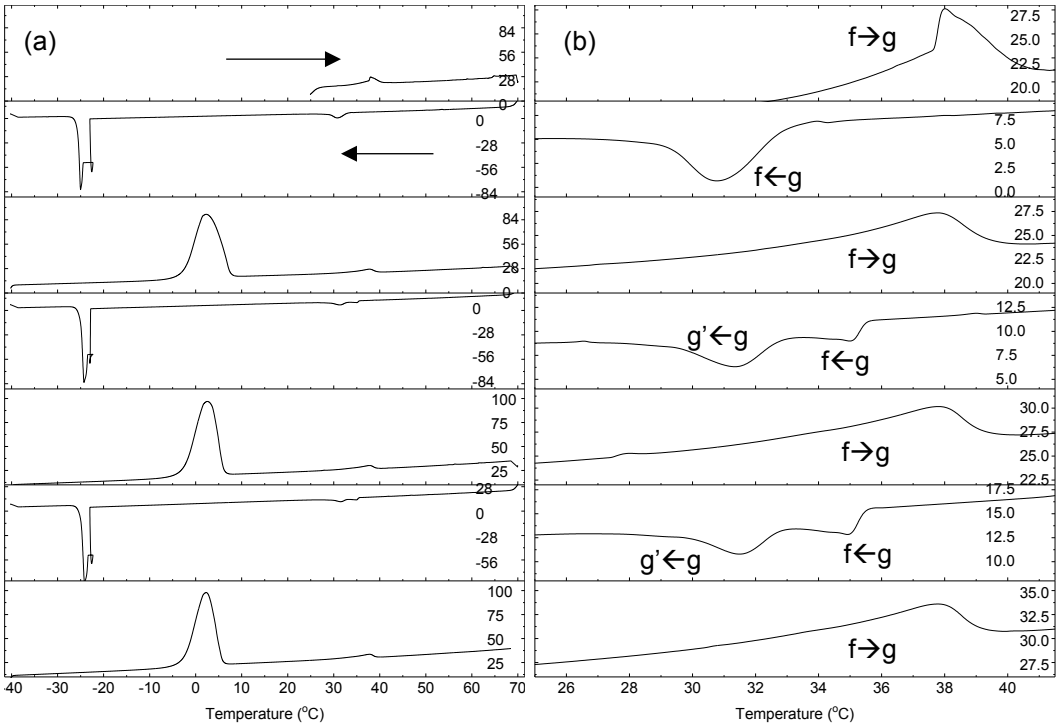


Figure A6.12. Shows the DSC thermographs for 14 wt% DODAC in an aqueous solution containing 0.085 wt% $CaCl_2$. The arrows represent the direction of the temperature, either heating or cooling and (b) is a zoomed in version of (a), showing the chain transitions. These are the same heating/cooling cycles as explained in figure 6.3, starting from the top and ending at the bottom.

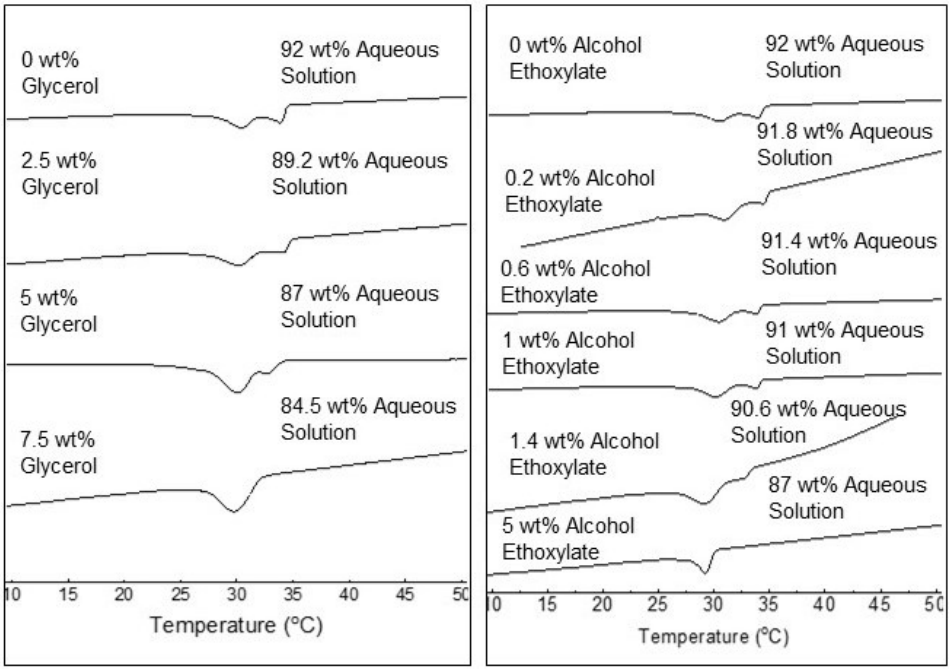


Figure A6.13. Second cooling chain transitions

Images for Chapter 7

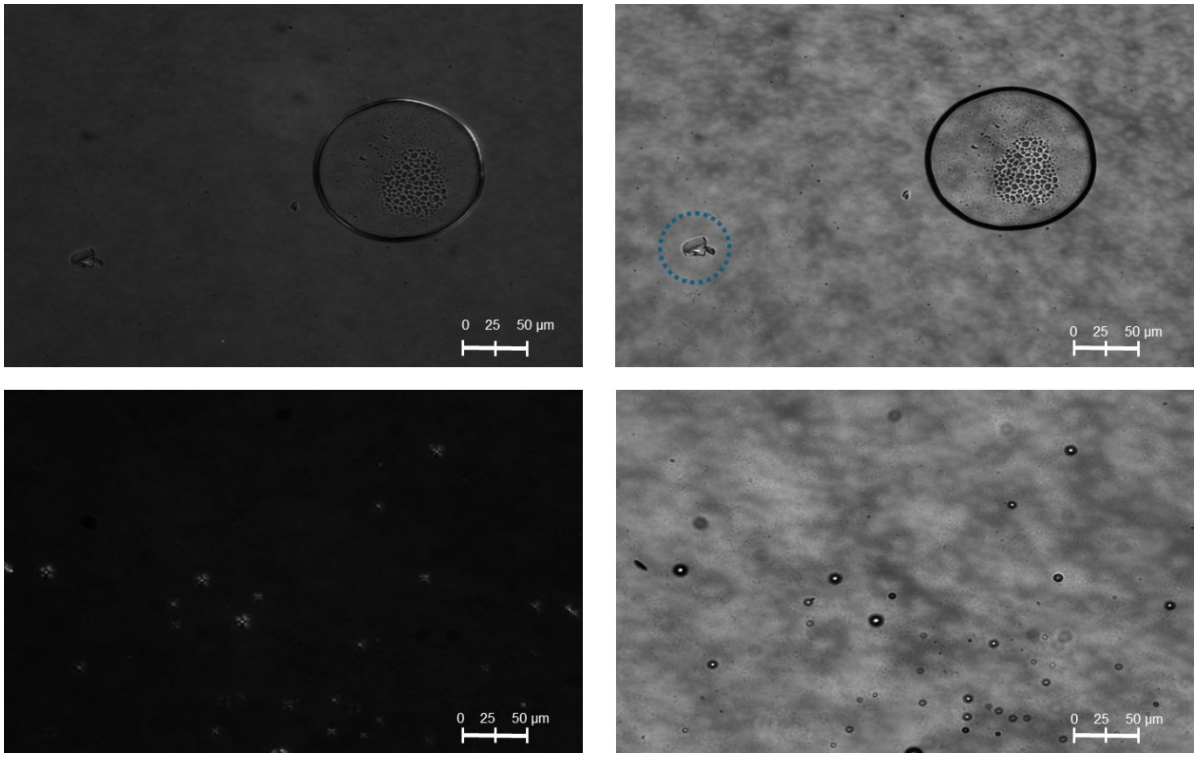


Figure A7.1. Images for probe sonicated DODAC solutions at room temperature (~20 ^{o}C)

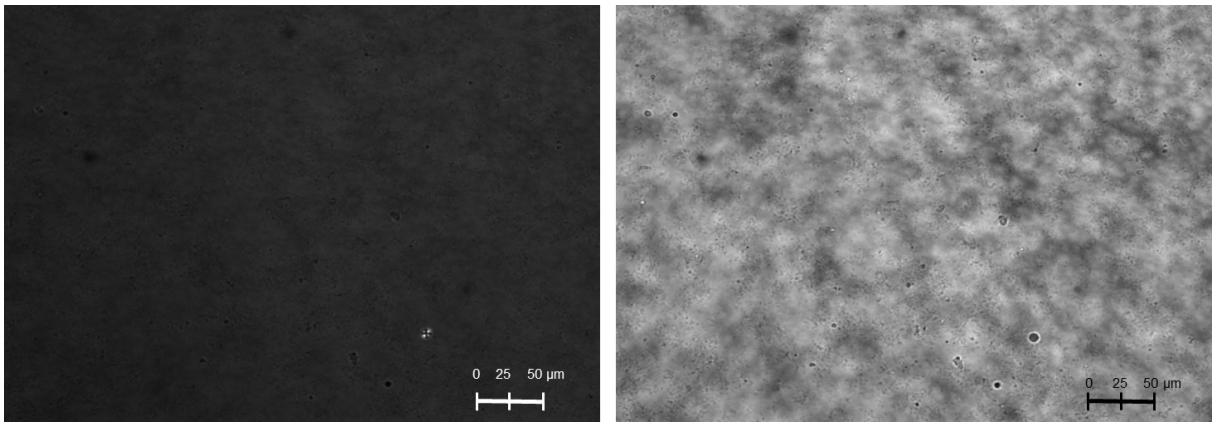


Figure A7.2. Images for bath sonicated DODAC solutions at room temperature (~20 ^{o}C)

Images for Chapter 8

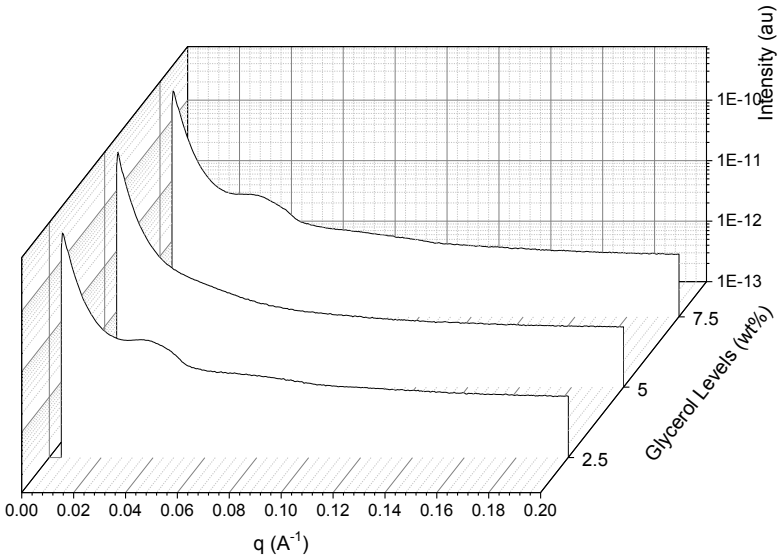


Figure A8.1. DODAC solutions containing glycerol before FT at 25 °C and 0.01 kbar

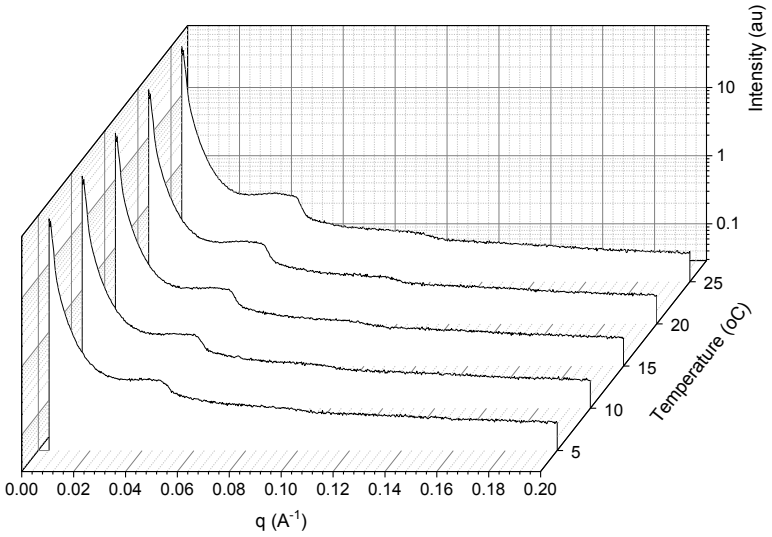


Figure A8.2. Cooling Linkam integrated SAXS patterns between 25-5.0 °C for DODAC solution

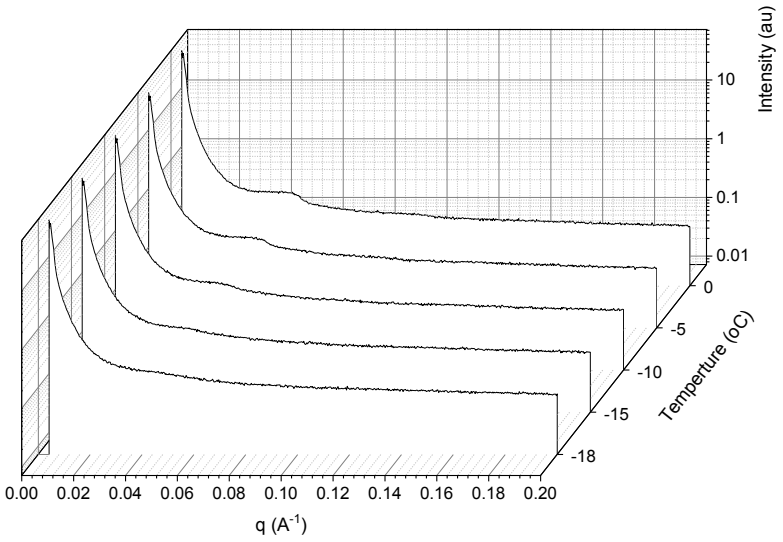


Figure A8.3. Cooling Linkam integrated SAXS patterns between 0 to -18 °C for DODAC solution

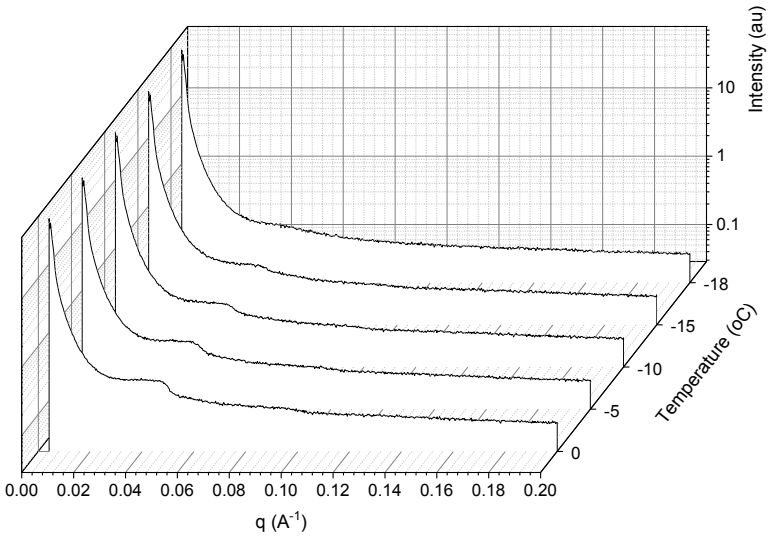


Figure A8.4. Heating Linkam integrated SAXS patterns between -18 to 0 °C for DODAC solution

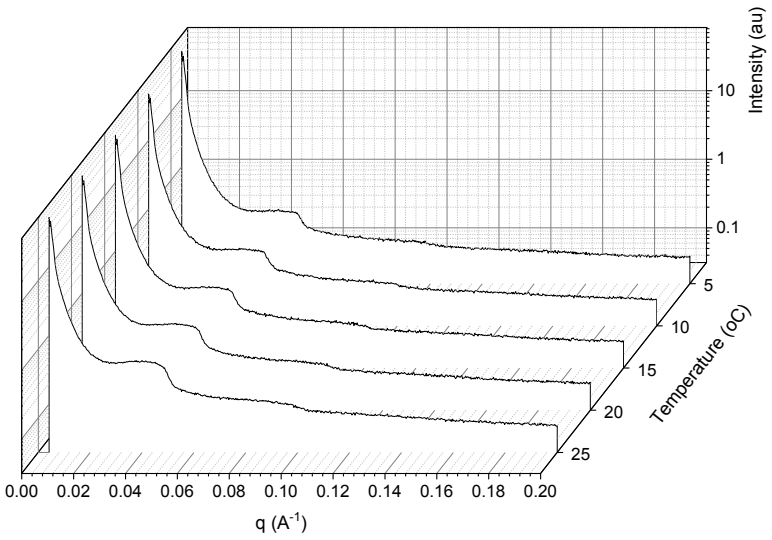


Figure A8.5. Heating Linkam integrated SAXS patterns between 5.0 to 25 ºC for DODAC solution

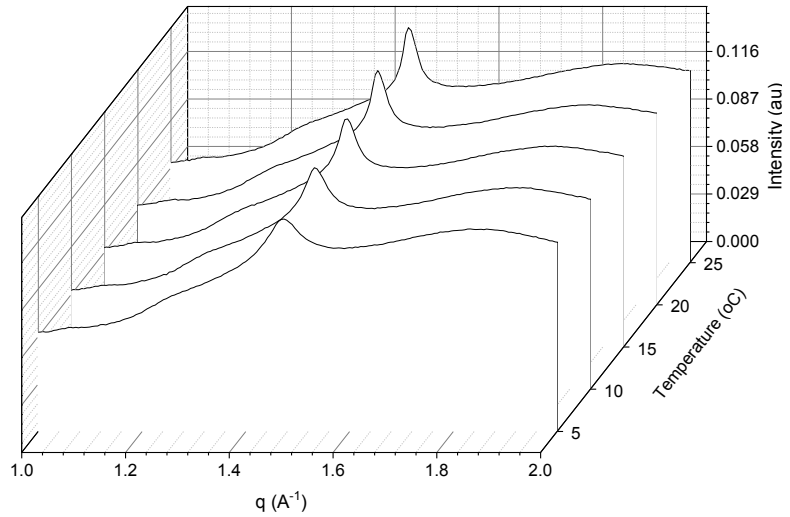


Figure A8.6. Cooling Linkam integrated WAXS patterns between 25-5.0 ºC for DODAC solution

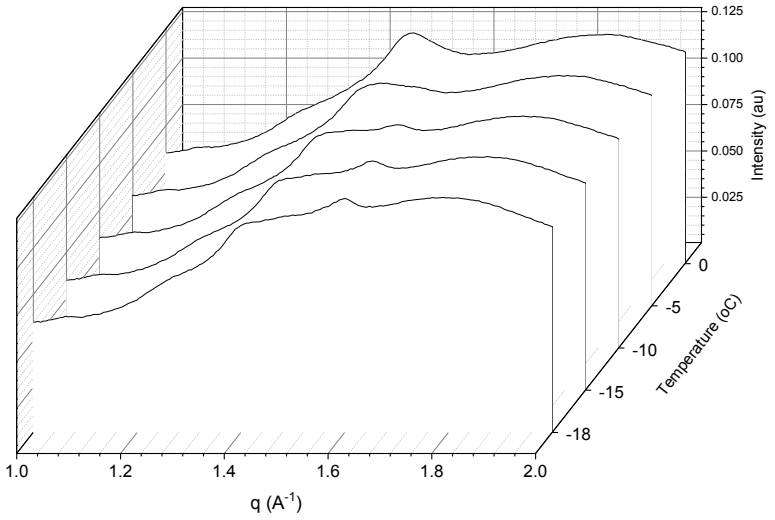


Figure A8.7. Cooling Linkam integrated WAXS patterns between 0 to -18 °C for DODAC solution

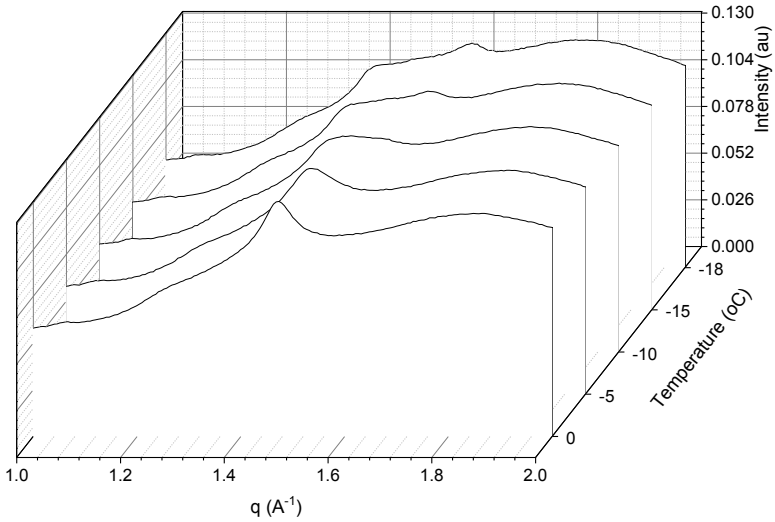


Figure A8.8. Heating Linkam integrated WAXS patterns between -18 to 0 °C for DODAC solution

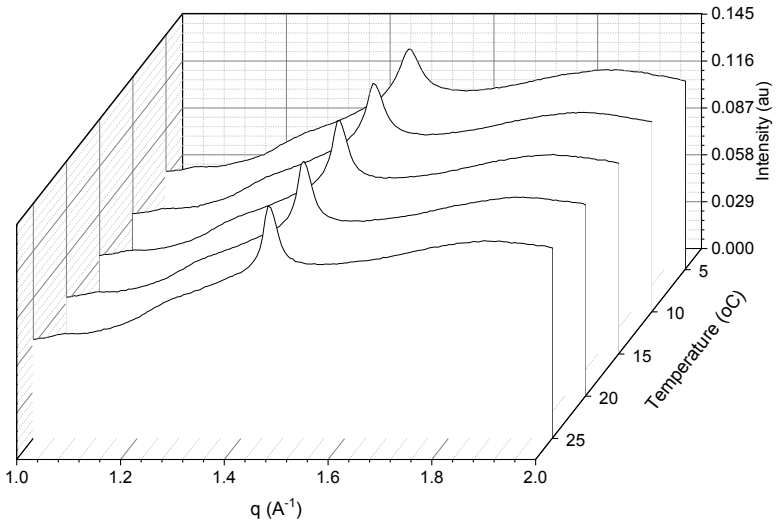


Figure A8.9. Heating Linkam integrated WAXS patterns between 5.0 to 25 °C for DODAC solution

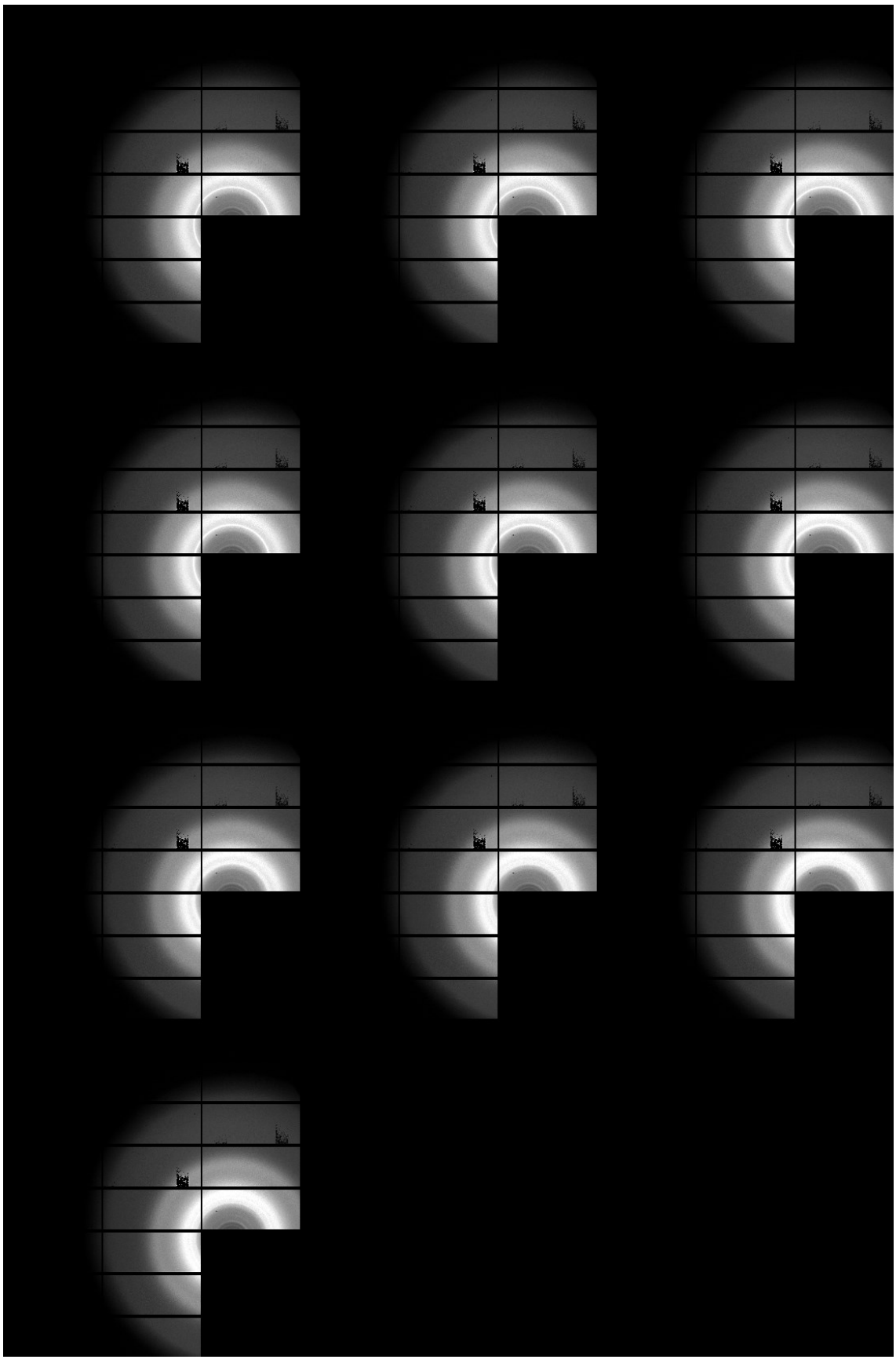
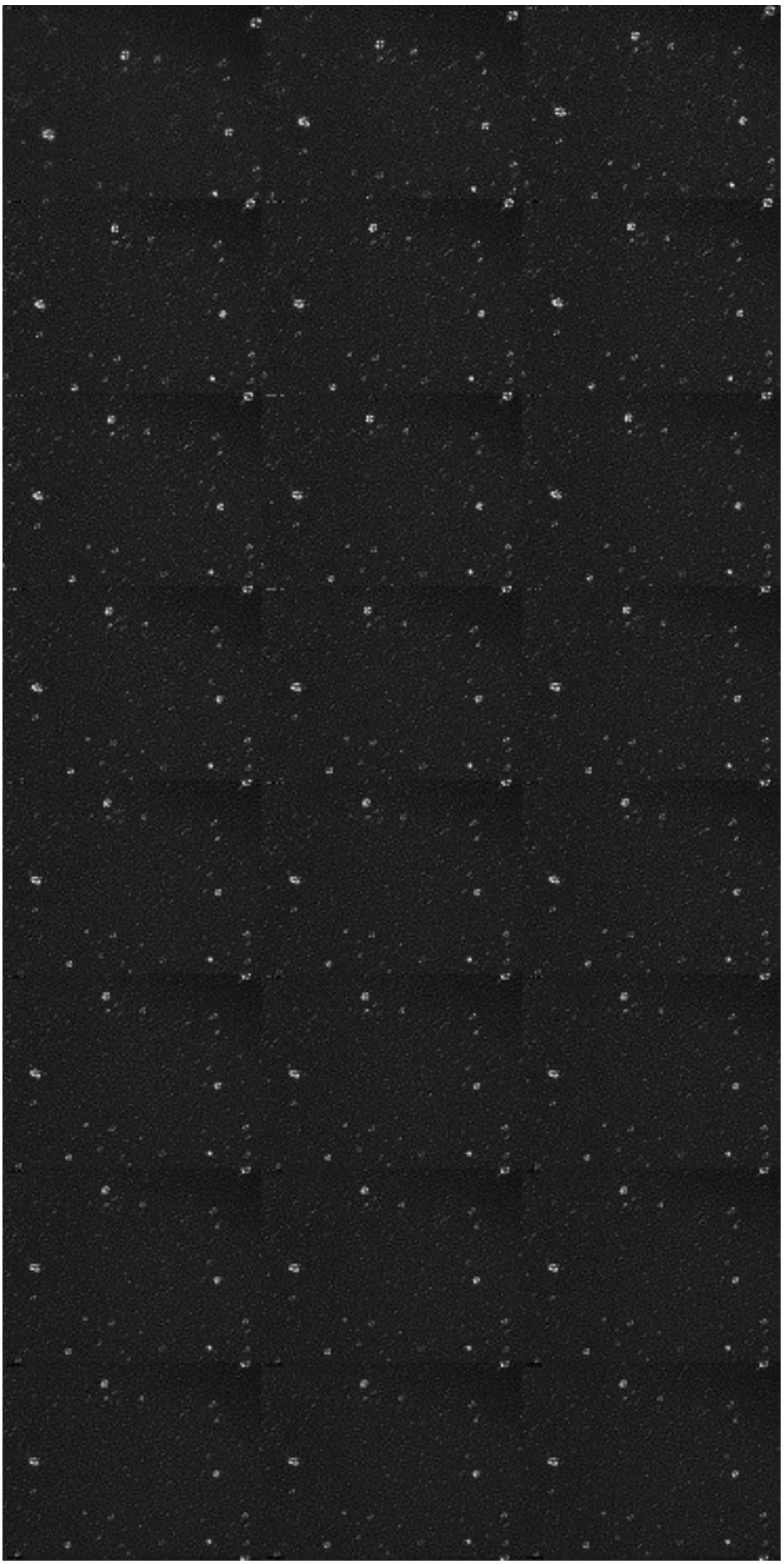
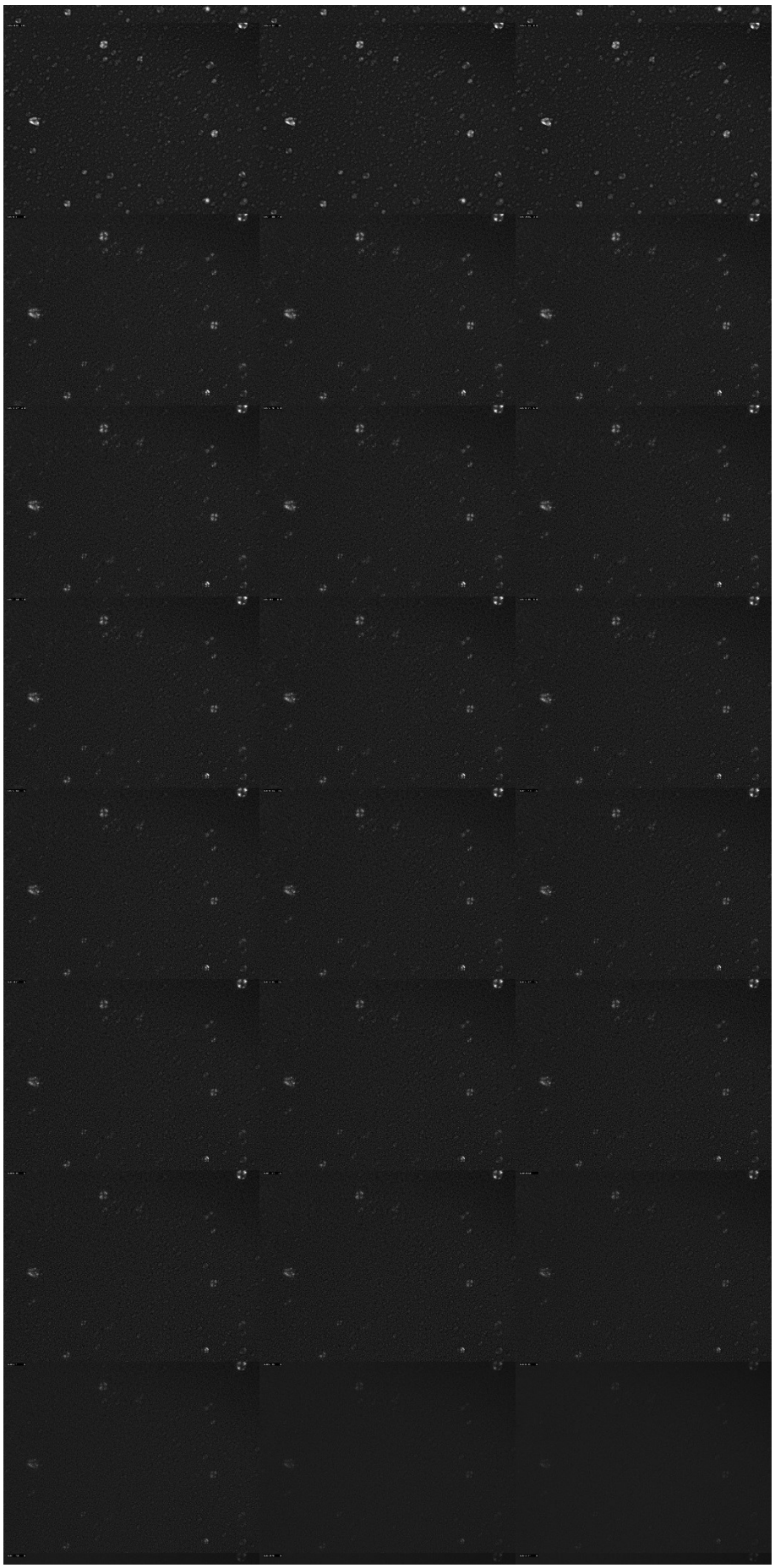


Figure A8.10. Cooling Linkam WAXS patterns between 25 to -18 ºC (from left to right) for DODAC solution





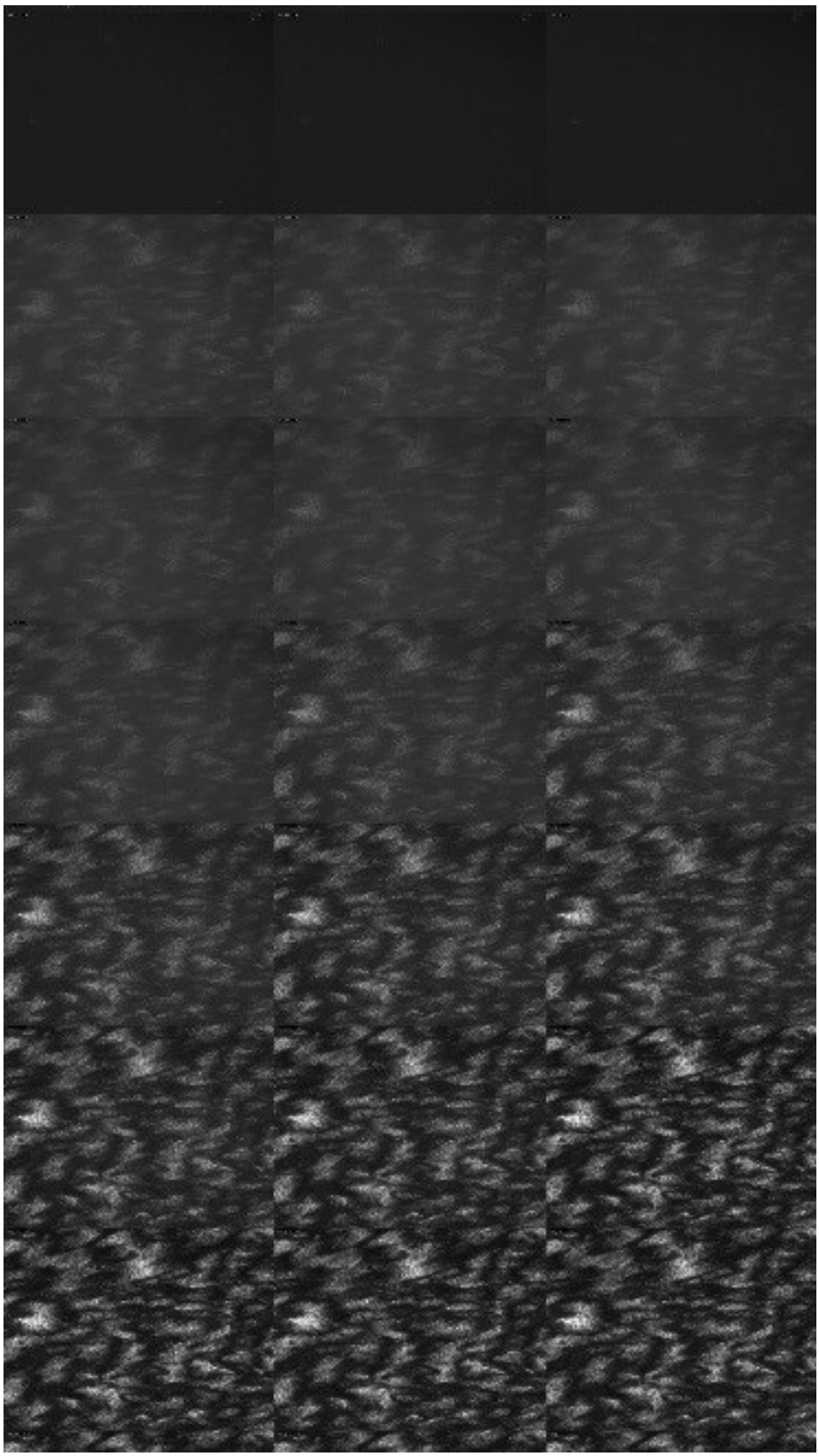


Figure A8.11. Shows figure 8.11 but for every -1.0 ºC

10. References

[1] K. Holmberg; B. Jonsson; B. Kronberg; B. Lindman, (2002) *Surfactants and Polymers in Aqueous Solution*, John Wiley & Sons, Ltd., 1-5

[2] M. R. Porter, (1991); Use of Surfactant Theory, In: *Handbook of Surfactants*, Springer, Blackie, USA, 24-48

[3] D. Myers (2006) *Surfactant Science and Technology*, 3rd edition, John Wiley & Sons. 1-25

[4] M. J. Rosen (2004) *Surfactants and Interfacial Phenomena*, 3rd edition, John Wiley & Sons, 1-33

[5] L. Margielewski, S. Plaza (2010) *Tribology-Materials, Surfaces & Interfaces*, **4**(2), 43-53

[6] Stig E. Friberg, (1997) Emulsion Stability In: *Food Emulsions*, S.E. Friberg, K. Larsson,(ed.), 3rd edition ; New York : Marcel Dekker

[7] E. Acosta, P. D. Mai, J. H. Harwell, D. A. Sabatini (2003) *J. Surfact. Deterg.*, **6**(4), 353-363

[8] P. Li, H. M. Nielsen, M. Fano, A. Müllertz (2013) *J. Pharm. Sci.*, **102**(8), 2689-2698

[9] J. D. V. Hamme, A. Singh, O. P. Ward (2006) *Biotechnology Advances*, **24**, 604-620

[10] Q. Y. Tang, Y. C. Chan, N. B. Wong, R. Cheung (2010) *Polym. Int.*, **59**, 1240-1245

[11] B.Shao (2010) Surfactants In*: Analysis of Endocrine Disrupting Compounds in Food*, Leo M. L. Nollet (ed.) 305-324

[12] P. Atkins, J. De Paula (2010) *Physical Chemistry*, 9th edition, Oxford University Press, Chapter 17, 649-652

[13] A. K. Chattopadhyay, L. Gaicha, R. M. Leblanc (1996) Branched Versus Linear Hydrocarbon Chains in Surfactants, In: *Surfactants in Solution*, A. K. Chattopadhyay, K. L. Mittal (ed.) **64**, Marcel Dekker, Inc., 1-31

[14] H. Sakai, A. Matsumura, S. Yokoyama, T. Saji, M. Abe (1999) *J. Phys. Chem. B*, **103**, 10737-10740

[15] E. F. Marques, O. Regev, A. Khan, M. G. Miguel, B. Lindman (1998) *J. Phys. Chem. B*, **102**, 6746-6758

[16] R. Lipowsky, E. Sackmann (1995) Structure and dynamics of membranes, In: *Handbook of Biological Physics*, Elsevier, Amsterdam

[17] J. T. Mang, S. Kumar, B. Hammoud (1994) *Europhysics Letters*, **28** (7), 489-494

[18] D. Myers (1991), *Surfaces, Interfaces, and Colloids*, VCH Pub., Inc., Chapter 3, 25-27

[19] X. Cui, S. Mao, M.Liu, H. Yuan, Y. Du, (2008) *Langmuir*, **24**, 10771-10775

[20] G. J. T. Tiddy, (1979) *Surfactants-water Liquid Crystal Phases*, **57** (1) of Physics report, 1-46

[21] E. D. Goddard (1986) *Colloids and Surfaces*, **19**, 255-300

[22] H. Kunieda, K. Shinoda (1976) *J.Phys. Chem*., **80**(22), 2468-2470

[23] J. N. Israelachvili, D. J. Mitchell, B. W. Ninham (1976) Theory of self-assembly of hydrocarbon amphiphiles into micelles and bilayers, *J. Chem. Soc. Faraday Trans 2*, **72**, 1525-1568

[24] C. Tanford (1972) *J. Phys. Chem*., **76**(21), 3020-3024

[25] A. M. Lapena, A. F. Gross, S. H. Tolbert, (2005) *Langmuir*, **21**, 470-480

[26] R. Nagarajan (2002) *Langmuir*, **18**, 31-38

[27] I. R. Cooke, M. Deserno (2006) Coupling between Lipid Shape and Membrane Curvature, *Biophysical Journal*, **91**, 487-495

[28] L. Courbin, J. P. Delville, J. Rouch, P. Panizza (2002) *Physical Review Letters*, **89**(14), 148305-1

[29] B. Medronho, S. Shafaei, R. Szopko, M. G. Miguel, U. Olsson, C. Schmidt (2008) *Langmuir*, **24**, 6480-6486

[30] B. L. S. Mui, P. R. Cullis, E. A. Evans, T. D. Madden (1993) *Biophys. J.*, **64**, 443-453

[31] D. Tareste, J. Shen, T. J. Melia, J. E. Rothman (2008) *PNAS*, **105**(7), 2380-2385

[32] C. M. Lin, C. S. Li, Y. J. Sheng, D. T. Wu, H. K. Tsao (2012) *Langmuir*, **28**(1), 689-700

[33] A. J. Sodt, R. W. Pastor, (2013) *Biophys. J.*, **104**, 2202-2211

[34] V. Luzzati, F. Husson (1962) *J. Cell Bio.,* **12**, 207-219

[35] V. Luzzati, A. Tardieu (1974) *Annu. Rev. Phys. Chem.*, **25**, 79-94

[36] T. Ichikawa, M. Yoshio, A. Hamasaki, S. Taguchi, F. Liu, X. Zeng, G. Ungar, H. Ohno, T. Kato (2012*) J. Am. Chem. Soc.*, **134**, 2634-2643

[37] A. Zabara, R. Negrini, O. Onaca-Fischer, R. Mezzenga (2013) *Small*, **9**(21), 3602-3609

[38] K. Fontell (1990) *Colloid Polym. Sci.*, **268**, 264-285

[39] K. Larsson (1989) *J. Phys. Chem.*, **93**(21), 7304-7314

[40] B. A. Lewis, D. M. Engelman (1983) *J. Mol. Biol.*, **166**, 211-217

[41] J. Pan, S. Tristram-Nagle, N. Kučerka, J. F. Nagle (2008) *Biophys. J.*, **94**(1), 117-124

[42] R. Bartucci, T. Páli, D. Marsh (1993) *Biochem.*, **32**, 274-281

[43] R. A. Böckmann, A. Hac, T. Heimburg, H. Grubmüller (2003) *Biophys. J.,* **85**, 1647-1655

[44] R. Ionov, A. Angelova (1996) *Thin Solid Films*, **284-285**, 809-812

[45] A. Aroti, E. Leontidis, M. Dubois, T. Zemb (2007) *Biophys. J.,* **93**, 1580-1590

[46] D. M. Leneveu, R. P. Rand, V. A. Parsegian (1976) *Nature*, **259**, 601-603

[47] S. A. Simon, T. J. McIntosh (1989) *Proc. Natl. Acad. Sci. USA*, **86**, 9263-9267

[48] W.-J. Sun, S. Tristram-Nagle, R. M. Suter, J. F. Nagle (1996) *Biophys. J.,* **71**, 885-891

[49] E. Evans, D. Needham (1987) *J. Phys. Chem.*, **91**, 4219-4228

[50] M. Kusube, N. Tamai, H. Matsuki, S. Kaneshina (2005) *Biophys. Chem*., **117**, 199-206

[51] E. N. Serrallach, R. Dijkman, G. H. De Haas, G. G. Shipley (1983) *J. Mol. Biol.*, **170**, 155-174

[52] T. Adachi, H. Takahashi, K. Ohki, I. Hatta (1995) *Biophys. J.*, **68**, 1850-1855

[53] J. Mou, J. Yang, C. Huang, Z. Shao (1994) *Biochem.*, **33**, 9981-9985

[54] B. Sanii, A. W. Szmodis, D. A. Bricarcllo, A. E. Oliver, A. N. Parikh (2010) *J. Phys. Chem. B*, **114**, 215-219

[55] S. Furuike, V.G. Levadny, S.J. Li, M. Yamazaki (1999) *Biophys. J.*, **77**, 2015-2023

[56] A. Tardieu, V. Luzzati (1973) *J. Mol. Biol.,* **75**, 711-733

[57] B. Tenchov, R. Koynova, G. Rapp (2001) *Biophys. J.*, **80**, 1873-1890

[58] M. J. Janiak, D. M. Small, G. G. Shipley (1979) *J. Biol. Chem. USA*, **254**, 6068-6078

[59] T. Heimburg (2000) *Biophys. J.,* **78**, 1154-1165

[60] R. Koynova, M. Caffrey (1998) *Biochimica et Biophysica Acta,* **1376**, 91-145

[61] J. M. Seddon, K. Harlos, D. Marsh (1983) *J. Biological Chem*., **258**(6), 3850-3854

[62] P. Saveyn, J. Cocquyt, M. Gradzielski, P. V. der Meeren (2008) *Colloids & Surfaces A: Physicochem. Eng. Aspects*, **319**, 62-70

[63] B. Maherani, E. Arab-Tehrany, A. Kheirolomoom, D. Geny, M. Linder (2013) *Biochimie*, **95**(11), 2018-2033

[64] E. A. Disalvo, L. I. Viera, L. S. Bakas, G. A. Senisterra (1996) *J. Colloid and Interface Sci*., **178**, 417-425

[65] B. Derjaguin, L. Landau (1993) *Progress in Surface Science*, **43**(1-4), 30-59

[66] B. Derjaguin (1940) *Trans. Faraday Soc*., **35**, 203-215

[67] H. Reerink, J. T. G. Overbeek (1954) *Discuss. Faraday Soc.,* **18**, 74-84

[68] D. Andelman (1995) Electrostatic Properties of Membranes: The Poisson-Boltzmann Theory*,* In: R. Lipowsky, E. Sacmann (eds.), *Handbook of Biological Physics*, Elsevier Science B. V**.**

[69] A. V. Dobrynin, M. Rubinstein, J. -F. Joanny (1998) *Journal of Chemical Physics*, **109**(20), 9172-9176

[70] K. S. Pitzer (1973) *J. Phys. Chem.,* **77**(2), 268-277

[71] A. M. Carmona-Ribeiro, B. R. Midmore (1992) *J. Phys. Chem*., **96**, 3542-3547

[72] J. E. Leibner, J. Jacobus (1977) *J. Phys. Chem.,* **81**, 130-135

[73] P. J. Missel, N. A. Mazer, G. B. Benedek, C.Y. Young (1980) *J. Phys. Chem.,* **84**, 1044-1057

[74] J. Eisenblätter, R. Winter (2006) *Biophys. J*., **90**, 956-966

[75] J. N. Israelachvili (2011) Steric (Polymer-Mediated) and Thermal Fluctuation Forces. In: *Intermolecular and Surface Forces*. 3rd edition, Academic Press, Waltham, Ma, 381-413

[76] W. Helfrich, Z. Naturforsh (1978) Steric Interaction of Fluid Membranes in Multilayer Systems, Zeitschrift für Naturforschung A, **33**(3), 305-315

[77] T. J. McIntosh, S. A. Simon (1993) *Biochemistry*, **32**, 8374-8384

[78] J. N. Israelachvili (2011) Interactions of Biological Membranes and Structures. In: *Intermolecular and Surface Forces.* 3rd edition, Academic Press, Waltham, MA, 577-616

[79] E. Feitosa, P. C. A. Barreleiro, G. Olofsson, (2000) *Chemistry and Physics of Lipids*, **105**, 201-213

[80] M. J. Hope, M. B. Bally, G. Webb, P. R. Cullis, (1985) *Biochim. Biophys. Acta,* **812**, 55-65

[81] R. C. MacDonald, R. I. MacDonal, B. P. M. Menco, K. Takeshita, N. K. Subbarao, L. -R. Hu (1991) *Biochim. Biophys. Acta*, **1061**(2), 297-303

[82] G. Maulucci, M. De Spirito, G. Arcovito, F. Boffi, A. C. Castellano, G. Briganti (2005) *bio. Phys. J.*, **88**, 3545-3550

[83] C. Huang (1969*) Bio. Chem.*, **8**(1), 344-352

[84] L. Kudsiova, J. Ho, B. Fridrich, R. Harvey, M. Keppler, T. Ng, S. L. Hart, A. B. Tabor, H. C. Hailes, M. J. Lawrence (2011) *Mol. Biosyst.,* **7**, 422-436

[85] B. Chaize, J. -P. Colletier, M. Winterhalter, D. Fournier (2004) *Artificial Cells, Blood Substitutes, and Biotechnology*, **32**(1), 67-75

[86] G. Strauss, H. Hauser (1986) *Proc. Natl. Acad. Sci. USA*, **83**, 2422-2426

[87] M. Ueno, S. Sriwongsitanont (2005) *Polymer,* **46**, 1257-1267

[88] C. Chen, D. Han, Y. Zhang, Y. Yuan, X. Tang (2010) *International Journal or Pharmaceutics*, **387**, 147-153

[89] M. C. Sandström, E. Johansson, K. Edwards (2008) *Biophys. Chem.*, **132,** 97-103

[90] H. Koide, A. Okamoto, H. Tsuchida, H. Ando, S. Ariizumi, C. Kiyokawa, M. Hashimoto, T. Asai, T. Dewa, N. Oku (2016) *Journal of Controlled Release*, **228**, 1-8

[91] K. Sugihara, B. Jang, M. Schneider, J. Vörös, T. Zambelli, (2012) *Soft Matter*, **8**, 5525-5531

[92] T. Kaasgaard, O. G. Mouritsen, K. Jørgensen (2003) *Biochimica et Biophysica Acta*, **1615**, 77-83

[93] V. L. Bronshteyn, P. L. Steponkus (1993) *Biophys. J.,* **65**, 1853-1865

[94] A. Miskowiec, Z. N. Buck, M. C. Brown, H. Kaiser, F. Y. Hansen, G. M. King, H. Taub, R. Jiji, J. W. Cooley, M. Tyagi, S. O. Diallo, E. Mamontov, K. W. Herwig (2014) *EPL*, **107**, 28008

[95] W. J. Gordon-Kamm, P. L. Steponkus (1984) *Proc. Natl. Acad. Sci. USA*, **81**, 6373-6377

[96] M. Uemura, R. A. Joseph, P. L. Steponkus (1995) *Plant Physiol*., **109**, 15-30

[97] M. Caffrey (1987) *Biochimica et Biophysica Acta*, **896**, 123-127

[98] P. L. Steponkus, D. V. Lynch (1988) Journal of Bioenergetics and Biomembrane, 21(1), 21-41

[99] M. I. Levinson (1999) Rinse-added Fabric Softener Technology at the Close of the Twentieth Century, *J. Surfact. Deterg.,* **2**(2), 223-253

[100] R. Puchta (1984) *J. Am. Oil Chem. Soc*., **61**, 367-376

[101] H. Kunieda, K. Shinoda (1978) *J. Phys. Chem*., **82**(15), 1710-1714

[102] R. G. Laughlin, R. L. Munyon, Y. C. Fu, A. J. Fehl (1990) *J. Phys. Chem*., **94**, 2546-2552

[103] R. G. Laughlin, R. L. Munyon, J. L. Burns, T. W. Coffindaffer, Y. Talmon (1992) *J. Phys. Chem*., **96**, 374-383

[104] M. Jung, A. L. German, H. R. Fisher (2001) *Colloid Polym. Sci*., **279**, 105-113

[105] T. Kawai, J. Umemura, T. Takenaka (1986) *Langmuir,* **2**, 739-743

[106] R. G. Laughlin, R. L. Munyon, Y. C. Fu, T. J. Emge (1991) *J. Phys. Chem.*, **95**, 3852-3856

[107] G. C. Shearman, S. Ugazio, L. Soubiran, J. Hubbard, O. Ces, J. Seddon, R. H. Templer (2009) *J. Colloid Interface Sci*., **331**, 463-469

[108] G. Cassin, C. de Costa, J. P. M. van Duynhoven, W. G. M. Agterof (1998) *Langmuir*, **14**, 5757-5763

[109] L. R. Tsuruta, M. M. Lessa, A. M. Carmona-Ribeiro (1995) *Langmuir*, **11**, 2938-2943

[110] I. M. Cuccovia, E. Feitosa, H. Chaimovich, L. Sepulveda, W. Reed (1990) *J. Phys. Chem*., **94**, 3722-3725

[111] A. M. Carmona-Ribeiro (1989) *J. Phys. Chem*. **93**, 2630-2634

[112] K. Kano, A. Romero, B. Djermouni, H. J. Ache, J. H. Fendler (1979) *J. Am. Chem. Soc*., **101**(15), 4030-4037

[113] R. A. Gonçalves, B. Lindman, M. G. Miguel, T. Iwata, Y. M. Lam, (2018) *J. Colloid and Interface Sci*., **528**, 400-409

[114] G. C. Shearman, S. Ugazio, L. Soubiran, J. Hubbard, O. Ces, J. M. Seddon, R. H. Templer (2009) *Journal of Colloid and Interface Science*, **331**, 463-469

[115] H. Z. Yuan, X. L. Tan, G. Z. Cheng, S. Zhao, L. Zhang, S. Z. Mao, J. Y. An, J. Y. Yu, Y. R. Du (2003) J. Phys. Chem. B, 107, 3644-3649

[116] R. L. Thurmond, G. Lindblom, M. F. Brown (1993) *Biochem.,* **32**, 5394-5410

[117] A. Steel, S. W. Carr, M. W. Anderson (1994) *J. Chem. Commun.,* 1571-1572

[118] S. Lasič, I. Åslund, C. Oppel, D. Topgaard, O. Söderman, M. Gradzielski (2011) *Soft Matter*, **7**, 3947-3955

[119] N. E. Jacobsen (2007) *NMR Spectroscopy Explained*, New Jersey, John Wiley & Sons, Inc.

[120] J. Keeler (2010) *Understanding NMR Spectroscopy*, 2nd, John Wiley & Sons, Ltd.

[121] T. Nakagawa (1966) *Bulletin of the Chemical Society of Japan*, **39**, 1006-1008

[122] H. Günther (2013) *NMR Spectroscopy: Basic Principles, Concepts, and Applications in Chemistry*, 3rd, Weinheim, Germany, Wiley-VCH.

[123] D. S. Wishart, B. D. Sykes, F. M. Richards (1991) *J. Mol. Biol.*, **222**, 311-333

[124] E. L. Hahn (1953) *Phys. Today*, **6**(11), 4-9

[125] R. Brown (1828) *The Philosophical Magazine*, **4**(21), 161-173

[126] J. T. Edward (1970) *Journal of Chemical Education*, **47**(4), 261-270

[127] E. O. Stejskal, J. E. Tanner (1965) *J. Chem. Phys*., **42**, 288-292

[128] K. Horbaschek, H. Hoffmann, C. Thunig (1998) *Journal of Colloid and Interface Science*, **206**, 439-456

[129] K. Rendall, G. J. T. Tiddy, M. A. Trevethan (1983) *J. Chem. Soc., Faraday Trans. 1*, **79**, 637-649

[130] Y. Rançon, J. Charvolin (1988) *J. Phys. Chem*., **92**, 2646-2651

[131] D. M. Murphy (2001) *Fundamentals of Light Microscopy and Electronic Imaging*. New York, John Wiley and Sons.

[132] T. Hatakeyama, F. X. Quinn (1999) *Thermal Analysis, Fundamentals and Applications to Polmer Science*, 2nd, Chichester, John Wiley & Sons Ltd.

[133] C. Huang, S. Li (1999) *Biochimica et Biophysica Acta*, **1422**, 273-307

[134] P. Atkins, J. De Paula (2010) *Atkins' Physical Chemistry*, 9th, USA, W. H. Freeman and Co.

[135] A. Guinier (1963) *X-ray Diffraction in Crystals, Imperfect Crystals, and Amorphous Bodies*, San Francisco, W. H. Freeman.

[136] B. E. Warren (1969) X-ray Diffraction, Reading, Addison-Wesley Publishing Company, Inc.

[137] D. Marsh (2012) *Chemistry and Physics of Lipids*, **165**, 59-76

[138] W. J. Sun, S. Tristram-Nagle, R. M. Suter, J. F. Nagle (1996*) Proc. Natl. Acad. Sci. USA*, **93**, 7008-7012

[139] N. Brooks, B. L. L. E. Gauthe, N. J. Terrill, S. E. Rogers, R. H. Templer, O. Ces, J. Seddon (2010) *Review of Scientific Instruments*, **81**, 064103

[140] H. Hoffmann, C. Thunig, P. Schmiedel, U. Munkert, (1994) *Langmuir*, **10**, 3972-3981

[141] E. F. Marques, O. Regev, A. Khan, M. da Graça Miguel, B. Lindman, (1998) *J. Phys. Chem. B*, **102**, 6746-6758

[142] E. Feitosa, P. C. A. Barreleiro, G. Olofsson, (2000) *Chem. & Phys. of Lipids*, **105**, 201-213

[143] H. Kunieda, K. Shinoda, (1978) *J. Phys. Chem*., **82** (15), 1710-1714

[144] T. Takano, Y. Kawabata, T. Suzuki, T. Kato, (2015) *J. Phys. Chem. B,* **119**, 11656-11663

[145] I. Daniel, P. Oger, R. Winter (2006) *Chem. Soc. Rev*., **35**, 858-875

[146] R. Winter, W. Dzwolak, (2005) *Phil. Trans. R. Soc. A*, **363**, 537-563

[147] R. Winter, (2001) *Current Opinion in Colloid & Interface Sci.* **6**, 303-312

[148] N. J. Brooks, O. Ces, R.H. Templer, J. M Seddon, (2011) *Chem. Phys. Lipids*, **164**, 89–98

[149] I. D. Skanes, J. Stewart, K. M. W. Keough, M. R. Morrow, (2006). *Phys. Rev. E*, **74**, 051913

[150] N. Brooks, B. L. L. E. Gauthe, N. J. Terrill, S. E. Rogers, R. H. Templer, O. Ces, J. Seddon (2010) *Review of Scientific Instruments*, **81**, 064103

[151] D. C. Wack, W. W. Webb (1989) *Physical Review A*, **40**(5), 2712-2730

[152] M. Kodama, M. Kuwabara, S. Seki, (1981) *Thermochimica Acta*, **50**, 81-91

[153] R. G. Laughlin, R. L. Munyon, Y. -C. Fu, A. J. Fehl, (1990) *J. Phys. Chem.*, **94**, 2546-2552

[154] A. M. Carmona-Ribeiro, H. Chaimovich (1983) *Biochimica et Biophysica Acta*, **733**, 172-179

[155] L. Liu, R. Pansu, J. Roncin, J. Faure, T. Arai, K. Tokumaru (1992) *J. Colloid Interface Sci.*, **148**(1), 118-128

[156] K. P. Shaw, N. J. Brooks, J. A. Clarke, O. Ces, J. M. Seddon, R. V. Law (2012) *Soft Matter*, **8**, 1070-1078

[157] B. A. Cunningham, A.-D. Brown, D. H. Wolfe, W. P. Williams, A. Brain, (1998), *Ripple phase formation in phosphatidylcholine: Effect of acyl chain relative length, position, and unsaturation,* Physical Review, **58** (3), 3662-3672

[158] O. Mertins, M. I. Z. Lionzo, Y. M. S. Micheletto, A. R. Pohlmann, N. P. da Silveira (2009) *Materials Science and Engineering C*, **29**, 463-469

[159] P. Saveyn, P. V. der Meeren, M. Zackrisson, T. Narayanan, U. Olsson (2009) *Soft Matter*, **5**, 1735-1742

[160] Y. Kobayashi, K. Fukada (1998) *Biochimica et Biophysica Act*, **1371**, 363-370.

[161] A. M. Carmona-Ribeiro, L. S. Yoshida, H. Chaimovich (1985) *J. Phys. Chem.*, **89**(13), 2928-2933

[162] H. Hoffmann, C. Thunig, P. Schmiedel, U. Munkert (1994), Langmuir, 10, 3972-3981

[163] P. Saveyn, J. Cocquyt, M. Gradzielski, P. V. der Meeren, (2008), *Colloids and Surfaces A: Physicochem. Eng. Aspects*, **319**, 62-70

[164] M. M. A. E. Claessen, B. F. van Oort, F. A. M. Leerrmakers, F. A. Hoekstra, M. A. C. Stuart (2004*) Biophys. J.*, **87**, 3882-3893

[165] S. W. Hui, T. P. Stewart, L. T. Boni, P. L. Yeagle, (1981) *Science 212*, 921-923.

[166] M. Traikia; D. E. Warschawski; M. Recouvreur; J. Cartaud; P. F. Devaux, (2000) *Eur. Biophys. J.*, **29**, 184-195

[167] K. Kano, T. Ishlbashi, T. Ogawa, (1983*) J. Phys. Chem.*, **87**, 3010-3012

[168] N. Du, R. Song, X. Zhu, W. Hou, H. Li, R. Zhang (2014) *Chem. Commun.,* **50**, 10573-10576

[169] N. Du, R. Song, H. Zhang, J. Sun, S. Yuan, R. Zhang (2016) *Colloids and Surfaces A: Eng. Aspects*, **509**, 195-202

[170] L. R. Tsuruta, M. M. Lessa, A. M. Carmona-Ribeiro (1995) *Langmuir,* **11**, 2938-2943

[171] G. C. Shearman, S. Ugazio, L. Soubiran, J. Hubbard, O. Ces, J. M. Seddon, R. H. Templer, (2009) *J. Colloid and Interface Sci.*, **331**, 463-469

[172] R. G Laughlin, R. L. Munyon, Y. -C. Fu, A. J. Fehl (1990) *J. Phys. Chem*., **94**, 2546-2552

[173] K. Deguchi, J. Mino, (1977), J. Colloid & Interface Sci., **65** (1), 155-161

[174] P. L. Steponkus, D. V. Lynch, (1989) *J. Bioenergetics and Biomembranes*, **21** (1), 21-41

[175] P. L. Steponkus, (1984) *Ann. Rev. Plant Physiol*, **35**, 543-584

[176] M. Caffrey, (1987) *Biochimica et Biophysica Acta*, **896**, 123-127

[177] M. Traikia, D. E. Warschawski, M. Recouvreur, J. Cartaud, P. F. Devaux, (2000) *Eur. Biophys. J.*, **29**, 184-195

[178] M. Ueno, S. Sriwongsitanont, (2005) *Polymer*, **46**, 1257-1267

[179] T. Arakawa, S. N. Timasheff (1982) *Biochemistry*, **21**(25), 6536-6544

[180] P. Westh (2003) *Biophysical Journal*, **84**, 341-349

[181] A. Nowacka, S. Douezan, L. Wadsö, D. Topgaard, E.Sparr (2012) *Soft Matter*, **8**, 1482-1491

[182] R. M. Hill (1998) *Current Opinion in Colloid & Interface Science*, **3**, 247-254

[183] E. Jurado, J. M. Vicaria, JF. García-Román (2012) *J. Surfact. Deterg*., **15**, 251-258

[184] J. Drelich, R. Zahn, J. D. Miller, J. K. Borchardt (2002) *Contact Angle, Wettability and Adhesion*, **2**, 253-264

[185] O. Tirosh, Y. Barenholz, J. Katzhendler, A. Priev (1998) *Biophysical Journal,* **74**, 1371-1379

[186] A. Priev, S. Zalipsky, R. Cohen, Y. Barenholz (2002) *Langmuir*, **18**, 612-617

[187] M. Rovira-Bru, D. H. Thompson, I. Szleifer (2002) *Biophysical Journal*, **83**, 2419-2439

[188] A. Pommella, S. Caserta, S. Guido (2013) *Soft Matter*, **9**, 7545-7552

[189] E. Feitosa, P. C. A. Barreleiro, G. Olofsson, (2000) *Chem. & Phys. of Lipids*, **105**, 201-213

[190] F. Bonosi, G. Gabrielli (1991) *Colloids and surfaces*, **52**, 277-285

[191] M. Gugliotto, M. J. Politi, H. Chaimovich (1998) *J. Colloid and Interface Sci.*, **198**, 1-5

[192] A. M. Carmona-Ribeiro, H. Chaimovich (1986) *Biophys. J.*, **50**, 621-628

[193] D. B. Nascimento, R. Rapuano, M. M. Lessa, A. M. Carmona-Ribeiro (1998) *Langmuir*, **14**, 7387-7391

[194] L. Liu, R. Pansu, J. Roncin, J. Faure, T. Arai, K. Tokumaru (1992) *J. Colloid and Interface Sci.*, **148**(1), 118-128

[195] E. Feitosa, N. M. Bonassi, W. Loh (2006) *Langmuir*, **22**, 4512-4517

[196] S. Lasič, I. Åslund, C. Oppel, D. Topgaard, O. Söderman, M. Gradzielski (2011) *Soft Matter*, **7**, 3947-3955

[197] Y. Yan, H. Hoffman, A. Makarsky, W. Richter, Y. Talmon (2007*) J. Phys. Chem. B*, **111**, 6374-6382

[198] R. Abdel-Rahem (2011) *J. Dispersion sci. & Tech.*, **32**, 784-794

[199] O. López, A. de le Maza, L. Coderch, C. López-Iglesias, E. Wehrli, J. L. Parra (1998) *FEBS Letters*, **426**, 314-318

[200] M. Silvander, G. Karlsson, K. Edwards (1996) *J. Colloid and Interface Sci.*, **179**, 104-113

[201] P. C. A. Barreleiro, G. Olofsson, W. Brown, K. Edwards, N. M. Bonassi, E. Feitosa (2002) *Langmuir*, **18**, 1024-1029

[202] D. J. Mitchell (1983) *J. Chem. Soc., Faraday Trans. 1*, **79**, 975-1000

[203] K. Edwards, M. Almgren (1990*) Progr. Colloid Polym. Sci.*, **82**, 190-197

[204] D. G. Hunter, B. J. Frisken (1998), *Bio. Phys. J.*, **74**, 2996-3002

[205] B. J Frisken, C. Asman, P. J. Patty (2000) *Langmuir*, **16**, 928-933

[206] A. Lopes, K. Edwards, E. Feitosa (2008) *J. Colloid Interface Sci*., **322**, 582-588

[207] R. Lawaczeck, M. Kianosho, J. L. Giraudet, S. I. Chan (1975) *Nature*, **256,** 584-586

[208] S. Mourtas, M. Haikou, M. Theodoropoulou, C. Tsakiroglou, S. G. Antimisiaris (2008) *Journal of Colloid and Interface Science*, **317**, 611-619

[209] Carmona-Ribeiro, A. M. (2010) *International Journal of Nanomedicine*, **5**, 249–259.

[210] R. F. Flewelling, W. L. Hubbell (1986) *Biophys. J.,* **49**(2), 531-540

[211] M. M. Lapinski, A. C. -Forero, A. J. Greiner, R. Y. Ofoli, G. J. Blanchard (2007) *Langmuir*, **23**, 11277-11683

[212] E. Feitosa, P. C. A. Barreleiro, G. Olofsson (2000) *Chem. Phys. of Lipids*, **105**, 201-213

[213] J. M. H. Kremer, M. W. J. v. d. Esker, C. Pathmamanoharan, P. H. Wiersema (1977) *Biochem.*, **16**(17), 3932-3935

[214] R. B. Pansu, B. Arrio, J. Roncin, J. Faure (1990) *J. Phys. Chem.*, **94**, 796-801

[215] U. Herrmann, J. H. Fendler (1979), *Chemical Physics Letters*, **64**(2), 270-274

[216] M. -P. Pileni (1980), *Chemical Physics Letters*, **71**(2), 317-321

[217] M. Andersson, L. Hammarstrom, K. Edwards (1995*) J. Phys. Chem.*, **99**, 14531-14538

[218] M. Holz, S. R. Heil, A. Sacco (2000) *Phys. Chem. Chem. Phys*., **2**, 4740-4742

[219] D. W. McCall, D. C. Douglass (1965) *J. Phys. Chem.*, **69**(6), 2001-2011

[220] S. E. Schullery, C. F. Schmidt, P. Felgner, T. W. Tillack, T. E. Thompson (1980) *Biochem.*, **19**, 3919-3923

[221] A. V. Okhulkov, Y. N. Demianets, Y. E. Gorbaty (1994) *J. Chem. Phys*., **100**, 1578-1588

[222] D. M. LeNeveu, R. P. Rand (1977) *Biophys. J*., **18**(2), 209-230

[223] A. C. Cowley, N. L. Fuller, R. P. Rand, V. A. Parsegian (1978), *Biochemistry*, **17**(15), 3163-3168

[224] M. Goto, Y. Ito, S. Ishida, N. Tamai, H. Matsuki, S. Kaneshina (2011) *Langmuir*, **27**(5), 1592-1598

[225] B. Tenchov, R. Koynova, G. Rapp (2001) *Biophys. J.,* **80**, 1873-1890